Analyzing and Characterizing Hydroclimatic Extremes over Canada

by

Xuezhi Tan

A thesis submitted in partial fulfillment of the requirements for the degree of

Doctor of Philosophy
in
Water Resources Engineering

Department of Civil and Environmental Engineering
University of Alberta

Abstract

Climate variability, climate change and human activities have impacted various components of the hydrologic cycle in many regions across the world. In particular, changes to the global climate system can affect the magnitude and frequency of extreme hydrological events, thus altering the risk to critical infrastructure. Therefore, under the possible impact of climate change, the stationary assumption of the conventional frequency analysis is generally invalid. Assessing the validity of the stationarity assumption for Canadian hydroclimatic variables is important to justify the practice of conventional hydrologic frequency analysis in a changing climate. On the other hand, understanding how non-stationarity have affected the magnitude and frequency of hydrologic events in Canada, and developing new statistical techniques (or extensions of existing techniques) are important to address non-stationarity and to reduce uncertainties associated with frequency analysis. Alternatively, it will be beneficial to reliably predict future Canadian precipitation and streamflow under a changing climate and the impact of anthropogenic influences. Most past studies of Canadian hydroclimate change detection have focused on trends or slow varying changes in the mean precipitation and streamflow of Canada even though extreme precipitation and streamflow could cause more severe damage to human beings.

The objectives of this dissertation are: 1) to understand the impact of changes in climatic and human factors to hydroclimatic processes over Canada, 2) to examine the nonstationary characteristics of the precipitation and streamflow under a changing climate, and 3) to assess the impacts of global changes in extreme climate on human and ecosystems.

Chapter 1 describes an analysis of the nonstationary behavior of extreme streamflow over Canada by identifying abrupt changes, monotonic temporal trends, non-stationary probability distributions and long-term persistence of Canadian annual maximum streamflow. The results show that nonstationary frequency analysis should be employed in the future, because of widespread non-stationarities of streamflow resulting from both climate change and human impacts have been detected across Canada.

Chapter 2 relates changes in streamflow over Canadian watersheds to climate change and human impacts. From elasticities of streamflow for each watershed are analytically derived using the Budyko Framework, it is shown that climate change caused an increase in the mean annual streamflow (MAS), while human impacts a decrease in MAS and such impact tends to become more severe with time.

Chapter 3 relates non-stationarities of heavy precipitation over Canada in terms of frequency and intensity to large-scale climate patterns, such as El Niño Southern Oscillation (ENSO), North Atlantic Oscillation (NAO), Pacific decadal oscillation (PDO) and North Pacific Oscillation. This analysis shows that large-scale climate anomalies have affected Canadian heavy precipitation which may trigger large floods.

Chapter 4 used variants of the Mann-Kendall (MK) test to analyze effects of short-term persistence (STP), long-term persistence (LTP) and large-scale climate anomalies on detected trends of seasonal (SMP) and annual extreme precipitation (AMP). The presence of LTP would increase the chances of detecting trends in AMP and SMPs, and similarly STP would also influence the detection of trends, while large-scale climate anomalies mainly contributed to trends detected for winter SMPs.

Chapter 5 investigates the multifractality of Canadian daily precipitation and streamflow based on the universal multifractal model and the modified multiplicative cascade model. The differences in the multifractality of streamflow before and post dam operations are also analyzed to show the effects of human influences on the characteristics of streamflow of Canada.

Chapter 6 shows significant interannual and interdecadal oscillations of Canadian extreme precipitation and their teleconnections to large-scale climate anomalies from applying variants of wavelet analysis methods and the composite analysis to 131 stations of climate data of Canada. Results show that both ENSO and PDO modulated the interannual variability, and PDO modulated the interdecadal variability, of extreme precipitation over Canada.

Chapter 7 identifies projected time of emergence (ToE) in global extreme climate, when the signal of extreme climate change will exceed the natural climate variability. This timing for terrestrial and marine ecoregions is identified for hot-spot regions across the world where the ecosystem could be severely impacted by changes in the magnitude, frequency and severity of extreme temperature and precipitation that exceed the tolerance limit of respective ecosystems. The impacts of extreme climate change on human society are also examined.

Conclusions and future work are provided in Chapter 8.

Preface

This dissertation is organized in an article format. Each chapter is written as a standalone article for journal submission. As such, each chapter contains standalone introductions and conclusions. A general introduction section is provided at the beginning of the thesis ("General introduction") and research conclusions are summarized in Chapter 8. An aggregated bibliography has been provided for the entire dissertation due to many overlapping references. Color figures and supplementary materials are available in online published papers. Figures and Tables indexed with "S" (e.g., Figure S1 and Table S1) are included in supplementary materials submitted to a journal. To shorten the dissertation, these supplementary figures and tables are not presented in this thesis, although they are cited in the text.

Dedication

This thesis is dedicated to my grandparents, parents, brothers, wife (Guofei Tu) and daughter (Tracy Tan), for their endless love, support and encouragement.

Acknowledgments

First I wish to express my sincere gratitude to my supervisor Professor Thian Yew Gan for all his continuous support of my PhD study and research, for his patience, motivation and guidance over the past four years we have known each other, without which I would not be where I am today. I could not have imagined having a better supervisor and mentor for my PhD study and research. His enthusiasm and love of learning has been a constant inspiration – thank you. I would like to thank my co-author Professor Daniel Horton for all his invaluable input. Finally, I would like to acknowledge the China Scholarship Council (CSC), the University of Alberta, Henry Kroeger Memorial Graduate Scholarship, and the Natural Sciences and Engineering Research Council of Canada (NSERC) for providing funding support.

Table of Contents

List of Tables

List of Figures

General Introduction

Extreme hydroclimatic events are relatively rare but could incur disproportionate and costly damage on the infrastructure, environment, ecosystems, socio-economic and loss of human life. Since the pioneer work of Gumbel (1941), the incorporation of extreme value analysis, also called hydrologic frequency analysis, has been a standard practice in civil engineering design, water resources management and water-related, natural hazards. Typically, the objective of extreme value analyses is to estimate the return level or the magnitude of an extreme hydroclimatic event associated with a given return period, or to estimate the frequency or risk of an extreme hydroclimatic event associated with a given magnitude (Katz et al. 2002). The assumptions behind a traditional extreme value analysis are summarized by Gumbel:

> "*In order to apply any theory we have to suppose that the data are homogeneous, i.e. that no systematical change of climate and no important change in the basin have occurred within the observation period and that no such changes will take place in the period for which extrapolations are made."* (Gumbel, 1941)

This means that statistical properties of hdyroclimatic variables are time-invariant. However, in recent years this assumption may be undermined by climate change and human impact across basins that it will be crucial to consider non-stationarities of hydroclimatic data. Canada, a huge northern land mass located in high-latitude, has experienced an almost twice the rate of average global warming over the past several decades (Cohen et al. 2014; Hartmann et al. 2013; IPCC 2013). Because of its size, the climate, landscape and ecosystems of Canada are very diverse (Figures 2-2 and 2-3c). Under the impact of global warming, various climate variables of Canada other than temperature may also have changed. Given characteristics of hydroclimatic extremes are important for hydrologic frequency analyses, the key objectives of this doctoral research are: 1) to detect nonstationary characteristics of Canadian precipitation and streamflow, 2) to relate nonstationary hydroclimitc time series to some atmospheric circulation patterns and 3) to attribute observed changes of streamflow to climate change and human impacts. Figure 1 shows the schematic diagram of this thesis presented in seven chapters (Chapters 1-7) in which different hydroclimatic variables and their non-stationary properties are analyzed, underlying causes for hydroclimatic changes are identified. As streamflow results from both climate (e.g., precipitation, evapotranspiration, snow-melt, infiltration and discharge of groundwater) and human impacts (e.g., water impoundment, landscape change, irrigated agriculture and pasture),

changes in streamflow result from both changes in climatic and human factors. In this thesis, the characteristics of streamflow are examined in Chapters 1 and 2. Then, in Chapters 3-6, changes in streamflow were specifically related to changes in precipitation which is the primary source of water to streamflow. After devoting the first six chapters on the hydroclimate research of Canada, the last chapter (Chapter 7) expands to research in extreme climate change globally. An overall summary of all conclusions from Chapters 1-7 is presented in Chapter 8 which also includes limitations this research and suggestions to future work. Lastly, essential summary and findings of this research work based on abstracts of Chapters 1-7 are also presented.

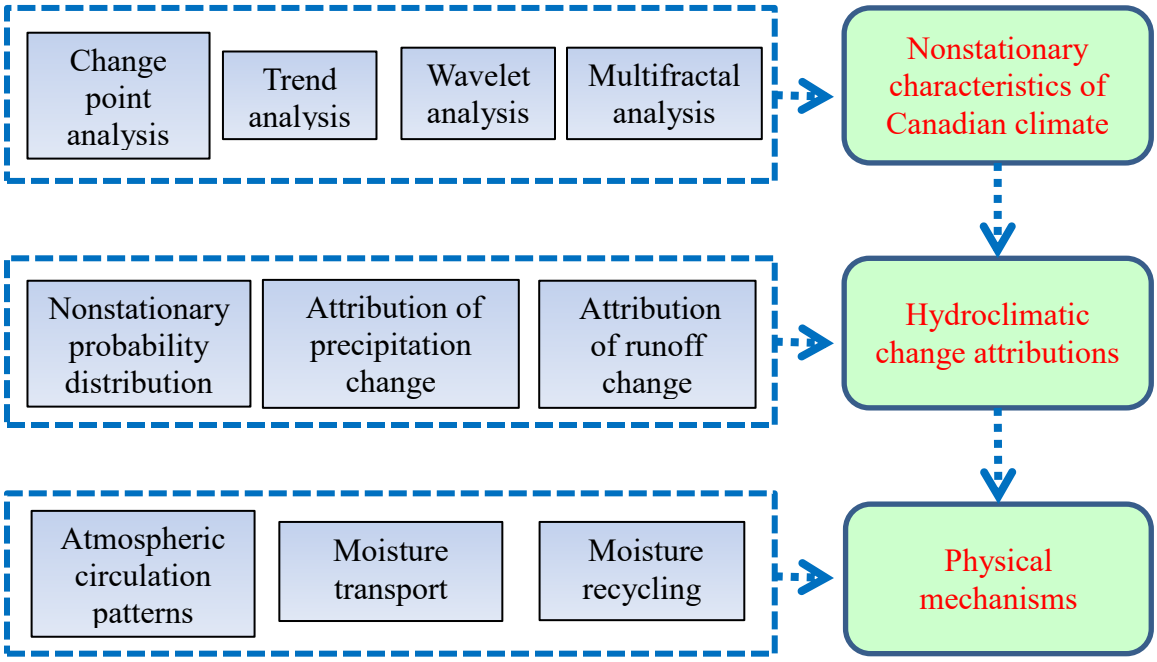

Figure 0-1 Schematic diagram of the research project

Chapter 1 has been published in the Journal of Climate with the following citation: Tan, X., and T. Y. Gan, 2015: Nonstationary analysis of annual maximum streamflow of Canada. *J Climate*, **28**, 1788-1805, doi: 10.1175/JCLI-D-14-00538.1.

Both natural climate change and anthropogenic impacts may cause nonstationarities in hydrological extremes. In this study, long-term annual maximum streamflow (AMS) records from 145 stations over Canada were used to investigate the nonstationary characteristics of AMS, which include abrupt changes and monotonic temporal trends. Nonparameteric Pettitt test was applied to detect abrupt changes, while temporal monotonic trend analysis in AMS series

was conducted using the nonparameteric Mann-Kendall and Spearman tests, and parametric Pearson test. Nonstationary frequency analysis of the AMS series was done using a group of non-stationary probability distributions. The nonstationary characteristics of Canadian AMS were further investigated in terms of the Hurst exponent (*H*) which represents the long-term persistence (LTP) of streamflow data. Our results indicate that for Canadian AMS data, abrupt changes are detected more frequently than monotonic trends, partly because many rivers began to be regulated in the 20th Century. Drainage basins which have experienced significant land-use changes are more likely to show temporal trends in AMS, compared to pristine basins with stable land-use conditions. The nonstationary characteristics of AMS were accounted for by fitting the data with probability distributions with time-varying parameters. Large *H* found in almost 2/3 of the Canadian AMS dataset indicates strong LTP, which may partly represent the presence of long-term memories in many Canadian river basins. Further, *H* values of AMS data are positively correlated with the basin area of Canadian rivers. It seems that nonstationary frequency analysis, instead of the traditional, stationary hydrologic frequency analysis should be employed in future.

Chapter 2 has been published in the Scientific Reports with the following citation: Tan, X., and T. Y. Gan, 2015: Contribution of human and climate change impacts to changes in streamflow of Canada. *Scientific Reports*, **5**, 17767, doi: 10.1038/srep17767.

Climate change exerts great influence on streamflow by changing precipitation, temperature, snowpack and potential evapotranspiration (PET), while human activities in a watershed can directly alter the runoff production and indirectly through affecting climatic variables. However, to separate contribution of anthropogenic and natural drivers to observed changes in streamflow is non-trivial. Here we estimated the direct influence of human activities and climate change effect to changes of the mean annual streamflow (MAS) of 96 Canadian watersheds based on the elasticity of streamflow in relation to precipitation, PET and human impacts such as land use and cover change. Elasticities of streamflow for each watershed are analytically derived using the Budyko Framework. We found that climate change generally caused an increase in MAS, while human impacts generally a decrease in MAS and such impact tends to become more severe with time, even though there are exceptions. Higher proportions of human contribution, compared to that of climate change contribution, resulted in generally decreased streamflow of Canada observed in recent decades. Furthermore, if without

contributions from retreating glaciers to streamflow, human impact would have resulted in a more severe decrease in Canadian streamflow.

Chapter 3 has been published in the Climate Dynamics with the following citation: Tan, X., and T. Y. Gan, 2016: Non-stationary analysis of the frequency and intensity of heavy precipitation over Canada and their relations to large-scale climate patterns. *Climate Dynamics*, 10.1007/s00382-016-3246-9.

In recent years, because the frequency and severity of floods have increased across Canada, it is important to understand the characteristics of Canadian heavy precipitation. Long-term precipitation data of 463 gauging stations of Canada were analyzed using non-stationary generalized extreme value distribution (GEV), Poisson distribution and generalized Pareto (GP) distribution. Time-varying covariates that represent large-scale climate patterns such as El Niño Southern Oscillation (ENSO), North Atlantic Oscillation (NAO), Pacific decadal oscillation (PDO) and North Pacific Oscillation (NP) were incorporated to parameters of GEV, Poisson and GP distributions. Results show that GEV distributions tend to under-estimate annual maximum daily precipitation (AMP) of western and eastern coastal regions of Canada, compared to GP distributions. Poisson regressions show that temporal clusters of heavy precipitation events in Canada are related to large-scale climate patterns. By modeling AMP time series with non-stationary GEV and heavy precipitation with non-stationary GP distributions, it is evident that AMP and heavy precipitation of Canada show strong non-stationarities (abrupt and slowly varying changes) likely because of the influence of large-scale climate patterns. AMP in southwestern coastal regions, southern Canadian Prairies and the Great Lakes tend to be higher in El Niño than in La Niña years, while AMP of other regions of Canada tends to be lower in El Niño than in La Niña years. The influence of ENSO on heavy precipitation was spatially consistent but stronger than on AMP. The effect of PDO, NAO and NP on extreme precipitation is also statistically significant at some stations across Canada.

Chapter 4: Slowly varying (trend) and abrupt (change points) changes in annual maximum daily precipitation (AMP) and seasonal maximum daily precipitation (SMP) data of 223 stations of Canada divided into four regions for 1900-2010, 1930-2010, 1950-2010 and 1970-2010, were analyzed, respectively. Several variants of the Mann-Kendall (MK) test that consider the influence of short-term persistence (STP), long-term persistence (LTP) and large-scale climate anomalies on each time series were applied to detect trends, while the Pettitt test

was applied to detect change points in AMP and SMP time series. Both significant increasing and decreasing trends had been detected in Canadian AMP and SMPs. AMP of most regions in western and southern British Columbia, western Ontario and the Atlantic Maritime that show significant trends are positive, but significant trends detected in AMP of central Canada, eastern Ontario and western Quebec, and northwestern Canada are mostly negative. More stations experienced statistically significant increasing than decreasing trends in spring, summer and autumn SMPs, while statistically significant trends detected in winter SMPs are decreasing (increasing) trends over southern (northern) Canada. The presence of LTP would increase the chances of detecting trends in AMP and SMPs, and similarly STP would also influence the detection of trends, as shown by different results obtained from MK tests that consider and MK tests that do not consider the effects of STP. The results show that large-scale climate anomalies mainly contributed to trends detected for winter SMPs. More than 1/4 of stations analyzed show statistically significant change points in AMP and SMPs in around 1960-1990. Further, more stations showed significant change points than trends, and winter SMPs showed more trends and change points than SMPs of other three seasons. Trends and change points detected were field-significant.

Chapter 5: The detrended fluctuation analysis (DFA) and multifractal DFA (MFDFA), which can detect nonstationarities of time series with trends, were applied to study long-term persistence (LTP) and multifractal behavior of 100 stations of daily precipitation and 145 stations of streamflow time series of Canada. All precipitation time series showed LTP at both small and large time scales, while streamflow time series generally showed nonstationary behavior at small time scales and LTP at large time scales. Widespread crossovers of fluctuation functions for streamflow data a time scale of about 120-250 days could be related to the cross-over between rain-induced and snowmelt-induced streamflow cycles. In general, the multifractal strength of precipitation data was location dependent but not so for streamflow data. The multifractal behavior of Canadian precipitation and streamflow data can be accurately described by the universal multifractal model and also described, though less consistently, by the modified multiplicative cascade model. About a third of fitted parameters of the universal multifractal model for precipitation data show positive temporal trends, and about half of the stations whose streamflow data exhibited statistically significant abrupt change points showed a weakening in the multifractal strength moving in the post-change period. Differences in the multifractal

strength between Canadian precipitation and streamflow data suggest that the persistence of streamflow was not only because streamflow is more auto-correlated than precipitation, it is also more consistently affected by human activities.

Chapter 6: To detect significant interannual and interdecadal oscillations and their teleconnections to large-scale climate anomalies such as El Niño Southern Oscillation (ENSO), Pacific Decadal Oscillation (PDO) and North Atlantic Oscillation (NAO), monthly and seasonal maximum daily precipitation (MMDP and SMDP) from 131 stations across Canada were analyzed using variants of wavelet analysis. Interannual (1-8 years) oscillations were found to be more significant than interdecadal (8-30 years) oscillations for all selected stations, and the oscillations are both spatial and time-dependent. Similarly, the significant wavelet coherence and the phase difference between leading principal components of monthly precipitation extremes and climate indices were highly variable in time and in periodicity, and a single climate index explains less than 40% of the total variability. Partial wavelet coherence analysis shows that both ENSO and PDO modulated the interannual variability, and PDO modulated the interdecadal variability, of MMDP over Canada. NAO is correlated with the western MMDP at interdecadal, and the eastern MMDP at interannual scales. The composite analysis shows that precipitation extremes at about 3/4 of the stations have been significantly influenced by ENSO and PDO patterns, while about 1/2 of the stations by the NAO patterns. The magnitude of SMDP in extreme El Niño years, and extreme PDO event of positive phase, was mostly lower (higher) over the Canadian Prairies in summer and winter (spring and autumn) than in extreme La Niña years. Overall, the degree of influence of large-scale climate patterns on Canadian precipitation extremes varies by season and by region.

Chapter 7: Since both natural and human systems can only tolerate certain degree of change from its existing level of climate variability, evaluation of the climate change impacts should consider the magnitude of change relative to natural climate variability. Whether and when the signal of extreme climate change (S) will exceed the natural climate variability (N) has yet to be globally examined. Here we investigate the timing of perceivable changes in the magnitude, frequency and severity of extreme temperature and precipitation when the signal-to-noise ratio (S/N) exceeds certain thresholds for global terrestrial biomes, marine realms, countries and major cities. The results show that under RCP8.5, the projected global changes in the magnitude, frequency and severity of hot extremes are projected to exceed their twofold

variance (S/N >2) before 2100, while counterparts of extreme precipitation are projected to exceed one variance (S/N >1) before 2100. In contrast to perceivable changes in the magnitude (magnitude and frequency) of both hot and cold extremes (precipitation extremes) projected to occur early in low- and high-latitudes, the frequency (severity) of both hot and cold extremes (precipitation extremes) are projected to occur earlier in mid-latitudes instead of low- and high-latitudes. As a result, tropical and subtropical forests (tropic Atlantic, Indo-Pacific, Tropical eastern Pacific) are projected to experience earlier perceivable changes in hot extremes than other terrestrial biomes (marine realms). Arctic tundra is projected to experience perceivable changes in the magnitude, frequency and severity of extreme precipitation before 2100, while biomes such as tropical and subtropical coniferous forests and Mediterranean forest are projected to experience earlier perceivable changes in severe droughts. All major urban residents (about 1.4 billion) are projected to experience perceivable changes in the frequency and severity of hot extremes, and more are projected to experience severe droughts (0.86 billion) than wet climate (0.08 billion). Lastly, early perceivable extreme climate change tends to occur in low-income than rich countries.

Chapter 1 Nonstationary analysis of annual maximum streamflow of Canada

1.1 Introduction

In recent years, climate variability and climate change have impacted various components of the hydrological cycle in many regions across the world. In particular, changes to the climate system can potentially affect the magnitude and frequency of extreme hydrological events, thus altering the risk to critical infrastructure (Burn et al. 2010; Ishak et al. 2013). Therefore, under the possible impact of climate change, the assumption of stationarity, the basis of conventional hydrologic frequency analysis, will no longer hold. Design storms or flood estimation for certain return periods derived from conventional frequency analysis for municipal infrastructure developments could be underestimated, and public safety standards could be compromised (Khaliq et al. 2006). Several recent major floods that occurred in some parts of the world highlight the necessity to address non-stationarity and possible changes to future occurrences of hydrological extremes which would affect water security, resources management and the operation of large dams (Jakob 2013; Milly et al. 2008).

Several past studies have examined temporal trends in Canadian streamflow records. Even though Zhang et al. (2001b) reported that annual and monthly mean streamflow of Canada had generally decreased since 1947 to 1996, significant increase in the monthly mean streamflow was observed in March and April probably because of the earlier onset of spring snowmelt, and major regional differences and variability of streamflow trends are observed across Canada (Burn and Elnur 2002; Whitfield and Cannon 2000). For example, statistically significant increasing trends in the streamflow were detected in the Winnipeg River (St. George 2007) and the northern part of British Columbia (BC) (Whitfield 2001), even though nationally daily streamflow has generally undergone a broad scale decreasing pattern (Zhang et al. 2001b). On the other hand, Whitfield et al. (2003) found an increase in frequency of flooding in the Georgia Basin, BC. Although in Canada the magnitude of low flows could be more significantly affected by the impact of climate change than high flows (Burn et al. 2010; Cunderlik and Ouarda 2009; Déry et al. 2009a; Khaliq et al. 2008; Zhang et al. 2001b), possible changes to future annual maximum floods warrant more attention than the past. For example, based on simulations of some general circulation models in relation to climate change impact, it seems more extreme

events may occur across Canada due to an enhanced hydrologic cycle, e.g., Mailhot et al. (2012) and Whitfield et al. (2003).

The cause of temporal trends in streamflow data can be ambiguous because floods could be caused by many complicating factors, such as natural and anthropogenic changes in atmospheric forcings and catchment characteristics, rising concentrations of greenhouse gases and landuse changes. Regulation of reservoirs further complicates the flow regimes of river basins of Canada. The downstream hydrological impact of dams (Assani et al. 2006), is an obvious cause leading to the change of annual maximum streamflow (AMS) Probability distributions (PDs) of many gauging stations globally. Similarly, the 20th Century had been a time of profound land use changes due to activities such as agricultural practice, urbanization and forest management. Studies show that landuse changes have significant impacts on river basins of Canada (Buttle 2011; Kerkhoven and Gan 2013) and USA (Villarini et al., 2009a, 2009b).

In addition to nonstationarity and temporal changes, limitations in the amount, frequency and accuracy of observed hydrologic data and analysis procedures could affect PDs of AMS derived from streamflow databases of Environment Canada (EC) and provincial agencies. A majority of past studies for analyzing streamflow trends over Canada are based on data provided by the Reference Hydrometric Basin Network (RHBN) of EC. By 2010, the average record length of streamflow stations of RHBN is about 50 years. In view of the possible impact of climate change, climate variability and landuse change to the streamflow of Canada, the key objective of this study is to examine nonstationary changes to Canadian AMS based on some selected, long-term streamflow records of HYDAT, which includes data from RHBN. HYDAT is a database of Water Survey Canada (WSC) that contains streamflow data mainly computed from station rating curves and water levels, and sediment data of rivers. Annual maximum daily streamflow data from 145 WSC stations each with a record of at least 50 years were selected for this study. Drainage areas for all the selected stations range from 87.6 km^2 (Pennask Creek near Quilchena, BC) to 347,000 km^2 (Saskatchewan River at The Pas, Manitoba).

Several major analyses conducted in this study include change point detection, possible effect of streamflow regulation, temporal trend analysis, nonstationary extreme flood PDs, nonstationary properties of the floods, and long-term persistence. According to Koutsoyiannis (2006), who examined stationarity and nonstationarity in hydrology, a hydrologic time series is usually regarded as stationary if the time series does not have trends, and without shifts in its

mean and variance. Conventionally, the stationary assumption is considered valid if there is no slowly varying trend or detected change point (abrupt changes in the mean and/or the variance of the PD of the variable of interest) in the time series.

Trend analysis is applied to find historical changes of a time series, while change point analysis is to distinguish a shift from one regime to another where the status is likely to remain the same until a new regime shift occurs (Khaliq et al. 2009b; Villarini et al. 2009a). Streamflow trends in many Canadian watersheds have been studied, e.g., Burn et al. (2010) and Yue et al. (2003), but we have yet to come across the application of change point analysis to characterize the nonstationarity of streamflow records in Canada. Therefore, we performed both trend and change point analysis in this study, in which the former is done after the latter, but not vice versa. If a change point is detected, the AMS time series is first divided into two subseries (before and after the change point) and trend analysis is performed on both subseries separately.

In addition to finding trends and detecting change points, the AMS data were also fitted to PDs and evaluated for nonstationary characteristics. Without considering spatial correlations between station streamflow data, we did the flood frequency analysis of observed AMS of stations individually by first estimating the location, scale and shape parameters of some selected PDs using the generalized additive model (GAMLSS) developed by Rigby and Stasinopoulos (2005b). GAMLSS was chosen for this study because it allows the choice of a wide range of PDs for best fitting a dataset of interest, and it can also estimate model parameters that are stationary, or parameters with trends that vary slowly over time, or parameters with abrupt changes.

Koutsoyiannis (2006) suggested that properties such as nonstationarity, persistence and scaling should be analyzed jointly, regardless of whether a time series possesses long-term persistence (LTP) or not. On the other hand, a time series with LTP may be falsely diagnosed as a time series with a statistically significant trend, even though no trend is present (Cohn and Lins 2005; Koutsoyiannis 2006; Koutsoyiannis and Montanari 2007). LTP, also referred to as the Hurst phenomenon, has been detected in many hydrologic time series particularly in river flows (e.g., Klemeš 1974; Potter 1976; Szolgayova et al. 2014). Although certain patterns observed in some hydrologic series could be better explained by LTP (Hurst 1951; Koutsoyiannis 2006), this phenomenon is often overlooked in the analysis of streamflow records. In this study, we investigated possible long-term persistent behavior of AMS of Canada.

This chapterer is organized as follows: Section 1.2 describes the AMS data of Canada; Section 1.3 explains basic aspects of the GAMLSS model, estimation of LTP in a time series, change point detection, and trend analysis; Section 1.4 presents the discussion of results, and Section 1.5 the summary and conclusions.

1.2 Data

A long-term dataset subjected to a sound quality control process is essential to achieve reliable change point and non-stationary analysis. The AMS data used in this study were taken from the HYDAT Database of WSC up to 2013. The RHBN data included in HYDAT have been extensively used for climate change studies, since RHBN data are characterized by relatively pristine and stable land-use conditions (<5% of the surface modified) and have a minimum of 20 years of record (Burn et al. 2010; Coulibaly and Burn 2004).

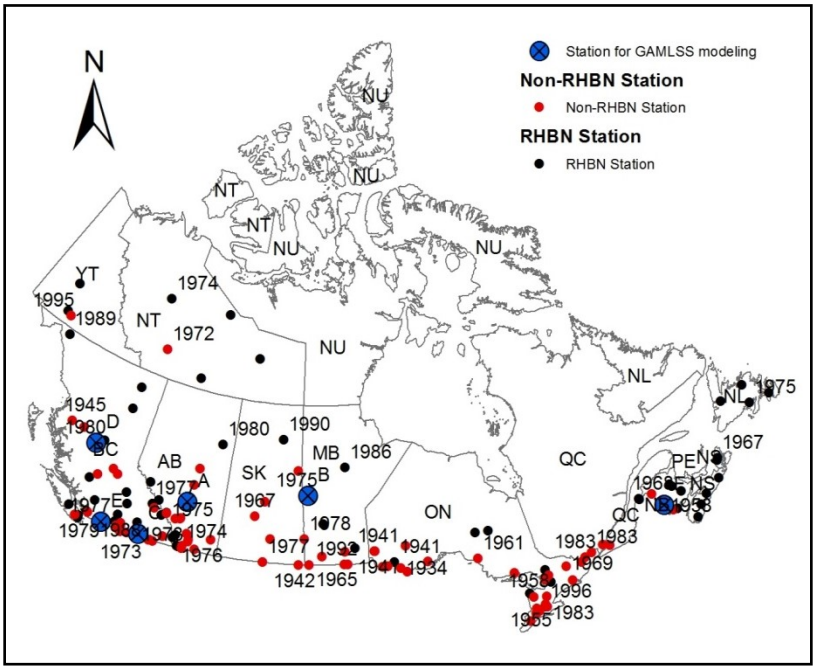

Figure 1-1 A map showing selected non-RHBN and RHBN streamflow gauge stations over Canada, and the corresponding abrupt change points of annual maximum daily streamflows detected using the Pettitt test and 5% significance level. Six selected stations for GAMLSS modeling are: A) 05CC002, B) 05KJ001, C) 08NE049, D) 08JB002, E) 08MH016 and F) 01AK001.

Out of over 200 active gauging stations in the RHBN network, 62 stations were selected in this study, each with a minimum record length of 50 years to ensure statistical validity of the study results. In addition, 83 non-RHBN stations from HYDAT (with a minimum record length of 70 years and a maximum total missing record of 4 years) are selected to provide data collected from a larger coverage of watersheds and a greater variety of geographic areas of Canada (Figure

1-1). River basins of non-RHBN stations had experienced anthropogenic influence such as land use changes, river regulations, agricultural production and other human activities. Missing AMS values at a station were gap filled with the mean AMS of that station. Average record lengths of RHBN and non-RHBN stations are 72 and 85 years, with a maximum record length of 102 and 118 years, and an average drainage area of 9070 km^2 and 31,403 km^2, respectively. All station data ended either in 2010 or 2011. There is a lack of stations in Quebec and all the stations of Quebec only have data available until 2001 or earlier. As shown in Figure 1-1, selected stations are mainly located in southern Canada and the Rocky Mountain area in British Columbia. By analyzing AMS records from 145 stations selected across river basins of Canada, we should obtain a representative history the occurrences of statistically significant change points and trends of AMS records of Canada over the 20^{th} and early 21^{st} centuries.

1.3 Research methodology

To fully evaluate the stationarity and nonstationarity of the observed AMS over Canada, several popular tests and estimators were employed to analyze the change point, temporal trend, and Hurst exponents for each selected station, respectively. Parametric PDs of GAMLSS were also fitted to the AMS data.

1.3.1 Change point analysis

From comparing results of six tests applied for change point detections, we found that the Pettitt test (PETT) of Pettitt (1979), a non-parameteric rank-based test to detect the change point position (time) is the best for reasons given below. These six tests are three non-parameteric tests, PETT (Pettitt 1979), cumulative sums test (Csörgö and Horváth 1997), and Wilcoxon rank sum test (Gibbons and Chakraborti 2011); and three parametric tests, structural change test in linear regressions (Zeileis et al. 2003), Bayesian change point test (Sarr et al. 2013), and spectral test using a wavelet approach (Islam 2008). These tests have been developed primarily to detect changes in the mean, but they may not be able to effectively detect changes in the variance. Given changes in the variance of AMS data is possible, we did some limited tests on changes to AMS variance using the cumulative sums of squares test proposed by Inclán and Tiao (1994).

Our focus is not to detect multiple change points but a single, “major” change point of AMS data of this study. We found that PETT consistently detected the change point that corresponds to the change point with the highest probability of occurrence identified by the Bayesian change

point and the spectral tests. Additionally, we analyzed AMS data of the Columbia River, where the year in which an abrupt change in the discharge resulted from starting the dam regulation (Environment Canada 1992; Lehner et al. 2011) was accepted as the change point, and PETT identified the change point that best agrees with the year the dam operation began. Villarini et al. (2009a) also found PETT tends to more accurately identify change points of annual flood peaks of USA. As a nonparametric, rank-based test, PETT is capable of detecting a change in the time series without having to assume its PD. It calculates *p* values of the Mann-Whitney test statistic using a limiting distribution of the Kolmogorov-Smirnov goodness-of-fit statistic for continuous variables to determine if two samples $Y_1,\cdots$ and $Y_{m+1},\cdots$ come from the same population (Pettitt, 1979).

1.3.2 Temporal trend analysis

To identify if a time series has statistically significant trend, the non-parametric, Mann–Kendall (Kendall 1975), the Spearman rank correlation (hereafter referred to Spearman) tests, and the parametric, least squares linear regression (hereafter referred to Pearson) test are commonly used (Khaliq et al. 2009b). After a change point is detected, these tests were applied to analyze trends of two subseries, one prior to and one after the detected change point in the original record. If no change point is detected, these tests will be applied to the whole record. The Mann–Kendall test determines whether a trend is statistically significant without specifying whether the trend is linear or nonlinear. It is the most widely adopted statistical test to detect temporal trends in discharge data (Khaliq et al. 2009b). It is based on the test statistic *S* defined as the proportion of concordant pairs minus the proportion of discordant pairs in the samples.

$$S = \sum_{i=1}^{N-1} \sum_{j=i+1}^{N} \operatorname{sgn}\left(Y_j - Y_i\right) \tag{1-1}$$

$$\operatorname{sgn}(\theta) = \begin{cases} 1, & \theta > 0 \\ 0, & \theta = 0 \\ -1, & \theta < 0 \end{cases} \tag{1-2}$$

where N is the total number of data, Y_i and Y_j are the sequential data. A positive (negative) value of S indicates an upward (downward) trend. For $N \geq 8$, the statistic S is approximately normally distributed with the mean of 0 and a variance related to the sample size. Where either there is

serial or cross correlation, the Mann–Kendall test will be affected and such correlations should be examined before conducting the test (Yue et al. 2003). We computed the lag-1 correlation of all selected AMS series and found all lag-1 correlation to be not significant statistically. Next, the Spearman rank correlation test is based on the Spearman rho (Helsel and Hirsch 2002):

$$rho = 1 - \left(6 \sum_{i=1}^{N} d_i^2 \right) \Big/ \left[N\left(N^2 - 1\right) \right] \tag{1-3}$$

where $d_i = RT_i - RY_i$ is the difference between two rankings, such that RT_i is the rank of the variable T_i, Y_i the observation series, and RY_i its rank presented in the chronological order *i*. If there are ties, RT becomes the average rank. The null hypothesis is based on the test statistic:

$$T = rho\left[\left(N - 2\right) / 1 - rho^2 \right]^{0.5} \tag{1-4}$$

where T has a Student's *t*-distribution with $\nu = N - 2$ degrees of freedom. At a two-sided test based on the α significance level, the time series has no trend if $t_{\nu,\alpha/2} < T < t_{\nu,1-\alpha/2}$.

The Pearson's *r*, a linear correlation between *Y* and *T* is the ratio of the covariance *Cov*(*Y, T*) over the standard deviations of *Y* and *T*. Since testing the significance of Pearson's *r* is based on the Gaussian distribution, we need to transform skewed data into Gaussian distributed deviates, which was done using the normal quantile transformation. However, this transformation may distort trends in the original streamflow data (Villarini et al. 2009a).

1.3.3 Nonstationary extreme distribution analysis

In fitting a suitable PD to a stationary AMS series Y, the parameters are usually assumed to remain constant with minimal change over the years. For nonstationary AMS series, parameters are expected to change with time and they can be expressed as a function of some explanatory variables (covariate). The simplest covariate is time such as years or seasons. Although other covariates, e.g., climate indices (Kwon et al. 2008) and socio-economic indices (Villarini et al. 2009b) may be more interpretational to describe the nonstationarity of floods, we only chose time as the covariate to examine whether there is nonstationarity in selected AMS time series.

The GAMLSS models provide a very flexible framework for estimating parameters of a wide range of PDs applicable to both stationary and nonstationary AMS. Compared with classical generalized additive models, GAMLSS is flexible and capable of using non-exponential distributions, such as highly skewed and/or kurtotic, continuous and discrete distributions with

heavy tails. It can model location, scale and shape parameters of a PD as linear and/or nonlinear, parametric, and/or additive non-parametric functions of covariates, and/or random effects.

A more comprehensive description of GAMLSS can be found in Rigby and Stasinopoulos (2005a) and Stasinopoulos and Rigby (2007), and in the GAMLSS website (http://www.gamlss.org/). Villarini et al. (2009a, 2009b) applied this model to conduct the frequency analysis of nonstationary annual flood peaks. For GAMLSS models, it is assumed that independent observations y_i, for $i = 1, \cdots$, have a cumulative PD function $F_Y\left(y_i;\theta^i\right)$ with $\theta^i = \left(\theta_1^i, \cdots\right.$, a vector of p parameters accounting for position, scale and shape of the PD. Usually p is less than or equal to four, since 1 to 4-parameter families provide enough flexibility for most applications to highly skewed and/or kurtotic continuous and discrete distributions. Given a n vector of the variable $y^T = \left(y_1, \cdots\right.$, let $g_k\left(\cdot\right)$, for $k = 1, \cdots$, be known monotonic link functions relating the distribution parameters to explanatory variables and random effects through an additive model given by:

$$g_k\left(\theta_k\right) = \eta_k = X_k\beta_k + \sum_{j=1}^{J_k} Z_{jk}\gamma_{jk} \tag{1-5}$$

where θ_k and η_k are vectors of length n, e.g., $\theta_k^T = \left\{\theta_k^1, \cdots\right.$, $\beta_k^T = \left\{\beta_{1k}, \cdots\right.$ is a parameter vector of length J_k, X_k is a known design matrix of order $n \times J_k$, Z_{jk} is a fixed known $n \times q_{jk}$ design matrix and γ_{jk} is a q_{jk} random variable. Additive terms in Equation (1-5) represent smoothing terms that allow for flexibility in modeling the dependence of the parameters of the PD on the covariates. If we choose $Z_{jk} = I_n$, where I_n is a $n \times n$ identity matrix, and $\gamma_{jk} = \mathbf{h}_{jk} = h_{jk}\left(x_{jk}\right)$ for all combinations of j and k, we obtain a semi-parametric additive equation of GAMLSS:

$$g_k\left(\theta_k\right) = \eta_k = X_k\beta_k + \sum_{j=1}^{J_k} h_{jk}\left(x_{jk}\right) \tag{1-6}$$

where h_{jk} is an unknown function of the covariate x_{jk} and $\mathbf{h}_{jk} = h_{jk}\left(x_{jk}\right)$ is the vector which represents the function h_{jk} at x_{jk}.

Table 1-1 Summary of the four two-parameter PDs (Rigby et al. 2014) considered in this study to model the Canadian AMS

	Probability density function	Distribution moments
Weibull	$f_Y(y\|\mu,\sigma)=\frac{\sigma y^{\sigma-1}}{\mu^{\sigma}}\exp\left\{-\left(\frac{y}{\mu}\right)^{\sigma}\right\}$ $y>0,\mu>0,\sigma>0$	$E[Y]=\mu\Gamma(1/\sigma+1)$ $Var[Y]=\mu^2\left\{\Gamma(2/\sigma+1)-\left[\Gamma(1/\sigma+1)\right]^2\right\}$
Gamma	$f_Y(y\|\mu,\sigma)=\frac{1}{(\sigma^2\mu)^{1/\sigma^2}}\frac{y^{1/\sigma^2-1}\exp\left[-y/(\sigma^2\mu)\right]}{\Gamma(1/\sigma^2)}$ $y>0,\mu>0,\sigma>0$	$E[Y]=\mu$ $Var[Y]=\mu^2\sigma^2$
Gumbel	$f_Y(y\|\mu,\sigma)=\frac{1}{\sigma}\exp\left[\left(\frac{y-\mu}{\sigma}\right)-\exp\left(\frac{y-\mu}{\sigma}\right)\right]$ $-\infty<y<\infty,-\infty<\mu<\infty,\sigma>0$	$E[Y]=\mu+\gamma\sigma\cong\mu+0.57722\sigma$ $Var[Y]=\pi^2\sigma^2/6\cong1.64493\sigma^2$
Lognormal	$f_Y(y\|\mu,\sigma)=\frac{1}{\sqrt{2\pi\sigma^2}}\frac{1}{y}\exp\left\{-\frac{\left[\log(y)-\mu\right]^2}{2\sigma^2}\right\}$ $y>0,\mu>0,\sigma>0$	$E[Y]=\sqrt{\exp(\sigma^2)}e^{\mu}$ $Var[Y]=\exp(\sigma^2)\left[\exp(\sigma^2)-1\right]e^{2\mu}$

In this study we considered four, widely used, 2-parameter PDs (Gumbel, gamma, lognormal and Weibull) (Table 1-1) to do the flood frequency analysis of selected Canadian AMS data (GREHYS 1996; Ouarda and El-Adlouni 2011; Ouarda et al. 2000). Given that some runoff data could be nonstationary, only 2-parameter PDs were chosen partly to avoid potential numerical round off problems when estimating the distribution parameters. For a 2-parameter PD, the parameters, θ_1 (θ_2) related to the mean (variance), are based on a generalized additive model with time t as the covariate to account for nonstationary. Therefore, Equation (1-6) can be simplified to:

$$g_k\left(\theta_k^i\right)=\eta_k^i=t_i\beta_k+h_k\left(t_i\right) \tag{1-7}$$

A cubic spline smoothing technique was used to derive $h(\cdot)$ for this additive model. Note that if we only consider the linear models in GAMLSS, then there is no additive term $h_k\left(t_i\right)$ shown in Equation (1-7). Both temporal trend and change point could be taken into account in

this GAMLSS model to investigate the nonstationarity assumption of the flood frequency analysis.

Selecting a particular PD is based on visual assessment of diagnostic plots and maximum likelihood values (L). Diagnostic plots of the residuals (van Buuren and Fredriks 2001) are visually inspected. The goodness-of-fit of PDs selected were assessed using the Akaike information criterion (AIC) (=$2k$ – 2ln(L)), where L is penalized by the number of parameters (k). The PD with the minimum AIC value, and that best fit the Canadian AMS data, are selected.

1.3.4 Long-term persistence (LTP) analysis

The LTP characteristics of Canadian runoff data are estimated from the Hurst exponent H (Hurst 1951). A H of 0.5 indicates a lack of LTP, but H larger than 0.5 indicates the presence of LTP, which increases with the H value. Several conceptual algorithms have been developed to detect LTP (Montanari et al. 1999). Among these, the most popular are the rescaled range statistic algorithm (R/S) developed by (Hurst 1951), the aggregated variance approach (Taqqu et al. 1995), and the detrended fluctuation analysis of Peng et al. (1994).

The aggregated variance approach is presented as below: For a stationary process y_i for a discrete time step i (years in this case) with a standard deviation σ,

$$Y_i^{(k)} = \left(Y_i + \cdots \right)/k \tag{1-8}$$

denotes the aggregated process at time scale k, with a standard deviation $\sigma^{(k)}$ (the notation implies that $Y_i^{(1)} = Y_i$). For a sufficiently large k, $Y_i^{(k)}$ represents the aggregated hydroclimatic process; $k = 30$ is often used to estimate H in terms of an elementary scaling property,

$$\sigma^{(k)} = \frac{\sigma}{k^{1-H}} \tag{1-9}$$

This aggregated variance approach is vulnerable to trends, abrupt changes, periodicities, and other sources of nonstationarities in the data (Rust et al. 2008). Five methods, namely, aggregated variance, aggregated variance (Teverovsky and Taqqu 1997), aggregated absolute value (Montanari et al. 1999), R/S (Hurst 1951), and Peng's (Peng et al. 1994) were used to derive *H*, since any single estimator for *H* is prone to draw false conclusions, as evident in Table 1-4 which shows different estimators of *H* resulted in different numbers of stations showing LTP.

1.4 Results

In this section, the nonstationary characteristics of AMS data of Canada will be illustrated based on results obtained from change point and temporal trend analysis, GAMLSS modeling, and the estimation of LTP.

1.4.1 Change point analysis

The presence of abrupt changes in the mean of annual maximum runoff records of Canada are examined using the PETT at a 5% significance level. The results show that 19 out of 62 RHBN stations, and 40 out of 83 non-RHBN stations (Figure 1-1) exhibited a significant abrupt change in the mean. The occurrences of abrupt change in the mean clustered around the 1940s and 1970s. However, there was no change point detected in the variance of all the stations examined in this study. Spatially, stations that show significant abrupt change in the mean spread across Canada, with the first two clusters centered on the southwestern and central Canada where the time of change point occurred around 1970s, and the 3rd cluster spread across southeastern Canada where the time of change point range from 1940s to 1990s. From applying wavelet analysis on 79 RHBN stations of runoff data, Coulibaly and Burn (2004) concluded that change points occurred around 1950 and 1970 in western and eastern Canada , which mainly agree with the time of change point (1970s) detected for the first two clusters of this study.

Given RHBN stations are stations selected from pristine catchments with stable land-use conditions, the abrupt changes detected in these stations should be primarily attributed to past changes in their regional climate and variability. In contrast, the timing of abrupt change detected in non-RHBN stations could be related to anthropogenic changes, such as dam regulation and land-use change, or past changes in their regional climate, or both. Among stations with abrupt change, we found that two stations at the lower Columbia River selected in this study (08NE049, Birchbank, and 08NE058, International Boundary), the detected change point (1973) happened in the year when several dams began to regulate flow for power generation and irrigation (Naik and Jay 2011). For the station located at the upper Columbia River (08NA002, Nicholson), where flow has not been regulated, no significant change point was detected. However, another unregulated station (08NB005, Donald) located at the upper Columbia River also showed a significant change point. It seems that even for a regional river basin such as the Columbia River, the reason behind detected abrupt change of AMS at different stations can be either caused by change in the climate, or by streamflow regulations, or both. Naik and Jay (2011) also found that

both flow regulation and climate change had affected the peak flow change of the Columbia River basin.

Among the 62 RHBN stations, only 1 out of 5 (18 out of 57) stations where streamflow has (has not) been regulated has detected change points in its AMS time series. Apparently the abrupt change of RHBN AMS was mostly linked to climatic than to human factors. For non-RHBN stations, 5 out of 21 non-regulated stations have detected change points, and 35 out of 62 regulated stations have detected change points. By comparing the detected change points of 22 non-RHBN stations with the respective year dam operation began at each station (Environment Canada 1992; Lehner et al. 2011), we found that for 16 out of 22 stations, the year a change point was detected coincide with the year that streamflow regulation began. Therefore, river regulation plays a more significant role than climatic factors on the occurrence of abrupt change in the AMS data of non-RHBN stations. However, for regulated rivers, the possibility of detecting change points in the AMS series should also depend on the operating policy of the dam sluice dates, e.g., the degree of streamflow regulation.

1.4.2 Temporal trend analysis

In this section, long-term temporal trends, which can be another cause of nonstationarity to AMS data, are investigated below. As explained in Section 1.3.2, if a change point is detected, several tests (Mann-Kendall, Spearman and Pearson two-side tests) will be applied to do a trend analysis on two subseries, one prior to and the other after the detected change point in the original record. Next, whether a change point is detected or not, these tests will be repeated to the whole record. Further, since none of the AMS record shows any significant lag-one autocorrelation, the possible effect of serial correlation was not considered in the trend analysis of these AMS data.

Table 1-2 Number of stations detected with statistically significant trend at the 10% significance level*

	Entire series		Before change point		After change point	
	Non-RHBN	RHBN	Non-RHBN	RHBN	Non-RHBN	RHBN
Pearson	32 (20-, 12+)	14 (11-, 3+)	11(7-, 4+)	3 (3-, 0+)	9 (5-, 4+)	4 (1-, 3+)
Mann-Kendall	37 (26-, 11+)	12 (7-, 1+)	8 (7-,1+)	4 (3-, 1+)	8 (4-, 4+)	3 (1-, 2+)
Spearman	36 (23-, 13+)	14 (10-, 4+)	9 (7-,2+)	3 (3-, 0+)	8 (4-, 4+)	2 (1-, 1+)

* The numerical values followed by sign "-" and "+" in brackets correspond to the number of stations that a significant negative (-) or positive (+) trend was detected on the basis of a Mann-Kendall test with the 10% significance level.

The results obtained differ marginally between the Mann-Kendall and Spearman tests, but not results from the Pearson test (Table 1-2), partly because the transformation of AMS data to normal quantiles required by the Pearson test might have distorted the trend. Without considering the presence of change point, about 50 out of 145 stations are detected with a significant trend at a 10% significance level. Again, more non-RHBN stations (37 out of 83) show a significant trend than RHBN stations (12 out of 62), which means that drainage basins which have experienced major land use changes are more likely to show temporal trends in their AMS data than pristine basins with stable land-use conditions. However, only 12 out of 59 stations with detected change points show significant temporal trends before and/or after the detected change point. Compared to subseries before change points, more subseries after change points showed increasing trends (Table 1-2 and Figure 1-3).

It is noted that 26 out of 59 stations detected with change points show significant trends if change points were not considered, even though no significant trend may be detected in their corresponding subseries before or after change points. On the other hand, some subseries showed significant trends both before and after change points, yet the entire series did not show a significant trend. The above results obtained for the same stations, with and without considering change points, indicate the importance of identifying the change point (if a change point exists) for estimating the monotonic trends of streamflow or other hydroclimatic data (Villarini et al. 2009a). However, in many past studies that estimated temporal trends of Canadian streamflow data, the detection of abrupt changes was mostly ignored, e.g., (Cunderlik and Ouarda 2009; Khaliq et al. 2009b; St. George 2007; Yue et al. 2003).

Figure 1-2 shows stations with significant trends obtained from the Mann-Kendall test applied to the entire series, while Figure 1-3 shows significant trends for subseries before and after the detected change point. The spatial distributions of trend magnitudes for the entire series are also plotted in Figure 1-2. Most significant trends are negative, which generally agree with other past streamflow trend studies conducted in Canada, e.g., (Burn et al. 2010; Cunderlik and Ouarda 2009; Gan 1998; Zhang et al. 2001b).

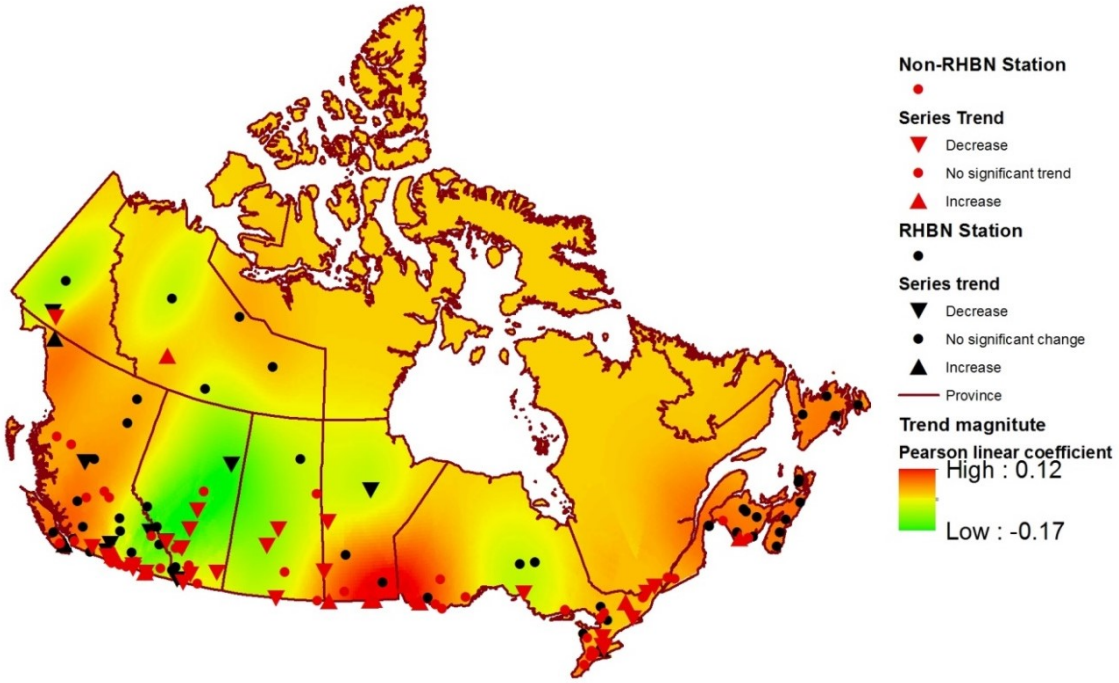

Figure 1-2 Significant temporal trends of AMS of RHBN and non-RHBN at 10% significance level without considering the presence of change points, as well as the spatial distribution of trend magnitudes based on Pearson linear regression coefficients estimated.

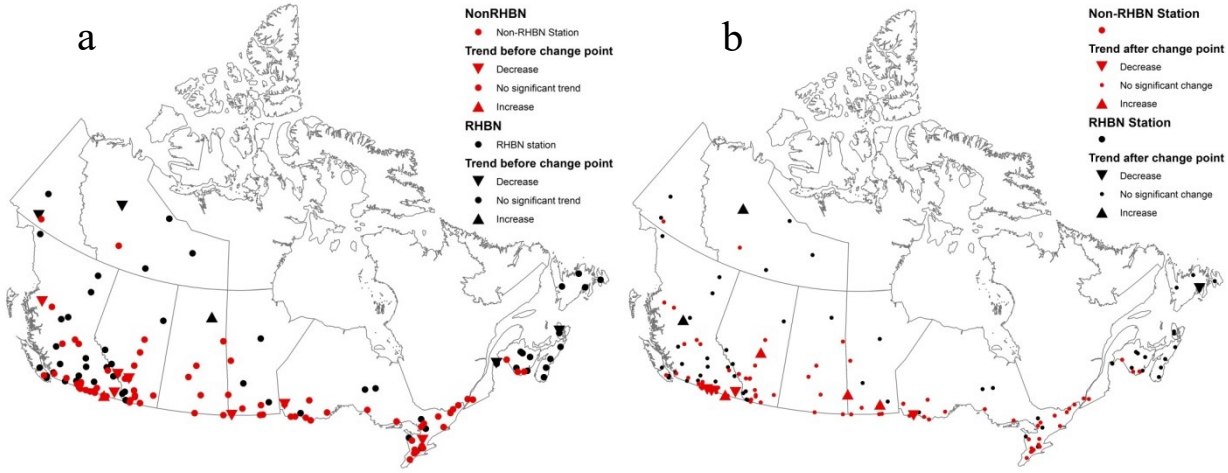

Figure 1-3 Temporal trends in AMS series of RHBN and non-RHBN stations at 10% significance level for a) before, and b) after change points are detected.

In general, a significant decline in the AMS is predominantly found in the Canadian Prairies (CP), which include the three Prairie Provinces of Alberta, Saskatchewan and Manitoba (green area in Figure 1-2), and which generally agree with trend analysis results of annual mean flows of Gan (1998). Given Gan (1998) also showed that about 30% of monthly precipitation data of 37 stations of the CP experienced a significant decrease in 1949-1989, which with a

possible increase in the evaporation loss because of climatic warming, we would expect the AMS of CP to generally decrease. Moreover, Ripley (1986) also found declining trends in the summer precipitation of CP, which likely implies that CP has been slowly becoming drier in recent decades. Burn (2008) attributed the decrease of streamflow to a combination of reductions in snowfall and increases in temperatures during the winter months for snowmelt runoff generation. In contrast, the Winnipeg River basin had experienced increasing trends in its AMS (red area in Figure 1-2) likely because its summer and autumn precipitation had increased (St. George 2007).

Agricultural practices can also affect regional hydrological regimes significantly. Compared to conventional tillage, soil infiltration and water seepage through soil layers of agriculture land subjected to conservation tillage will increase, and therefore, for the same amount of precipitation, surface runoff and peak streamflow will decrease (Shelton et al. 2000). Thus, the increasing use of conservation tillage in agricultural land of CP could be partly responsible for the decrease in the AMS over CP (Shelton et al. 2000).

The diversion of water from rivers for irrigation and other consumptive usage will also decrease the streamflow. The areas of agricultural land in Canada has increased in recent decades, which generally resulted in a significant decrease in the AMS, especially in areas cultivated for intensive agricultural production (Environment Canada 2004). The agricultural lands of CP account for about 82% of the total land used for agriculture in Canada. Other human-related land use practices such as deforestation (Lin and Wei 2008), afforestation (Buttle 2011), mining and petroleum production (Environment Canada 2004) may also play a major role in changes to flood regimes of Canada.

Past studies of Canadian streamflow trends (e.g., (Burn 2008; Burn and Elnur 2002; Burn et al. 2010; Cunderlik and Ouarda 2009; Déry et al. 2009b; St. George 2007; Whitfield and Cannon 2000; Whitfield et al. 2003; Zhang et al. 2001b) usually assumed that streamflow was not affected by human activities but to climatic factors alone. St. Jacques et al. (2010), who analyzed unregulated, regulated and naturalized streamflow records of Southern Alberta, found that the declining streamflows are due to hydroclimatic changes (probably from global warming) and severe human impacts, which could be of the same order of magnitude, if not greater. Unfortunately, it is very difficult, if not impossible, to separate the impact of climatic and human

factors on the streamflow of a river basin because of the complex interactions between climate, human, and hydrologic processes.

1.4.3 GAMLSS modeling of extreme distribution

Since both long-term monotonic trends and abrupt changes have been detected in some AMS series, we further evaluate the nonstationarities of these streamflow data by fitting these data with several PDs designed to characterize data nonstationarities.

If no statistically significant change point was detected in an AMS series, that dataset was fitted with four different two-parameter PDs (gamma, Weibull, Gumbel and lognormal) of GAMLSS. PDs for streamflow series with no significant change points include: (1) a PD with stationary θ_1 and θ_2 , (2) a PD with one time-varying parameter θ_1 , or both time-varying parameters, θ_1 and θ_2 modelled as a link function, $g(\theta)$, dependent on certain linear functions of time, (3) a PD with one, θ_1 , or two time-varying parameters, θ_1 and θ_2 , modelled as $g(\theta)$, dependent on certain additive functions of time such as a cubic splines function adopted in this study. If a significant change point is detected in the mean of AMS series, more complicated PDs of GAMLSS will be chosen to model both abrupt changes and a time varying, θ_1 based on certain piecewise linear functions of time that are discontinuous at the time the change point is detected. Due to numerical convergence problems encountered while applying piecewise linear functions of GAMLSS, only θ_1 may be modeled as a time varying parameter. The goodness-of-fit of all PDs, ranging from a PD with two stationary parameters to a PD with two nonstationary parameters was assessed in terms of bias and AIC scores.

Table 1-3 shows that for 39 out of 85 stations without a detected change point, the AMS series were fitted with several stationary PDs and the PDs with the best goodness-of-fit statistics were selected. For the remaining 46 stations without detected change points, it turns out that the data were better fitted using nonstationary PDs with time varying parameters based on either linear or nonlinear functions of time. Out of 60 stations with detected change points, nonstationary PDs with the time-varying location parameter θ_1 based on certain piecewise functions of time evidently gave the best fit to 36 stations, nonstationary PDs with certain nonlinear descriptions of time-varying parameters gave the best fit to another 21 stations, and stationary PDs gave the best fit to the remaining 3 stations of the AMS. On a whole, the AMS of

103 out of 145 stations was better fitted with nonstationary PDs, which indicates that over 70% of the AMS records over Canada are nonstationary, and most of the AMS records are best fitted by either lognormal and gamma distributions.

Table 1-3 Numbers of stations fitted to the specific GAMLSS model in the absence and presence of a change point

Model #	Type of GAMLSS model	PD	Numbers of stations	
			No change point	With change point
1	Stationary	Weibull	4	0
2		Gamma	15	1
3		Gumbel	1	0
4		Lognormal	19	2
5	Linear (Piecewise linear) [a] model of only location parameter	Weibull	0	8
6		Gamma	0	11
7		Gumbel	0	0
8		Lognormal	0	17
9	Linear (Piecewise linear) model of both location and shape parameters	Weibull	3	-- [b]
10		Gamma	4	--
11		Gumbel	0	--
12		Lognormal	5	--
13	Nonlinear model of only location parameter	Weibull	5	3
14		Gamma	4	7
15		Gumbel	0	0
16		Lognormal	13	5
17	Nonlinear model of both location and shape parameters	Weibull	0	1
18		Gamma	4	2
19		Gumbel	0	0
20		Lognormal	8	3

[a] Linear models are used for series from stations without abrupt change point detected, while piecewise linear models are fitted for series from stations without abrupt change point.

[b] Models are not fitted to the series due to the numerical problem present in the fitting.

The effectiveness of five nonstationary and one stationary PDs applied to model the AMS series of six stations (see Figure 1-1) are further examined. These stations with their best fitted PDs are, respectively: 1) 05CC002, Red Deer River at Red Deer, a lognormal distribution with one location parameter based on a piecewise linear function of time, 2) 05KJ001, Saskatchewan River at The Pas, a gamma distribution with one location parameter based on a piecewise linear function of time, 3) 08NE049, Columbia River at Birchbank, a lognormal distribution with one location parameter based on a nonlinear function of time, 4) 08JB002, Stellako River at Glenannan, a lognormal distribution with both location and shape parameters based on a nonlinear function of time, 5) 08MH016, Chilliwack River at Outlet of Chilliwack Lake, a

lognormal distribution with both location and shape parameters based on a linear function of time, and 6) 01AK001, Shogomoc Stream near Trans Canada Highway, a stationary lognormal distribution.

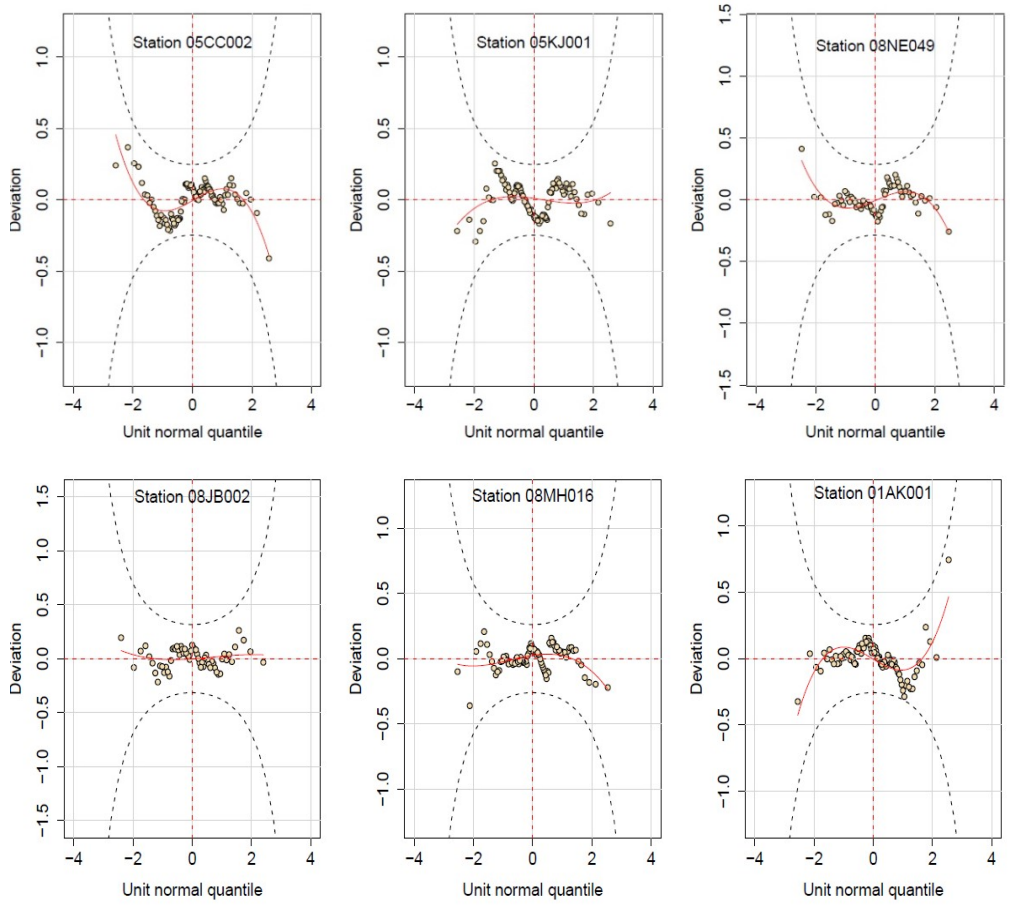

Figure 1-4 Worm plots for six representative stations showing the goodness-of-fit of 2-parameter PDs to their corresponding measured AMS. For a good fit, the data points should be aligned preferably along the grey solid curve but within the 95 percentile confidence interval represented by two grey dashed curves (van Buuren and Fredriks 2001).

The first four stations had abrupt changes but not the latter two stations. The first three are non-RHBN stations while the latter three are RHBN stations. Worm plots of residuals (Figure 1-4) for these six stations generally demonstrate good agreements between the fitted PDs with their observed AMS series, with the data points primarily aligned on the fitted red curves that generally fluctuate closely along the zero deviation line, and within the 95% confidence intervals (grey curves). Figure 1-5 shows that for Station 08MH016 with no significant abrupt change and trend detected, the percentiles of AMS with low probability of occurrences (5% and 25%) increased more significantly compared to other quantiles. Also, extreme annual maximum flood events (5^{th} percentiles) for Stations 05CC002, 05KJ001 and 08JB002 increased significantly

after 1980s, and at faster rates than other quantiles, which demonstrate generally larger increase to extreme events that occurred after 1980s, or chances of the occurrence of extreme events seem to be increasing, which likely implies that achieving reliable flood forecast in Canada will become more challenging in the future. Different temporal variations of quantiles in the AMS series of these 6 stations probably confirm predominantly nonstationarities in the AMS series of Canada, which include observed changes in the mean, increased streamflow variability and severity of extreme events.

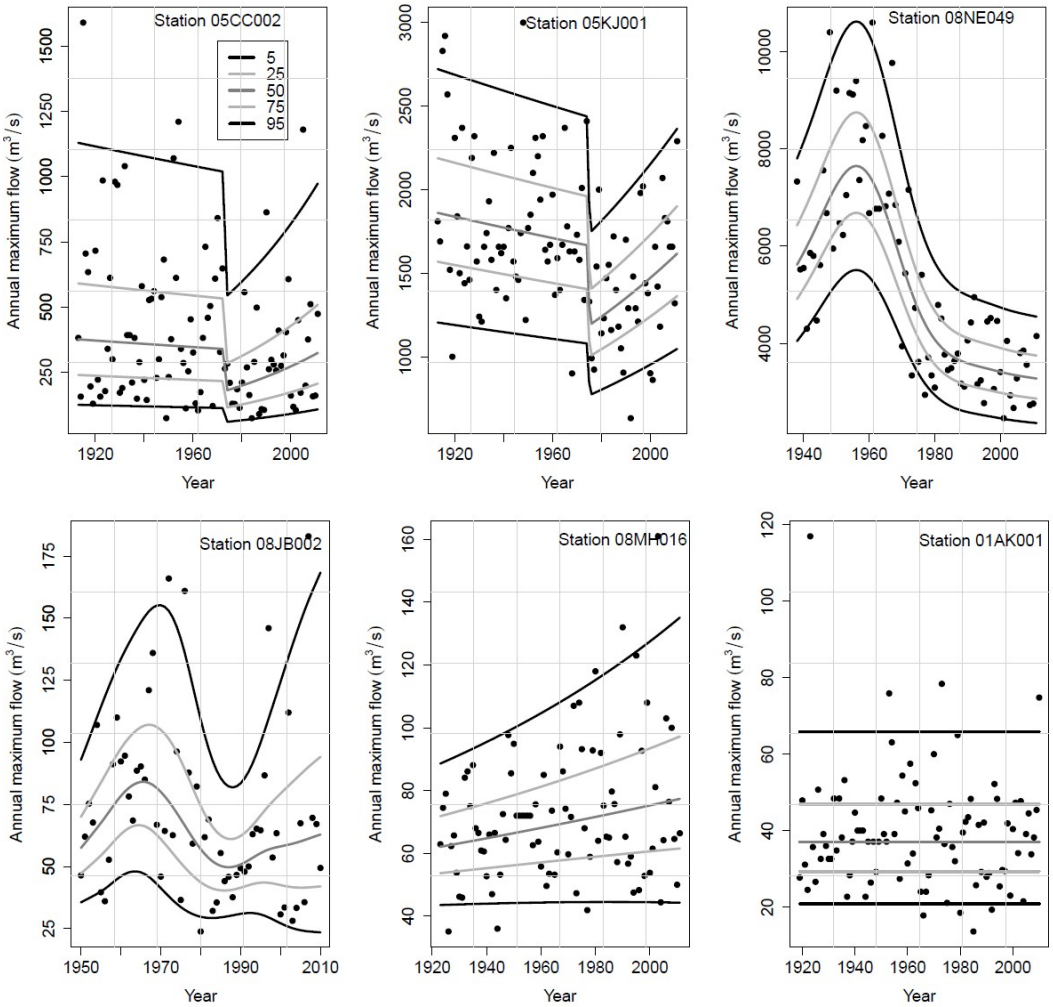

Figure 1-5 Fitting of AMS series for six selected stations (locations shown in Figure 1) to five nonstationary and one stationary PDs, with solid dots representing measured AMS values scattered between five levels of percentiles (5^{th}, 25^{th}, 50^{th}, 75^{th}, and 95^{th}).

1.4.4 Long-term persistence (LTP)

For natural processes such as streamflow, the range of cumulative departure from the mean normalized by the standard deviation generally follows a power law behavior (Hurst 1951;

Klemeš 1974; Potter 1976). If the exponent of this power law phenomenon is larger than 0.5, it is known as the Hurst phenomenon (Hurst 1951), which tends to strongly increase the large time scale variability or statistical uncertainty. Results of Hurst exponents (H) obtained in this study are used to suggest some plausible physical explanations to properties of the Canadian AMS data. Table 1-4 presents number of AMS series showing LTP, i.e., H larger than 0.5.

Table 1-4 Numbers of stations whose Hurst exponents (H) are larger than 0.5 calculated from different estimators

	Aggregated variance	Differenced aggregated variance	Aggregated absolute value	R/S rescaled range statistic	Peng's
Non-RHBN (83)*	30	71	50	58	63
RHBN (62)	29	47	44	45	38

* Values in the brackets are the total selected station to be analyzed.

Given that H values calculated for the same station by different methods can differ widely, it seems that detecting the presence of LTP for AMS involves large uncertainties. For example, the number stations with $H > 0.5$ by the differenced aggregated variance method is more than double that estimated using the aggregated variance method. By comparing many H estimators, Teverovsky and Taqqu (1997) concluded that the aggregated variance method tends to produce large errors when trends or abrupt changes present. Therefore, results obtained by the aggregated variance method for stations with detected trends or abrupt changes are hence forth discarded. Out of 145 stations, both the R/S method and the Peng's method estimated slightly over 100 stations with H larger than 0.5, while the aggregated absolute value method estimated slightly less than 100 stations showing LTP.

The inconsistent results obtained from different methods may be partly caused by limited sample sizes. The reliability of results can also be affected by the nonstationarities of the time series. To estimate the uncertainty of H estimated with sample size, a bootstrapping resampling procedure (Davison and Hinkley 1997) was used to derive the PDs and confidence intervals of H using the R/S and the Peng's methods. The time series of each station was resampled with replacement for 10,000 times, and the H for each sample estimated. Spatial distributions of the mean and the 95% confidence intervals of H values estimated by this bootstrapping approach are shown in Figure 1-6. The average H derived from the R/S method and Peng's method are 0.67 and 0.58, with corresponding 95% confidence intervals of 0.46-0.89 and 0.35-0.74, respectively. Apparently the Peng's method estimated lower H values than the R/S method. At the lower confidence limit (2.5%), the R/S method estimated 46 and Peng's method estimated 15 stations,

out of 145 stations, with *H* higher than 0.5, which suggest the strong (statistically significant) presence of LTP in the Canadian AMS series. The spatial patterns of *H* derived from the R/S and Peng's methods are similar to each other (Figure 1-6). The above results show that stations located in southern Canada and in inland generally exhibit higher *H* than other parts of Canada, e.g., clusters of high *H* values are located in Southeastern BC, southwestern Manitoba and Southeastern Ontario.

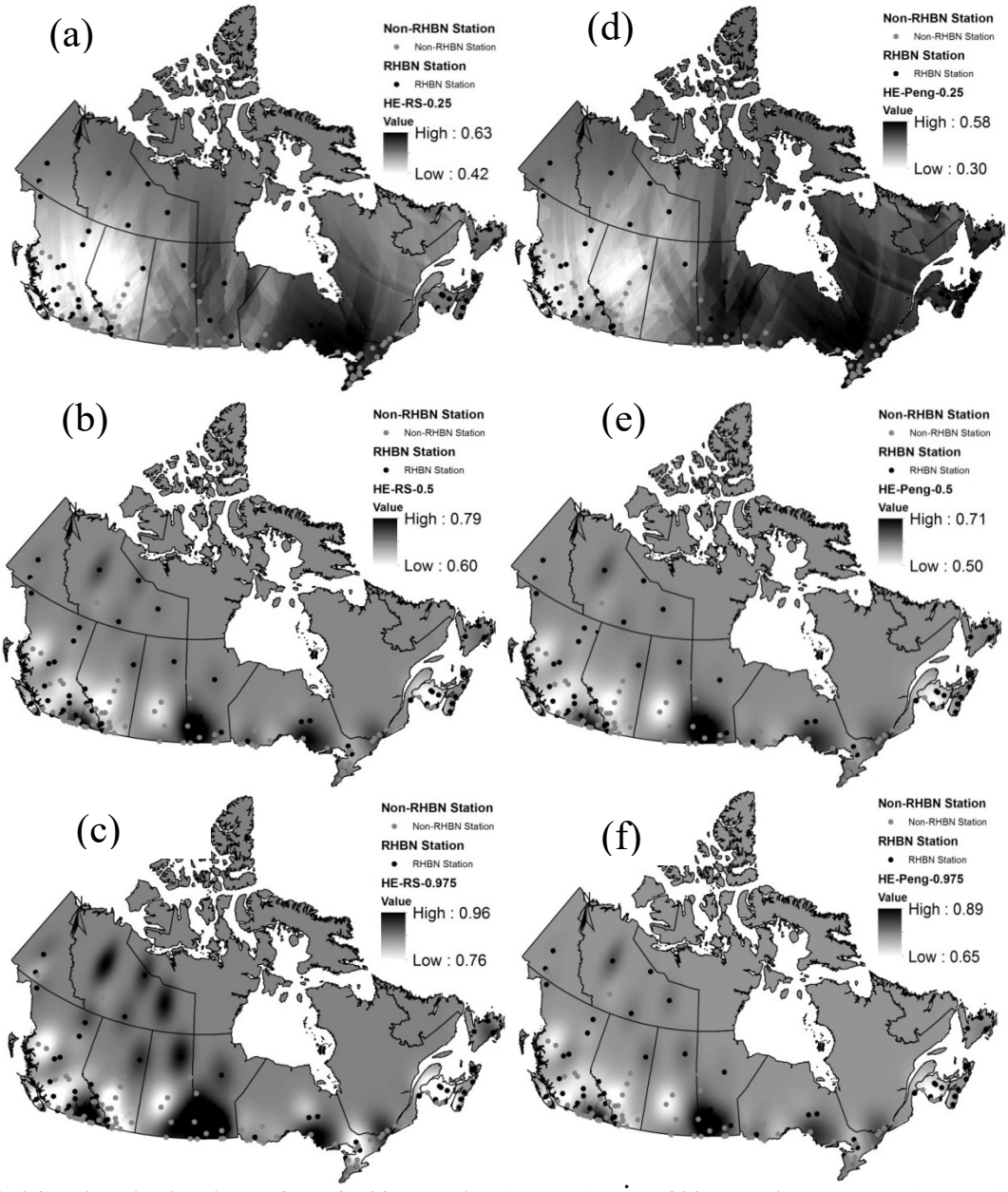

Figure 1-6 Spatial distributions of the 2.5% quantile (a and d), the 50% quantile or mean (b and e) and the 97.5% quantile (c and f) of Hurst exponent (H) re-sampled by the bootstrap method applied to station (represented by dots) H values estimated from the R/S method (a, b and c) and the Peng's method, respectively.

Bras and Rodriguez-Iturbe (1985) offered three possible physical explanations underlying the Hurst phenomenon. First, the Hurst phenomenon is transitory because our data are not long enough to test the steady-state behavior of *R*, the range of cumulative departures from the mean (Cohn and Lins 2005; Franzke 2012; Koutsoyiannis 2006). Second, it is due to nonstationarities in the mean of the process (Klemeš 1974; Potter 1976). And third, it is due to stationary processes with infinite memories (Mandelbrot and Wallis 1969). By showing strong positive correlation between *H* and the mean discharge, air temperature, and basin area of European rivers, Szolgayova et al. (2014) claimed to have found evidence to the 3rd explanation.

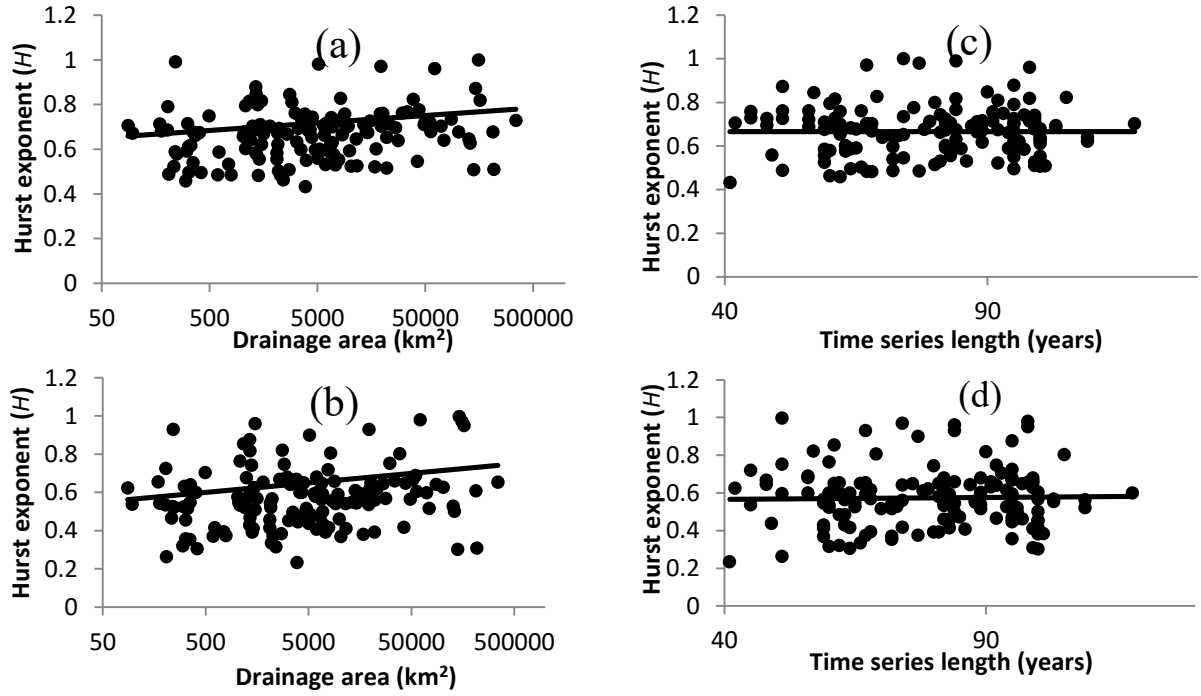

Figure 1-7 Scatterplots between Hurst exponent (*H*) of Canadian AMS estimated using the R/S (a, b) and the Peng's (c, d) method with basin area, and length of the AMS time series, respectively.

Figure 1-7, scatterplots of the mean *H* value derived from bootstrap re-sampling with basin drainage area and the length of time series, shows a modest positive correlation between *H* estimated by the R/S and Peng's method and basin drainage area, with statistically significant Kendal's *S*, 0.14 and 0.12, and Spearman's rho, 0.21 and 0.18, respectively. It seems that the AMS of larger watersheds are more likely to show stronger LTP, possibly because of their larger capacity to store inundated flood water. However, Figure 1-7 also shows that *H* values do not depend on the length of time series but the result is inconclusive because in this study the AMS series are only limited to just over 100 years long.

Trends in environmental data can be attributed to stochastic or deterministic processes or both. Stochastic trends can exist in very simple stationary stochastic processes over long periods of time, as shown by Cohn and Lins (2005), Koutsoyiannis (2006) and Franzke (2012) who linked LTP to multidecadal oscillations in climate regimes or other internal climate variabilities. Deterministic trends driven by external forcings such as greenhouse gases and land use changes can also lead to high values of *H* (Potter 1976; Rust et al. 2008). Among the 46 (15) stations showing statistically significantly LTP in AMS data detected by the R/S (Peng's) method, only 16 (2) are RHBN stations while 30 (13) are non-RHBN stations.

On the basis of these results, it seems that having human-induced nonstationarities in a time series can enhance the LTP represented by the *H* exponent. Furthermore, similar effect of nonstationarities on *H* was also found by Klemeš (1974), Potter (1976) and Rust et al. (2008) in their simulation studies on hydroclimatic time series. However, our results are not sufficient to conclude whether LTP detected in Canadian AMS series are the results of nonstationarities caused by stochastic and/or deterministic processes or both. Moreover, a lack of additional information, limited sample sizes, the appropriateness of the estimation methods used in this study and some unknown external forcings that can possibly contribute to deterministic trends are unresolved issues that are beyond the scope of this study.

1.5 Summary and conclusions

Based on 145 RHBN and non-RHBN stations of Canada with long-term AMS series and hydrological observations, we investigated the nonstationary characteristics of AMS of Canada. The research results can be summarized as follows:

1. Results from the PETT show that almost half of the stations, including non-RHBN stations, experienced an abrupt shift in the mean of the AMS. The timing of abrupt change points have been shown to be closely related to the years when the regulation of streamflow began. Given that only about 1/6 of the RHBN stations with minimal streamflow regulation and stable land-use conditions experienced abrupt changes, it seems that human interference of nature has been instrumental in causing an abrupt shift in the mean of AMS of Canada. However, in this study, no change point was detected in the variance of AMS of any station.

2. Trend analysis on complete time series of AMS shows that about 50 out of 145 stations exhibit monotonic temporal (more negative than positive) trends, e.g., abrupt change points were not considered in the analysis. However, further trend analysis show that only about 12 out of 59

stations detected with abrupt change points showed significant monotonic trends in the time series before and/or after change points were detected. Thus, abrupt changes are more likely the cause of nonstationarities to AMS series over Canada than monotonic trends. Similar to abrupt changes attributed to regulations of streamflow, drainage basins subjected to significant land use changes are more likely to show temporal trends in the AMS compared to pristine basins with stable land-use conditions. Climate change impact due to human activities could also contribute to monotonic trends, and possibly abrupt changes to AMS series of Canada.

3. More than 2/3 of the AMS series could be accurately fitted with lognormal and gamma PDs. The nonstationarities of the AMS series which include monotonic trends, nonlinear fluctuations and abrupt changes were modeled using PDs with time varying parameters. Other factors such as climate anomalies and land use change descriptors will be necessary to more fully investigate physical explanations behind various types of nonstationarities found in the streamflow series.

4. The LTP analysis using the R/S and the Peng's methods reveals that almost 2/3 of the Canadian AMS series show significant LTP (high H). It seems that widespread LTP detected in the AMS of Canada should be primarily related to the predominant nonstationarities characteristics of AMS data attributed mainly to climatic changes, climate variability and landuse impacts of human activities. Further, the degree of LTP (H) is also found to be positively correlated with the areas of Canadian river basins.

A possible future extension to this study is to explore changes of climate variables and evidence of human activities that contribute to abrupt changes, trends, and non-stationarity in the streamflow of Canada presented above.

Chapter 2 Contribution of human and climate change impacts to changes in streamflow of Canada

2.1 Introduction

Regional changes in precipitation (P) minus evapotranspiration (E), $P - E$, caused by changes in specific humidity, circulation, and moisture transports complicate impacts of climate change on changes to streamflow (Seager and Vecchi 2010). Human activities such as river regulations (Assani et al. 2006; Destouni et al. 2013; Grill et al. 2015; Nilsson et al. 2005; Poff et al. 2007), land use change (Gordon et al. 2005; Sterling et al. 2012; Vörösmarty and Sahagian 2000), deforestation (Zhang and Wei 2012), reforestation (Buttle 2011), and extraction or diversion from surface water and groundwater (Milly et al. 2005; Schindler and Donahue 2006; Vörösmarty and Sahagian 2000; Zhou et al. 2015) generally incur a direct change to streamflow. Most studies attributed changes in streamflow to climate change impact only, such as a shift from snowfall towards rainfall in USA (Berghuijs et al. 2014), increasing trends in annual total precipitation in Canada (Mekis and Vincent 2011), without considering possible impact of human activities which can alter the streamflow directly through influencing the runoff production and indirectly through affecting the climatic variables (Barnett et al. 2008; Milly et al. 2008; Pall et al. 2011).

It is a challenge to quantify human contribution to changes in streamflow (Gedney et al. 2006) partly because human disturbances incur changes to many subsystems such as atmosphere, hydrosphere, cryosphere, land surface and biosphere (Pall et al. 2011). Instead of using deterministic rainfall-runoff models to assess the impacts of climate change or human activities on runoff for each watershed, in this study we used observed precipitation, streamflow and estimated PET data to separate direct impacts of human activities from impacts of climate change (even though the latter is related to human impacts) to changes in Canadian streamflow based on the Budyko Framework (Budyko 1961). The Budyko Framework assumes that the long-term water balance of a watershed based on the dryness index of actual evaporation to precipitation, E/P, is primarily a function of the atmospheric supply and demand of water, expressed as the ratio of PET to precipitation, E_p/P, i.e., $E/P=f(E_p/P, n)$, where n is an empirical coefficient representing the combined watershed landscape properties that control water-energy

balances (Xu et al. 2013) (Figure 2-1). In other words, the Budyko Framework enables us to predict hydrologic responses of a watershed to a wide range of climatic conditions with respect to the characteristics of the watershed, such as land properties, terrain features and others.

The long-term moving average water balance with a 20-year window, $P = E + R$ (R is streamflow), of 96 Canadian watersheds (Figures 2-2 and 2-3, and see Supplementary Tables S1 and S2 in Tan and Gan 2015b) was analyzed, but changes in water storages of watersheds are ignored in the analysis. The elasticity of streamflow, defined as the percentage change of streamflow from a 1% annual change in climate or land conditions and analytically derived from the Budyko Framework (Yang and Yang 2011), was used to estimate hydrological responses to climate change, land use and cover changes (LUCC) for each watershed. Hydroclimatic data was separated to two subseries for pre- and post-change periods (periods-1 and -2, respectively) from an abrupt change-point. Thus, the relative contribution of changes in precipitation and PET, and the relative contribution of human activities (LUCC) to streamflow change from periods-1 and -2, can be obtained from the difference in precipitation, PET and n between periods-1 and -2, and the corresponding streamflow change based on its elasticity to the above changes. The separate results were further validated by a decomposition method (Wang and Hejazi 2011) that are also analytically derived from the Budyko Framework. Details of the above processes are described in Section 2.4 Methods.

2.2 Results

2.2.1 Hydroclimatic trends and change-points

Change-point and trend analysis (Methods) of 96 selected watersheds are shown in Figure 2-4. Out of 60 non-RHBN (Reference Hydrometric Basin Network) watersheds, the streamflow and PET of 41 watersheds and the precipitation of 45 watersheds show statistically significant change-points. However, for 36 RHBN watersheds, the corresponding number of watersheds decreases to 9 and 2 respectively, mainly because of pristine land-use conditions of RHBN watersheds. Change-points of streamflow data are mainly detected in 1929-1997 (mean 1969) and 1977-2004 (mean 1991) for non-RHBN and RHBN stations, respectively. Therefore, we adopt 1990 as the change point year for RHBN stations. However, for non-RHBN stations, because data begins no later than 1960, we adopt 1980 as the change point year to ensure sufficient length of data before and after change points. By adopting a common change point

year for non-RHBN and RHBN stations, we have a better basis to compare the attribution results between different non-RHBN and RHBN watersheds.

From periods-1 to -2, the annual streamflow generally decreased (0-81 mm) along the Canadian Rockies (CR) which are Boreal and Montane Cordillera shown in Figure 2-2 but increased (0-58 mm) elsewhere, and 35 non-RHBN in mid- and eastern Canada, and 3 RHBN watersheds show statistically significant increasing trends between 1940s-2010 (Figure 2-4c). However, depending on the periods considered (30-, 40- and 50-year), some RHBN streamflow data in southern Canada showed significant decreasing trends (Zhang et al. 2001b), but most showed insignificant decreasing trends between 1970-2010.

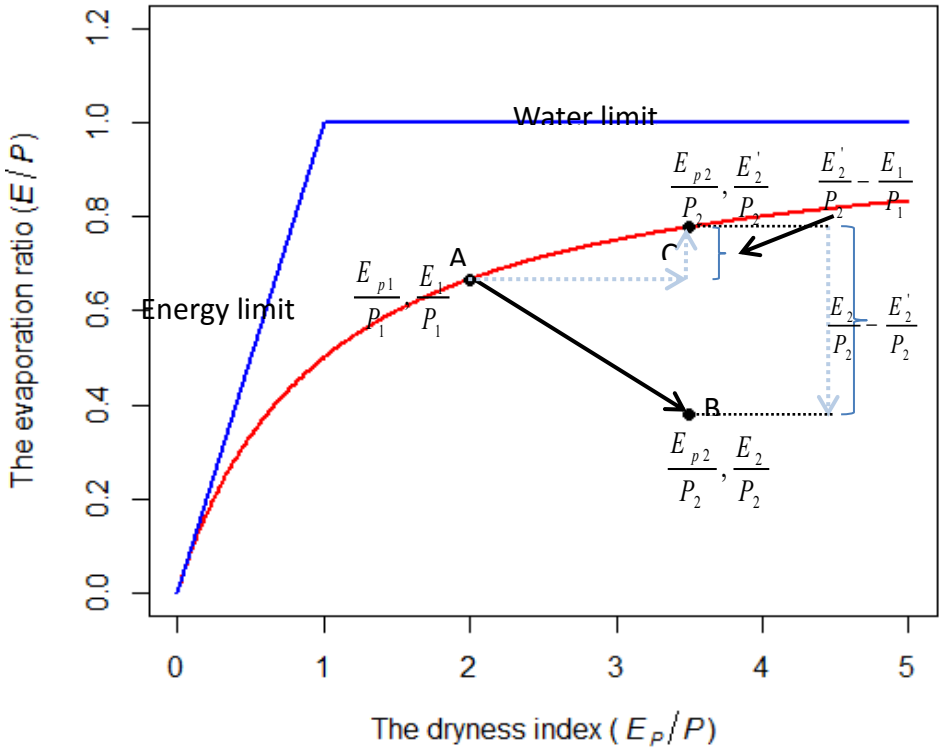

Figure 2-1 Typical Budyko curve (red line, n=1) and the schematic of decomposition method. Assuming point A is the catchment water balance under the stationary condition of the pre-change period (period-1), point B is under another stationary condition of the post-change period, and point C is a hypothetical point under a stationary condition which has the same catchment property as point A and the same climate condition (including precipitation and PET) as point B.

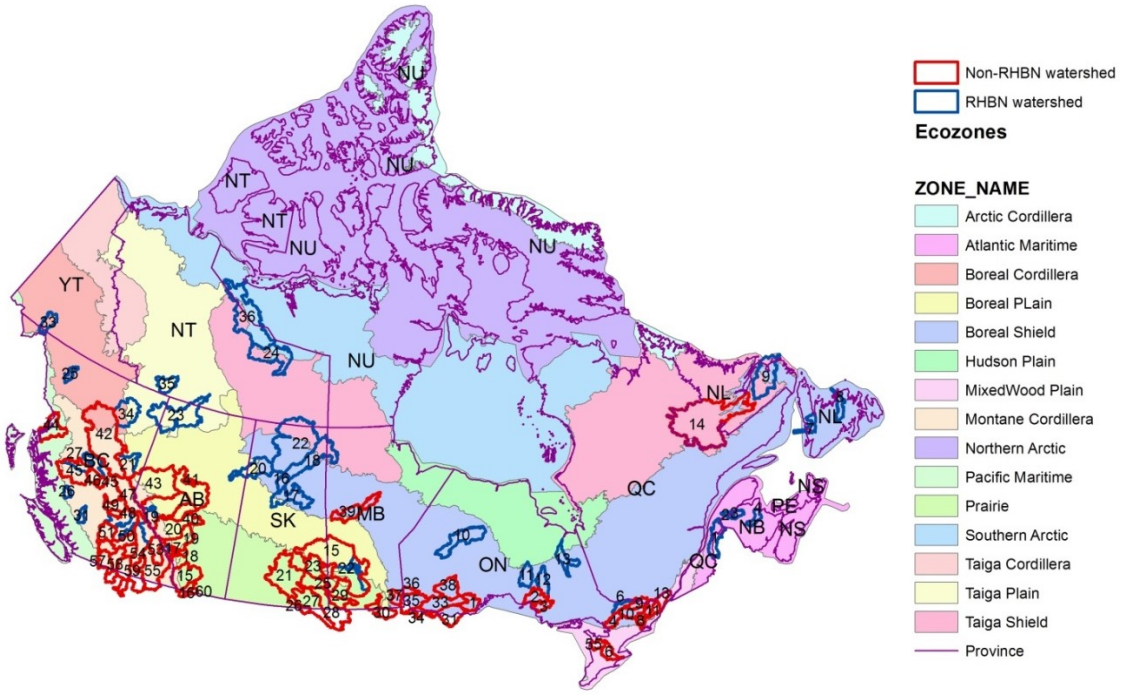

Figure 2-2 **Geographic locations of the 96 studied drainage watersheds (polygons). The 15 terrestrial ecozones for Canada's landmass are also shown. The watershed number and the mean annual hydroclimatic variable values are shown in detail in the Tables S1 and S2.**

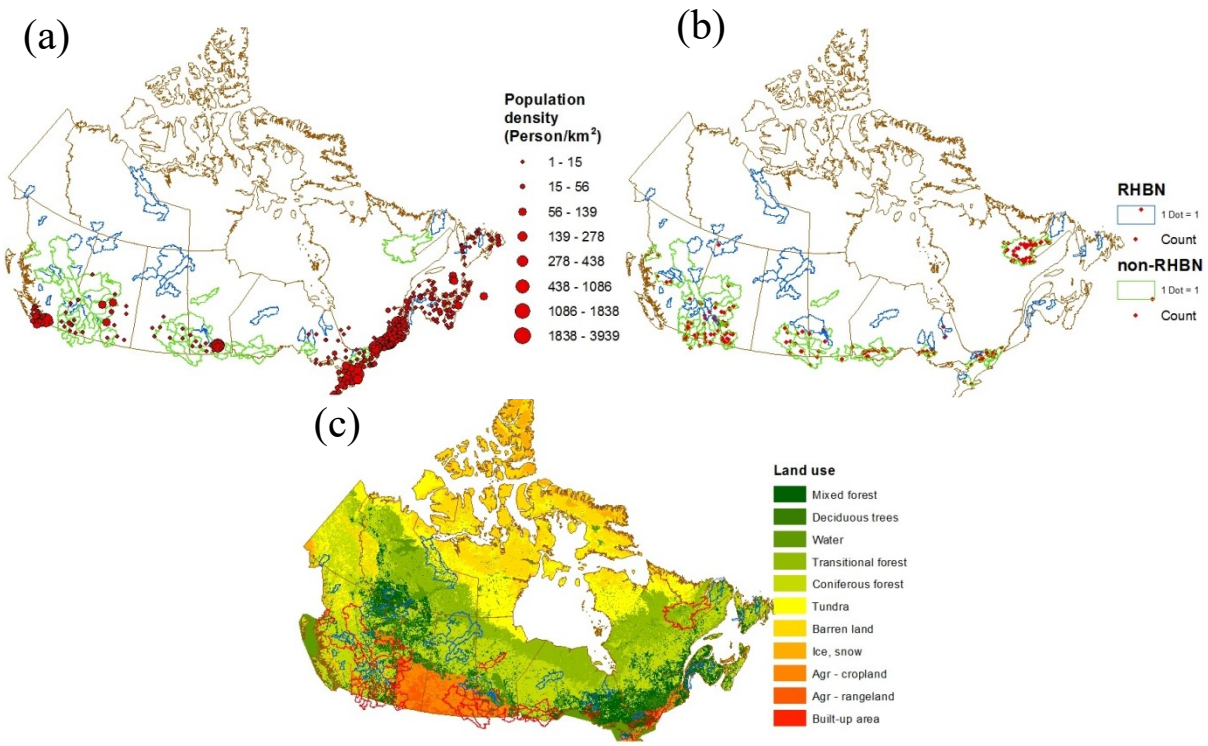

Figure 2-3 **Spatial coverage of exogenous information used as a validation of the landscape change impacts due to human activities on mean annual streamflow, a) population density, b) number of dams in each watershed, and c) land use and cover.**

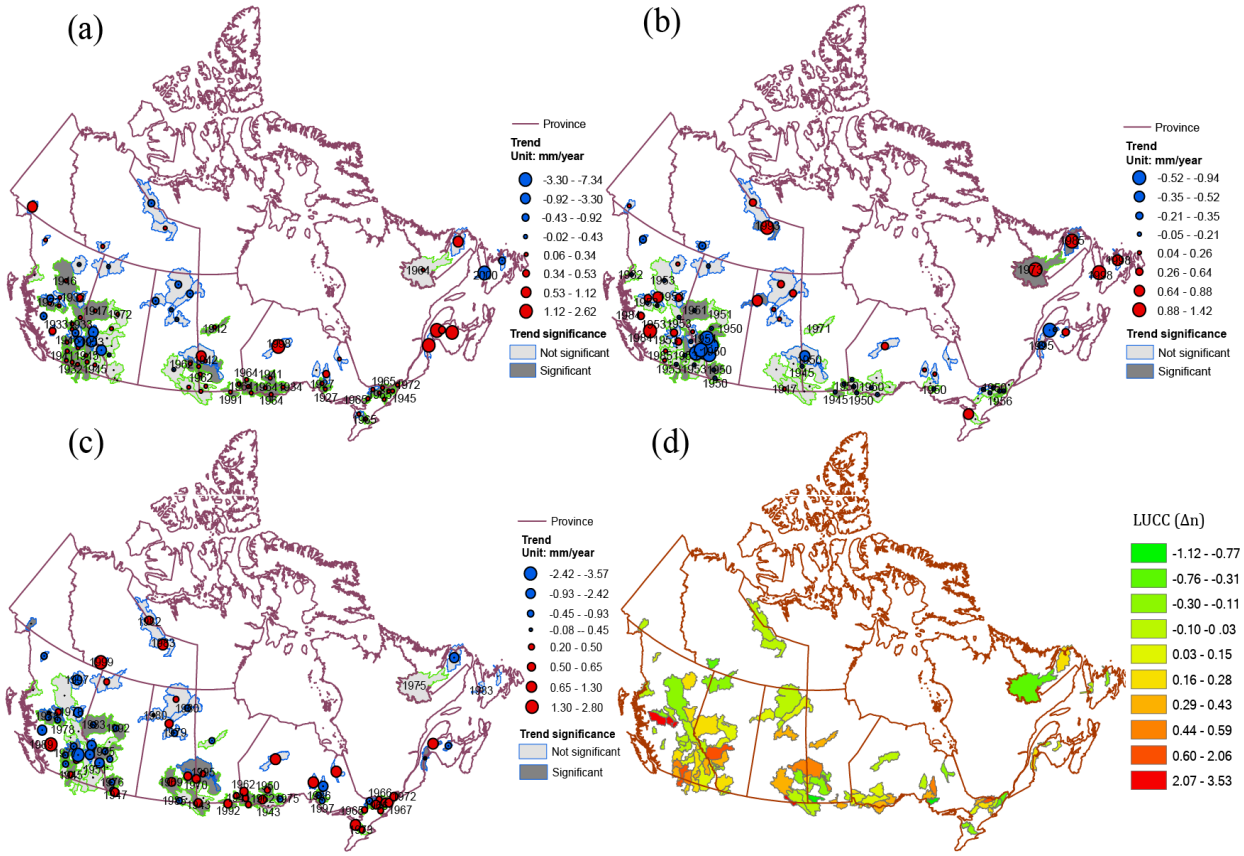

Figure 2-4 Change-points and trends of the annual precipitation (a), potential evaporation (b) and streamflow (c) in mm/year, and (d) change in landscape parameter n (d; $\Delta n = n_2 - n_1$) of 96 selected watersheds across Canada. For figures 1 a-c, only change-points (in year) that are statistically significant at 10% significant level are presented. Blue (green) boundaries show RHBN (non-RHBN) watersheds selected. Light (deep) grey watersheds represent trends that are not (are) statistically significant. The magnitudes of trends are presented in terms of circle sizes, in which green (red) circles represent decreasing (increasing) trends.

Change-points of annual precipitation (PET) occurred in about 1955 (1950) and 1992 (1989) for non-RHBN and RHBN watersheds, respectively. Annual precipitation has increased 5-35% in southern Canada over 1990-1998 (Zhang et al. 2000), and abrupt changes often happened earlier in western than in eastern watersheds (Figure 2-4a). For non-RHBN watersheds, differences in detected change-points between streamflow and climate data can be attributed to human activities. From periods-1 to -2, changes to the mean annual precipitation range from -44 to 158 mm, with a significant decrease in central CR and northern Canada but a significant increase in southern Canada. Most British Columbia (BC) and northern Canada showed an increase (0-30 mm) in the mean annual PET, but southern Canada generally a decrease (0-18mm) (Figure 2-4b), while *n* had generally increased in southern but some had decreased in northern watersheds of Canada (Figure 2-4d).

2.2.2 Elasticities of streamflow

For RHBN and non-RHBN watersheds, n ranges 0.442-3.295 and 0.285-9.305, with a mean value of 1.279 and 2.218, respectively (see Supplementary Tables S1 and S2 in Tan and Gan 2015b). Higher n means higher E for a given P and E_p, and hence a lower runoff (R). For example, non-RHBN watersheds #4 and #13 have similar P (about 1000mm) and E_p (about 700mm), but watershed #4 has high R (about 500mm) because of low n (1.525) while watershed #13 has low R (about 350mm) because of high n (2.712). From periods-1 to -2, most southern (northern) watersheds have become wetter (drier), as E_p/P in the south (north) decreases (increases). E/P tends to increase especially in CR but it also decreases elsewhere (Figure 2-5). E/P~E_p/P relationships for most watersheds in periods-1 and -2 do not follow the same Budyko curve (Figure 2-6), which likely implies that streamflow changes were induced by human impacts, especially when they change in an opposite manner.

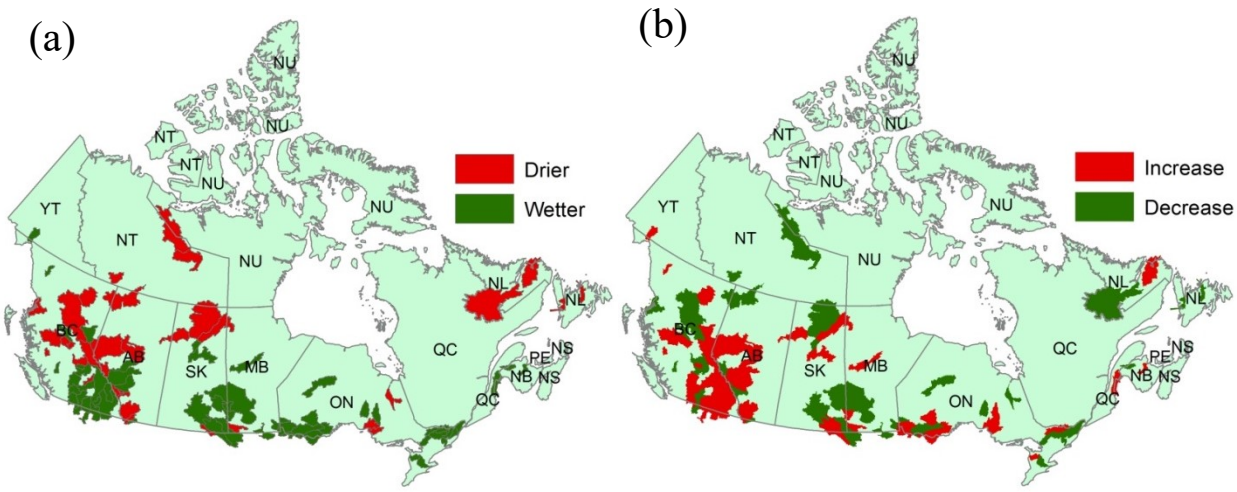

Figure 2-5 Difference in (a) the dryness index and (b) the evaporation ratio between the period-1 and period-2. Red (green) watersheds in (a) were getting drier (wetter) as the dryness index during period-2 was higher (lower) than that during period-1. Red (green) watersheds in (b) show an increase (decrease) in the evaporation ratio as the evaporation ratio during period-2 was higher (lower) than that during period-1.

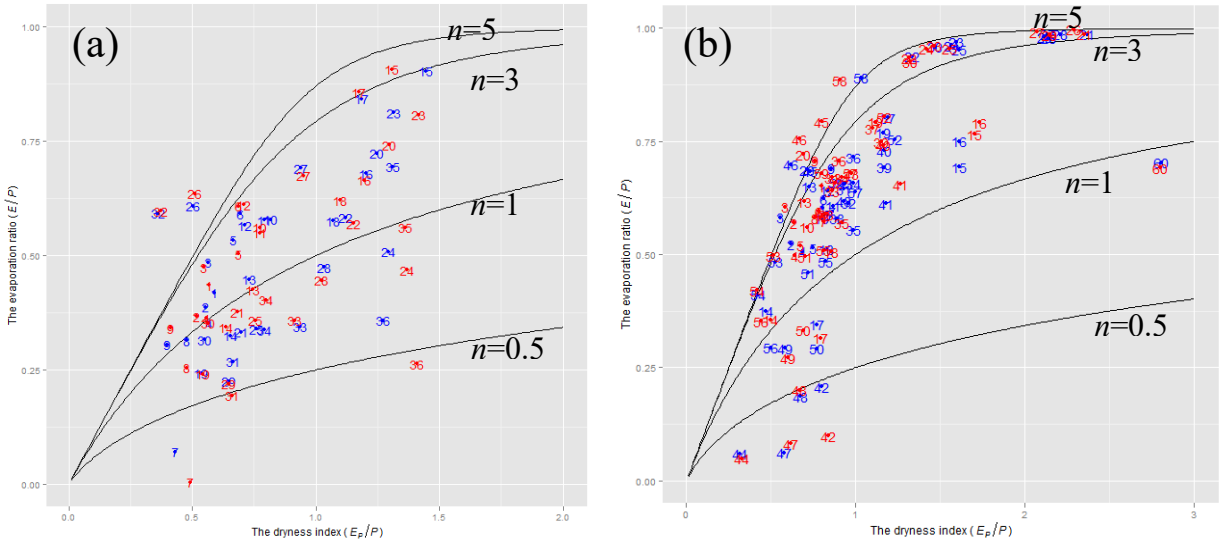

Figure 2-6 Distribution of the mean annual evaporation ratio (*E*/*P*) versus mean annual dryness index (E_0/*P*) for selected RHBN (a), and non-RHBN (b) watersheds during the period-1(blue dots) and period-2 (red dots). The Budyko curves calculated by Equation (2-2) are plotted as black solid lines. The watershed numbers shown in the figures are described in Supplementary Table S2 of Tan and Gan (2015b).

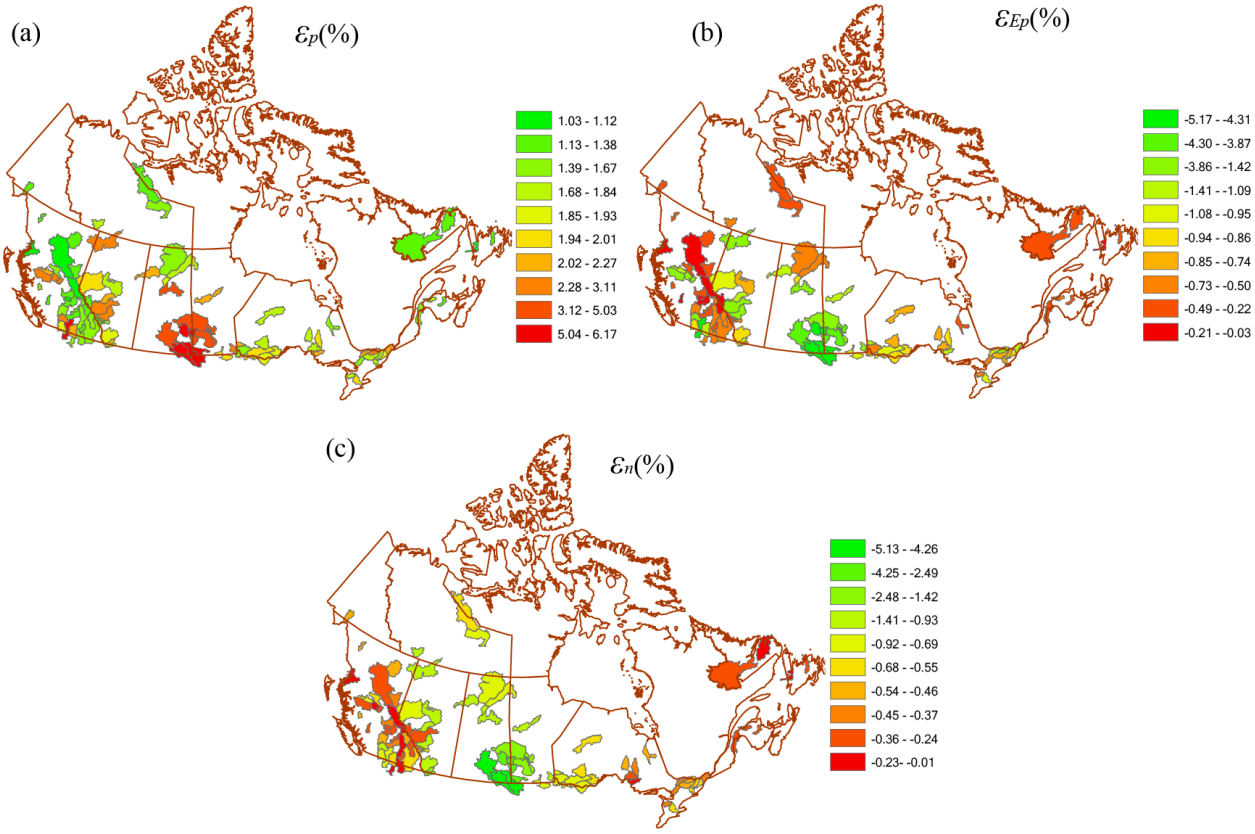

Figure 2-7 Elasticity of streamflow of 96 watersheds of Canada to (a) precipitation ε_p, (b) potential evaporation (PET), ε_{Ep}, and (c) the watershed landscape ε_n.

Figure 2-7 shows the spatial distribution of elasticity of streamflow to precipitation, ε_p, to PET, ε_{Ep} and to LUCC, ε_n for Canada. The ranges of ε_p are 0.03-5.17, for ε_{Ep} are -5.17-0.03, and for ε_n are -5.14-0.02. The mean ε_p, ε_{Ep} and ε_n values are 2.38, -1.38 and -1.03 for non-RHBN watersheds, and 1.65, -0.65 and 0.61 for RHBN watersheds, respectively. The spatial pattern of ε_p is somewhat similar to that of ecozone, and land use/cover (Figures 2-2 and 2-3). As expected, streamflow of the semi-arid Canadian Prairies (CP), which comprises of Alberta (AB), Saskatchewan (SK), and Manitoba (MB), is highly sensitive to LUCC, but less sensitive to LUCC in CR and northern Canada, e.g., absolute values of ε_p, ε_{Ep} and ε_n of southern CP are higher than other parts of Canada (Figure 2-7).

2.2.3 Direct human impacts and climate change to streamflow change

Streamflow change results from changes in precipitation, ΔR^{CP}, PET, ΔR^{CE_P}, and LUCC, ΔR^{l} representing human impacts (Figure 2-8). The modeled streamflow change ΔR^{s} ($\Delta R^{s} = \Delta R^{CP} + \Delta R^{CE_P} + \Delta R^{l}$) based on the elasticity method generally agrees well with the observed ΔR (Figure 2-9), with an average absolute error and a Pearson correlation of 4.3 mm and 0.98, respectively. Since precipitation and LUCC exerts opposite influence on streamflow, the net effect might lead to a minimal change in streamflow of watersheds subjected to both climate and LUCC impacts. However, their relative contributions to streamflow change can be deciphered, e.g., RHBN (#1, #4) and non-RHBN (#9, #10, #57 and #64) watersheds showed significant increase in streamflow (26-88mm) due to increasing precipitation, but significant decrease in streamflow (28-87mm) due to increasing *n*, which results in minimal streamflow changes. Therefore, human activities represented by LUCC tend to decrease the streamflow, as already observed in Canadian streamflow, albeit precipitation over Canada has generally increased.

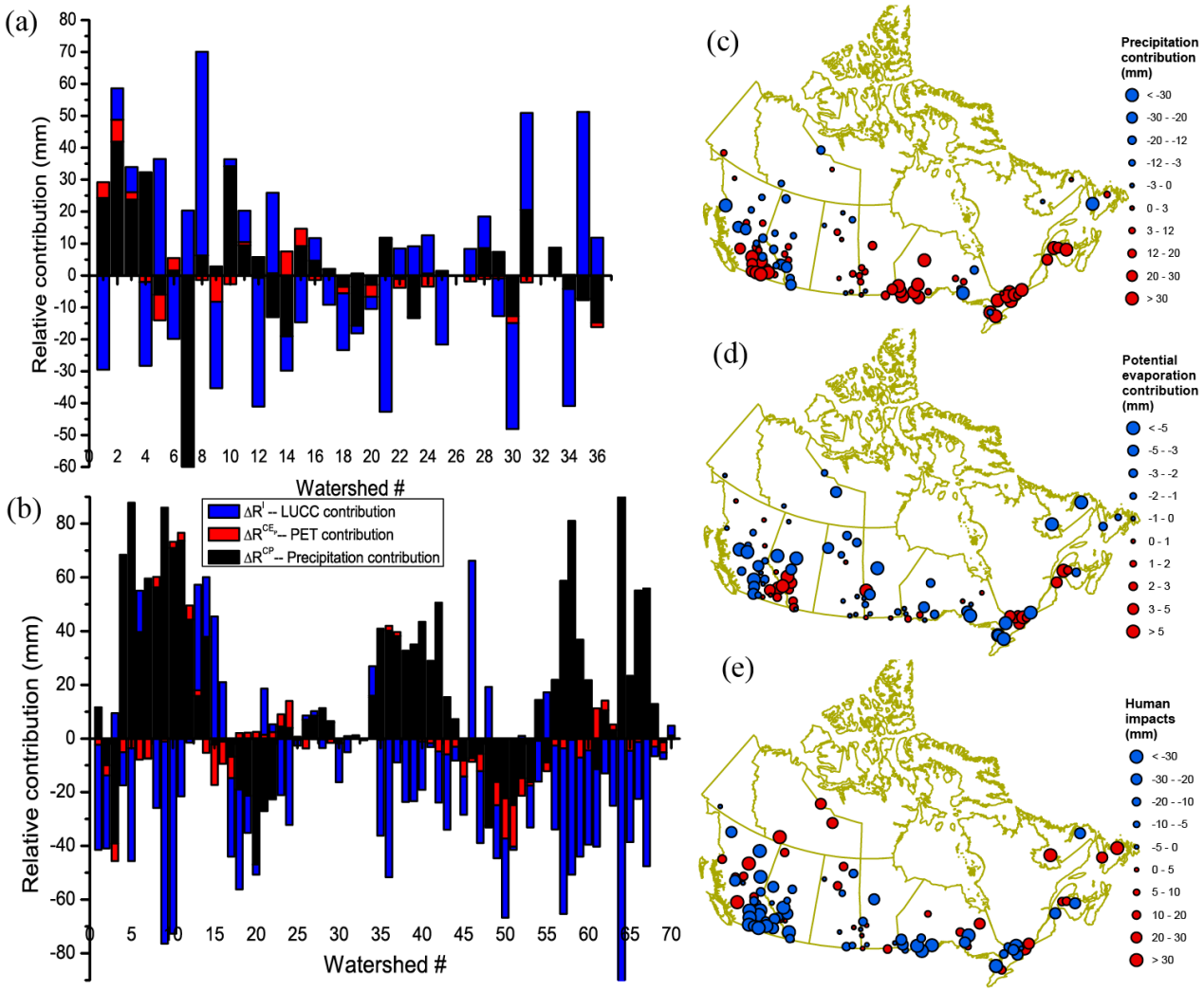

Figure 2-8 Relative contributions of changes in precipitation (c), PET (d) and landscape (e) to changes in the annual streamflow of selected Canadian RHBN (a) and non-RHBN (b) watersheds, represented by blue, red and black bars, respectively. Descriptions of watersheds of # shown in Figure 2-8a are given in Supplementary Table S1 and in Figure 2-8b are given in Supplementary Table S2 of Tan and Gan (2015b), respectively.

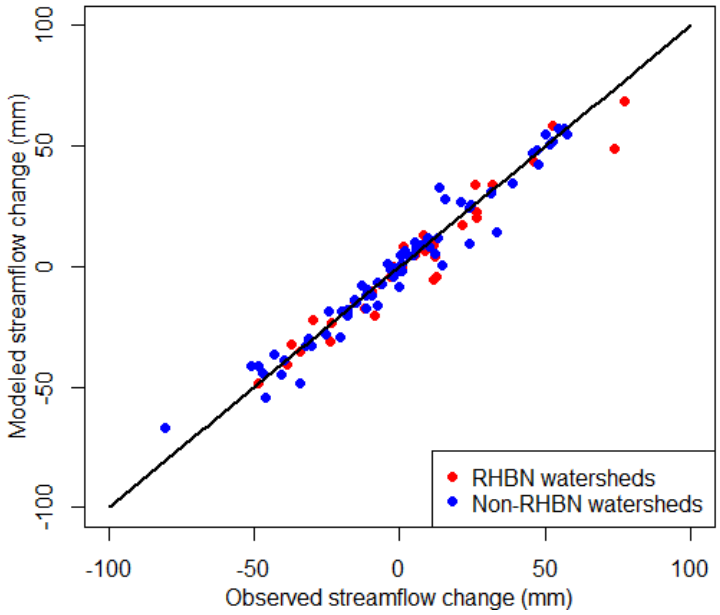

Figure 2-9 Comparison between the modeled and the observed streamflow change, the black solid line is a 1:1 straight line.

In Canada, streamflow change is more controlled by changes in precipitation than PET (Figures 2-8a-b). From periods-1 to -2, ranges of ΔR^{CP}, ΔR^{CE_P} and ΔR^{l} are [-140.5, 41.9], [-8.2, 7.5] and [-42.7, 63.8] mm for RHBN watersheds, and [-46.9, 137.4], [-15.4, 11.2] and [-123.6, 66.2] mm for non-RHBN watersheds, respectively. Their corresponding mean values are 2.4, -0.5 and -0.7mm for RHBN watersheds, and 17.3, -1.9 and -14.8mm for non-RHBN watersheds, respectively. As expected, human impacts have a significantly higher contribution to the decrease of streamflow in non-RHBN watersheds than RHBN watersheds. Spatial patterns of ΔR^{CP}, ΔR^{CE_P} and ΔR^{l} are shown in Figures 2-8c-e, which are similar to trend analysis of precipitation, PET and n (Figure 2-4). Precipitation (human impacts) generally contributed to an increase (decrease) in the streamflow of southern Canada, even though there are exceptions.

We also used the decomposition method (Wang and Hejazi 2011) based on Budyko Framework (Figure 2-1 and Methods) to validate the relative contribution of human activities and climate change to streamflow change. Although the former merely attributes streamflow change to climate change and direct human impacts, without considering the contribution of precipitation and PET separately, the overall results are similar to that of the elasticity method from comparing the results derived from the decomposition and elasticity methods (Figure 2-10).

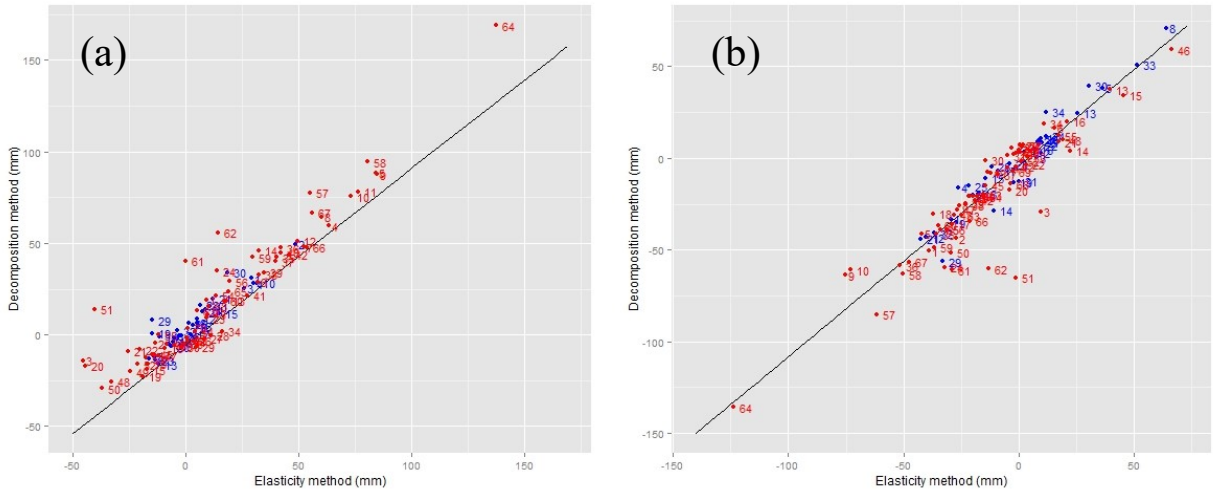

Figure 2-10 Comparisons of the contribution of climate (a) and human activities (b) to the streamflow change for watersheds described in Table S1 (blue dots) and S2 (red dots) derived from the decomposition method and the elasticity method. The watershed numbers shown in the figures are described in Supplementary Table S2 of Tan and Gan (2015b).

2.3 Discussion

The elasticity and decomposition methods built on the Budyko framework involve uncertainties, such as separating relative contributions of climate change and human impacts on changes to streamflow, abrupt change and temporal trends of streamflow. For example, assuming 1980 and 1990 to be the change-point year for non-RHBN and RHBN watersheds, respectively, and climatic regimes and human impacts remained relatively stable in both periods, etc., may not be true. Therefore, we further analyzed streamflow changes under five 10-year windows attributed to climate change and human impacts from 1961 to 2010, relative to the 1930-1960 base period, for 30 (mostly non-RHBN) watersheds.

From the 1960s onward, human activities generally lead to decreasing streamflow until 2010 (Figure 2-11a), while climate change predominantly lead to increasing streamflow but the impact could be opposite for some watersheds until about the 1980s, when the reverse happened (Figure 2-11b). The range of standard deviations (mean) in climate and human contributions to streamflow change over the five 10-year windows of data analyzed for the 30 watersheds was 8.5-75.3 mm (33.7mm) and 8.8-54.8 mm (29.4mm), respectively. It seems that the mean contributions of climate change and human activities to streamflow change of these 30 watersheds obtained from the five 10-year window analysis for 1961-2010 agree well with the results obtained from using 1980 as the common change-point for the 30 watersheds (Figure 2-11c).

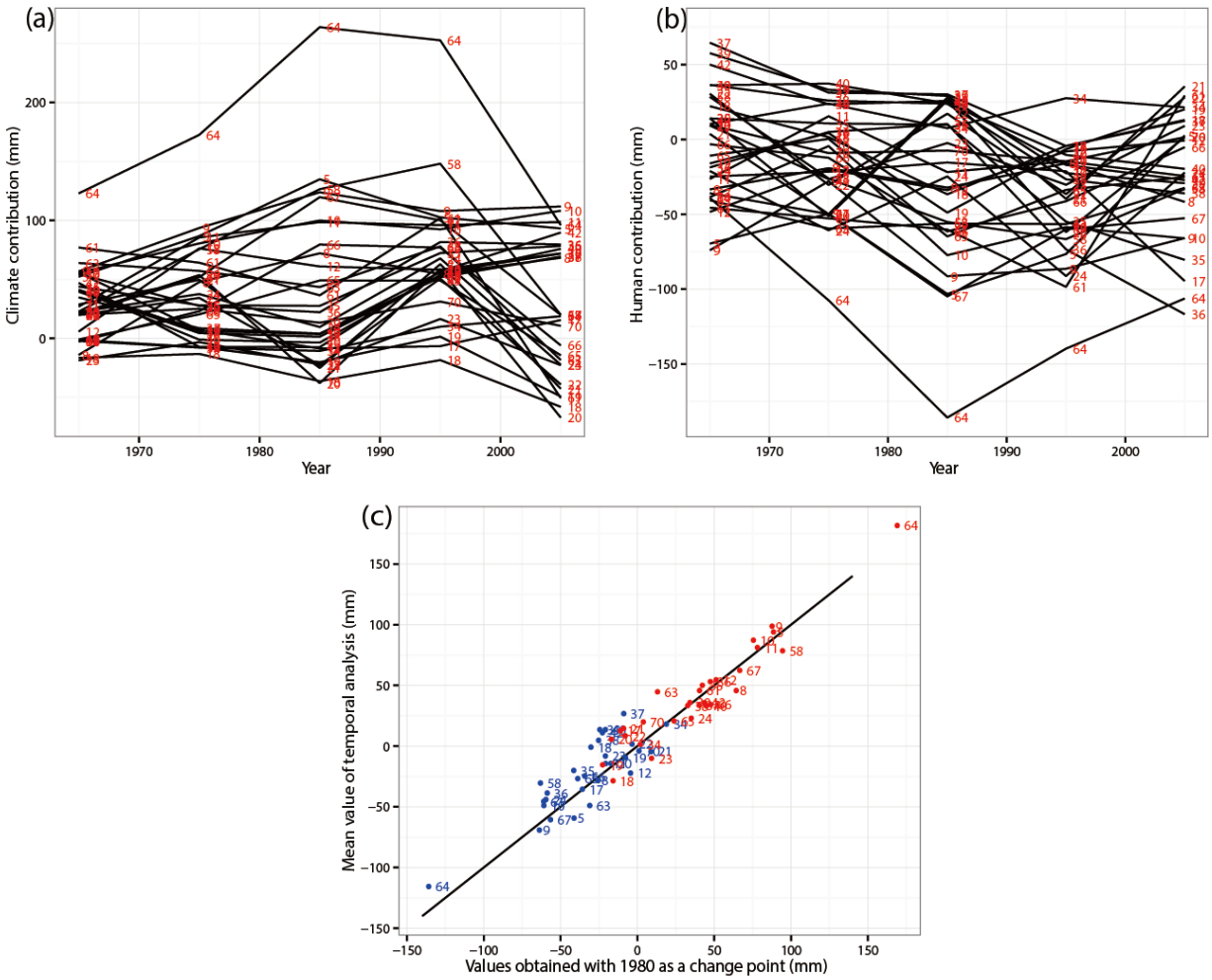

Figure 2-11 Temporal Budyko analysis results of Contributions of climate (a) and human (b) to changes in MAS from the baseline 1931-1960 period at 10 year intervals for 30 watersheds estimated from the decomposition method based on the Budyko framework; and scatterplots between changes in MAS due to contributions of climate (red dots) and human (blue dots) averaged over 5 10-year periods, and changes in MAS based on 1980 as the assumed change-point for each watershed. The watershed numbers shown in the figures are described in Supplementary Table S2 of Tan and Gan (2015b).

Human impacts on streamflow change of the 96 watersheds divided into 10 groups were further explored using a correlation analysis between streamflow change and human activities such as LUCC, increased municipal water consumption due to population increase and increased evaporation due to water impoundment behind dams. In each group all watersheds have comparable range of streamflow change and human activities categorized under population density, number of dams, percentage of cropland and rangeland.

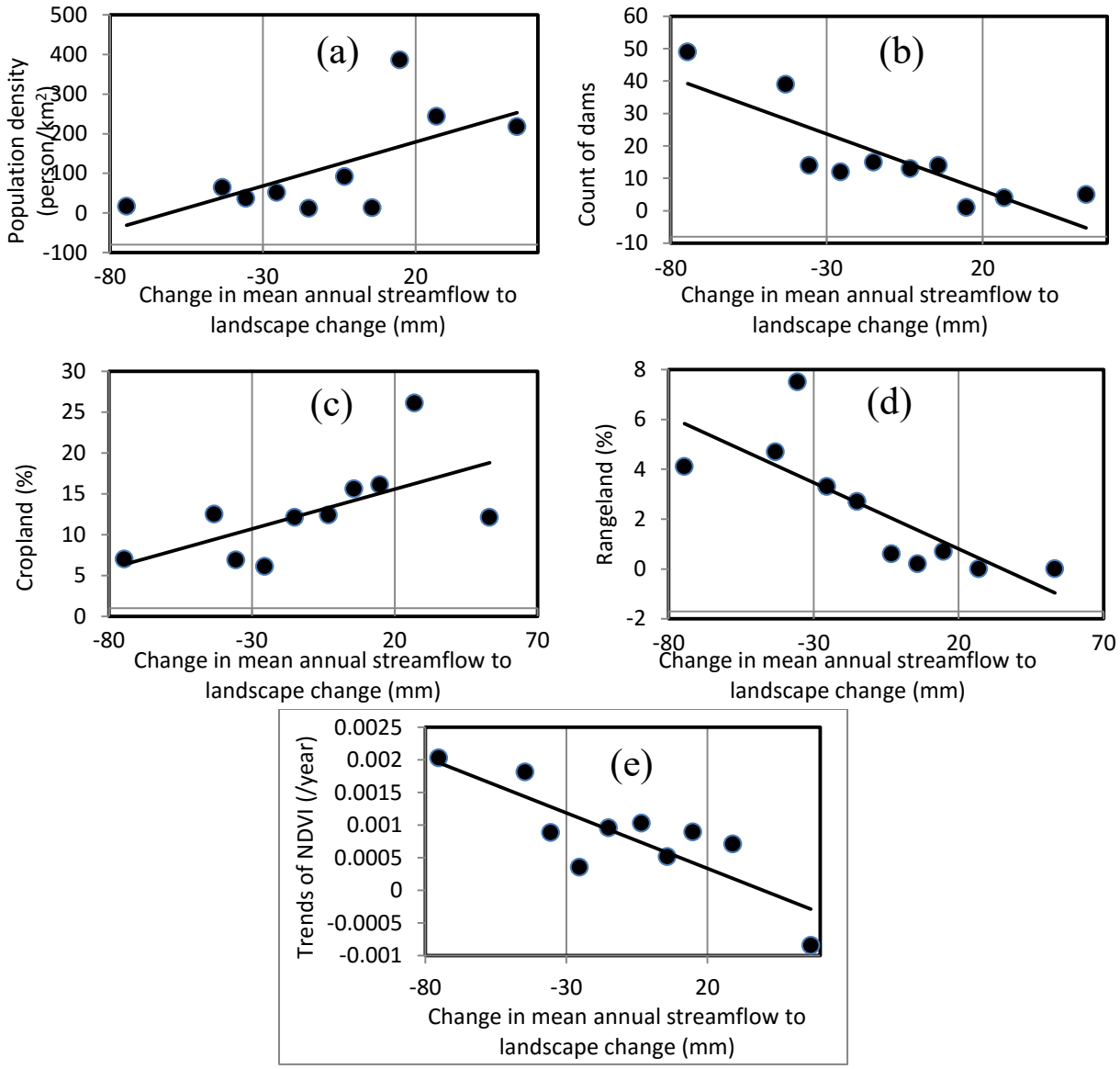

Figure 2-12 Relationships between estimated human contributions to streamflow change in terms of selected, external validation data, namely, (a) population density, (b) number of dams, (c) percentage of cropland, (d) percentage of irrigated land and (e) trend magnitudes of NDVI.

Because of a lack of long-term data related to human activities, we assume that streamflow to landscape changes detected for each watershed to be directly dependent on certain indicators collected in a particular year only. The relationships between "human" indicators and streamflow change for these 10 groups of watersheds are shown in Figure 2-12. The proportion of impervious areas of urban watersheds with large population density tends to grow over the years, resulting in decreased infiltration but increased surface runoff. Conversely, water impoundment by dams results in increased evaporation loss and so decreased streamflow. The expansion of cropland means converting perennial vegetation to seasonal cropping systems that reduces

annual evapotranspiration and increased streamflow during non-growing season. On the other hand, rangelands could have higher evapotranspiration than natural lands, resulting in less streamflow. However, streamflow could change in a manner opposite to above relationships, e.g., irrigated lands could have higher evapotranspiration than natural lands which resulted in less streamflow. Further, crop water consumption depends on crop types, and so streamflow could decrease with intensive cultivation of certain crop types. Therefore, human impacts on the streamflow change could depend on various combinations of physical and climatic factors.

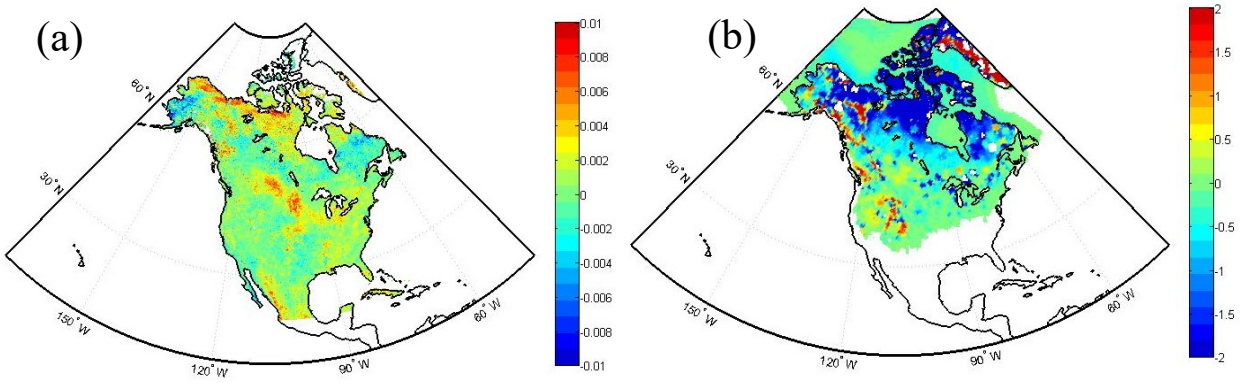

Figure 2-13 Trends of NDVI (a, year^{-1}) and snow ratio (b, % year^{-1}) over North America. Maps in Figure 2-13 were generated with licensed Matlab R2014a using public domain data, such as NDVI data of the Global Inventory Modeling and Mapping Studies (GIMMS) (http://staff.glcf.umd.edu/sns/branch/htdocs.sns/data/gimms/) and snow ratio data of the North American Regional Reanalysis (NARR). (http://www.esrl.noaa.gov/psd/data/gridded/data.narr.html).

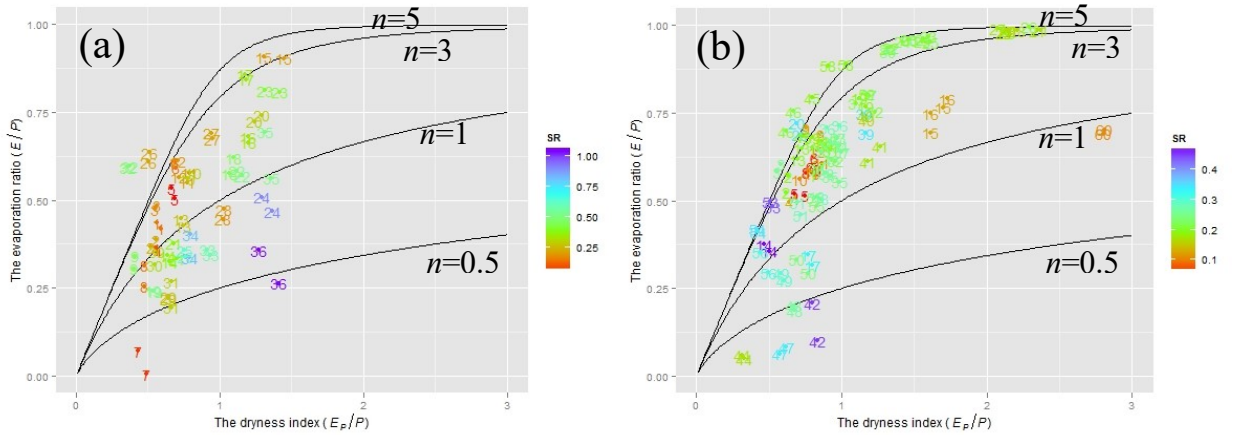

Figure 2-14 Same as Figure 2-6, but based on the snow ratio for selected RHBN (a) and non-RHBN (b) watersheds during period-1 and period-2 (see Figure 2-6 about the period of data points). The Budyko curves calculated by Equation (2-2) are plotted as black solid lines.

In addition to the above human indicators, we have also considered trends of normalized difference vegetation index (NDVI), which is related to the percent of green cover, as a possible factor contributing to decreased streamflow in Canada. Figure 2-12e shows the negative correlation between NDVI trends for the first half of August over 1981-2011 and annual streamflow change of Canada. As most Canada landmass became greener (NDVI increase) in southern and Arctic regions (Figure 2-13a) over 1981-2011, annual evapotranspiration could increase because of increased NDVI even though there is no consistently positive trend detected in the evapotranspiration of Canada (Greve et al. 2014; Jung et al. 2010; Sterling et al. 2012; Zhang et al. 2009a). Even though increased NDVI could be related to both the climate change and human contribution (Pouliot et al. 2009), it is difficult to separate their relative contributions to the increased NDVI.

In high-latitude and mountainous regions of Canada, the widespread retreat of glaciers has contributed to increase in streamflow (Clarke et al. 2015; Immerzeel et al. 2013; Lutz et al. 2014; Wang et al. 2014c). Since this study does not account for impacts of climate change on retreat of glaciers, it underestimated the actual human contribution to decreased streamflow. Some studies show that potential impacts of a warmer climate do not significantly affect the availability of water in snow-dominated regions such as Canada (Barnett et al. 2008; Stewart et al. 2005). However, recent studies reported conflicting results on the sensitivity of streamflow to global warming impact, e.g., a general decrease in observed streamflow caused by a shift from snowfall to rainfall in USA (Berghuijs et al. 2014); and a projected increase (decrease) in streamflow of Canada (USA) under climatic change impact (Zhang et al. 2014b) which may be partly because hydrologic impacts of human activities are not considered in hydroclimatic models. More detailed analysis will be necessary to better estimate anthropogenic impacts such as landuse changes and streamflow regulations to watersheds studied.

A limitation of Budyko-based methods for separating the relative contribution of human impacts and effects of climate change to the streamflow change in snow-dominated watersheds is that the change in snow ratio (SR, amount of snowfall to total precipitation) which is more related to the effect of climate change than direct human impact. Watersheds with a higher SR tend to have a lower E/P (Figure 2-14). This means that under similar climatic conditions and landscape properties, streamflow will tend to be higher. This empirical relationship has been found in watersheds of USA (Berghuijs et al. 2014) and China (Zhang et al. 2015), but its

mechanism is still unknown. The stationary assumption of SR in Budyko-based methods is violated in some watersheds given North American Regional Reanalysis (NARR) data show that SR has increased in southern Canada because of the increase in winter precipitation, but SR has decreased in northern Canada over 1979-2014 (Figure 2-13b), as also been observed in station climate data (Zhang et al. 2000). Given that streamflow in southern Canada has decreased even though it should have increased because of increased SR, the contribution of human impact to decreased streamflow could have been higher.

2.4 Methods

From analyzing the 1961-2010 annual water balance of 370 watersheds using streamflow data of Water Survey Canada (WSC), Wang et al. (2014b) found that large spatial variabilities of basin-scale water budget over Canada, and some significant discrepancies in the water budget of some watersheds in northern Canada (above 60°N) were partly due to mass loss of glaciers. Given the Budyko framework is meant for the long-term (> 1 year) water balance analysis, 96 Canadian watersheds with drainage area > 2,000 km^2 and an annual water imbalance < 10% of the annual precipitation were selected for this study.

Since available streamflow data is less complete than precipitation and temperature data, only watersheds with long-term streamflow data were selected in this study. The RHBN streamflow data of WSC have been extensively used for climate change studies, since RHBN data are characterized by relatively pristine and stable land-use conditions (< 5% of the land surface modified) with at least 20 years of record. A total of 36 RHBN watersheds with daily streamflow data of 1971-2010 were selected for this study. Further, daily streamflow data of 60 non-RHBN stations that began no later than 1960 were also selected for this study (Figures 2-2 and 2-3, and see Supplementary Tables S1 and S2 in Tan and Gan 2015b). In this study, the total annual depth of streamflow was estimated for station drainage areas while the total annual values of other hydroclimatic variables were estimated for actual watershed areas. Next, the gridded, monthly precipitation dataset (McKenney et al. 2011), and the monthly PET dataset of CRU TS v. 3.22 (Harris et al. 2014) were also used under the Budyko framework. To estimate the change in SR over watersheds, we used the NARR (Mesinger et al. 2006) snowfall and precipitation data over 1979-2014. Abrupt changes in the mean hydroclimatic data due to climatic changes and/or anthropogenic effects were detected using the nonparameteric Pettitt test (Pettitt 1979), monotonic trends was investigated by the Mann-Kendall (MK) test (Kendall 1975), and

magnitudes of trend were estimated using the Theil–Sen approach (Sen 1968), at 10% significance level.

Various significant hydroclimatic change-points for Canada, mainly between 1970-1990, have been detected (Tan and Gan 2015a). We first divided RHBN (non-RHBN) streamflow datasets into pre-1990 (pre-1980) and post-1990 (post-1980) parts, respectively. Hydroclimatic changes from periods-1 to -2 were estimated for the 96 watersheds. The contributions of human impacts to observed changes in MAS of Canada were assessed in terms of population density, dam distribution, and land uses (Figure 2-3) obtained from Natural Resources Canada (www.geogratis.cgdi.gc.ca/geogratis/DownloadDirectory?lang=en), and remotely sensed, 8-km resolution, NDVI data of the first half of August for 1981-2011 obtained from the Global Inventory Modeling and Mapping Studies (GIMMS) (Tucker et al. 2005).

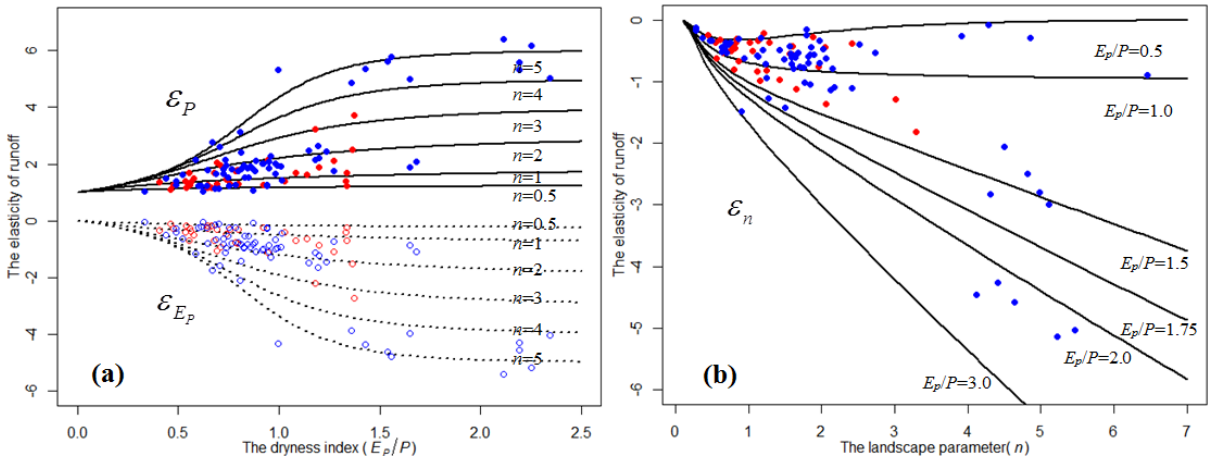

Figure 2-15 The elasticity of streamflow dependent on (a) the dryness index (E_p/P) and (b) the landscape parameter (n). The lines represent the elasticity of runoff, and the blue and red circles or dots represent the non-RHBN and RHBN watersheds, respectively.

The Budyko framework simplifies the water-energy balance of large watersheds (>1,000 km^2) over long time periods (>1 year) by apportioning precipitation to actual evaporation (E) and streamflow (R). Since PET (E_P) and precipitation (P) are measures of energy and water available, respectively, the Budyko framework, $E/P=f(E_p/P, n)$, represents the water balance of a watershed in a stationary condition (Figures 2-1, 2-6, 2-14 and 2-15). Various climatic conditions represented by E_p/P fall on a Budyko curve that only depends on watershed properties represented by one or more parameters. In this study, the Budyko curve (Yang et al. 2008), Equation (2-1), was chosen because it is only described by one parameter n that is an empirical

coefficient representing combined watershed landscape properties. A larger n value means more evaporation is partitioned from the precipitation and vice versa.

$$\frac{E}{P}=\left[1+\left(\frac{E_P}{P}\right)^{-n}\right]^{-1/n} \tag{2-1}$$

The long-term moving average E with a 10-year window is derived by water balance, $P = R + E$, where variations of water storages were neglected:

$$R=P-\frac{PE_P}{\left(P^n+E_P^n\right)^{1/n}} \tag{2-2}$$

Next, ε_p, ε_{Ep}, and ε_n can be analytically derived and estimated from long-term P, E_P and n data. Assuming P, E_P and n are independent variables, thus Equation (2-2) can be interpreted as $R=f\left(P,E_p,n\right)$ with the total differential, dR:

$$dR=\frac{\partial f}{\partial P}dP+\frac{\partial f}{\partial E_p}dE_p+\frac{\partial f}{\partial n}dn \tag{2-3}$$

The elasticity of streamflow to, precipitation, PET and watershed landscape can be defined as $\varepsilon_P=\frac{dR}{R}\Big/\frac{dP}{P}$, $\varepsilon_{E_P}\left(E_P,R\right)=\frac{dR}{R}\Big/\frac{dE_P}{E_P}$ and $\varepsilon_n\left(n,R\right)=\frac{dR}{R}\Big/\frac{dn}{n}$, respectively. Equation (2-3) can be rearranged as:

$$\frac{dR}{R}=\varepsilon_P\frac{dP}{P}+\varepsilon_{E_p}\frac{dE_p}{E_p}+\varepsilon_n\frac{dn}{n} \tag{2-4}$$

$$\varepsilon_P=\left\{1-\left[\frac{\left(E_p/P\right)^n}{1+\left(E_p/P\right)^n}\right]^{1/n+1}\right\}\Bigg/\left\{1-\left[\frac{\left(E_p/P\right)^n}{1+\left(E_p/P\right)^n}\right]^{1/n}\right\} \tag{2-5}$$

$$\varepsilon_{E_p}=\frac{1}{1+\left(E_p/P\right)^n}\frac{1}{1-\left[\frac{\left(E_p/P\right)^n}{1+\left(E_p/P\right)^n}\right]^{1/n}} \tag{2-6}$$

$$\varepsilon_n=\frac{A-B}{\left[1+\left(P/E_p\right)^n\right]^{1/n}-1},A=\frac{P^n\ln\left(P\right)+E_p^n\ln\left(E_p\right)}{P^n+E_p^n},B=\frac{\ln\left(P^n+E_p^n\right)}{n} \tag{2-7}$$

Using Equations (2-5)-(2-7), the elasticity of streamflow for a watershed can be estimated from its long-term data of P, E_P and n.

Figure 2-15 illustrates the relationship between ε_p and E_p/P for selected watersheds of Canada. As expected, ε_p increases with E_p/P, but, ε_{Ep} decreases with E_p/P because streamflow

increases with precipitation but decreases with PET. The elasticity of streamflow is less dependent on E_p/P when climate is dry ($E_p/P > 1.5$), but less dependent on n when climate is extremely wet ($E_p/P < 0.5$). ε_p is close to 1.0 but ε_{Ep} is close to 0.0 under extremely humid climate, and are almost independent of landscape conditions. On the other hand, n tends to affect the climate elasticity when E_p/P is between 0.5 and 1.5. Changes of the mean annual runoff of a watershed from period-1 (R_1) to period-2 (R_2), $\Delta R = R_2 - R_1$, could be due to the combined effect of climate change ΔR^C, and the watershed LUCC ΔR^L, i.e., $\Delta R = \Delta R^C + \Delta R^l$, where $\Delta R^C = \Delta R^{CP} + \Delta R^{CEP}$, and ΔR^{CP} and ΔR^{CEP} are the streamflow change caused by changes in precipitation and PET, respectively. Therefore, $\Delta R^{CP} = \varepsilon_P \times R/P \times \Delta P$, $\Delta R^{CE_p} = \varepsilon_{E_p} \times R/E_p \times \Delta E_p$ and $\Delta R^l = \varepsilon_n \times R/n \times \Delta n$, where $\Delta P = P_2 - P_1$, $\Delta E_P = E_{P2} - E_{P1}$ and $\Delta n = n_2 - n_1$, respectively.

Since the elasticity method uses only a first-order approximation of streamflow change in Equation (2-4), an error analysis was conducted to test the validity of the elasticity method. Following Yang et al. (2014), Equation (2-2) was expanded by Taylor's series to estimate errors associated with using a first-order approximation for estimating streamflow change. The results show that in 94 out of 96 watersheds, the relative error of approximating precipitation change to the streamflow change is less than 9%. Therefore, it is acceptable to apply the elasticity method in this study.

The decomposition method (Wang and Hejazi 2011) offers another explanation to streamflow responding to effects of climate change and human activities based on the Budyko framework. This method also assumes no indirect human-induced streamflow change resulted from human influence on the climate change. Unlike the elasticity method which uses a first-order approximation of the Budyko equation (Equation 2-3), the decomposition method considers that changes of E_p/P of a watershed along the horizontal direction in its Budyko curve only result from climate change impact, while changes of E/P along the vertical direction in its Budyko curve result from both climate change and direct human impacts (Wang and Hejazi 2011) (Figure 2-1). The streamflow change is divided into two parts, so that Budyko-based methods can separately account for direct human-induced and climate-induced streamflow changes due to changes in both precipitation and PET.

Decomposition method: Because of both climate change and direct human interferences, a watershed could shift over time from points A at period-1 (E_{p1}/P_1) to B at period-2 (E_{p2}/P_2) in

Figure 2-1. However, based on the Budyko hypothesis, the watershed should evolve from A to C along the Budyko curve that represents the impact of climate change only. Given same climatic conditions between B and C but without impacts of human activities at C, the precipitation, evaporation, dryness and evaporation indices of C are also P_2, E'_2, E_{p2}/P_2 and E'_2/P_2, respectively. Thus, the horizontal shift from E_{p1}/P_1 to E_{p2}/P_2 is due to the climate change, while the vertical shift from E_1/P_1 to E_2/P_2 is due to both climate change and direct human impacts. So the vertical shift can be decomposed to climate change effects from E_1/P_1 to E'_2/P_2 and direct human activity effects from E'_2/P_2 to E_2/P_2. This method first calibrates the Budyko curve to each watershed with data of period-1 to obtain n without the effect of human activities, and then the evaporation ratio of period-2 due to climate change only is E'_2/P_2, where the observed dryness index is E_{p2}/P_2. Thus, the streamflow change caused by direct human impacts is $\Delta R^H = \Delta P - \Delta E = P_2(E'_2/P_2 - E_2/P_2)$ while that by climate change is $\Delta R^C = \Delta R - \Delta R^H = P_2(1 - E'_2/P_2) - R_1$.

Chapter 3 Non-stationary analysis of the frequency and intensity of heavy precipitation over Canada and their relations to large-scale climate patterns

3.1 Introduction

In recent decades, Canada has experienced extreme flood events such as the Saint John River flood in 2008 (Newton and Burrell 2015), the Red River Flood in 2009 (Wazney and Clark 2015) and 2011 (Blais et al. 2015), the South Saskatchewan and Elk River flood in 2013 (Pomeroy et al. 2015), the Assiniboine River flood in 2011 (Blais et al. 2015) and 2014 (Ahmari et al. 2015), the Richelieu River flood in 2011 (Saad et al. 2015), the southern Alberta flood in 2013 (Milrad et al. 2015), and the Southeastern Canadian Prairies (CP, which consists of Alberta, Saskatchewan and Manitoba) flood in 2014 (Szeto et al. 2015). These extreme flood events have caused substantial damage to Canada, such as damage to infrastructure, financial losses, and even loss of human life. For instance, the total damage of the June, 2013 flood of southern Alberta is estimated at $5–6 billion, making it the costliest natural disaster in Canadian history (Environment Canada 2014; Government of Alberta 2014).

For large river basins of Canada, floods are often associated with spring snowmelt, rain-on-snow, or long-duration heavy precipitation with large areal coverage, even though the significance of heavy rainstorms and snowstorms that resulted in floods varies across the country (Buttle et al. 2016). Because Canada is seasonally covered with snow, floods related to spring snowmelt or rain-on-snow events are common in Canada. In southern Canada, convective and frontal systems can give rise to long-duration heavy, summer rainfall events that trigger floods in large river basins, or intensive, short-duration storms which can also trigger floods in small to medium river basins.

Changes to Canadian extreme and heavy precipitation under the global warming impact can increase the risk of flooding. Climate warming due to increasing atmospheric greenhouse gasses can intensify the hydrologic cycle (Seager et al. 2012). For example, according to the Clausius-Clapeyron equation, the water-holding capacity of the atmosphere increases at about 7% per K temperature rise, and so warming will increase atmospheric moisture, and so severe storms become more intensive (Allan and Soden 2008). The potential cost associated with heavy precipitation (rainfall and snowfall) for Canadian society motivates us to assess whether the

frequency and intensity of extreme or heavy precipitation have changed over Canada. Therefore in this study, our specific objective is to detect possible changes in extreme and heavy precipitation over Canada: 1) temporal non-stationarities (abrupt and slowly varying changes); 2) Frequency analyses and upper tail properties of annual maximum daily precipitation (AMP); 3) Occurrences of heavy precipitation temporal clusters; and 4) Relationships between Canadian extreme and heavy precipitation and some large-scale climate patterns.

For Canada, previous studies detected overall increasing trends in the annual total precipitation in the twentieth century mostly because of the increase in small to moderate precipitation events (Mekis and Vincent 2011; Vincent and Mekis 2006; Zhang et al. 2001a; Zhang et al. 2000), while winter total snowfall has mainly increased in the north but decreased in southwestern Canada since 1950 (Mekis and Vincent 2011; Vincent and Mekis 2006). In contrast, results of past studies on the trend analysis of heavy or extreme precipitation over Canada are inconsistent in the twentieth century possibly because of different datasets or methods used. Some studies found no statistically significant trend (Kunkel 2003; Kunkel and Andsager 1999; Vincent and Mekis 2006; Zhang et al. 2001a), while others detected statistically significant increasing trends (Alexander et al. 2006; Burn and Taleghani 2013; Peterson et al. 2008) in either the frequency or intensity of extreme precipitation. Some regional climate modeling studies projected more intensive and frequent daily and multi-day precipitation events in a warmer future climate for most Canadian regions (Kuo et al. 2015; Mailhot et al. 2010; Mladjic et al. 2011).

Extreme events are usually defined by the block maxima, peaks-over-threshold (POT) or point processes (Coles 2001; Khaliq et al. 2006). Compared to the block maxima approach that models extreme events using a generalized extreme value (GEV) distribution, the POT approach fits all events exceeding a specified threshold to a generalized Pareto (GP) distribution and the occurrence of an exceedance to a Poisson process. By accepting hydroclimatic processes as inherently probabilistic, a changing climate can be modeled using a non-stationary probability distribution. To avoid possible confusion about definitions regarding extremes, samples of maximum events for the block maxima method will be referred to as *extreme* events while events for the POT approach as *heavy* events.

Temporal clustering of events contributes to the non-stationarity of a time series (Franzke 2013; Mailier et al. 2006; Mallakpour and Villarini 2015; Pinto et al. 2013; Tramblay et al. 2013;

Villarini et al. 2013; Villarini et al. 2011), which is often overlooked in hydroclimatic frequency analysis. If heavy events are stationary, the number of occurrences of such events follows a homogeneous Poisson distribution. However, large-scale weather patterns or other factors can affect storm tracks responsible for the occurrence of heavy events in clusters, making the homogeneous assumption invalid.

As the probability of occurrences of climate extremes can be strongly affected by large-scale climate patterns, considerable progress has been made in deriving possible relationships between such climate patterns and extreme climate variables by modeling the latter with non-stationary GEV and GP distributions using climate indices as time-varying covariates (Kenyon and Hegerl 2008). Zhang et al. (2010) fitted winter daily maximum precipitation over North America (NA) to a GEV distribution, using climate indices such as El Niño Southern Oscillation (ENSO), Pacific decadal oscillation (PDO), and North Atlantic Oscillation (NAO) as covariates for the location and/or scale parameters of the GEV distribution. They found that ENSO and PDO have spatially consistent and statistically significant influences on NA extreme winter precipitation. Sillmann et al. (2011) fitted the monthly minima of European winter 6-hourly minimum temperature to a GEV distribution with an indicator for atmospheric blocking conditions as a covariate to the location and scale parameters of the GEV distribution and detected the cooling effect of atmospheric blocking. Min et al. (2013) conducted a non-stationary GEV analysis of seasonal temperature and precipitation extremes over Australia, by specifying GEV parameters as linear functions of large-scale climate patterns such as ENSO, Indian Ocean Dipole, and Southern Annular Mode. Maraun et al. (2010) developed a generalized linear model to relate the influence of atmospheric circulations on extreme daily precipitation across the UK, by incorporating synoptic scale airflow strength, direction and vorticity to the location and scale parameters of the GEV distribution. Instead of modeling winter precipitation of multiple sites in California to a GEV model separately, Shang et al. (2011) jointly modeled the winter maximum daily precipitation of 192 sites of California with spatial, max-stable process models by incorporating the Southern Oscillation Index (SOI) as a co-variate to the marginal GEV distributions of this spatial model. All these are examples on modeling recent changes in the frequency and intensity of extreme climate and weather events using non-stationary distributions. Given that no study has been conducted to model possible changes to all of Canadian extreme and heavy precipitation using non-stationary probability distributions, several

non-stationary approaches were used to characterize the changing frequency and intensity of extreme and heavy precipitation over Canada and the possible influence of large-scale climate patterns on Canadian extreme and heavy precipitation.

The remainder of this chapter is organized as follows: data description is given in Section 3.2, methods applied to detect nonstationarities of Canadian heavy precipitation are given in Section 3.2.3, discussion of results in section 3.4, and summary and conclusions in Section 3.5.

3.2 Data and methods

3.2.1 Precipitation

The daily precipitation measurements, including total precipitation, rainfall and snowfall data used in this study were obtained from the second generation, adjusted historical Canadian climate data (AHCCD) database, which contains 463 stations (Figure 3-1) of precipitation observations statistically adjusted for known measurement issues such as wind undercatch, evaporation and wetting loss for each type of rain-gauge, snow water equivalent from ruler measurements, trace observations and accumulated amounts from several days. More detailed information on this datasets is given in (Mekis and Vincent 2011). Because station closures and relocation were ongoing issues, observations from some nearby stations (a total of 12.3% of all stations) after 1990 were occasionally combined to create long-term precipitation time series for climate change studies.

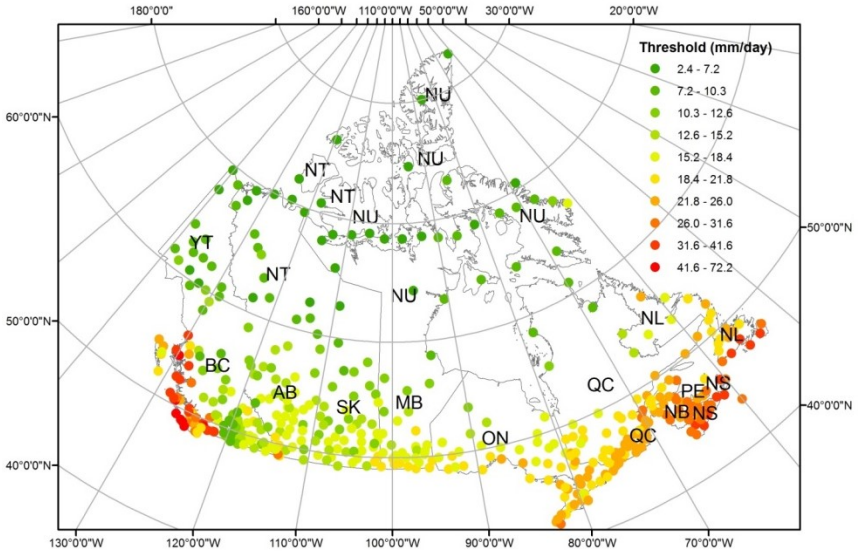

Figure 3-1 Location of the 463 Canadian precipitation stations used in this study, together with the threshold values used for the POT analyzes.

AHCCD is the most homogeneous long-term measured data currently available for Canadian daily precipitation. The length of the measured daily precipitation ranges 27 to 172 years, with an average of 84 years. The year that precipitation measurements began at stations of northern Canada is much later than southern Canada, so stations with short precipitation measurements are usually located in northern Canada. Because our objective is to investigate extreme and heavy precipitation changes over the whole country, all the second generation precipitation data from AHCCD were included for this study. To check the uncertainties of non-stationary analysis because of the inconsistent length of time series, we also analyzed data within four periods with the same non-stationary analysis. These four periods are: (1) 1900-2010 (111 years for 41 stations), (2) 1930-2010 (81 years for 140 stations), (3) 1950-2010 (61 years for 201 stations) and (4) 1970-2010 (41 years for 223 stations). However, we report results by analyzing all available data and stations, unless otherwise specified.

Since we have no knowledge of the weather condition in days without precipitation records, precipitation of these days was first replaced with 0. The annual maximum daily precipitation (AMP) was extracted from the daily time series for each station. The missing AMPs (less than 3% of all the years of data for each station) were replaced with the mean value of that AMP time series excluding missing values. To extract heavy precipitation, Groisman et al. (1999) used a threshold of 25.4 mm (1 inch) in Canada, but Mekis and Hogg (1999) considered the largest 10% of daily precipitation events as heavy precipitation events to account for substantial variations in heavy precipitation across Canada, since the mean intensity of extreme events decreases rapidly in latitudes above 50°N. For every season of each station over Canada, Zhang et al. (2001a) defined the heavy precipitation by a threshold that is exceeded on an average three events per year.

For the POT analysis of this study, the 95^{th} percentile of nonzero daily precipitation based on the precipitation empirical probability distribution is chosen as the threshold to define heavy precipitation of Canada, which was also used by Villarini et al. (2013) for distribution changes of heavy rainfall over the central United States. Across Canada, the magnitude of the 95^{th} percentile of nonzero daily precipitation decreases from south to north with relatively high values in southwestern and eastern coastal regions (Figure 3-1). Using the 95^{th} percentile criterion, threshold values chosen for Canada range from 2 to 70 mm. Based on the threshold value for

each station, the number (counts) of heavy precipitation in each year and the amount each heavy precipitation exceeded the threshold is noted.

From the spatial distribution of AMP that had occurred in each month over Canada (Figure S1 in Tan and Gan 2016), it is clear that for the CP and northwestern Canada, AMP mainly occurred either during summer or early autumn (from June to September), more in mid-winter (January) for eastern and northern Canada (above 60°N), but almost year round in localized, southwestern and southeastern coastal areas (Figure S1 in Tan and Gan 2016). Thus, seasonal distributions of AMP are unimodal in southwestern Canada during summers but bimodal in northern and southeastern Canada with peaks during both summers and winters. However, heavy precipitation of Canada as defined above were more evenly distributed yearly than AMP, even though heavy precipitation events tend to occur more frequently during summer and early Autumn, and relatively infrequently during winters (Figure S2 in Tan and Gan 2016).

3.2.2 Large-scale climate anomalies

We selected five large-scale climate indices that have been linked to precipitation variability over Canada (Gan et al. 2007; Shabbar et al. 1997) or over NA (Ropelewski and Halpert 1986; Zhang et al. 2010). These five climate indices are SOI (Ropelewski and Jones 1987), NINO3 (Rayner et al. 2003) which is a time series of equatorial Pacific (Niño 3 region) sea surface temperature (SST) anomalies, NAO (Hurrell and Loon 1997), PDO (Mantua et al. 1997), and North Pacific (NP) (Trenberth and Hurrell 1994) Index which is the area-weighted sea level pressure anomalies over 30˚N-65˚N, 160˚E-140˚W. SOI and NINO3 represent the ENSO phenomenon. Because many high-frequent and small-scale phenomena in the atmosphere can influence the pressures at stations (Darwin and Tahiti) involved in forming the SOI but do not reflect the ENSO itself, we also use NINO3, which is more robust to identify El Niño and La Niña events (Trenberth 1997), to represent ENSO. Monthly time series of SOI, NINO3, NAO, PDO and NP were downloaded from the Global Climate Observing System Working Group on Surface Pressure website (www.esrl.noaa.gov/psd/gcos_wgsp/Timeseries/). Time series of yearly values were derived from averaging monthly values over the entire year. We also used National Centers for Environmental Prediction/National Centre for Atmospheric Research Reanalysis 1 dataset (Kalnay et al. 1996) to estimate daily circulation patterns concerning geopotential heights, wind field and vertically integrated precipitable water content (PWC).

3.2.3 Research methodology

The non-stationary frequency analysis of extreme or heavy events was conducted using the non-stationary block maxima and POT approaches (Coles 2001). Block maxima of extreme precipitation events were fitted with both stationary and non-stationary GEV distributions (Appendix I). The number of heavy precipitation events was fitted with a non-stationary Poisson distribution (Appendix II), and exceedances of precipitation events over a threshold defined as the 95^{th} percentile of non-zero precipitation were fitted to a non-stationary GP distribution (Appendix III) with time-varying parameters. Trends of the intensity of extreme precipitation were analyzed using time as a covariate to the parameters of GEV and GP distributions. Because most heavy precipitation of Canada shows an over-dispersion behavior (see Figure 3-2 and Section 3.3.2), trends and change points to the number of occurrences of heavy precipitation events were modeled by a Poisson regression and a segmented regression models (Muggeo 2003; Appendix II), respectively. We used annual time series of five climate indices, namely, SOI, NINO3, NAO, PDO and NP, as covariates of parameters of non-stationary GEV, Poisson and GP distributions to examine the influence of large-scale climate patterns on extreme and heavy precipitation over Canada. The likelihood-ratio test (Coles 2001; Appendix IV) was applied to test the significance of the relationship between parameters of distributions and covariates.

We used composite methods to assess the impact of extreme phases of ENSO, PDO, NAO and NP on Canadian heavy precipitation. Represented by the geopotential height, wind field and PWC, composite circulation patterns associated with the 10 largest and 10 smallest values for each climate index during 1948-2010 were computed for the summer (somewhere between May and August) and winter (between October and February) when heavy precipitations are more likely to occur (Figure S2 in Tan and Gan 2016). A systematic comparison of the composite analysis of synoptic circulation patterns that gave rise to heavy precipitation was conducted for different regions by dividing Canada into western, central and eastern Canada (Figure 3-1), respectively. From the 35^{th} to 65^{th} percentile (30% interval) of the empirical cumulative distribution for Julian days on which heavy precipitation most likely occurred in the summer or winter of each region, we extracted large-scale anomalies (with respect to the long-term mean of 1948-2010) of geopotential heights, wind field, and PWC for this 30% interval selected for each composite year. Composite anomalies are the mean of climate anomalies in years with extremely high and low climate indices, respectively.

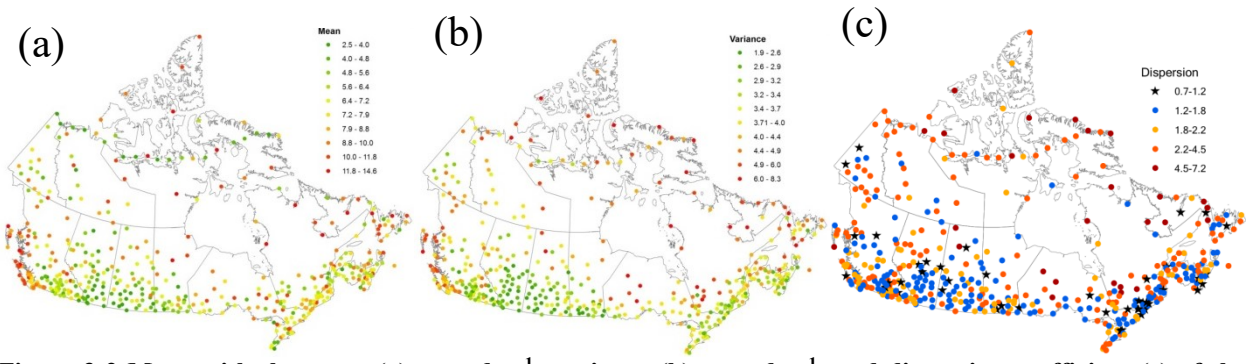

Figure 3-2 Maps with the mean (a), mm day^{-1}; variance (b), mm day^{-1}; and dispersion coefficient (c) of the number of days exceeding corresponding 95th percentile daily precipitation. The dispersion coefficient is defined as the ratio of variance to mean.

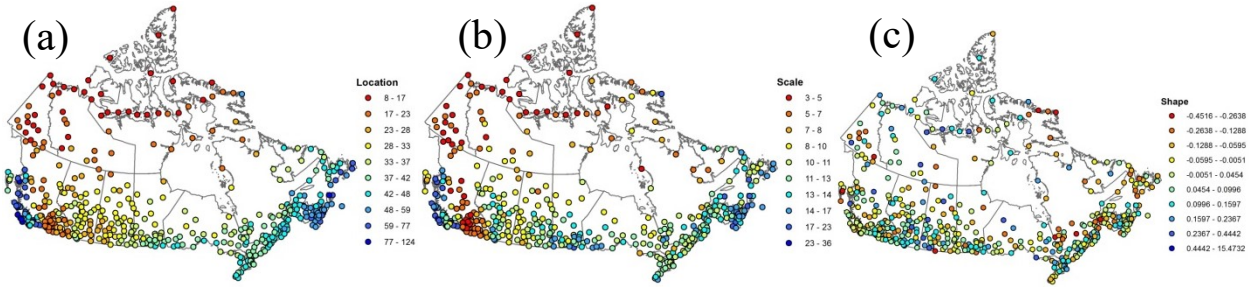

Figure 3-3 Maps of location (a), scale (b) and shape (c) parameters of the GEV distribution for AMP time series derived from the stationary analysis.

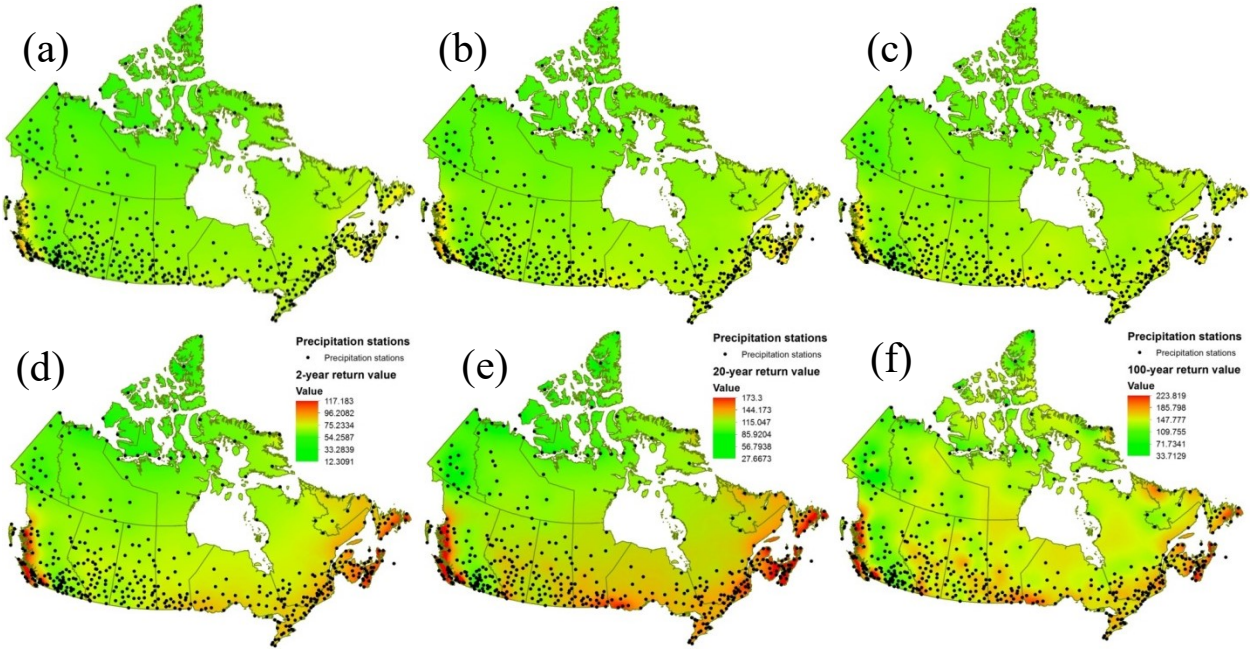

Figure 3-4 Maps of AMP with the (a and d) 2-, (b and e) 20- and (c and f) 100-year return period derived from the stationary GEV (a-c) and GP (d-f) modeling. Spatial interpolation is performed by a simple Kriging method.

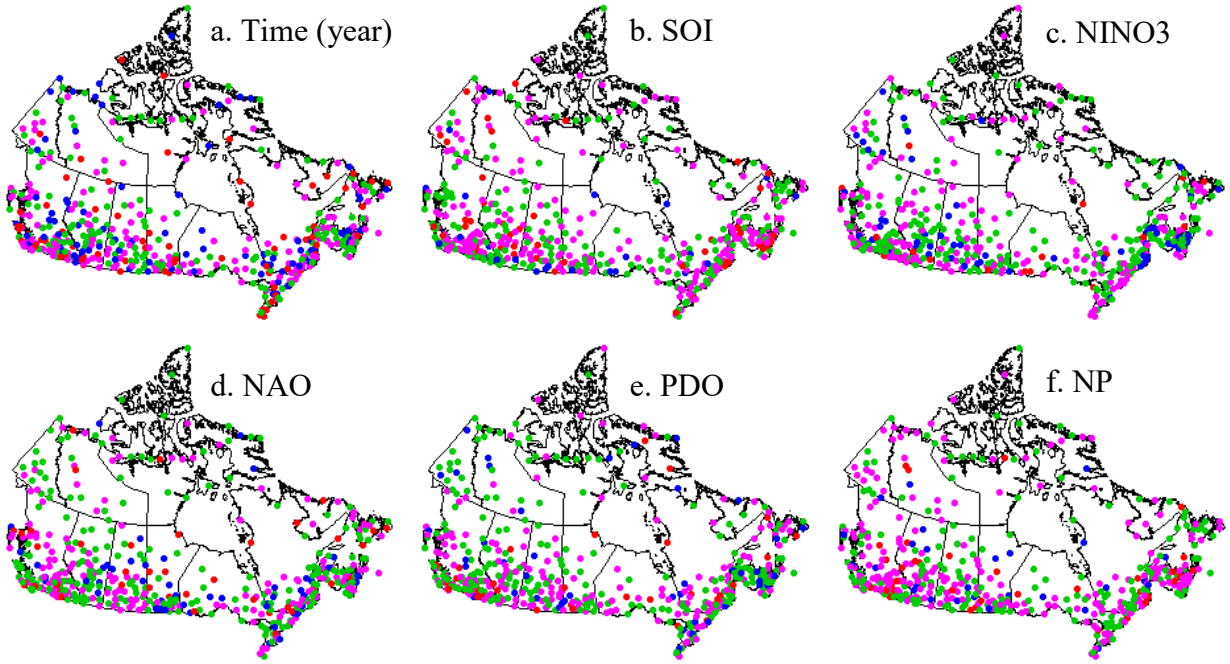

Figure 3-5 Maps showing the sign of difference ($P_+\left[p=0.95\right]-P_-\left[p=0.95\right]$) in precipitation return levels of 20 year return period conditional on positive ($P_+\left[p=0.95\right]$) and negative ($P_-\left[p=0.95\right]$) phases of covariates, i.e., the time and the five selected climate indices, for the GEV models of Canadian AMP with time-varying location and scale parameters ($\mu=\beta_\mu x$ and $\log(\sigma)=\beta_\sigma x$, x is a covariate). The red and magenta dots represent the higher AMP values in years with high values of a particular covariate ($P_+\left[p=0.95\right]>P_-\left[p=0.95\right]$) while the blue and green dots show the lower AMP values in years with high values of a particular covariate ($P_+\left[p=0.95\right]<P_-\left[p=0.95\right]$). Blue and red dots indicate stations whose GEV modeling of AMP is significantly improved by implementing the covariates at the 5% level.

3.3 Discussion of results

3.3.1 Extreme value distribution of Canadian precipitation

The Kolmogorov-Smirnov and Anderson-Darling tests were used to assess the goodness-of-fit of stationary GEV distributions applied to AMP series. Results of these two tests confirm the null hypothesis at 5% significance level that AMP time series are sampled from stationary GEV distributions for all stations, thus justifying the assumption that AMP time series can be modeled using GEV distributions. The spatial distribution of stationary GEV parameters is shown in Figure 3-3, and the spatial distribution of extreme precipitation of various return periods derived from these GEV distributions is shown in Figures 3-4a-c. Overall, the location and scale parameters increase from north to south and from inland to coastal regions of Canada, with highest location and scale parameters located in southwestern and southeastern coastal regions of Canada. However, there is no clear spatial pattern for the shape parameters. Most

stations have a non-zero shape parameter, which implies that most Canadian AMP series can be modeled by GEV Type II or Type III (Appendix I) distributions with heavy tail behavior.

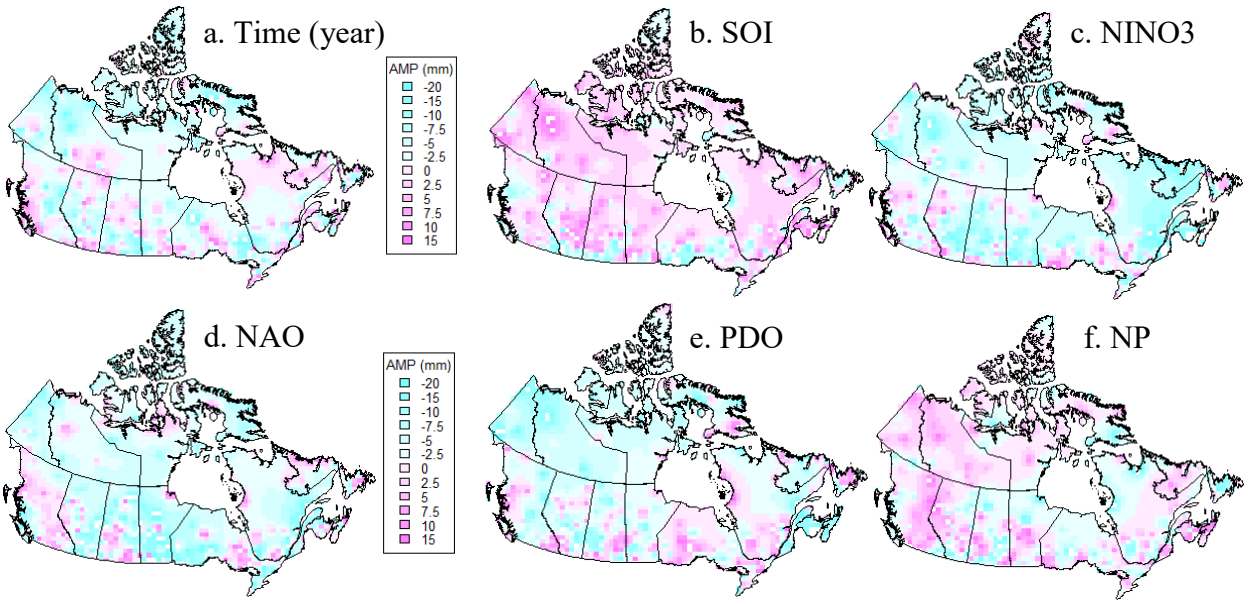

Figure 3-6 The spatial distributions of differences in precipitation return levels of 20-year return period predicted by GEV distributions based on parameters estimated from the maximum and the minimum historical values of a given covariate. The respective covariate used was year for (a), SOI for (b), Nino3 for (c), NAO for (d), PDO for (e), and NP for (f). The red (blue) grids means that the difference in AMP estimated from the GEV derived from the maximum covariate values are higher (lower) than that derived from the minimum historical values of the covariate, and the gridded, difference in AMP values were interpolated from station AMP values by a simple Kriging method. The difference in AMP estimated from GEV distributions based on the maximum versus the minimum covariates such as El Niño or La Niña can exceed 20 mm.

Figure 3-5 shows stations at which the fitted GEV distribution is significantly improved statistically by incorporating climate indices as covariates for both location and scale parameters, and Table 3-1 lists the number of these stations. Figure 3-5 also shows the spatial distribution of signs (+ or -) of differences between AMPs of 20-year return period estimated from GEV distributions conditioned on positive and negative phases of selected climate patterns, while Figure 3-6 shows the spatial distributions of actual differences between AMPs of 20-year return period estimated from GEV distributions conditioned on the mean of five largest positive and the mean of five largest negative phases of a given climate pattern. By modeling AMP using non-stationary GEV distributions with parameters based on time as the covariate, e.g., the first and the last 5-year of the study period for each station, which for the 1930-2010 period refers to 1930-1934 and 2006-2010, respectively. We have also shown the difference in AMP estimated between the last and the first 5-year of the study period for each station. Figures 3-5 and 3-6 show that the influence of large-scale climate patterns on the spatial variations of Canadian AMP

differs between the climate patterns, while Figures 3-5a and 3-6a show temporal changes in AMP over the study period of each station. Even though there are minor differences between results derived from different periods, the overall significance of the relationships (Table 3-1, Figure 3-5, and Figures S4 and S6 in Tan and Gan 2016) and their spatial distributions (Figure 3-6, and Figures S5 and S7 in Tan and Gan 2016) are consistent.

Table 3-1 Percentages (%) of stations where incorporating each covariate showed statistically significant improvement in the extreme precipitation modeling, compared to the stationary extreme precipitation modeling.

Period	Distribution	Parameter	Time	SOI	NINO3	NAO	PDO	NP
All data	GEV	Location	29.4	10.6	11.5	14.7	11.7	14.3
	GEV	Location + Scale	33.9	15.8	16.4	19.7	16.2	13.6
	Poisson	Rate of Occurrences	66.5	21.8	21.0	22.5	30.9	17.7
	GP	Scale	22.3	10.8	34.3	11.5	10.8	35.0
1900-2010	GEV	Location	34.1	12.2	14.8	19.5	9.8	16.8
	GEV	Location + Scale	31.7	19.8	17.1	22.0	14.6	19.8
	Poisson	Rate of Occurrences	78.5	22.2	19.8	31.7	22.0	21.0
	GP	Scale	19.5	19.5	35.9	12.4	14.6	39.2
1930-2010	GEV	Location	19.3	15.0	15.0	17.9	10.0	13.4
	GEV	Location + Scale	22.2	14.1	17.1	23.6	13.6	17.9
	Poisson	Rate of Occurrences	67.8	17.9	22.9	22.9	24.3	27.1
	GP	Scale	16.4	14.3	44.3	10.7	12.1	32.9
1950-2010	GEV	Location	27.9	11.9	12.9	15.9	12.9	13.4
	GEV	Location + Scale	23.4	15.9	17.4	18.4	11.9	10.0
	Poisson	Rate of Occurrences	45.0	20.4	19.4	30.8	35.3	35.3
	GP	Scale	14.4	11.9	34.8	11.4	12.9	29.9
1970-2010	GEV	Location	17.9	15.7	16.1	14.3	10.8	13.9
	GEV	Location + Scale	43.8	15.7	20.2	17.1	12.1	12.6
	Poisson	Rate of Occurrences	55.1	17.1	17.1	26.5	20.2	21.5
	GP	Scale	15.2	13.9	33.6	11.2	13.9	24.2

Approximately 29.3% of the AMP time series fitted to GEV distributions show significantly better fit to GEV distributions if the time was used as a covariate for the location parameter of GEV distributions. The proportion of AMP time series that fitted well to GEV distributions increased to about 33.9% when the time was used as a covariate for both location and scale parameters for GEV distributions. Apparently, about 1/3 of AMP time series shows non-stationary characteristics. Stations that show significant increase in AMP of 20-year return period are mainly located in southwestern Canada, northern CP and Quebec (QC),

Newfoundland (NL), and southwestern ON, while stations in southern CP, southeastern ON and Arctic region show significant decrease in AMPs of 20-year return period (Figures 3-5a and 3-6a). (Shook and Pomeroy 2012) also found that the single-day summer rainfalls had decreased at many locations in Southern CP over 1901–2000 and 1951–2000.

The effects of ENSO represented by SOI and NINO3 on AMP time series are shown in Figures. 3-5b-c and 3-6b-c where SOI and NINO3 were covariates for the location and scale parameters of GEV distributions fitted to Canadian AMP. Although only about 10.6 and 11.5% (Table 3-1) of the GEV distributions fitted to AMP time series show significant improvement when SOI and NINO3 were used as covariates for the location parameter, respectively, according to results obtained from the Walker's test and the false discovery rate (FDR) approach (Wilks 2006), the improvement is considered as field-significant across Canada. However, when SOI and NINO3 were incorporated as covariates to both the location and scale parameters of GEV distributions fitted to AMP time series, about 15.8 and 16.4% of the GEV distributions show significant improvement, respectively, and so their improvements are also considered to be field-significant.

In Figure 3-6c, areas colored pink (light green) are areas where a high NINO3 index means a wetter (drier) climate than a low NINO3 index, and vice versa. Therefore, a high NINO3 index (when El Niño is active) means that Canada will tend to be dry. In contrast, when NINO3 is low (which means when La Niña is active), Canada tends to be wet. As expected, Figure 3-6b shows a more or less opposite pattern to Figure 3-6c because when the SOI index is positive (negative), La Niña (El Niño) is active. However, there are minor differences in AMPs of 20-year return period estimated from GEV distributions using either SOI or NINO3 as covariates to represent the effect of ENSO on the Canadian AMP (Figures 3-5b-c and 3-6b-c). The influence of ENSO on the Canadian AMP represented shows more spatially consistent effect if SOI instead of NINO3 is used as the ENSO index.

The AMP of southwestern coastal areas, southern CP and the Great Lakes regions (light green area in Figure 3-6b for SOI and the pink area in Figure 3-6c for NINO3) tended to be higher in El Niño years than in La Niña years. Our results that AMP in the Great Lakes region during El Niño years tends to be high are consistent with that of Zhang et al. (2010) who found that extreme winter precipitation tends to be high during El Niño years. Because AMP in the

Great Lakes region can occur either in summer or winter, it seems the effects of ENSO on the extreme winter and summer precipitation of the Great Lakes region are similar to each other.

The AMP in central CP tends to be lower in El Niño than in La Niña years, which was in agreement with the higher winter total precipitation in La Niña than in El Niño years found by Shabbar et al. (1997) and Gan et al. (2007) for the southwestern Canada, including the CP. However, Zhang et al. (2010) found high extreme winter precipitation associated with El Niño for the central CP. Most northern Canada experienced inconsistent changes to AMP in El Niño than in La Niña years (Figures 3-5b-c), which is different from the results of Zhang et al. (2010) who found that extreme winter precipitation in El Niño years was usually higher than that in the La Niña years. Differences between their results and ours are believed to be partly due to the much smaller number of stations used by Zhang et al. (2010) for representing northern Canada, and for comparing maximum winter precipitation instead of AMP since AMP can occur either in winter or summer in northern Canada.

Compared to fitting AMP data to stationary GEV distributions (Table 3-1), more AMP time series show significantly better fit to GEV distributions if NAO was used as a covariate for the location parameter (14.7%) or both the location and shape parameters (19.7%) of GEV distributions. Such a level of improvements is field-significant which demonstrates the influence of NAO on some of the AMP of Canada. The spatial patterns of NAO effects are similar to those of ENSO. High AMP in BC (except its southwestern coastal region), central CP and eastern ON is related to the warm phase of NAO, in contrast to low AMP in most northern Canada, northern CP and western ON also during the warm phase of NAO (Figures 3-5d and 3-6d). However, based on composite analysis and GEV modeling, Zhang et al. (2010) suggested no field-significant influence of NAO on the NA extreme winter precipitation. Bonsal and Shabbar (2008) also found the effect of NAO on the Canadian total precipitation to be modest and restricted to northeastern regions where the warm phase of NAO is related to negative winter precipitation anomalies. Again, since AMP of Canada tends to occur in the summer, the influence of NAO on the AMP of Canada is not expected to be similar to its influence on the winter precipitation. For example, Coulibaly and Burn (2005) and Coulibaly (2006) found significant differences in the relationships between NAO and spring, summer or autumn precipitation and streamflow of Canada.

The effect of PDO on Canadian AMP is also field-significant, as 11.6% (16.1%) of AMP series fitted to GEV distributions are significantly improved if PDO is used as a covariate for the location (both location and scale) parameters of GEV distributions. In northwest Canada (the light green region in Figure 3-6e), AMP tends to be high during the cold phase of PDO, but low during the warm phase of PDO. This agrees with the effects of PDO on the streamflow of northwest Canada found by (St. Jacques et al. 2010; St. Jacques et al. 2014). In contrast, the warm phase of PDO results in high AMP in ON, QC and western BC (pink region), but exerts both increasing and decreasing effects on the AMP of CP. Again, the relations between Canadian AMP and PDO are different from the relations between winter extreme precipitation and PDO, since Zhang et al. (2010) found that extreme winter precipitation of the CP and the Great Lakes tends to be lower during the cold phase than the warm phase of PDO. It is needed to further explore variations in seasonal relationships between extreme precipitation such as AMP and large-scale climate patterns.

NP seems to have more influence marginally on the location than both the location and scale parameters of GEV, for the percentage of stations that shows better fit to GEV distributions is 14.3% if NP was only used to estimate the location parameter, compared to 13.6% of stations showing better fit to GEV if NP was used to estimate both location and scale parameters. In contrast to the effect of PDO, the warm phase of NP primarily resulted in high AMP in Canada except in some local areas of CP and ON.

3.3.2 Modeling heavy precipitation clusters with Poisson regression

Occurrences of heavy precipitation (larger than the 95^{th} percentile) presented in terms of the mean, variance and coefficient of dispersion (ratio between the variance and the mean) show a well-organized spatial pattern (Figure 3-2), similar to that shown in Figures 3-3 and 3-4. These three statistics decrease from north to south except in the southwestern coastal region where these values are very large. The CP has the lowest mean, variance and coefficient of dispersion, with a mean lower than 5 days, a variance lower than 3 days, and a coefficient of dispersion lower than 2.0, while northern Canada has the highest variance (> 4.0 days) and the coefficient of dispersion (> 2.5). For the mean counts of heavy precipitation, the spatial pattern in Northern Canada is less consistent since stations show a mix of high and low mean count values. 80.3% stations have a coefficient of dispersion statistically significantly greater than 1, except for some stations in the CP and the southern border of Canada. These over-dispersion characteristics

indicate that Canadian heavy precipitation exhibits temporal clustering or non-stationary behavior.

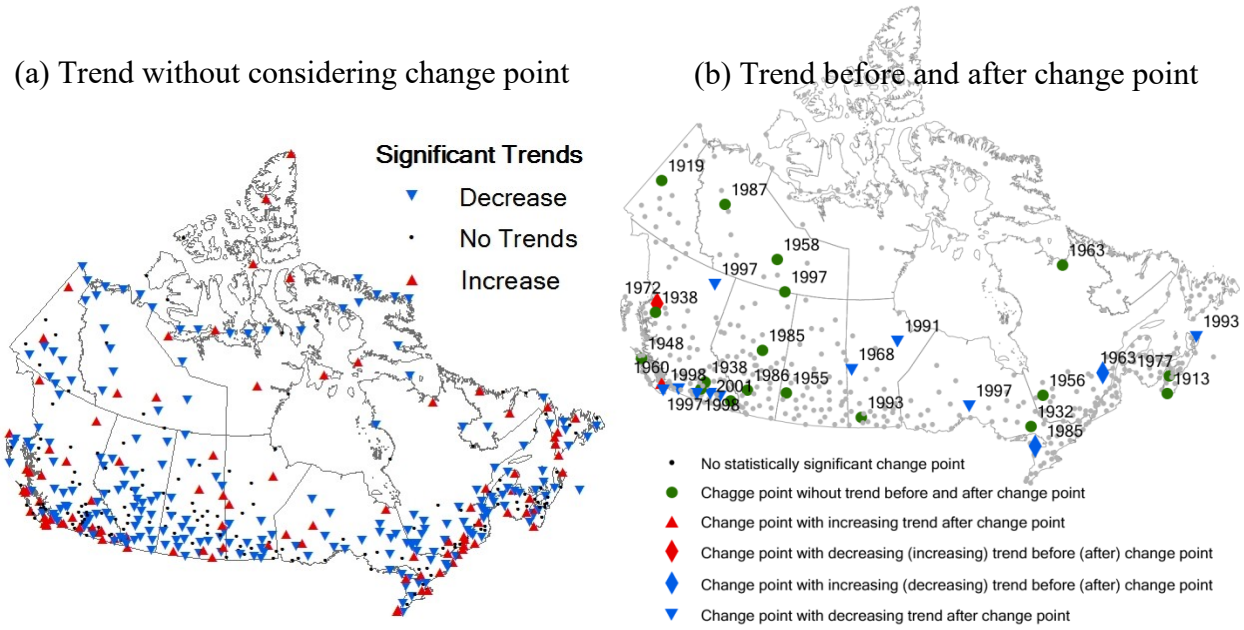

Figure 3-7 Results of the fitting of the counts of heavy precipitation with a Poisson regression model with rate of occurrence that depends linearly on time (via a logarithmic link function) without (a) and with (b) a change point detected using the segmented regression. All change points and trends showing with green circles, red and blue triangles or diamonds are statistically significant at the 5% significance level. The year when statistically significant change point occurred is numbered next to the station.

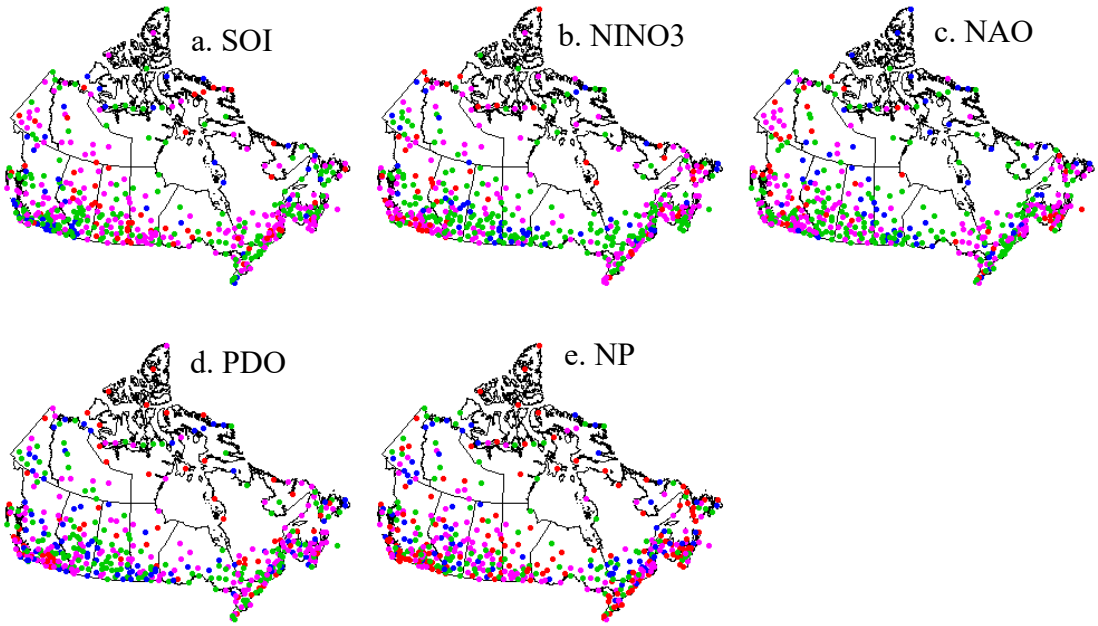

Figure 3-8 Map showing the stations for which the five selected climate indices are covariates in the Poisson regression model. The red and magenta (blue and green) dots represent the positive (negative) relations between the rate of heavy precipitation occurrence and particular climate indices. Blue and red dots indicate stations whose Poisson regression modeling of the rate of heavy precipitation occurrence is significantly improved by implementing the covariates at the 5% level.

Out of 463 stations (Figure 3-7b), only 32 stations show statistically significant change points in the occurrences of heavy precipitation. However, for these 32 stations, only 12 (1) stations show increasing (decreasing) trends before the change point and 2 (2) stations showed increasing (decreasing) trends after the change point occurred, while the remaining 18 stations show no trends either before or after the change point. The years the change point occurred are not spatially consistent. Given that change points were only detected in about 7% of stations (less than 9% of stations for the four periods studied), other than in southwestern Canada, abrupt changes to occurrences of heavy precipitation events in Canada are not field-significant.

In contrast, slowly varying trends in the occurrence of heavy precipitation events are field-significant across Canada as both the Walker's test and FDR approach rejected the joint, multiple-site null hypothesis ($\beta_1 = 0$) to be statistically significant. In the Poisson regression analysis, for stations without detected change points, statistically significant decreasing trends dominate over increasing trends (45.5% vs. 21.0%), with trend magnitudes, β_1 (years) ranging from -0.062 to 0.021. Most stations showing increasing trends are located in the southwestern, east coast, northern Arctic and northeastern CP, while decreasing trends are widespread in the CP, eastern and northern Canada (Figure 3-7a). Results obtained from all the four-period analysis consistently demonstrated changing characteristics of the frequency of heavy precipitation over Canada. However, considerably fewer stations with short data record over 1970-2010 (55.1%) and 1950-2010 (45.0%) were identified with significant trends than those with long data record over 1930-2010 (67.8%) and 1900-2010 (78.5%) (Table 3-1). By averaging counts of heavy events across Canada, e.g., no consideration of the spatial variability of occurrences of heavy events, Zhang et al. (2001a) found no monotonically increasing or decreasing trends in the annual counts of heavy precipitation events. However, they detected interdecadal variability in the heavy precipitation events of Canada.

Spatial distributions of positive/negative relationships between occurrences of heavy precipitation and climate indices are shown in Figure 3-8. The influence of ENSO on occurrences of heavy precipitation (> 95 percentile) is more significant than on the AMP time series because the number of stations (21.8% for SOI and 21.0% for NINO3, respectively; Table 3-1) with heavy precipitation significantly related to ENSO was almost 2 times of that of AMP. However, positive or negative influences of El Niño and La Niña on the occurrences of heavy precipitation are spatially consistent to that on AMP. For example, CP experiences more heavy

precipitation in La Niña years than in El Niño years. Spatially, PDO exerts similar but more significant positive or negative influences on occurrences of heavy precipitation than on AMP. NAO and NP also exert similar influences on occurrences of heavy precipitation and AMP across Canada.

3.3.3 GP distribution

As a comparison, spatially distributed precipitation return levels of corresponding return periods were also calculated using a stationary GP model (Figure 3-4d-f). Spatially, precipitation return levels increase in the north-south direction, and as expected, peaked in the southwestern and southeastern coastal regions of Canada, which is consistent with the location and scale parameters of GEV as shown in Figure 3-3. Differences between precipitation return levels of 2-, 20- and 100-year return periods derived from GEV versus GP distributions are minor across Canada, except in the southwestern and eastern coastal areas, where GEV distributions estimate smaller extreme precipitation of the 2-, 20- and 100-year return period than GP distributions. For the above three return periods, overall GEV estimates precipitation return levels that are smaller than that of GP by about 8.0%, 1.4% and 3.7%, respectively.

Figure S3 in Tan and Gan (2016) shows the spatial distribution of signs (+ or -) of differences between precipitation return levels of 20-year return period estimated from GP distributions conditioned on positive and negative phases of selected climate indices used as covariates for scale parameters of GP distributions. The spatial relationships between AMP and covariates such as the time, SOI, NAO and PDO derived from GP distributions are similar to that derived from GEV distributions (Figure 3-5). However, the scale parameter of GP distributions of many stations or the magnitude of AMP is significantly correlated with NINO3 and NP indices, which is different from that derived from GEV distributions. Because a fixed threshold was used in GP distributions, only the scale parameter of GP varies with time-varying covariates (climate indices). However, under the impact of a changing climate, the threshold value of GP can change more significantly than its scale parameter (Kyselý et al. 2010; Sugahara et al. 2009). This is the reason that the GP distributions with only its scale parameter to be time-varying tends to estimate lower precipitation return levels of 20-year return period for some stations during the warm phase of NP than GEV distributions with both time-varying location and scale parameters. Further studies should be conducted to examine the threshold of GP distributions related to time-varying climate indices. The high proportion of stations showing statistically significant

correlation between the GP scale parameter and time-varying climate indices is strong evidence that extreme Canadian daily precipitation is non-stationary.

3.3.4 Composite circulation patterns

Because composite winter circulation anomaly patterns associated with heavy precipitation for western and eastern Canada are similar and have similar composite days (Julian days 309-335), only the winter patterns for western Canada are shown in Figure 3-9. Composite analysis has advantage over the non-stationary extreme value analysis because the former separately investigates the influence of large-scale climate patterns on extreme summer and winter precipitation of Canada, while the latter is based on annual climate indices in which seasonal differences of large-scale climate patterns have been averaged out, which could decrease the statistical significance of extreme precipitation response to such climate patterns.

For total winter precipitation, Shabbar et al. (1997) found that strong El Niño episodes tend to associate with a deepened Aleutian low and an amplified western Canadian ridge which enhanced anticyclones and caused a northward shift of the mid-latitude jet stream, resulting in a drier southern Canada. On the other hand, La Niña winters are usually associated with an enhanced westerly flow, giving rise to more moisture in southern Canada. Wetter (drier) southern Canada in La Niña (El Niño) winters is also consistent with the positive (negative) PWC anomalies associated with La Niña (El Niño) (Figures 3-9a-b). However, in central Canada, positive PWC anomalies are also associated with El Niño (Figures 3-S8a-b in Tan and Gan 2016), and synoptic circulation patterns associated with heavy precipitation are likely more complicated than patterns associated with total winter precipitation found by Shabbar et al. (1997) because heavy precipitation involves higher spatiotemporal variabilities than total winter precipitation.

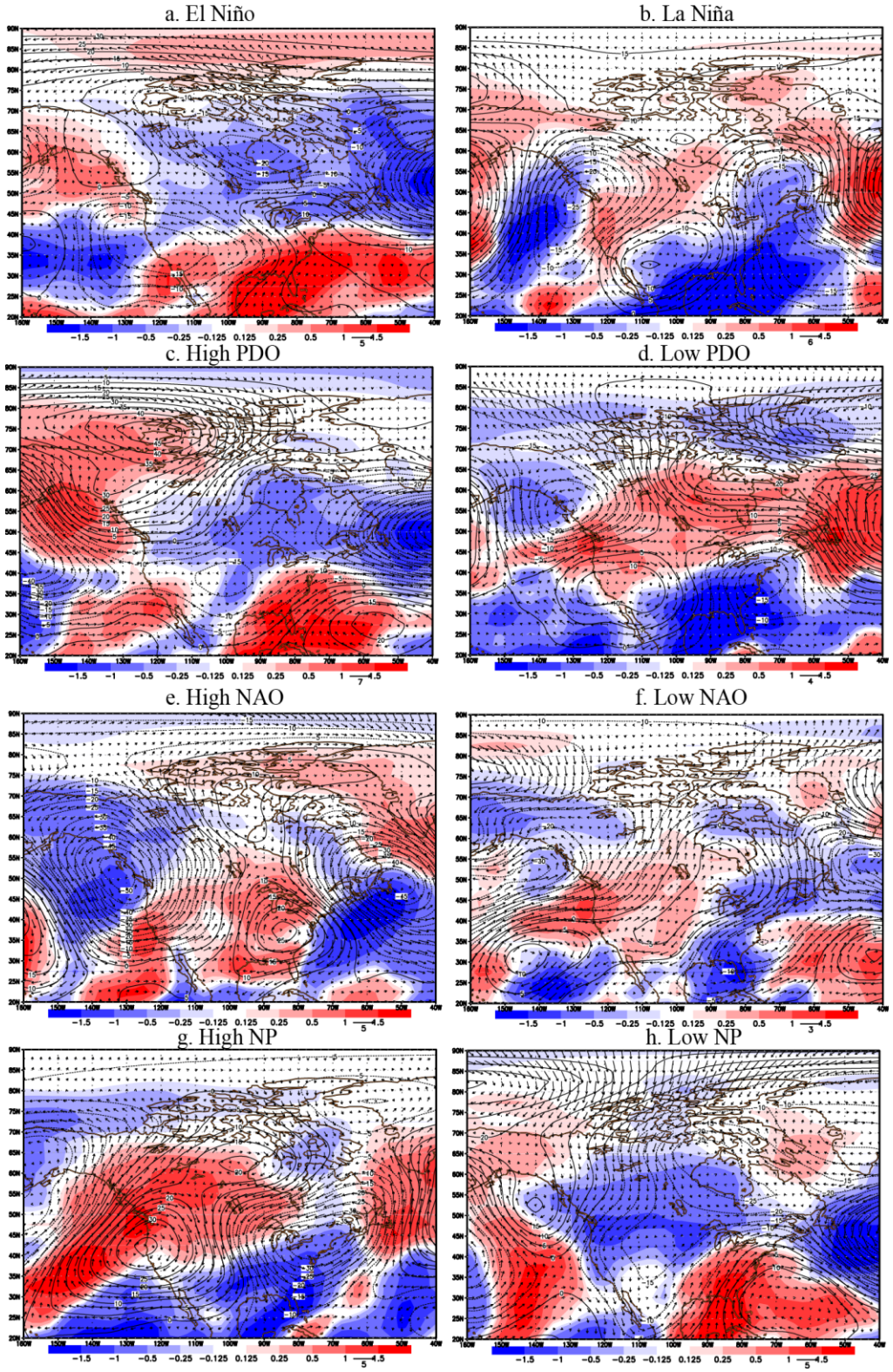

Figure 3-9 Composite winter 500-hPa geopotential height (m; contour with numbers), 500-hPa wind field (m s^{-1}; vectors) and vertically integrated precipitable-water-content (mm day^{-1}; shaded) anomaly patterns for *western* Canada in *winter* days (Julian days 309-335) on which heavy precipitation most likely occurred, associated with (a) extreme El Niño (high NINO3), (b) extreme La Niña (low NINO3), (c) high PDO, (d) low PDO, (e) high NAO, (f) low NAO, (g) high NP and (h) low NP.

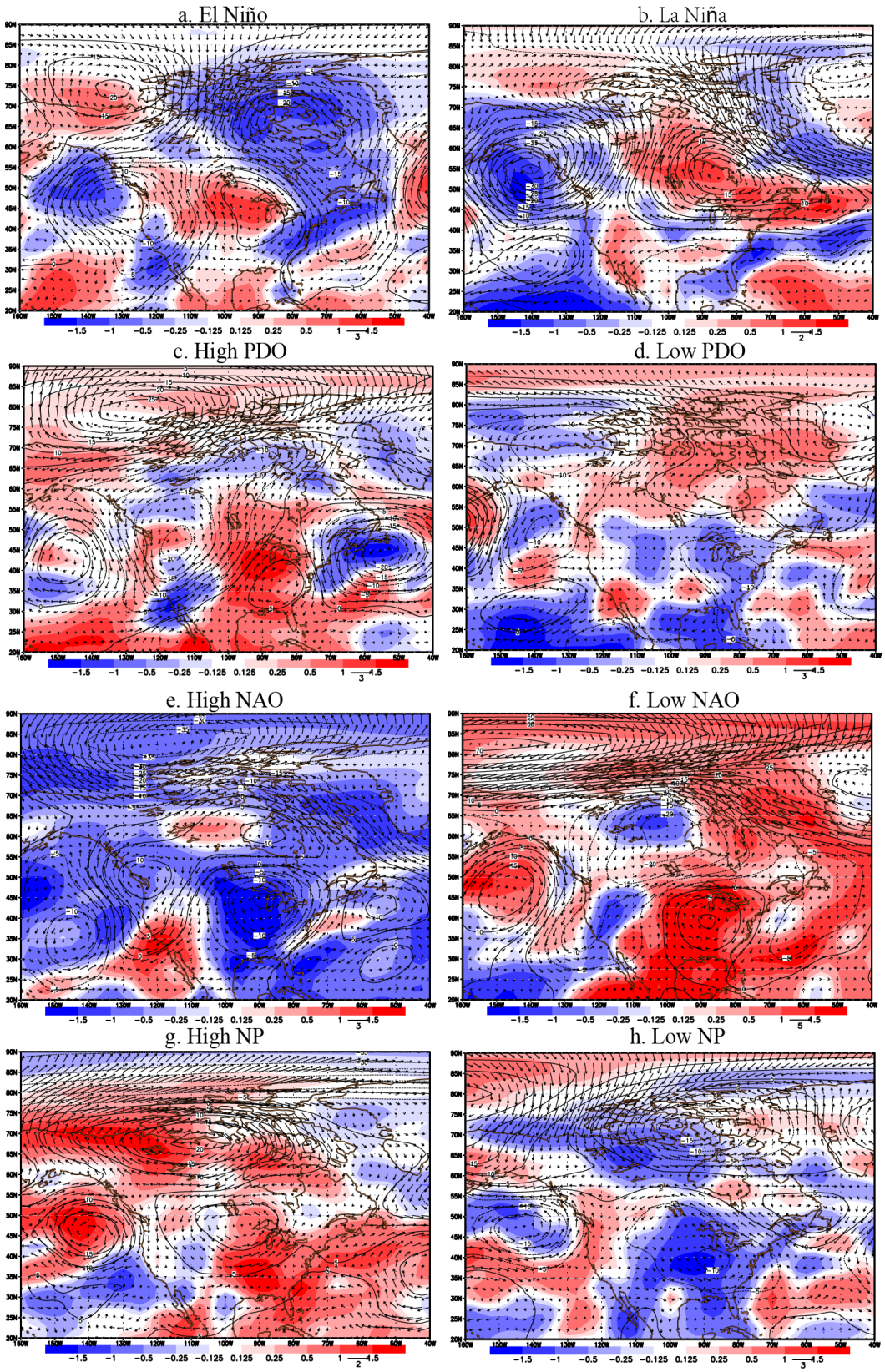

Figure 3-10 Same as Figure 3-9, but for *western* Canada in *summer* days (Julian days 184-227) on which heavy precipitation most likely occurred.

In western Canada, heavy precipitation that occur during El Niño winters tend to be relatively moderate because the lower branch of Pacific jet streams described by Shabbar et al. (1997) and Higgins et al. (2002) shifts north, thus missing western Canada (Figure 3-9a), which is similar to circulation patterns giving rise to negative total winter precipitation anomaly in western Canada (Gan et al. 2007; Jiang et al. 2014; Shabbar et al. 1997). During La Niña winters, the subtropical Pacific jet stream Higgins et al. (2002) shift north, from southwestern (Figure 3-9a) to the northwestern (Figure 3-9b) United States, thus bringing positive heavy precipitation anomalies to western and central Canada. Heavy winter precipitation that occurs in central Canada during La Niña winters associated with deepened and northward shifted Aleutian Low (Figure S8b in Tan and Gan 2016) tend to be lower than heavy winter precipitation that occurs during El Niño winters associated with a normal and southeastward shifted Aleutian Low, positive geopotential heights, and intense polar jet streams (Figure S8a in Tan and Gan 2016). The above mechanism is in direct contrast to the mechanism behind that of total winter precipitation described in the previous paragraph.

In western Canada, summer days with heavy precipitation tend to be higher (lower) during El Niño (La Niña) years with positive (negative) moisture anomaly as shown in Figure 3-10a (Figure 3-10b), which agrees with the spatial pattern of AMP (see Figure 3-6c) but in contrast to what was found by Shabbar and Skinner (2004). This is due to abundant moisture brought by the northeastward, subtropical jet stream to the western and central NA in El Niño summers (Figure 3-10a and Figure S9a in Tan and Gan 2016). In La Niña summers, the deepened and southward shifted Aleutian low leads to positive wind anomalies to western Canada but that does not result in positive PWC anomalies for western Canada likely because of low moisture content in the north Pacific atmosphere (Figure 3-10b). For eastern Canada, polar (North Atlantic) jet streams dominate El Niño (La Niña) summers (Figure 3-10 and Figures S9 and S10 in Tan and Gan 2016), which result in negative (positive) PWC anomalies, which are consistent with low (high) AMP in eastern Canada during El Niño (La Niña) years (Figures 3-6b-c).

The circulation patterns during active (inactive) PDO years are similar to those during El Niño (La Niña) years, but different in terms of the center location and strength of these circulation patterns, both during winters (Figure 3-9 and Figure S8 in Tan and Gan 2016) and summers (Figure 3-10 and Figures S9 and S10 in Tan and Gan 2016), e.g., when PDO is inactive, the Aleutian Low (Figures 9d and S8d) is shifted northward compared to when La Niña

is active (Figure 3-9b and Figure S8b in Tan and Gan 2016), which results in different spatial PWC anomalies between inactive PDO and La Niña winters. Bond and Harrison (2000) found that anomalously low (high) SST over the central North Pacific Ocean (west coast of Americas) typically occurs during active PDO winters. Active PDO leads to low pressure zones occurring over the North Pacific Ocean with enhanced anticlockwise winds, resulting in dry conditions in western Canada (Figure 3-9c). In contrast, inactive PDO typically leads to wet conditions in western Canada. The influence of PDO on the heavy winter precipitation is similar to its influence on the winter total precipitation, of western Canada (Gan et al. 2007; Jiang et al. 2014; Mantua and Hare 2002).

Positive (negative) summer PWC anomalies (Figures 3-10e-f and Figures S9e-f and S10e-f in Tan and Gan 2016) in northern Canada are associated with low (high) NAO. This pattern is similar to that of AMP shown in Figure 3-6d, which is likely caused by a shift in the direction of jet streams from the southwest during high NAO to northwest during low NAO between Arctic and North Atlantic. However, there are no consistent winter circulation anomaly patterns for NAO composites. The shift of the axis of maximum winter moisture from southwest to northeast across the Atlantic Ocean mainly affects the winter precipitation of northern Europe instead of NA (Hurrell and Loon 1997). Therefore, the correlation between NAO and Canadian extreme precipitation derived from the non-stationary analysis may be misleading as NAO index is the difference of atmospheric pressure at sea level between the Icelandic low located near Iceland and the Azores high located south of Canada.

A deepened and eastward shifted Aleutian Low during years of high NP index advects moist air towards the west coast of Canada, resulting in positive PWC anomalies (Figures 3-9g and 3-10g, and Figures S9g and S10g in Tan and Gan 2016) over western Canada. On the other hand, predominant wind patterns are in opposite directions during low NP years, resulting in typically negative PWC anomalies (Figures 3-9h and 3-10h, and Figures S9h and S10h in Tan and Gan 2016). These PWC anomalies derived from NP composite are consistent with composite differences of AMP shown in Figure 3-6f. The impact of circulation patterns associated with the NP index on the heavy precipitation of Canada is similar to that of ENSO, because the inter-decadal variability of the northern Pacific described by the NP index are linked to the inter-annual variability of ENSO (Trenberth and Hurrell 1994). Even though ENSO, PDO and NP are all associated with the heavy precipitation of Canada, there are also local-scale synoptic

processes that affect the heavy precipitation of Canada not accounted in our composite analysis of these climate anomalies. More detailed studies on circulation patterns associated with Canadian heavy and extreme precipitation should be conducted in the future.

3.4 Summary and conclusions

In this study, we have analyzed time series of AMP, POT and counts of extreme/heavy precipitation of 463 gauging stations of Canada using stationary and non-stationary GEV, GP distributions and Poisson regression, respectively. To create the non-stationary distributions, time-varying covariates that represent large-scale climate patterns such as ENSO, NAO, PDO and NP were incorporated to the location and scale parameters of GEV distributions, the rate of occurrence parameter of Poisson distributions and the scale parameter of GP distributions. To detect non-stationarities of Canadian extreme and heavy precipitation, we also used the time (year) as a covariate to estimate the parameters of non-stationary distributions.

Location and scale parameters of stationary GEV distributions fitted to the AMP data increase from north to south, and from inland to coastal regions of Canada. However, there was no clear spatial pattern for the shape parameters. Most stations had a non-zero shape parameter, which implies that most Canadian AMP series can be modeled by GEV Type II or Type III distributions with heavy tail behavior. Stationary GEV distributions estimated smaller extreme precipitation of the 2-, 20- and 100-year return period than stationary GP distributions by about 8.0%, 1.4% and 3.7%, respectively. In general, GEV distributions tend to under-estimate AMP of western and eastern coastal regions more than other regions of Canada. About 1/3 of the AMP time series shows non-stationary characteristics. Stations located in southwestern Canada, northern CP and QC, NL, and southwestern ON showed statistically significant increase in AMP, while AMP in southern CP, southeastern ON and Arctic region significantly decreased.

By using time-varying, climate indices as covariates in Poisson regression distributions, the results show that clusters of heavy precipitation events in Canada are related to large-scale climate patterns. The strength of storm clusters decreases spatially from north to south, but trends and abrupt changes to occurrences of the heavy precipitation appear to be less spatially consistent. By modeling AMP time series with non-stationary GEV and heavy precipitation with non-stationary GP distributions, it is evident that AMP and heavy precipitation of Canada show strong non-stationarities which are likely related to the influence of large-scale climate patterns given strong correlations are found between extreme Canadian precipitations and climate indices.

AMP in southwestern coastal regions, southern CP and the Great Lakes regions tend to be higher in El Niño years than in La Niña years, while other regions of Canada showed a lower AMP in El Niño years than in La Niña years. The effect of other climate patterns such as PDO, NAO and NP on extreme precipitation is also significant at some stations across Canada. Given the influence of climate patterns on extreme precipitation of Canada is the primary focus of this study, future studies should focus on expected changes in Canadian extreme and heavy precipitation resulting from changes in large-scale climate patterns due to anthropogenic climate change.

3.5 Appendix

I. GEV distribution

Let $M = \max\{Z_1, \cdots$ for large n, where $Z_1, Z_2, \cdots$ is a sequence of independent (or weakly dependent) identically distributed observations. In this study, Z_t represents daily observed precipitation recorded at a particular station on day *t*, and *M* is the AMP. Asymptotic results state that under some regularity conditions, normalizing sequences $\{a_n\}$ and $\{b_n > 0\}$ can be found such that (Coles 2001):

$$\Pr\left(\frac{M - a_n}{b_n} \le y\right) \to \mathrm{GEV}(y) \tag{3-1}$$

as $n \to \infty$, for a non-degenerate distribution function, which is the GEV distribution with the cumulative distribution function:

$$\mathrm{GEV}(y;\mu,\sigma,\xi) = \begin{cases} \exp\left\{-\left[1+\xi\dfrac{y-\mu}{\sigma}\right]^{-1/\xi}\right\} & \xi \neq 0 \\ \exp\left[-\exp\left(\dfrac{(y-\mu)}{\sigma}\right)\right] & \xi = 0 \end{cases} \tag{3-2}$$

where $1+\xi(y-\mu)/\sigma > 0$, μ, σ and ξ are the location, scale, and shape parameters, respectively. The shape parameter ξ determines the type of tail behavior. $\xi < 0$, $\xi = 0$ and $\xi > 0$ correspond to the Weibull (Type III), Gumbel (Type I) and Fréchet (Type II) distributions, respectively.

For a non-stationary process, the time-varying GEV parameters can be estimated by time-varying covariates. For instance, the GEV location parameter is defined through a linear function of covariates:

$$\mu = \beta X = \beta_0 + \beta_1 x_1 + \cdots \tag{3-3}$$

where $X = (1, x_1, \cdots$ is a matrix of the time-varying covariate vectors $x_1, \cdots$, $\beta = (\beta_0, \beta_1, \cdots$ is the parameter vector to be estimated, in which β_0 is the intercept and $\beta_1, \cdots$ are the regression coefficients for the corresponding covariates; m is the number of covariates considered. The scale and shape parameters of the GEV distribution can be similarly expressed as Equation (3-3).

II. Poisson regression

The numbers of days (counts) of extreme values exceeding a threshold over a specified time interval (a year in this study) can be modeled by a Poisson distribution with an equal-dispersion (the mean equals the variance). However, the variance of observed data tends to be larger than the mean, known as over-dispersion, which can partly be attributed to the effect of temporal clustering (Mallakpour and Villarini 2015; Pinto et al. 2013; Villarini et al. 2013; Villarini et al. 2011). The statistical significance of dispersion coefficients different from unity at 5% significance level can be tested using the regression-based tests (Cameron and Trivedi 1990) for testing over-dispersion in a Poisson model.

A Poisson regression models discrete data, in which the predictand follows a Poisson distribution. The counts in year i as N_i have a conditional Poisson distribution with the rate of occurrence parameter λ_i, given that:

$$P(N_i = k | \lambda_i) = \frac{e^{-\lambda_i} \lambda_i^k}{k!} \quad (k = 0, 1, 2, \cdots \tag{3-4}$$

where λ_i is a non-negative random variable. In a Poisson regression model, λ_i can be modeled as a function of predictors $x_{1i}, x_{2i}, \cdots$ in a manner similar to parameters of a non-stationary GEV (see Equation 3-3):

$$\lambda_i = \exp(\beta_0 + \beta_1 x_{1i} + \beta_2 x_{2i} + \cdots \quad) \tag{3-5}$$

where β_j is the coefficient for the j-th predictor (x_{ji}) estimated by the maximum likelihood method. If β_j estimated is non-zero at a 5% significance level, then there is a statistically significant relationship between the occurrence of extreme events and the predictor x_j. By relating λ_i to the time using an exponential function $\lambda_i = \exp(\beta_0 + \beta_1 i)$, changes in the mean

number of occurrences of heavy precipitation with time can be examined. If β_1 is non-zero at the 5% significance level, temporal changes in the mean number of extreme events are statistically significant (Villarini et al. 2011; 2012; 2013). The abrupt change points of the occurrences of extreme events can be further identified by a segmented regression in which the relation between the predictand and the predictor is piecewise linear. We used the function *segmented* in the R package 'segmented' (Muggeo 2003) to detect change points and to estimate β_0 and β_1 for the Poisson regression model.

III. GP distribution

The exceedance, $Q = Z - u$ (where Z is the observed precipitation and u the threshold) can be modeled as a GP distribution (Coles 2001):

$$\Pr\left(Q \le q \middle| Z > u\right) = GP_{\sigma,\xi}\left(q\right) = \begin{cases} 1 - \exp\left[-q/\sigma\right] & \xi = 0 \\ 1 - \left[1 + \xi q/\sigma\right]^{-1/\xi} & \xi \neq 0 \end{cases} \tag{3-6}$$

for $q \ge 0$ and $1 + \xi q/\sigma > 0$, $\sigma > 0$, where σ and ξ are the scale and shape parameters of a GP distribution. For $\xi = 0$, GP reduces to an exponential distribution. The GP distribution can be set up to model non-stationary processes, usually by making the scale parameter σ depend on particular covariate(s) (Coles 2001; Khaliq et al. 2006). The log of σ is regressed against covariates X, $\log\left(\sigma\right) = \beta X$, as shown in Equations 3-3 and 3-5.

The return level y_l is exceeded on average l times over a fixed period. Since there are on average λ peaks in the whole time series, the probability that an arbitrary peak exceeds y_l equals l/λ. Thus, y_l is obtained by adding the threshold to the $\left(1 - l/\lambda\right)$ quantile of the excess distribution (Coles 2001):

$$y_l = u + GP_{\sigma,\xi}^{-1}\left(1 - l/\lambda\right) = \begin{cases} u + \sigma \ln\left(l/\lambda\right) & \xi = 0 \\ u + \dfrac{\sigma}{\xi}\left[1 - \left(\dfrac{l}{\lambda}\right)^{-\xi}\right] & \xi \neq 0 \end{cases} \tag{3-7}$$

For presentation, it is often more convenient to give return levels on an annual scale, so that the *N*-year return level is the level expected to be exceeded once every *N* years.

IV. The likelihood-ratio test

The likelihood-ratio test can compare results obtained from GEV and GP distributions of parameters expressed with covariates of various complexities, such that the base covariate (e.g., M_o) is a subset of a more complex covariate (e.g., M_1). The likelihood-ratio test can determine which sets of model parameters will lead to the overall best model performance for GEV and GP. Suppose a base model M_0 is nested within a model M_1, and L_0 (L_1) is the negative log-likelihood value for M_0 (M_1), then a deviance statistics is given by (Coles 2001):

$$D = -2\left(L_1 - L_0\right) \tag{3-8}$$

Large values of D indicate that M_1 is more adequate for representing the data than its base counterpart M_0. The D statistic follows a chi-square distribution with degree of freedom, ν (difference between the number of parameters of the models M_0 and M_1). D_α is the $(1-\alpha)$ quantile of the chi-square distribution at the α significant level. The null hypothesis $D = 0$ is rejected if $D > D_\alpha$. We used functions in the R package 'extRemes' (Gilleland and Katz 2011) for inferring the parameters of GEV and GP distributions and testing the significance of the relations between parameters and covariates.

Chapter 4 Effects of persistence and large-scale climate anomalies on trends and change points in extreme precipitation of Canada

4.1 Introduction

Impacts of climate variability and human activities can result in gradual (trend) or abrupt (shift) changes in the hydrologic cycle. A changing hydroclimate could result in under- or over-designed civil engineering projects based on design tools developed from historical data (Forsee and Ahmad 2011; Jakob 2013; Kuo and Gan 2015; Kuo et al. 2015). Thus, in view of recently observed changes in the magnitude and frequency of various hydroclimatic variables, the fundamental assumption of stationarity for traditional frequency analysis may no longer apply (Milly et al. 2008; 2015), even though nonstationary analysis of hydroclimatic processes under anthropogenic climate change has been criticized because of additional uncertainties associated with nonstationary models (Montanari and Koutsoyiannis 2014; Serinaldi and Kilsby 2015). Furthermore, because of large sampling error in analyzing time series with long-term persistence (LTP), a stationary process could be mistaken to be nonstationary (Koutsoyiannis and Montanari 2015; Montanari and Koutsoyiannis 2014). In this study, we have focused on detecting both slowly varying (trend) and abrupt (change points) changes in Canadian extreme precipitation, and the possible effects of persistence and climate anomalies in the precipitation trends.

A stationary time series has a time-invariant probability distribution function that does not exhibit trends or change points (Brillinger 2001; Koutsoyiannis 2006). For Canada, several studies have examined the stationarity of annual or seasonal total precipitation time series by trend analysis and they found an increase in the annual total precipitation mostly due to an increase in the number of small to moderate precipitation events (Mekis and Vincent 2011; Vincent and Mekis 2006; Zhang et al. 2001a; Zhang et al. 2000), while statistically significant increase (decrease) in snowfall has been mainly detected in northern (southwestern) Canada (Mekis and Vincent 2011; Vincent and Mekis 2006). In contrast, past studies in trend analysis of observed heavy or extreme precipitation over Canada show inconsistent results on the detection of statistically significant trend (Alexander et al. 2006; Burn and Taleghani 2013; Kunkel 2003; Kunkel and Andsager 1999; Peterson et al. 2008; Vincent and Mekis 2006; Zhang et al. 2001a) in either the frequency or the intensity of extreme precipitation, partly because of different data

sets and techniques used in these studies. On the other hand, climate change scenarios of global climate models downscaled by regional climate models mostly project a more intense and frequent daily and multi-day precipitation events for most Canadian regions (Kuo et al. 2015; Mailhot et al. 2010; Mladjic et al. 2011). A comprehensive investigation on changes to historical extreme precipitation of Canada will address inconsistent results obtained in past studies, and also to gain some knowledge on the possible impact of climate change to such historical precipitation data of Canada.

There have been limited studies on the change points in the probability distribution of precipitation, especially on extreme precipitation, such as Fu et al. (2015) who analyzed change points of precipitation over western Canada, given a shift could have significant impacts on the regime of extreme precipitation, as Villarini et al. (2009a; 2011; 2013) found in the continental US. Therefore, as a follow-up of Fu et al. (2015), we investigated both trends and change points in the time series of annual maximum daily precipitation (AMP) and seasonal maximum daily precipitation (SMP) for all regions of Canada.

Next, recent trend analysis of extreme and heavy Canadian precipitation (e.g., Mekis and Vincent 2011; Vincent and Mekis 2006; Zhang et al. 2001a; Zhang et al. 2000) did not explicitly consider the possible influence of large-scale climate anomalies, even though extreme and heavy precipitation could be linked to large-scale climate anomalies over North America (Raible 2007; Yin and Branstator 2008; Yiou and Nogaj 2004; Zhang et al. 2010). St. Jacques et al. (2010; 2014) found that trends in streamflow of watersheds in Northern Rocky Mountain and Canadian Prairie Provinces are partly due to the ~60-year cycle of the Pacific Decadal Oscillation (PDO).

In the trend analysis of station precipitation data, the serial and inter-station correlations between stations of a regional domain are usually overlooked even though correlations between station streamflow data were widely considered in the trend analysis of Canadian streamflow data (e.g., Burn and Elnur 2002; Ehsanzadeh and Adamowski 2010; Khaliq and Gachon 2010; Khaliq et al. 2009a; 2009b; Yue et al. 2003; 2003). In this study, the trends of Canadian extreme precipitation were estimated with the serial correlation, inter-station correlation and impacts of large-scale climate anomalies removed.

Hydroclimatic variables tend to exhibit temporal persistence in extremes such as floods and droughts. Short-term persistence (STP) is usually accounted for by an autoregressive-1 model (Sagarika et al. 2014; Yue et al. 2003), while LTP, first detected by Hurst (1951), can

significantly influence trends estimated from conventional tests based on the independent assumption, such as the Mann-Kendall (MK) test (Cohn and Lins 2005; Kendall 1975). The MK test tends to over-estimate the significance of trends of data with LTP (Cohn and Lins 2005; Franzke 2010, 2012; Koutsoyiannis 2006; Koutsoyiannis and Montanari 2007; Sagarika et al. 2014). The LTP of a hydroclimatic series is usually related to large-scale climate anomalies of interannual and/or interdecadal scales (Klemeš 1974; Potter 1976). The consideration of LTP can better explain certain nonstationary behaviors such as temporal trends in a time series (Koutsoyiannis 2006; Koutsoyiannis and Montanari 2007; Potter 1976).

On the other hand, the presence of cross-correlation in a regional dataset could either "inflate" or "deflate" the actual number of significant trends in a region, and distort the outcome of certain statistical tests (Lettenmaier et al. 1994; Livezey and Chen 1983). Therefore, in this study, we used five variants of the MK tests to evaluate the effect of STP, LTP and large-scale climate anomalies on the trend identification of Canadian AMP and SMP, and then the field-significance of each regional trend test was estimated. In addition, possible change points of Canadian AMP and SMP time series were also estimated using the nonparametric, Pettitt test (Pettitt 1979) to further investigate their nonstationary characteristics. All trends and change points estimated were tested for their field-significance using the Walker test and the false discovery rate (FDR) method (Wilks 2006).

The chapter is organized as follows: Section 4.2 gives an overview of precipitation data used and large-scale climate anomalies in terms of climate indices; Section 4.3 describes the research methodology; Section 4.4 discusses the results and finally Section 4.5 the summary and conclusions.

4.2 Data

Given Canada is the second largest country in the world, its climate varies widely from the north (west) to south (east), and so to analyze changes to extreme Canadian precipitation can be challenging and has to be done on a regional basis. In this study, on the basis of provincial and geographical areas, we divided Canada into four regions (Figure 4-1), which are the Canada West, North, Centre and East. Then trends, change points and their field-significance were analyzed region by region. To investigate long-term changes in extreme precipitation, we analyzed precipitation data of AHCCD which is described in Section 3.2.1, using four different periods (the same as selected for study in Section 3.2.1) to assess uncertainties associated with

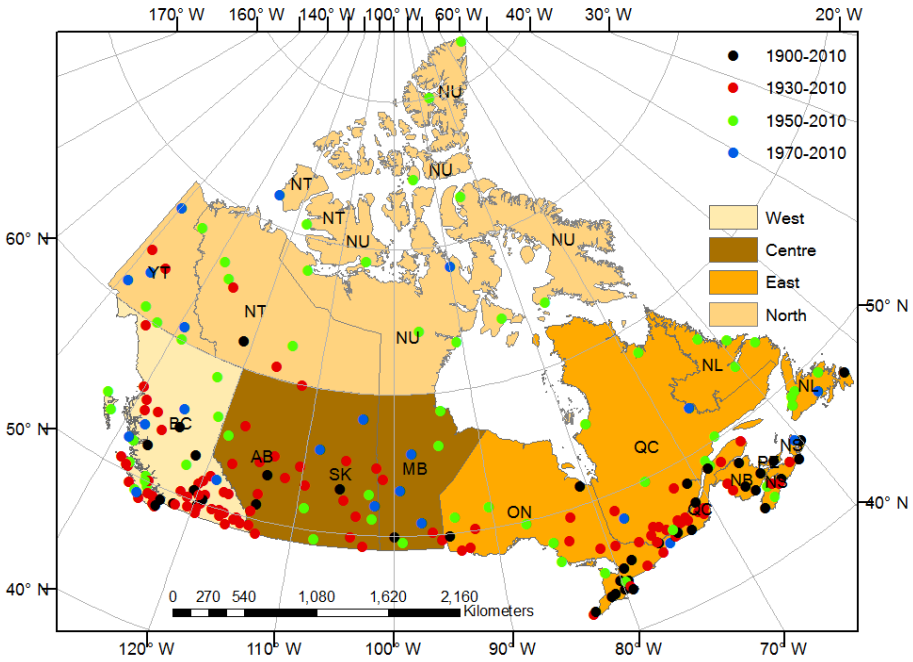

Figure 4-1 Map of Canada showing the spatial distribution of precipitation stations analyzed over four regions. Canada west includes BC; Canada Centre includes AB, SK and MB; Canada North includes YT, NT and NU; and Canada East includes ON, QC, NL, NB, PE and NS.

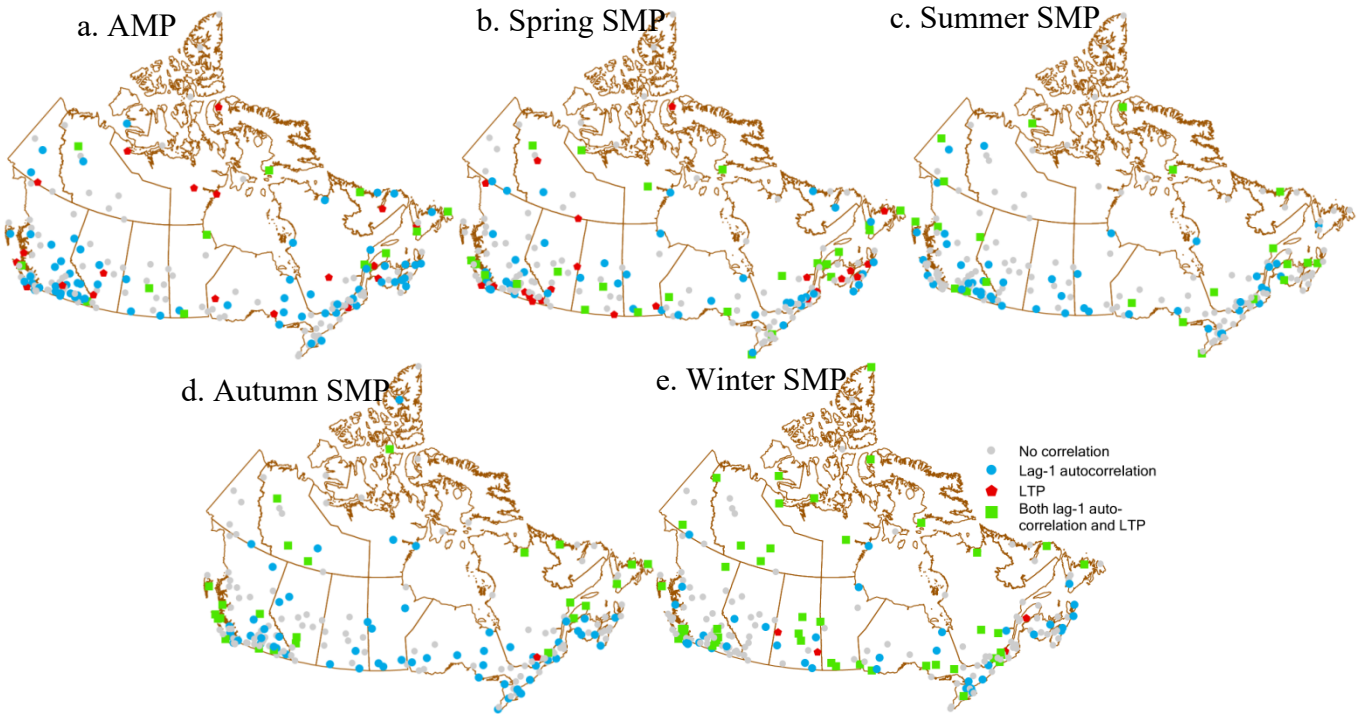

Figure 4-2 Maps showing the spatial distribution of stations with statistically significant lag-1 autocorrelations and LTP in AMP (a) and SMPs (b-e) of 1950-2010 at $p \leq 0.10$.

trends and change points estimated with respect to the length of historical record. AMP and SMP time series of spring (March-May), summer (June-August), autumn (September-November) and winter (December-February) were extracted from daily time series for each station studied. Four climate indices including Southern Oscillation Index (SOI), the North Atlantic Oscillation (NAO) index, the PDO index and the North Pacific (NP) index are described in Section 3.2.2.

4.3 Research methodology

The MK test has been widely used to detect statistically significant trends in time series of hydroclimatic variables (e.g., Dinpashoh et al. 2014; Ehsanzadeh and Adamowski 2010; Hamed 2008; Hamed and Rao 1998; Ishak et al. 2013; Khaliq et al. 2009a; 2009b; Sagarika et al. 2014; Yue et al. 2002; 2003), because it is non-parametric and it is robust to data that may contain outliers and non-linear trends. Five variants of the MK test, one change-point test and two field-significance tests were used to assess trends and change points in Canadian extreme precipitation. The most popularly used (regular) MK test (Kendall 1975; hereinafter referred to as regMK) was applied to estimate trends of AMP and SMP time series. The magnitudes of trends were estimated using the Theil–Sen approach (TSA) (Sen 1968). To eliminate the effect of serial correlations, the trend-free pre-whitening (TFPW) method developed by Yue et al. (2002) was first applied to remove the lag-1 serial correlation before applying the MK test (tfpwMK) to the time series, while the modified MK test proposed by Hamed and Rao (1998) and Yue and Wang (2004) (modMK) was based on a test statistic computed from an effective (instead of the actual) sample size to account for the effect of serial correlation. The MK test of Hamed (2008) (ltpMK) considering the influence of LTP was also chosen. The partial MK (partMK) test (El-Shaarawi 1993; Libiseller and Grimvall 2002) was used to examine the influence of climate anomalies on trends of AMP and SMP data. The nonparametric, Pettitt test (Pettitt 1979) that has been widely used for the change point detection of hydroclimatic data was also chosen because it is robust against outliers and data of skewed probability distributions (Tan and Gan 2015a; Villarini et al. 2009a; Wijngaard et al. 2003). The field-significance of trends and change points detected for the four regions were further evaluated using the Walker test and the FDR approach (Wilks 2006). Detailed descriptions of these methods are given in the above literature. All significance tests are based on the 10% significant level.

4.4 Results

4.4.1 Trends at local scales

Figure 4-2 and Figure S1 show the spatial distribution of stations showing statistically significant lag-1 autocorrelation and LTP in the AMP and SMP time series for the four time frames, while Figure 4-3 shows the percentage of stations with positive and negative lag-1 autocorrelation coefficient (ρ_1) and the percentage of stations where ρ_1 values are significant. There are more stations in southeastern and southwestern Canada showing significant lag-1 autocorrelation and LTP than other regions, especially for time series of 61-year (Figure 4-2) than for time series of 81-year periods. It seems that maximum precipitation data of some stations in southeastern and southwestern Canada tend to be correlated to data of the previous or the following years, even though such interannual autocorrelations are not because of carryover processes in the atmospheric system.

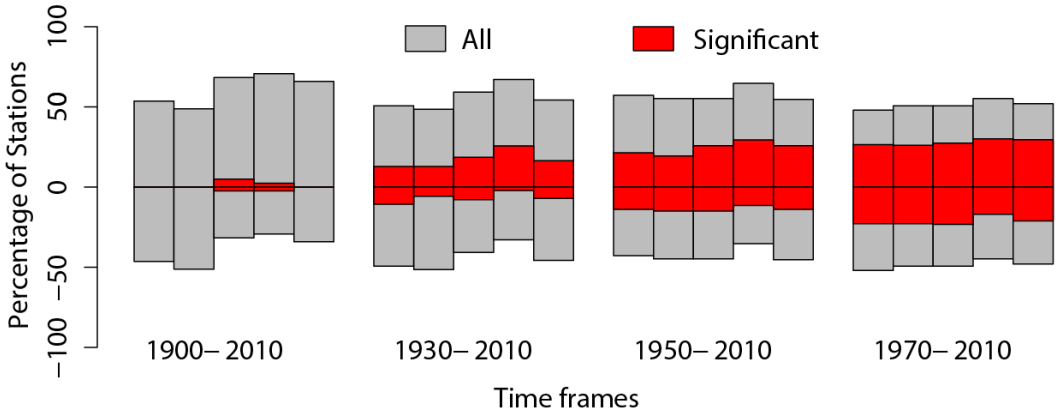

Figure 4-3 Percentage of stations with positive and negative (shown along positive and negative y-axis, respectively) lag-1 autocorrelation coefficient (ρ_1), along with percentage of stations showing ρ_1 values that are significant at $p \leq 0.10$ (red). The five columns for four time periods show the percentage of stations with ρ_1 for the AMP, spring, summer, autumn and winter SMPs, respectively.

The total (positive and negative) percentage of stations with significant ρ_1 values decreases with the length of time series, as the mean percentage of stations for the 41-, 61-, 81- and 111-year periods is 27.9, 24.4, 17.3 and 1.5%, respectively (Table 4-1). As expected, this implies that very few stations show consistent STP over extended periods. The percentage of stations showing significant positive ρ_1 values is ~10% higher than that with the negative ρ_1 values. This implies that marginally more stations exhibit consistent wet, dry or average climate longer than a year, which as mentioned above, depends on the length of each time series. However, the

percentages of stations showing significant LTP are similar in the four selected periods (Table S1). Seasonally, more winter SMP time series show significant LTP than other seasons, especially among time series of 81- and 111-year periods (Figure S1 and Table S1), while a similar percentage of stations shows significant ρ_1 values in all four seasons. Moreover, winter SMP data tends to show both significant ρ_1 values and LTP, while stations tend to show either a significant ρ_1 value or a significant LTP for AMP and spring SMP data. More stations show both STP and LTP during winters than other seasons probably because winter precipitation tends to be more related to large-scale climate patterns (Vincent et al. 2015).

Figure 4-4 and Figure S2 shows the percentages of stations that present positive and negative trends. Different regions (Figure S2) show different number of stations exhibiting trends estimated from various trend tests, which shows that the results of trend analysis are sensitive to the test adopted to eliminate the effect of serial correlation. The modMK test generally detected ~5% more percentage of stations showing significant trends in AMP and SMPs data than the regMK test for all periods studied, while the ltpMK test detected ~8% less percentage of stations than the regMK test. However, the difference in the percentage detected by the tfpwMK and regMK tests is minimal. The number of stations showing significant trends based on the four tests for stations showing significant lag-1 autocorrelation and LTP (Tables 4-1 and 4-2) demonstrates that the regMK test tends to underestimate (overestimate) of the significance of trends in time series showing significant lag-1 autocorrelation (LTP), compared to the modMK (ltpMK) test.

Without considering differences in results obtained from applying different tests, the percentage (average of the four tests) of stations showing significant trends increases with the length of periods studied (Figure 4-4), as the percentage varies from 16 to 42% for the 111-year period, 9 to 22% for the 41-year period partly because slow changes (trends) are more affected by climate fluctuations over short than extended periods probably because the effect of such fluctuations tend to be averaged out over extended periods. AMP, spring and autumn SMPs are dominated by positive trends that vary from 5 to 10% for the 41-year period, and 12 to 28% for the 111-year period. However, for summer and winter SMPs, there are large differences in the percentage of stations showing positive and negative trends between the four different periods. For example, winter SMP is dominated by positive trends for the 111-year period while negative trends for the other three periods studied. Summer SMP is dominated by positive trends for the

111- and 81-year periods while similar percentage of stations are detected with positive and negative trends for the 61- and 41-year periods. These inconsistent results with no clear spatial or seasonal patterns show that changes in maximum precipitation vary across Canada spatially and temporarily over a wide range of time scales, which are further compounded by uneven distributions of climate stations (predominantly in southern parts), different terrains, different study periods and diversified landuse covers across Canada.

Table 4-1 Comparison of the number of stations showing both statistically significant lag-1 autocorrelations at $p \leq 0.10$ and statistically significant trends in AMP and SMPs detected by the regMK, tfpwMK and modMK tests at $p \leq 0.10$

Time frames	1900-2010				1930-2010			
Test	Total*	regMK	tfpwMK	modMK	Total	regMK	tfpwMK	modMK
Annual	1	1	1	1	34	10	12	12
Spring	1	0	1	1	34	6	7	7
Summer	1	1	1	1	27	6	5	8
Autumn	4	2	1	1	38	14	11	15
Winter	3	1	1	1	40	16	12	17
	1950-2010				1970-2010			
Annual	81	16	18	22	114	19	15	28
Spring	72	16	19	20	111	16	15	22
Summer	70	10	10	16	110	18	16	31
Autumn	83	15	16	20	114	13	11	19
Winter	83	26	20	33	106	19	19	25

* Total is the number of stations showing statistically significant lag-1 autocorrelations at $p \leq 0.10$.

Table 4-2 Comparison of the number of stations showing both statistically significant LTP at $p \leq 0.10$ and statistically significant trends in AMP and SMPs detected by the regMK and ltpMK tests at $p \leq 0.10$

Time frames	1900-2010			1930-2010			1950-2010			1970-2010		
Test	Total	regMK	ltpMK	Total	regMK	ltpMK	Total	regMK	ltpMK	Total	regMK	ltpMK
Annual	7	6	3	20	11	5	34	12	1	39	16	1
Spring	7	4	2	18	9	2	32	17	3	38	13	0
Summer	3	2	0	17	11	2	22	7	1	23	9	1
Autumn	6	4	1	21	11	4	25	10	2	27	9	0
Winter	16	10	3	37	20	3	48	23	3	40	12	0

* Total is the number of stations showing statistically significant lag-1 autocorrelations at $p \leq 0.10$.

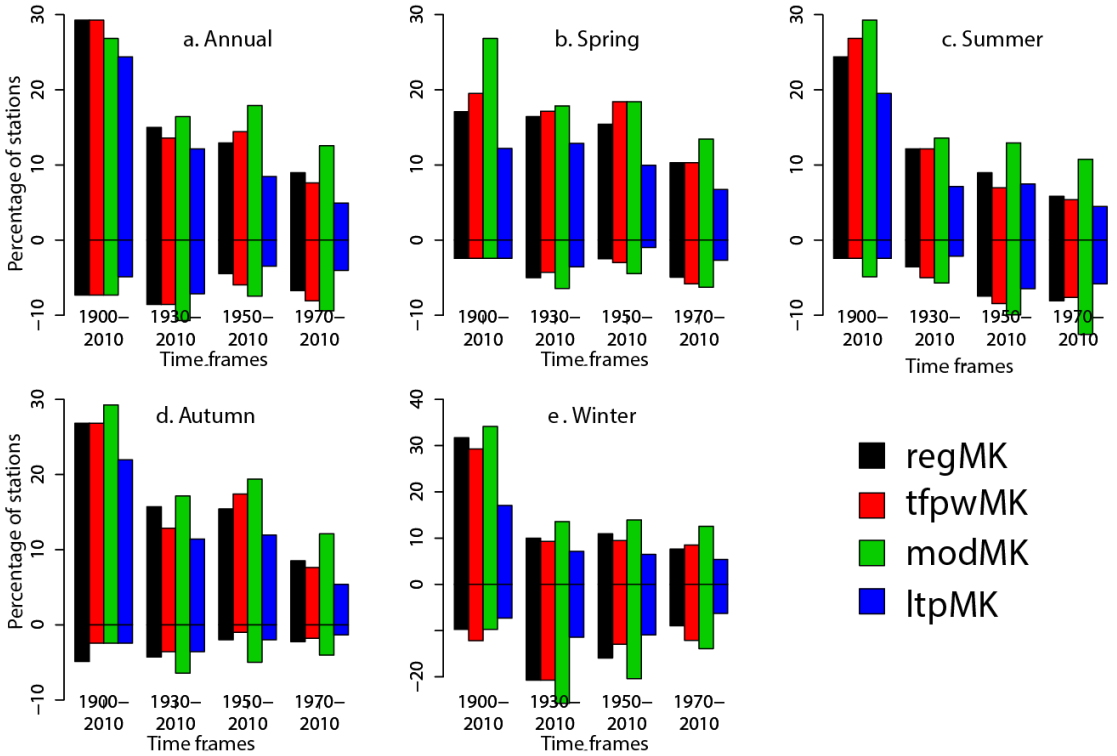

Figure 4-4 Percentage of stations showing statistically significant, positive and negative trends (plotted along the positive and negative y-axis, respectively) in AMP (a) and SMPs (b-e) time series of 1950-2010 detected by the regMK, tfpwMK, modMK and ltpMK tests at $p \leq 0.10$.

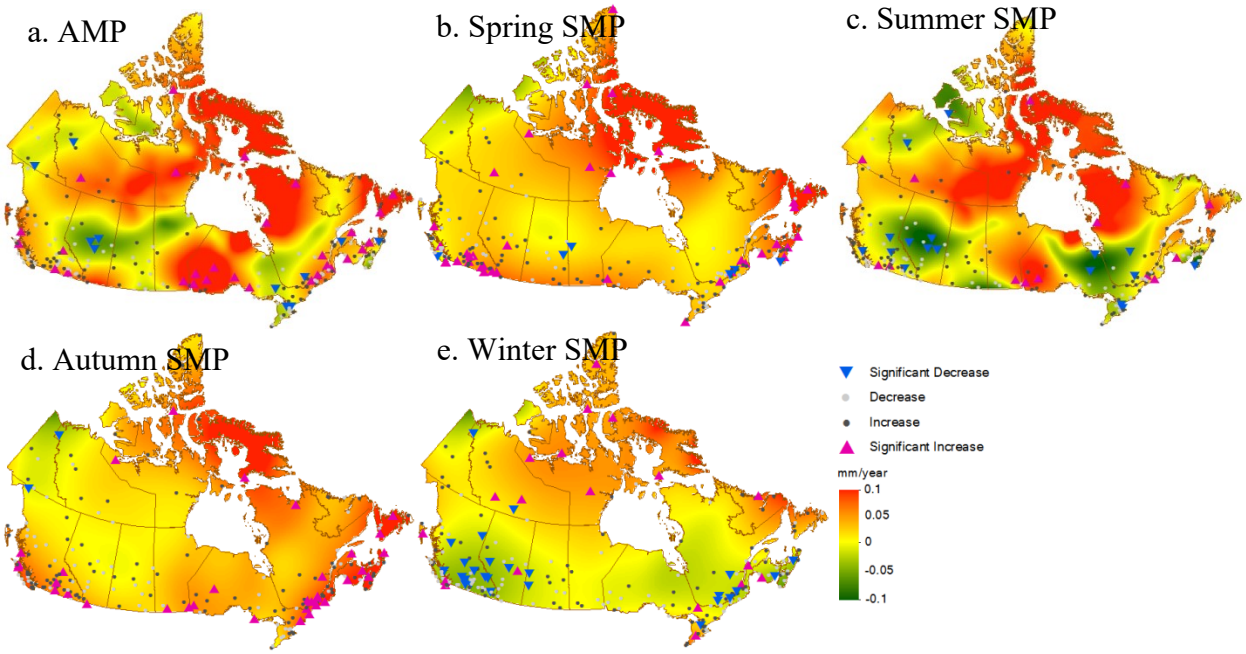

Figure 4-5 Maps showing trends in AMP (a) and SMPs (b-e) of 1950-2010 detected by the regMK test at $p \leq 0.10$. The red upward-pointing triangles indicate statistically significant while the green downward-pointing triangles indicate statistically significant trends at $p \leq 0.10$, respectively. Grey and black dots indicate stations with non-significant trends, respectively. The shaded color represents spatially interpolated trend magnitude in mm year^{-1} for AMP (a) and SMPs (b-e).

4.4.2 Spatial distribution of trends

Figure 4-5 and Figure S3 show the spatial distribution of stations showing significant trends in the 1950-2010 (61-year) and 1930-2010 (81-year) periods, respectively. Color maps of both significant and insignificant trends are given in these two figures which show some spatial differences in the magnitude of trends estimated for these two periods. For example, in terms of trend magnitude and number of stations showing significantly decreasing trends, the decreasing trends in AMP, summer and winter SMPs in the 61-year period are stronger than those in the 81-year period. However, the general spatial patterns of decreasing and increasing trends in AMP and SMPs are consistent between these two periods.

AMP had increased in western and southern British Columbia (BC), western Ontario (ON) and the Atlantic Maritime, but had decreased in Central Canada, eastern ON and western (Quebec) QC, and northwestern Canada. These findings are consistent with previous studies (e.g., Mekis and Hogg 1999; Zhang et al. 2001a). However, as expected, AMP trends detected are different from general increasing trends of total precipitation (e.g., Mekis and Vincent 2011; Zhang et al. 2000). The magnitude of trends estimated by the TSA shows 0.22 (0.25) mm year^{-1} of maximal increase (decrease) in AMP over the 61-year period.

Spatially, there are major differences between trends of spring SMP and AMP, such that the former generally shows increasing trends while the latter a mixture of increasing and decreasing trends. The spatial patterns of AMP and summer SMP are generally similar, as AMP is dominated by the summer SMP, with upward trends in the North and eastern Canada, and downward trends in the Canadian Prairies. Clusters of significant increasing trends for autumn SMP are found in western BC, Canada East and Canada North, even though increasing trend magnitudes in autumn SMP are relatively small compared to spring and summer SMPs. In contrast, decreasing (increasing) trends in winter SMP are more widespread across southern (northern) Canada, which agree with total snowfall trends found by Mekis and Vincent (2011) and Vincent and Mekis (2006). This may partly be explained by the positive (negative) snowfall-temperature relationship found by Davis et al. (1999) in northern (southern) Canada as warming occurs because increase in both winter precipitation and temperature tend to be more significant in northern than in southern Canada (Vincent et al. 2015).

4.4.3 Field-significance of the trends

To assess the possible influence of cross-correlation of AMP and SMP data of the stations on the field-significance of results we obtained, we first analyzed the cross-correlations between station AMP and SMPs data. The Pearson's product moment cross-correlation coefficient (PPMCC) (a parametric approach), the Kendall's rank cross-correlation (KRCC) (a nonparametric approach) and the Spearman's rank order cross-correlation coefficient (SRCC) (a nonparametric approach) were estimated considering all possible pairs of stations. The probability density distributions of the above coefficients are shown in Figure 4-6 for the four regions over the four periods studied. The PPMCC and SRCC coefficients are similar but higher than the KRCC coefficients. However, all three coefficients show that AMP and SMPs are dominated by positive cross-correlations represented by the probability distributions and the percentage of statistically significant cross-correlations, which indicate the necessity to use approaches such as the FDR approach and the Walker test that account for the effect of spatial correlation on the trend analysis results.

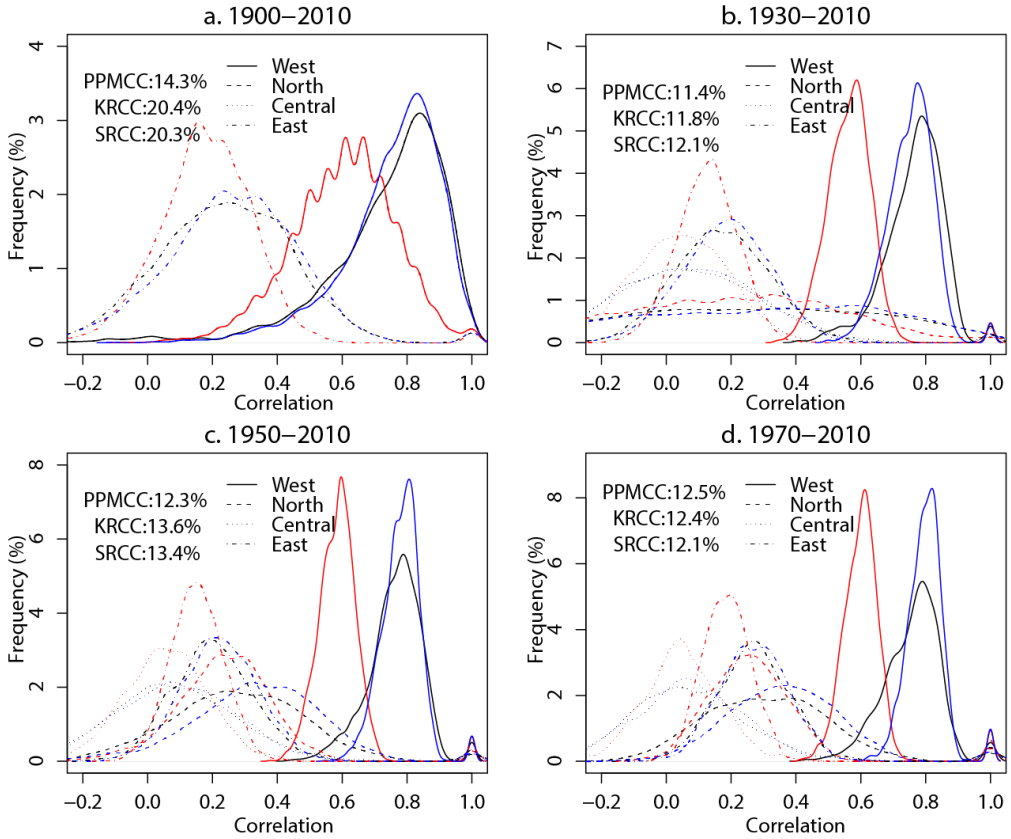

Figure 4-6 Probability distributions of Pearson's product moment cross-correlation (PPMCC, black color), Kendall's rank cross-correlation (KRCC, red color) and Spearman's rank cross-correlation (SRCC, blue color) of four regions over four periods, (a)-(d). The overall percentage of significant positive and negative cross-correlations obtained from all possible pairs of AMP and SMPs data are shown in each figure.

Table 4-3 shows results of trends with field-significance derived from the Walker test and the FDR approach for the 1950-2010 (61-year period), while Table S2 for 1930-2010 (81-year) and 1970-2010 (41-year). Similar results for the 1900-2010 (111-year) were not obtained because of the small number of stations involved. By the FDR approach, the trend result is considered to be of field-significance if at least one station shows field-significant trends. The FDR approach and the Walker test generally (>96%) declare consistent field-significance of trends in AMP and SMPs derived by the four tests conducted for four Canadian regions studied, which shows that the field-significance of trends detected by these four MK tests for these regions are not sensitive to the approach used for testing the field-significance.

These two approaches agree that locally detected trends for the 81-year period are generally of field-significance, but not so for the 61- and 41-year periods. For various MK tests, the trends detected by the ltpMK test are generally not field-significant for the four study periods. More trends derived by the modMK test are field-significant than those derived by the regMK test. In general, AMP and spring SMP data in the West and Canada East show more field-significant trends than SMPs in other regions.

4.4.4 Effects of large-scale climate anomalies on trend detection

Figure 4-7 and Figure S4 are scatterplots of the statistical significance (p-value) of trends ($p \leq 0.3$) derived by the regMK and the partMK tests for station AMP and SMPs data with four climate indices as covariates. The scatterplots are divided into four quadrants by two lines representing $p = 0.10$. Dots in the bottom right quadrant, marked as (1) represent stations where the trend of AMP or SMP is not statistically significant by the regMK test, but is significant by the partMK test which considers a climate anomaly as a co-variate. However, station AMP or SMP data in quadrant (1) do not covary with climate anomalies, whereas dots in the top left quadrant denoted as (2) indicate that station AMP or SMP data covary with climate anomalies because trends of such data are statistically significant by the regMK test but not so by the partMK test. Figure 4-7 shows that differences in p-values derived by the regMK and the partMK tests are evidence that winter SMP of Canada shows more significant relationships with large-scale climate indices than other seasons (Gan et al. 2007; Ropelewski and Halpert 1986; Shabbar et al. 1997; Zhang et al. 2010).

As similar number of stations was detected in quadrants (1) and (2) for the winter SMP of the 1930-2010, 1950-2010 and 1970-2010 periods (Figure 4-7), it means that there is no

significant difference in the number of stations showing significant trends with or without accounting for the effect of large-scale climate anomalies on the trend analysis (Table S3). This is partly because of the large spatial variation of relationships between Canadian precipitation and climate anomalies. Figure 4-7 shows that the four climate anomalies, SOI, NAO, PDO and NP, exert similar effects on trends of Canadian winter SMPs. On a whole, NAO exerted more significant influences on the trends of the summer and autumn SMPs, and is more significant for data of the 1950-2010 period. PDO exerted its effects on trends of AMP, spring and summer SMPs of some stations for the 1950-2010 period (Figure S4). Compared to the regMK test, the partMK test does not seem to change the field-significance of the station AMP, and SMP data of Canada.

Table 4-3 Number of stations showing field-significant trends detected by the FDR approach at $p \leq 0.10$ in AMP and SMPs detected by the regMK, tfpwMK, modMK and ltpMK tests, and the field-significance of local trends identified by the Walker test, for the period 1950-2010. A significant Walker test at $p \leq 0.10$ is indicated by a ''*" symbol and a nonsignificant test at $p \leq 0.10$ is indicated as "NS".

	Canada West (59)[a]		Canada North (24)		Canada Centre (32)		Canada East (86)	
	FDR	Walker	FDR	Walker	FDR	Walker	FDR	Walker
Annual								
regMK	**0**[b]	*	0	NS	0	NS	2	*
tfpwMK	**0**	*	0	NS	0	NS	2	*
modMK	0	NS	0	NS	0	NS	7	*
ltpMK	**0**	*	0	NS	0	NS	0	NS
Spring								
regMK	0	NS	6	*	0	NS	1	*
tfpwMK	1	*	7	*	0	NS	2	*
modMK	2	*	7	*	2	*	0	NS
ltpMK	0	NS	0	NS	0	NS	0	NS
Summer								
regMK	0	NS	1	*	0	NS	0	NS
tfpwMK	0	NS	1	*	0	NS	0	NS
modMK	0	NS	1	*	1	*	0	NS
ltpMK	0	NS	0	NS	0	NS	0	NS
Autumn								
regMK	0	NS	1	*	0	NS	4	*
tfpwMK	0	NS	0	NS	0	NS	4	*
modMK	0	NS	3	*	0	NS	0	NS
ltpMK	0	NS	0	NS	0	NS	1	*
Winter								
regMK	0	NS	12	*	0	NS	2	*
tfpwMK	0	NS	8	*	0	NS	2	*
modMK	0	NS	0	NS	4	*	0	NS
ltpMK	0	NS	3	*	0	NS	2	*

4.4.5 Change point tests

Figure 4-8 and Figure S5 shows the spatial distribution of stations showing significant change points in AMP and SMPs for the 1930-2010 and 1950-2010 periods, respectively. The years that significant and non-significant change points occurred are interpolated and presented by different colors in the figures. Table 4-4 summarizes the total number of stations showing significant local change points and their field-significance in four regions. There are significant variations in the timing (year) of detected change points and their statistical field-significance obtained from analyzing precipitation data of the four periods. For example, the average year that change points of winter SMP in Canada West and Canada Centre detected over 1930-2010 is ~15 years later than that detected over 1950-2010. The detected change points obtained for 1900-2010 and 1930-2010 are generally statistically field-significant while those obtained for 1970-2010 are mostly not field-significant. However, the percentage of stations individually showing significant increasing or decreasing change points is comparable for 1930-2010, 1950-2010 and 1970-2010. An increasing (decreasing) change point means that the mean value of the pre-change period is lower (higher) than that of the post-change period.

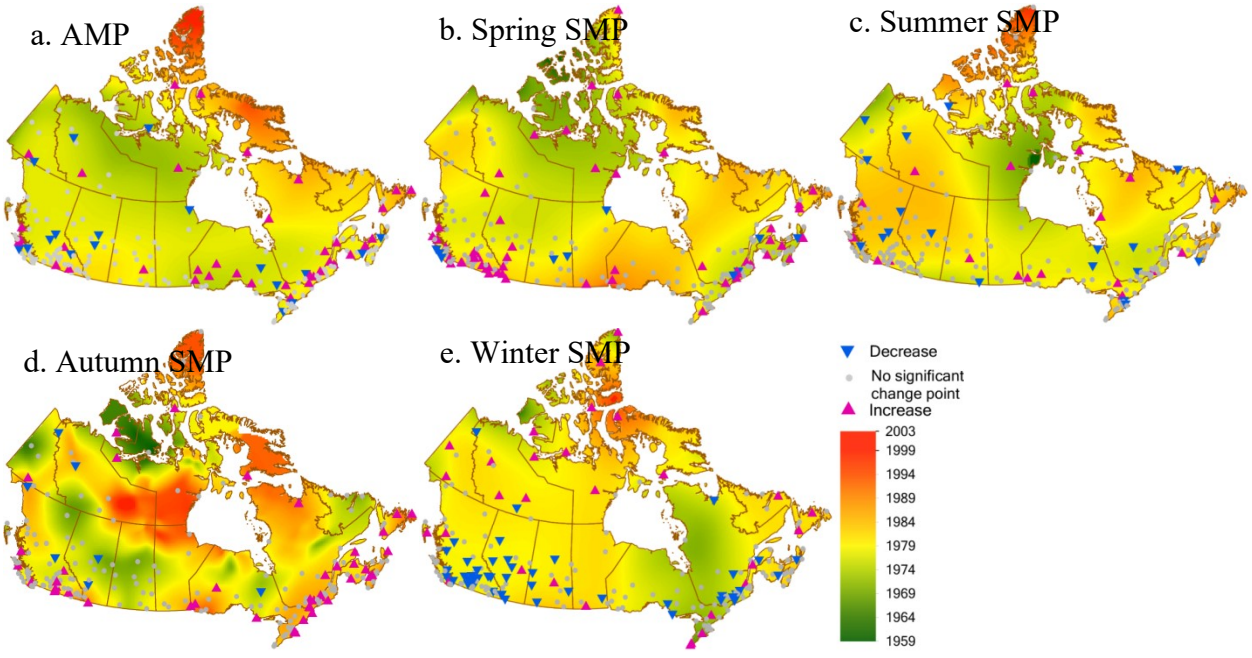

Figure 4-7 Maps showing change points of stations for AMP (a) and SMPs (b-e) of 1950-2010. The upward-pointing triangles represent increasing change points while downward- pointing triangles represent decreasing change points for various stations at $p \leq 0.10$. The shaded color represents spatially interpolated timing (years) of both significant and non-significant change points detected.

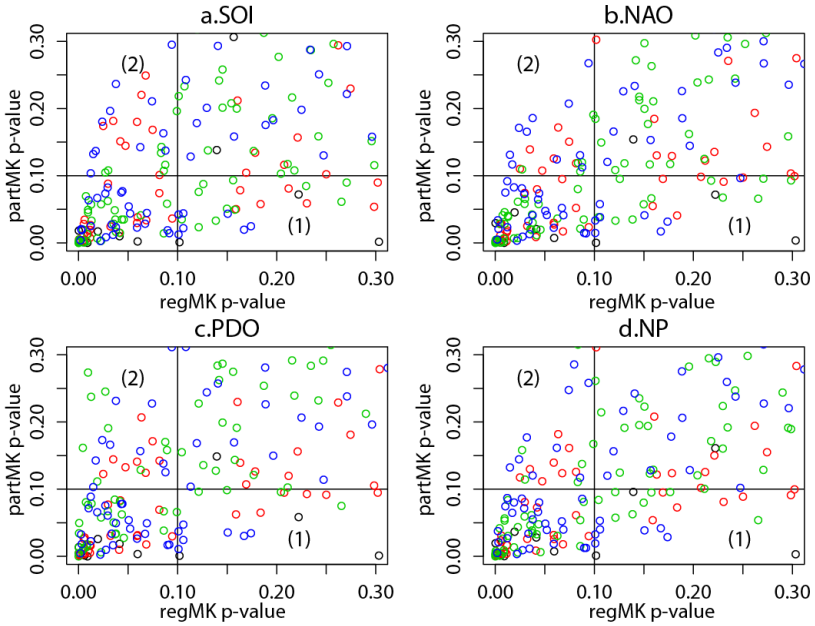

Figure 4-8 Scatterplots between statistical significance (*p*-value) of trends in winter SMPs for stations with $p \leq 0.30$ detected by the regMK test versus those detected by the partMK test with climate indices, SOI (a), NAO (b), PDO (c) and NP (d) as the covariates. The *p*-values obtained are represented by black for the 1900-2010, red for 1930-2010, green for 1950-2010 and blue for 1970-2010 periods, respectively.

Since there were not many stations with data spanning over the 1900-2010 period and data of the 1970-2010 period may not be long enough to detect a change point, only the overall results of change point analysis for 1930-2010 and 1950-2010 are further discussed. For the change point analysis of AMP data, field-significant change points are detected in all regions except in Canada West over the 1950-2010 period. The percentage of stations showing significant change points in AMP varies from 10.4 and 20.8% in Canada Centre and Canada West, to 35.4 and 37.3% in Canada North and Canada East, respectively. For AMP, Canada West is dominated by increasing change points while a comparable number of increasing and decreasing change points are found in the other three regions. The timing of change points occurred is relatively late in Canada West and Centre (around 1970-1980) compared Canada North and East (around 1960-1970), except in some parts of the Atlantic Maritime change points only occurred in around 1990-2000 (Figure 4-8a).

For the four SMPs, there are great variations in statistically significant change points detected across Canada. Spring and autumn SMPs tend to be dominated by increasing change points in all regions, while the summer SMP tend to have both decreasing and increasing change points. On the other hand, the winter SMP is dominated by significant increasing change points in northern Canada but decreasing change points in southern Canada. The percentage of stations

showing significant change points in winter SMP (42%) is relatively high compared to spring (32.0%), autumn (24.3%), summer SMPs (22.8%), and AMP (26.0%). The timing (year) of detected change points are similar between AMP and SMPs (Figure 4-9 and Figure S6). For the 1950-2010 analysis, most change points were detected during 1970-1990 even though among the four SMPs, there are significant spatial variations in the years change points are detected. For spring SMP, change points in Canada North and Centre occurred relatively early (around 1960-1975) than in Canada West and East (around 1980-1990). On a whole, Canada Centre (1960-1970) had experienced relatively early change points in autumn while Canada West late change points (around 1985-1995) in summer. For winter, change points that had occurred across Canada had been spatially homogenous in around 1975-1985, except for the region of Canada East.

Table 4-4 The number of stations in each region detected with statistically significant local increasing (↑) and decreasing (↓) change points at $p \leq 0.10$; the number of stations showing the field-significance at $p \leq 0.10$ detected by the FDR approach; and the field-significance of local trends identified by the Walker test, in which a significant test at $p \leq 0.10$ is indicated by a ''*" symbol and a nonsignificant test at 10% level is indicated as ''NS".

	Canada West				Canada North				Canada Centre				Canada East			
	↓	↑	FDR	Walker	↓	↑	FDR	Walker	↓	↑	FDR	Walker	↓	↑	FDR	Walker
1900-2010	9[a]				1				4				27			
Annual	1	3	3	*	0	1	1	*	0	0	0	NS	2	9	3	*
Spring	0	4	1	*	0	0	0	NS	0	0	0	NS	1	6	3	*
Summer	0	3	2	*	0	1	1	*	0	0	0	NS	1	5	4	*
Autumn	2	4	1	*	0	0	0	NS	0	0	0	NS	1	7	0	NS
Winter	2	4	0	*	0	0	0	NS	2	0	0	NS	2	11	11	*
1930-2010	48				6				24				62			
Annual	4	7	3	*	1	1	2	NS	1	1	1	*	8	16	3	*
Spring	4	11	8	*	0	0	0	NS	1	6	1	*	5	15	0	NS
Summer	0	6	1	*	1	2	0	NS	2	1	1	*	3	10	1	*
Autumn	5	8	0	NS	1	0	0	NS	5	3	0	NS	0	15	2	*
Winter	15	5	2	*	1	1	0	NS	10	0	0	NS	15	13	19	*
1950-2010	59				24				32				86			
Annual	5	6	0	NS	3	6	2	*	3	1	0	NS	7	24	4	*
Spring	3	18	3	*	0	9	5	*	3	7	0	NS	4	19	2	*
Summer	4	4	1	*	4	5	2	*	2	2	0	NS	8	9	0	NS
Autumn	2	9	0	NS	2	5	3	*	2	2	0	NS	1	27	4	*
Winter	18	3	2	NS	2	14	14	*	13	3	0	NS	14	9	5	NS
1970-2010	64				30				38				91			
Annual	6	5	0	NS	4	5	1	*	6	1	0	NS	7	16	0	NS
Spring	4	12	0	NS	3	5	0	NS	2	7	0	NS	9	8	0	NS
Summer	5	6	0	NS	1	3	0	NS	4	4	0	NS	6	8	0	NS
Autumn	2	2	0	NS	2	2	0	NS	4	1	0	NS	2	17	0	NS
Winter	15	4	0	NS	0	9	0	NS	4	9	1	*	13	4	0	NS

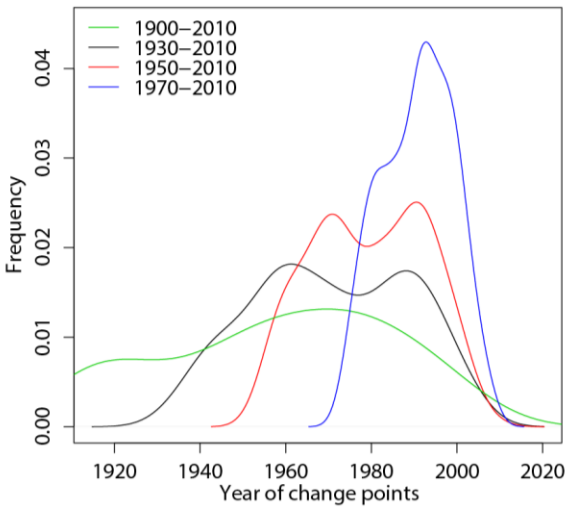

Figure 4-9 Temporal distributions of the timing (years) of both significant and non-significant change points detected for the four periods.

4.5 Discussions of results

4.5.1 Trend test for Canadian extreme precipitation

The presence of positive (negative) serial or inter-station correlations in a hydroclimatic time series inflates (deflates) the chance of falsely accepting a null hypothesis (no trend) even though significant trend exists (Douglas et al. 2000; Khaliq et al. 2009b). In other words, trend detection analysis may result in misleading results if we ignore strong serial or inter-station correlations of the data to be analyzed (Khaliq et al. 2008; 2009a). Moreover, some fluctuation behaviors in time series could be better explained by LTP instead of trends (Cohn and Lins 2005; Franzke 2010; 2012; 2013; Klemeš 1974; Koutsoyiannis 2003, 2006; Koutsoyiannis and Montanari 2007). Without accounting for the influence of LTP if it exists, a trend test may greatly overestimate the statistical significance of observed trends (Cohn and Lins 2005; Khaliq et al. 2008; 2009a). In this study, the percentage of stations showing significant trends in AMP and SMPs detected by the ltpMK test was ~8% less than that by the regMK test. 1/3 of stations that showed both significant lag-1 autocorrelation and trends in AMP and SMPs by the modMK test that considers the effects of STP, did not show significant trends if the regMK test was used. Persistence characteristics of SMPs were more prevalent in winter than in other seasons. Therefore, using modMK or ltpMK tests instead of the regMK test that assumes the data to be serially independent could make a difference to the trend analysis result.

Considering only the lag-1 autocorrelation may not be sufficient to remove all significant serial correlations in a time series (Dinpashoh et al. 2014; Kumar et al. 2009; Sagarika et al. 2014). However, using the modMK test that consider all form of serial correlations by an effective sample size approach resulted in more stations detected with significant trends in AMP and SMPs, than results obtained from using regMK and tfpwMK tests. Note that in the tfpwMK test, only time series of stations showing statistically significant lag-1 autocorrelations were trend-free pre-whitened before using the regMK test (Yue et al. 2002). However, using the modMK test always led to trend results different from the regMK test, irrespective of whether the serial correlation is statistically significant or not (Hamed and Rao 1998; Yue and Wang 2004). Conversely, results obtained from tfpwMK and modMK tests are expected to be different. Further, for AMP and SMP time series which exhibit negative autocorrelations (significant or not significant), significant trends may not be detected by using regMK and tfpwMK tests, but significant trends could be detected by the modMK test. For time series with positive autocorrelations, the tfpwMK test will tend to detect fewer stations with significant trends than the regMK test but not the modMK test which lead to more stations with significant trends. Overall, the modMK test detected more significant trends than regMK and tfpwMK tests because more stations exhibit positive than negative autocorrelations (Table S1).

Trend analysis results for extreme precipitation across Canada are also expected to be related to the impact of large-scale climate anomalies which could lead to drier or wetter conditions in different regions of Canada (Gan et al. 2007; Khaliq and Gachon 2010; Raible 2007; Ropelewski and Halpert 1986; Shabbar et al. 1997; Yin and Branstator 2008; Yiou and Nogaj 2004; Zhang et al. 2010). Even though overall the number of stations showing significant trends detected by the partMK test that considers the effect of climate indices generally do not differ much from results based on the regMK test, significant trends could be detected at some stations or some seasons by the regMK test but not detected by the partMK test, and vice versa. Thus, the partMK test can either be more, or less likely to reject the null hypothesis of no trend than the regMK and the partMK tests, which means that the influence of large-scale climate anomalies on the temporal trends of extreme AMP and SMP of Canada is likely haphazard. In other words, the temporal trend in AMP and SMP data of Canada may or may not covary with certain climate anomalies represented by climate indices over time, or their positive or negative relationships could “appear” or “disappear” or even interchange between positive and negative

relationships on a long-term basis (Coulibaly 2006; Coulibaly and Burn 2004, 2005; Gan et al. 2007). Therefore, the partMK test is not effective in detecting the influence of large-scale climate anomalies on the AMP and SMP of Canada this test only consider the monotonic, linear relationship between two variables.

4.5.2 Change point test for Canadian extreme precipitation

Results from the change point test show that more than 1/4 of the stations experienced a significant shift in AMP and SMPs. Decreasing (increasing) change points were spatially consistent with the negative (positive) trends (Figures 4-5 and 4-7). More stations were detected with significant change points than with significant trends for AMP and SMPs in Canada, and the characteristics of trends and change points vary from season to season, and spatially, clusters of increasing or decreasing change points were not as extensive as that of trends. Among the four seasons, winter seems to have experienced the most evident change in extreme precipitation for nearly half of the winter SMP of stations showed significant trends and change points. Even though this study was conducted for four different periods, on a whole significant change points are primarily detected between 1960 and 1990. However, differences in the spatial density and distribution of stations and different data length considered in the four periods result in uncertainties associated with the years change points were estimated. More reliable estimation of change points can be achieved if longer periods of AMP and SMP data, and/or more station data could be supplemented from other database.

There have been past studies on the effects of climate anomalies on precipitation and streamflow for various regions and river basins of Canada (e.g., Coulibaly 2006; Coulibaly and Burn 2004, 2005; Gan et al. 2007; Whitfield et al. 2010). Using wavelet analysis, Coulibaly and Burn (2004; 2005) found significant relationships between Canadian streamflow and climate anomalies such as ENSO and NAO after 1970s but not significant prior to 1950s, and were teleconnected to other climate anomalies in other time periods. Given that changes in the relationships between large-scale climate anomalies and regional climate and/or hydrology over the study periods could lead to the detection of change points in AMP and SMPs.

Because AMP and SMPs are affected by climate indices, their change points could also be related to the phase change of climate indices. McCabe et al. (2004) found that PDO shifted from the cold (warm) phase to the warm (cold) phase at about 1976 (2000), while Atlantic Multidecadal Oscillation (AMO) shifted from the warm (cold) phase to the cold (warm) phase

around 1963 (1995). Given more change points were detected in Canadian AMP and SMPs at around 1976 and 1963 (Figures 9 and S6), this likely means that change points of AMP and SMP were at least partly associated with shifts in PDO and AMO. Conversely, there are many clusters of change points associated with the transition between warm or cold phases of large-scale climate anomalies (Figures 8 and S5). Combined effects of some climate indices can contribute to the variability and prediction of AMP and SMP. For example, McCabe et al. (2004) also assessed the combined effects of PDO and AMO over four periods: PDO warm and AMO warm (1926-1943), PDO cold and AMO warm (1944-1963), PDO cold and AMO cold (1964-1976), and PDO warm and AMO cold (1977-1994). The change points detected in the Canadian AMP and SMP (Figures 8 and 9) can be partly attributable to these combined effects of phase changes in climate anomalies. For example, Canadian hydroclimate was found to be significantly correlated with PDO (Whitfield et al. 2010) and AMO (Assani et al. 2010).

Change points that represent shifts in climatic regimes are mostly of interdecadal time scale, as found in this study and other climate data (Alley et al. 2003; Sagarika et al. 2014). In contrast to a hydroclimate regime shift that will likely remain relatively constant until a new shift occurs, trends that are gradual changes attributed to global warming or interactions of the earth system tend to continue in the future (McCabe 2002; Mccabe and Dettinger 2002). In some sense, under a changing climate, identifying a shift in a climatic regime could be more important than estimating gradual changes in hydroclimatic predictions. In this study, relationships between change points and climate anomalies were purely derived from statistical analysis. A more vigorous investigation using more in-depth analysis of regional responses to one or more climate anomalies will be helpful to obtain more definitive conclusions on possible changes in climatic regimes in relation to the effect of climate anomalies and global warming.

4.6 Summary and conclusions

In this study, we did a comprehensive study on the analysis of trends and change points of AMP and SMP time series of 223 climate stations of Canada distributed over four regions for four different time periods. Monotonic trends were estimated from time series of AMP and spring, summer, autumn and winter SMPs, using variants of the non-parameteric MK test designed to account for the effects of STP, LTP and large-scale climate anomalies, while change points were detected by the non-parametric Pettitt test, with the following conclusions:

(1) For AMP, most regions in western and southern BC, western ON and the Atlantic Maritime experienced an increase but Canada Centre, eastern ON and western QC, and northwestern Canada generally experienced a decrease. As expected, SMPs could either increase or decrease and historical seasonal changes varied spatially and from season to season. However, trends of SMPs were more spatially coherent than those of AMP. Across Canada, there were more stations showing a significant increase in spring, summer and autumn SMPs than a decrease, while the winter SMP experienced a significant decrease (increase) over southern (northern) Canada;

(2) Trends detected using the tfpwMK, modMK and ltpMK tests differed from trends detected by the regMK test that assumes serial independence in a time series. As expected, the regMK test generally detected more significant trends than the ltpMK test that accounts for LTP. However, the number of significant trends detected by tfpwMK that only considers STP and regMK tests was comparable, while the modMK test that accounts for all form of serial correlations marginally detected more significant trends than the regMK test. The partMK test shows that the influence of large-scale climate anomalies on the detected trends of winter SMP were statistically significant;

(3) The Pettitt test detected more than 1/4 of the stations with a shift in the AMP and the four SMPs. Results of this test show that spring, summer and autumn, SMPs tend to experience more increasing than decreasing change points, but the reverse were detected in winter SMP. More stations had shown significant change points than trends in AMP and the four SMPs for all four regions of Canada. Compared to other seasons, winter had experienced more significant trends and change points in extreme precipitation, and most change points had occurred around 1960-1990;

(4) Based on results obtained from the Walker and FDR tests, trends and change points detected in 1900-2010 and 1930-2010 were mostly field-significant, even though spatial correlations between time series are statistically significant. Trends and change points detected in Canadian precipitation are likely associated the influence of large scale climate anomalies that vary spatially across Canada.

Chapter 5 Multifractality of Canadian precipitation and streamflow

5.1 Introduction

Precipitation and streamflow records represent valuable historical data for physical understanding of hydroclimatic patterns that have received considerable attention in the geophysical science in recent decades. In the last several decades, scaling and fractal behavior of some geophysical fields, e.g., streamflow, precipitation and temperature, has been widely studied (Kantelhardt et al. 2006; Labat et al. 2013; Lovejoy and Mandelbrot 1985; Lovejoy and Schertzer 1986; Matsoukas et al. 2000; Movahed and Hermanis 2008; Rego et al. 2013; Veneziano and Langousis 2005; Veneziano et al. 2006; Yu et al. 2014; Zhang et al. 2008; Zhang et al. 2009b). Many studies show that persistence is a common characteristic in climatological and hydrologic time series over a wide range of space-time scales. As the hydrological cycle is accelerated by global warming, there is a growing interest to model hydrologic extremes such as extreme precipitation, snowfall, flood and drought of river basins (especially ungauged) which could have significant impact to our environment and water security. For example, scaling and fractal properties of hydroclimatic time series are closely related to their nonstationary behavior, the frequency and severity of the occurrence of extreme events, etc.

Since Hurst (1951) first discovered long-term persistence (LTP) or long-term autocorrelation in hydrologic time series using the rescaled-range technique, many types of signals were found to exhibit complex behavior with LTP and/or nonstationary trends, e.g., DNA sequences (Peng et al. 1994), heart rate dynamics (Ivanov et al. 1999) and hydroclimatic time series mentioned above. Such complex behavior was generally characterized by the Hurst exponent (H) that quantifies the correlation property of a signal. Earlier scaling studies generally focused on the mean (first moment $F_1(s)$) or the variance (second moment $F_2(s)$) of the fluctuations in certain length segments, s. Furthermore, between monofractal and multifractal analysis, the latter is likely more appropriate for studying scaling properties of geophysical fields and time series, given geophysical phenomena can exhibit scaling behavior over a wide range of moments (Lovejoy and Schertzer 2007; Pandey et al. 1998; Tessier et al. 1996; Veneziano et al. 2006). Therefore, a wide range of moments $F_q(s)$ have to be analyzed to comprehensively characterize fluctuations of a time series.

Next, the presence of LTP represented by Hurst exponents may lead to spurious detections of trends in a signal. To eliminate the effect of trends in detecting LTP, Peng et al. (1994) introduced the detrended fluctuation analysis (DFA) to estimate *H* and to estimate scaling properties in monofractal and nonstationary time series. Since then, DFA has been widely applied to detect LTP in various time series (Kantelhardt et al. 2006; Koscielny-Bunde et al. 2006; Rybski et al. 2011). Kantelhardt et al. (2002) proposed the multifractal DFA (MFDFA), a modified version of DFA, to estimate multifractal properties of a time series. In this study, we applied both DFA and MFDFA to investigate the scaling behavior and multifractal spectrum of both daily precipitation and daily streamflow records which may or may not have trends. The multifractal properties of precipitation and streamflow time series are "fingerprints" that can be used in some hydrologic or climate models for re-constructing these time series.

Compared to classical statistical tests, sample uncertainties associated with statistical testing of a time series involving scaling or fractal behavior are generally larger (Kerkhoven and Gan 2011; Koutsoyiannis and Montanari 2007; Koutsoyiannis et al. 2007; Rybski et al. 2006). A typical sample of observed hydroclimatic data only represents a small portion of a population and so it may be difficult to accurately estimate properties of the population from the available data. Therefore, based on the hypothesis of short-term persistence (STP) and/or the assumption of independent and identically distributed variables, it will be difficult to use classical statistical methods to decipher processes characterized by LTP, or multifractal behavior. The detection of trends in a hydroclimatic time series with STP, LTP, or multifractal properties is affected by the presence of positive (negative) autocorrelation in that time series, which could increase (decrease) the probability of rejecting the null hypothesis (e.g., no trend) even when there is trend (Koutsoyiannis and Montanari 2007).

For Canada, there has been limited analyses conducted for detecting the scaling or fractal properties of precipitation and streamflow record, e.g., the scaling or fractal characteristics of daily snowfall (Shook and Pomeroy 2010) and summer daily rainfall (Shook and Pomeroy 2010) of the Canadian prairies had been examined. Gan et al. (2007) found that daily precipitation of southwestern Canada generally reveal two linear decay regions of different slopes separated by a breakpoint located approximately at 20 to 30 days, and different multifractal behavior of stations were detected because rainfall generating mechanisms vary from station to station. It will be useful to conduct a comprehensive analysis on the multifractal behavior of both precipitation and

streamflow data for the whole of Canada which can be divided into seven climatic zones, especially in recent years climate warming and human impacts have intensified the global hydrologic cycle, and so in recent years statistical properties of precipitation and streamflow of Canada might have experienced changes.

The objectives of this chapter are to detect: 1) multifractal properties of Canadian precipitation and streamflow data, 2) changes to multifractal properties of Canadian precipitation, and 3) effects of river regulation to multifractal properties of Canadian streamflow using DFA and MFDFA. The chapter is organized as follows: description of precipitation and streamflow dataset in Section 5.2, research methods using DFA and MFDFA in Section 5.3, discussions of results in Section 5.4, and summary and conclusions in Section 5.5.

5.2 Data

We analyzed long-term, daily precipitation records P_i of 100 stations and long-term daily streamflow records Q_i of 145 stations, which are representative of Canadian rivers and climatic zones (Figure 5-1). The precipitation records were taken from the 2nd generation, adjusted historical Canadian climate data with 463 stations of precipitation data statistically adjusted for known measurement issues such as wind under-catch, evaporation and wetting loss for each type of rain-gauge, snow water equivalent from ruler measurements, trace observations and accumulated amounts from several days (Mekis and Vincent 2011). Missing data were gap filled using data from nearby stations. This is likely the best long-term observed precipitation data currently available for Canada. Stations with more than 85 years by 2010, 2011 or 2012 were selected for this study. The length of stations ranges from 85 to 173 years, with an average of 106 years. Generally, precipitation measurements in northern Canada began much later than in southern Canada and so relatively few stations of long-term records are available in northern Canada (Figure 5-1). Detailed information of the dataset is given in Mekis and Vincent (2011).

The daily streamflow records taken from the HYDAT Database of Water Survey Canada were previously used for nonstationary analysis by Tan and Gan (2015a). The RHBN (Reference Hydrometric Basin Network) data included in HYDAT have been extensively used for climate change studies, since these data are characterized by relatively pristine and stable land-use conditions (<5% of landcover modified) and have a minimum of 20 years of record (Burn et al. 2010; Coulibaly and Burn 2004). 62 stations with at least 50 years of data, out of over 200 RHBN stations, were selected for this study. To ensure a large coverage of watersheds over

various geographic areas of Canada, another 83 non-RHBN stations from HYDAT, each with a minimum record length of 70 years and a maximum total missing length of 4 years were selected (Figure 5-1). River basins of non-RHBN stations could experience anthropogenic influence such as land use changes, river regulations, agricultural production and other human activities. Average lengths of RHBN and non-RHBN stations are 72 and 85 years, with a maximum length of 102 and 118 years, and an average drainage area of 9070 km^2 and 31,403 km^2, respectively. Stations are mainly selected from southern Canada and around the Rocky Mountain of British Columbia.

5.3 Methodology

5.3.1 Detrended fluctuation analysis (DFA)

DFA was applied to the anomaly of daily data by applying:

$$\varphi_i^P = P_i^j - \overline{P_j} \quad \text{and} \quad \varphi_i^Q = Q_i^j - \overline{Q_j} \tag{5-1}$$

where i = 1,…,N (N is the number of days in the record), the mean daily precipitation $\overline{P_j}$ or streamflow $\overline{Q_j}$ are the mean daily values computed for each Julian day j = 1,…,365/366, e.g., for j = 1, for 1st of January, etc. Equation (5-1) is then standardized by the standard deviation for each calendar date, i.e.,

$$\varphi_i^P = \frac{P_i^j - \overline{P_j}}{\sqrt{\overline{P_i^{j2}} - \overline{P_j}^2}} \text{ and } \varphi_i^Q = \frac{Q_i^{j2} - \overline{Q_j}}{\sqrt{\overline{Q_i^{j2}} - \overline{Q_j}^2}} \tag{5-2}$$

To avoid unnecessary repetitions, subsequent equations, each written only once, will represent both P and Q, e.g., applicable to both φ_i^P and φ_i^Q. Correlations between standardized precipitation or streamflow anomalies separated by s days are computed as:

$$C(s) \equiv \frac{\langle \varphi_i \varphi_{i+s} \rangle}{\langle \varphi_i^2 \rangle} = \frac{1}{(N-s)\langle \varphi_i^2 \rangle} \sum_{i=1}^{N-s} \varphi_i \varphi_{i+s} \tag{5-3}$$

where $\langle \bullet$ means the average is taken over all values of i. $C(s)$ that ranges from -1 to +1 decays with the lag in days, which can be represented by a power law relationship if the time series exhibits LTP,

$$C(s) \sim \quad , \ 0 < \gamma < 1 \tag{5-4}$$

For large lags with finite record length, $C(s)$ could be unstable and it may be difficult to achieve a reasonable estimate of $C(s)$. Further, a stationary time series with LTP can exhibit

persistent behavior with a tendency to remain more or less unchanged for a prolonged period, or could switch abruptly between positive or negative anomalies, which could complicate the distinction between trends and LTP (Koutsoyiannis and Montanari 2007). To overcome the aforementioned problems, we applied the DFA method developed by Peng et al. (1994) which consists of four steps:

Step 1: Determine the "profile"

$$Y(i) \equiv \sum_{k=1}^{i} \varphi_k \ , \quad i = 1, \cdots \tag{5-5}$$

of the data series φ_k of length N. The cumulative sum generates a nonstationary profile $Y(i)$.

Step 2: Divide the profile $Y(i)$ into $N_s \equiv \mathrm{int}(N/s)$ non-overlapping segments of equal length s. Since the length N is usually not a multiple of a chosen timescale s, very likely a small part will remain at the end of $Y(i)$. In order not to disregard this remaining part, the same procedure is repeated starting from the opposite end of $Y(i)$. Thereby, $2N_s$ segments are obtained altogether.

Step 3: Calculate the local trend for each of the $2N_s$ segments by least-square fitting a polynomial $p_v(i)$ of order n to the data and determine the variance

$$F^2(v,s) = \frac{1}{s} \sum_{i=1}^{s} \left[Y\left((v-1)s + i\right) - p_v(i) \right]^2 \tag{5-6}$$

for each segment v, v=1,…, $2N_s$. Linear, quadratic (n=1), cubic (n=2), or higher-order (n>2) polynomials can be used in fitting a segment. When linear polynomials are used, the DFA is called DFA1, for quadratic polynomials we have DFA2, for cubic polynomials DFA3, etc. In this study, DFA2 was used to remove quadratic trends in the profile $Y(i)$, which equals to removing linear trends in the original series φ_i. DFA2 was used partly because higher order polynomials, such as DFA3 and DFA4 could lead to over-fitting problems.

Step 4: Average the variance of all segments and take the square root to obtain the mean fluctuation function,

$$F(s) = \left[\frac{1}{2N_s} \sum_{v=1}^{2N_s} F^2(v,s) \right]^{1/2} \tag{5-7}$$

To find out how $F(s)$ changes with the timescale s, steps 2 to 4 for several timescale s were repeated. Apparently, $F(s)$ will increase with s. Since the correlation of φ_i follows a power law

relationship shown in Equation (5-4), $F(s)$ will increase with s in a manner represented by a power law function (Kantelhardt 2009; Peng et al. 1994),

$$F(s) \sim s^{h(2)} \text{ and } h(2) = \begin{cases} 1-\gamma/2, & \text{for } 0 < \gamma < 1 \\ 1/2, & \text{for } \gamma \geq 1 \end{cases} \tag{5-8}$$

This means when the autocorrelation function decreases faster than $1/s$ in time, asymptotically we have $F(s) \sim s^{1/2}$. Data with STP tends to undergo exponential decay, which means that in Equation (5-4), $\gamma > 1$ or by setting $h(2)=1/2$ when s exceeds the correlation time $\bar{s}$. If the time series φ_i is stationary, we can also apply standard spectral analysis techniques and calculate the power spectrum $S(f)$ as a function of the frequency f. The exponent β in the scaling law $S(f) \sim f^{-\beta}$ is related to $h(2)$ of $F(s)$ by $\beta=2h(2)-1$ (Ihlen 2012; Kantelhardt 2009; Kantelhardt et al. 2002; Rybski et al. 2011).

Movahed et al. (2006) and Movahed and Hermanis (2008) showed that for small scales where the sinusoidal behavior of a time series is not pronounced, $h(2) > 1$ indicates that the time series is non-stationary, and the relation between $h(2)$ for small scales and the Hurst exponent H is $H= h(2)-1$. For stationary time series, $h(2)$ for small scales is identical to H. Further, for uncorrelated series, H equals to 0.5; $0.5 < H < 1$ indicates long-term persistence; $0 < H < 0.5$ indicates short memory or anti-persistence. Hence we can use the value of $h(2)$ to determine whether a time series is stationary or nonstationary, and also to estimate its correlation, $C(s)$.

5.3.2 Multifractal detrended fluctuation analysis (MFDFA)

For multifractal time series, a single scaling exponent like $h(2)$ or γ cannot completely characterized the record, since many subsets of the series have different scaling behavior, e.g., large fluctuations are less correlated than small fluctuations (Ihlen 2012; Kantelhardt et al. 2002). To study multifractal scaling properties, we use the MFDFA proposed by Kantelhardt et al. (2002). In this procedure, the variance $F^2(v, s)$ in Equation (5-7) is replaced by its $q/2$-th power and the square root is replaced by the $1/q$-th power, where $q \neq 0$ is a real parameter,

$$F_q(s) = \left[\frac{1}{2N_s} \sum_{v=1}^{2N_s} \left[F^2(v,s) \right]^{q/2} \right]^{1/q} \tag{5-9}$$

Analogous to Equation (5-8), the generalized fluctuation exponent $h(q)$ is defined as

$$F_q(s) \sim s^{h(q)} \tag{5-10}$$

where $h(1)$ corresponds to the classical Hurst exponent H determined by the rescaled range analysis, and MFDFA and DFA are the same if $q = 2$, given as $h(2)$ in Equation (5-8).

For a monofractal time series, $h(q)$ is independent of q, since the scaling behavior of the variance $F^2(v, s)$ is identical for all segments v. On the other hand, if small and large fluctuations scale differently, $h(q)$ will depend on q. For positive (negative) values of q, the segments v with large (small) variance $F^2(v, s)$ will dominate $F_q(s)$, and $h(q)$ describes the scaling behavior of segments with large (small) fluctuations. $h(q)$ of Equation (5-10) are directly related to the classical Renyi exponent $\tau(q)$ via (Kantelhardt et al. 2002):

$$h(q) = \left[\tau(q) + 1\right] / q \tag{5-11}$$

such that the basic Renyi exponent $\tau(q)$ can be calculated for both negative and positive q values.

5.3.3 Other related multifractal formalisms

In geophysics, other multifractal indicators that are related to $h(q)$ are:

(1) The "generalized variogram" $C_q(s)$ is defined as,

$$C_q(s) \equiv \left\langle \left| Y(i+s) - Y(i) \right|^q \right\rangle \sim s^{K(q)} \tag{5-12}$$

Olsson (1995) showed that $h(q)$ and the moment scaling function, $K(q)$ are related by

$$K(q) = qh(q) \tag{5-13}$$

(2) In some geophysics and turbulence papers (Lovejoy and Schertzer 2007; Pandey et al. 1998; Tessier et al. 1996), the structural function

$$S_q(s) \equiv \left\langle \left| \varphi_{i+s} - \varphi_i \right|^q \right\rangle \sim s^{\varsigma(q)} = s^{qH(q)} \tag{5-14}$$

was analyzed without employing the profile $Y(i)$ as done in Equation (5-6) and (5-12). It can be shown that $H(q)$ is related to $h(q)$ by

$$H(q) = \varsigma(q)/q = h(q) - 1 \tag{5-15}$$

The multifractal exponent $H(q)$ defined by Davis et al. (1994) and the exponent $h(q)$ defined in the MFDFA method of Kantelhardt et al. (2002) in Equation (5-10) differ only by 1, because MFDFA analyzes the cumulative sum of φ_i or $Y(i)$, while Davis et al. (1994) analyzed φ_i directly.

(3) A multifractal series can also be characterized by a singularity spectrum $f(\alpha)$ related to $\tau(q)$ via the Legendre transform,

$$\alpha = \frac{d\tau(q)}{dq} \quad \text{and} \quad f(\alpha) = q\alpha - \tau(q) \tag{5-16}$$

Here, α is the singularity strength or the Hölder exponent, while $f(\alpha)$ represents the dimension of a subset of a time series characterized by α. From Equation (5-11), α and $f(\alpha)$ are related to $h(q)$,

$$\alpha = h(q) + q\frac{dh(q)}{dq} \quad \text{and} \quad f(\alpha) = q\left[\alpha - h(q)\right] + 1 \tag{5-17}$$

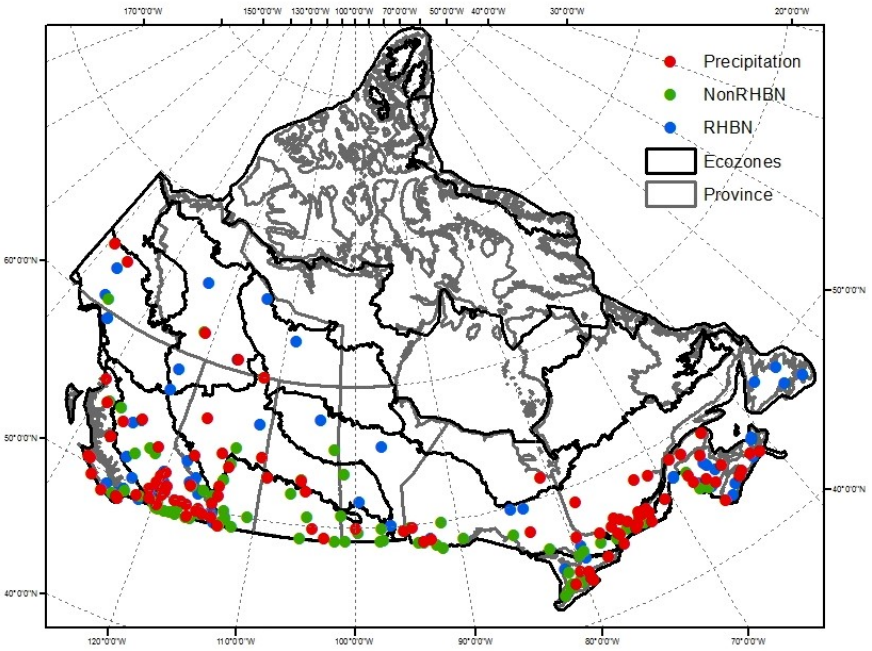

Figure 5-1 A map of Canada showing precipitation and streamflow stations selected for this study.

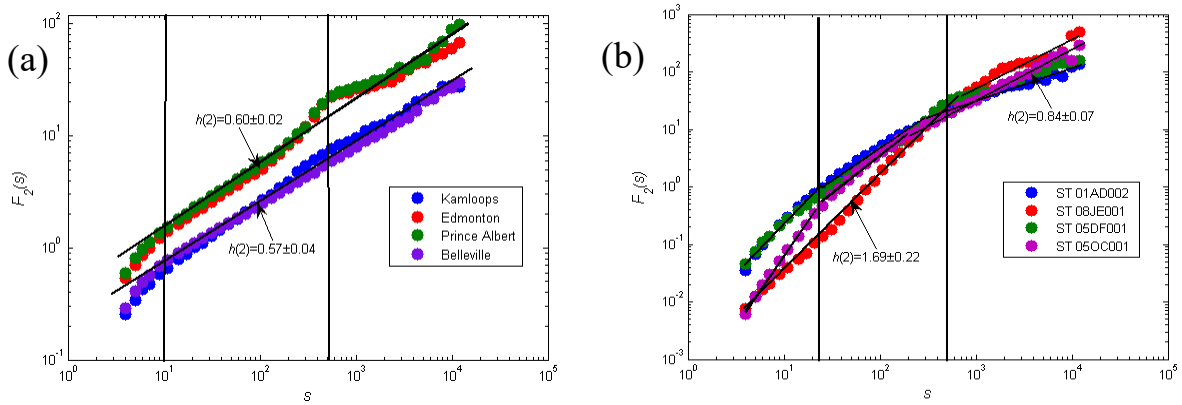

Figure 5-2 Fluctuation functions $F_2(s)$ versus timescale s obtained from a DFA2 analysis for four sets of representative precipitation (a) and streamflow records (b).

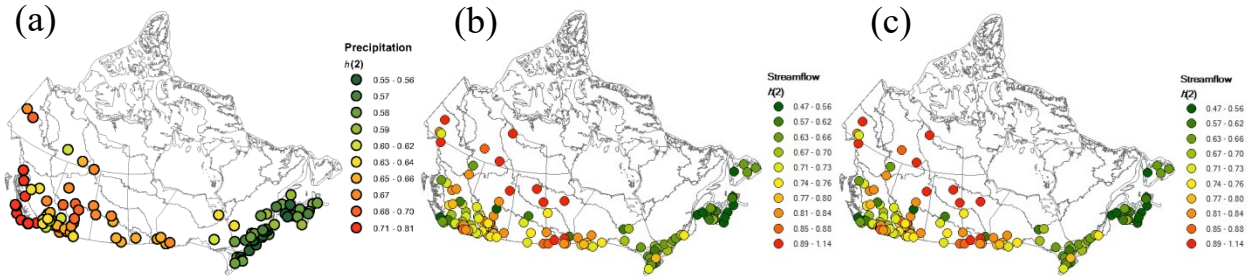

Figure 5-3 The spatial distribution of generalized Hurst exponents $h(2)$ for all 100 daily precipitation records (a) and all 145 daily streamflow records (b and c). $h(2)$ of streamflow data have been obtained from power law fits of fluctuation functions for (b) small ($4 < s < 300$ days) and (c) large ($400 < s < 12000$ days) timescales, while $h(2)$ of precipitation data were obtained for (a) time scales of $4 < s < 12000$ days.

The multifractal strength of a time series is characterized by the difference between the maximum and minimum singularity strength of α, $\Delta\alpha = \alpha_{max} - \alpha_{min}$. To find α_{max} and α_{min}, $f(\alpha)$ is set to 0.

In general, there are two types of multifractality in time series (Kantelhardt et al. 2002): (1) multifractality due to a broadening of the probability density function (PDF) of the time series, which cannot be removed by shuffling the series, (2) multifractality due to different correlations in small and large scale fluctuations of the time series that have a PDF with finite moments. In the latter case, the shuffled time series will show monofractal scaling because all long-term correlations are destroyed by the shuffling procedure. Therefore, the easiest way to clarify the type of multifractality is to analyze the corresponding shuffled time series. If the multifractality is only due to long-term correlation, $h_{shulf}(q) = 0.5$. However, the multifractality nature due to the broadening of the PDF is not affected by the shuffling procedure. However, if both kinds of multifractality are present, the shuffled series will show a weaker multifractality when compared to the original time series.

5.4 Results and discussion

5.4.1 Long-term persistence (LTP)

We did a large scale DFA2 and MF-DFA2 analysis on 100 stations of daily precipitation and 145 stations of daily streamflow time series. Figures 5-2a and 5-2b show fluctuation functions $F_2(s)$ obtained from DFA2 for four representative daily precipitation records and four streamflow records, respectively. There are differences in fluctuation properties between precipitation and streamflow time series. The log-log plots for precipitation are approximately straight lines on time scales larger than 10, with some obvious deviations at time scales (s) smaller than 10 days (Figure 5-2a), which could be caused by some kinds of artifact (Kantelhardt

et al. 2001). These results concur with that of Kantelhardt et al. (2006), who analyzed 99 stations of daily precipitation records collected from different continents, but they differ from results of Gan et al. (2007) who applied a power spectral analysis to daily precipitation of southwestern Canada and found crossovers approximately at a timescale of 20 to 30 days. The differences may be caused by trends in the time series (Zhang et al. 2014a), or by using two different methods, DFA and spectral analysis (Kantelhardt et al. 2001). For time scales larger than 10 days, fluctuation functions of these four precipitation records show a power law behavior with exponents $h(2) \approx 0.60$. From analyzing 9 precipitation records of United States of 15 min resolution, Matsoukas et al. (2000) found a crossover at around 5-10 days. Similar scaling properties on time scales less than 10 days were also detected from high temporal resolution (1 min to hourly) precipitation data by others (de Montera et al. 2009; Deidda et al. 1999; Olsson 1995; Tessier et al. 1996; Verrier et al. 2011). Crossover behavior in precipitation time series usually represents different precipitation generating mechanisms under different temporal scales, such as convective or stratiform storms (Gan et al. 2007; Lovejoy and Mandelbrot 1985; Matsoukas et al. 2000). Because we do not have precipitation data of high temporal resolutions, we did not attempt to analyze scaling properties of Canadian precipitation at time scales less than 10 days.

In contrast to precipitation data, streamflow data showed a pronounced crossover at time scales of 1-2 weeks and about 120-205 days. Similar crossover at time scales of several weeks, which is approximately the time scale of Rossby waves (Laštovička et al. 2003), were also detected by other studies for daily streamflow (Kantelhardt et al. 2006; Koscielny-Bunde et al. 2006; Rego et al. 2013; Zhang et al. 2008; Zhang et al. 2009b). Crossovers at time scale of about 120-250 days could be related to rain-induced and snowmelt-induced streamflow cycles, for different streamflow generating mechanisms could lead to different spatial and temporal scaling behavior (Gan et al. 2007). Beyond a time scale of 120-250 days, the fluctuation functions of streamflow showed a power law behavior with exponents $h(2) \approx 0.84$, while at time scales between 1-2 weeks and 120-250 days, $h(2) \approx 1.69$. For time scales less than 1-2 weeks, $h(2)$ were even larger than 1.69. Given that $h(2)$ for streamflow data were mostly larger than 1, it means that streamflow time series were generally nonstationary. Therefore for time scales less than 120-250 days, with $h(2) > 1$, we found that Hurst exponent H (= $h(2)$-1) ranges from 0 to 0.99, with an average of 0.37 for all the streamflow data analyzed in this study.

Figure 5-3 shows the spatial distribution of $h(2)$ obtained from applying DFA2 on 100 stations of precipitation records at time scales $4 < s < 12000$ days (Figure 5-3a); on 145 stations of streamflow records at time scales of $4 < s < 300$ days (Figure 5-3b), and $400 < s < 12000$ days (Figure 5-3c), respectively. We investigated scaling exponents $h(2)$ of streamflow data for two sets of time scales because of large differences between scaling properties of streamflow of small and large time scales. All 100 stations of precipitation records exhibited long-term persistence ($0.55 < h(2) < 0.81$), which agrees with Gan et al. (2007) who found $0.56 < h(2) < 0.67$ for 21 stations of weekly precipitation data of southwestern Canada; with Matsoukas et al. (2000) who found $0.6 < h(2) < 1.0$ for precipitation of USA of 15 min to 16 months of time resolutions; with Kantelhardt et al. (2006) who got $0.50 < h(2) < 0.56$ for Germany daily precipitation records at time scales greater than 30 days; and Peters and Christensen (2002) and Peters et al. (2001) who got $h(1) \approx 0.76 > h(2)$ for radar precipitation data of Germany at time scales ranging from 1 to 30 min.

Figure 5-3a shows spatial distributions of $h(2)$ for Canadian precipitation, which essentially reflects different climatic regimes and geographical factors such as topography, landcover, soil types, etc., of Canada. Daily precipitation of eastern Canada predominantly exhibits weak LTP, while that of central and western Canada show strong LTP (Figure 5-3a). On the other hand, spatial distributions of $h(2)$ of streamflow records are related to time scales considered. Similar to precipitation records, at large time scales (Figure 5-3c), most streamflow records of western and central Canada exhibited significant LTP, while streamflow records of eastern Canada showed weak or no LTP. $h(2)$ for streamflow records of northern Canada were significantly higher than that of southern Canada. It is interesting that west coastal region of Canada showed highest $h(2)$ values for precipitation but relatively low or medium $h(2)$ for streamflow at large time scales. At small time scales (Figure 5-3b), $h(2)$ for streamflow were mostly larger than 1, except for six stations located in eastern Canada where streamflow $h(2)$ was less than 1. This means that at small time scales, streamflow data are mostly nonstationary ($h(2) > 1$) but streamflow series that show LTP mostly come from northern Canada where Hurst exponents H ($= h(2) - 1$) ranged from 0.5 to 0.99. Generally, $h(2)$ of Canadian streamflow varied more spatially than Canadian precipitation. This is expected given scaling properties of streamflow are generally affected by various climatic, geographic and anthropogenic factors more than precipitation. For example, Koscielny-Bunde et al. (2006) found that streamflow data

with significant contributions from snowmelt are less auto-correlated than streamflow that are predominantly rain fed. More comprehensive analyses are needed to confirm factors that influence scaling properties of Canadian streamflow.

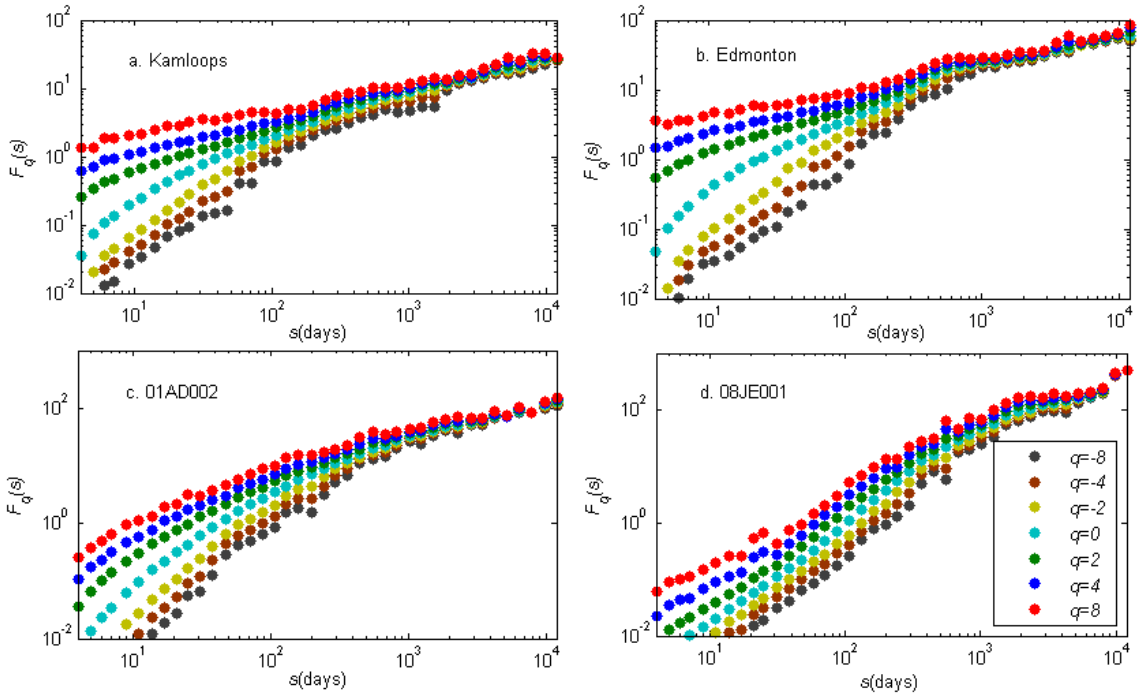

Figure 5-4 Fluctuation functions of four sets of precipitation (a and b) and streamflow (c and d) records for different *q*-order moments.

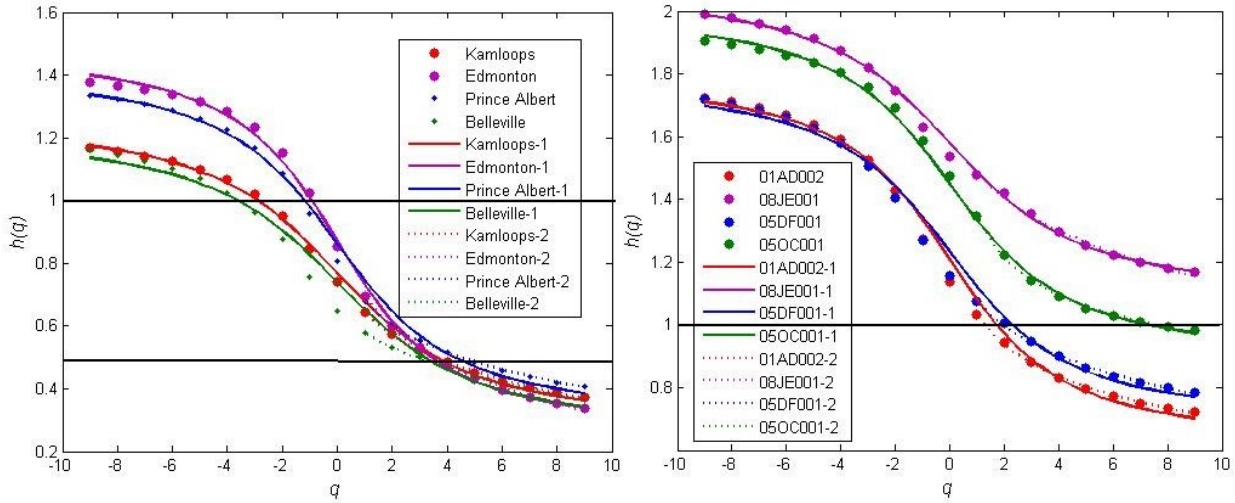

Figure 5-5 Generalized Hurst exponents *h*(*q*) fitted to Equations (5-18) and (5-19), for representative precipitation (a) and streamflow (b) records.

5.4.2 Multifractal characterization

In this section, analytical relations are developed to characterize multifractal behavior of 100 daily precipitation and 145 daily streamflow records of Canada. Figure 5-4 shows examples of MF-DFA2 fluctuations $F_q(s)$ for precipitation data of Kamloops and Edmonton, and streamflow data of stations, 01AD002 (Saint John River at Fort Kent) and 08JE001 (Stuart River near Fort St. James). Figures 5-4c and 5-4d show that before crossovers, slopes of $F_q(s)$ versus s for these two stations tends to decrease as s increases, and more so for negative than for positive q moments. However, there were also significant crossovers for precipitation data under negative q-order moments at time scale of approximately 500-600 days. Differences between q-order $F_q(s)$ for positive and negative q's are generally more obvious at small than at large time scales. From fitting $F_q(s)$ functions with linear regression lines in the double logarithmic space for each q-order at time scales $4 < s < 12000$ days, the slope of these regression lines represent the $h(q)$ for these time series. Moving from high positive toward high negative q-order moments, these slopes increased significantly, which are signatures of multifractality (Figure 5-5). For example, for precipitation of Edmonton (Figure 5-5a), the slope changes from 0.40 for q=9 to 1.33 for q=-9. For the streamflow at Stuart River near Fort St. James (Figure 5-5b), the slope changes from 0.67 for q=9 to 1.99 for q=-9. Similar to DFA2 results, on an average, $h(q)$ of streamflow are larger than that of precipitation.

Figure 5-5 also shows two models developed to describe multifractality (Equations 5-18 and 5-19) fitted to $h(q)$ results derived from MF-DFA. First, the universal multifractal equation of Kantelhardt et al. (2006):

$$\begin{aligned} K(q) &= \frac{C_1}{\alpha' - 1}\left(q^{\alpha'} - q\right) \\ h(q) &= H' + 1 - \frac{C_1}{\alpha' - 1}\left(q^{\alpha'-1} - 1\right) \quad \text{for } q \geq 0 \end{aligned} \tag{5-18}$$

with three parameters H', C_1 and α', that has been widely used to describe multifractal behavior of rainfall and runoff records at smaller time scales (Kantelhardt et al. 2006; Koscielny-Bunde et al. 2006; Rego et al. 2013; Rybski et al. 2006; Schertzer and Lovejoy 1989; Tessier et al. 1996; Yu et al. 2014). $H' = 0$ and $H' \neq 0$ mean that fluctuations are scale independent and scale dependent, respectively. In Equation (5-18), because C_1 is a numerator while α' a denominator, their numerical values have opposite effect to $K(q)$ and $h(q)$, e.g., small α' and/or

large C_1 are indicative of tendencies to large fluctuations in the data, while large α' and/or small C_1 are indicative of greater temporal homogeneity (Koscielny-Bunde et al. 2006; Shook and Pomeroy 2010; 2012). Values of the three parameters are listed in Tables S1 and S2 for all precipitation and streamflow records analyzed in this study, respectively. Equation 5-18 was applied only to positive q-order moments and dashed lines in Figure 5-5 represents best fit lines to $h(q)$ versus q.

Figures 5-6a-6c and 5-6g-6i show histograms of H', C_1 and α' derived for all precipitation and streamflow data selected for this study, respectively. In terms of $Mean \pm 1\, Std.Dev.$, $H' = -0.27 \pm 0.08$, $C_1 = 0.15 \pm 0.05$ and $\alpha' = 1.10 \pm 0.14$ for precipitation, and $H' = 0.15 \pm 0.16$, $C_1 = 0.13 \pm 0.04$ and $\alpha' = 1.04 \pm 0.15$ for streamflow data. Tessier et al. (1996) reported $H' = -0.35 \pm 0.20$ for precipitation records and $H' = -0.05 \pm 0.2$ for streamflow records of France. Pandey et al. (1998) obtained $H' = -0.03 \pm 0.14$ for streamflow records in 19 river basins of USA. Kantelhardt et al. (2006) obtained $H' = -0.45 \pm 0.06$ for precipitation records and $H' = -0.25 \pm 0.10$ for streamflow records over Germany. The above values are slightly lower than those derived from Canadian precipitation and streamflow data in this study. Similarly, our C_1 values are similar to the above studies, but our α' are much lower than the above studies. Tessier et al. (1996) and Kantelhardt et al. (2006) concluded that differences between H' for precipitation and streamflow ($\Delta H'$) are about 0.3 and 0.2, respectively, while we found $\Delta H'$ to be about 0.4.

However, C_1 and α' are more important parameters than H' to characterize multifractal properties of climate data shown by $h(q) \sim q$ curves (Kantelhardt et al. 2006; Koscielny-Bunde et al. 2006; Lovejoy and Schertzer 1986; Schertzer and Lovejoy 1989; Shook and Pomeroy 2010; 2012; Tessier et al. 1996). Previous studies reported ranges of C_1 and α' are 0.01~0.20 and 1.40~2.00, respectively (Kantelhardt et al. 2006; Koscielny-Bunde et al. 2006; Pandey et al. 1998; Tessier et al. 1996). Our average C_1 and α' values for precipitation and streamflow only differ marginally, $\Delta C_1 \approx 0.02$, $\Delta \alpha' \approx 0.06$, even though the distribution of their histograms are not similar (Figure 5-6). However, streamflow fluctuations are generally higher than precipitation because streamflow data is rarely generated by a simple time integration of rainfall data but by a complex, highly nonlinear, basin-scale rainfall-runoff transformation process

involving multiple forms of surface and subsurface runoff that are affected by heterogeneous vegetation cover, terrains, soil types and moisture, etc. (Tan and Gan 2015a).

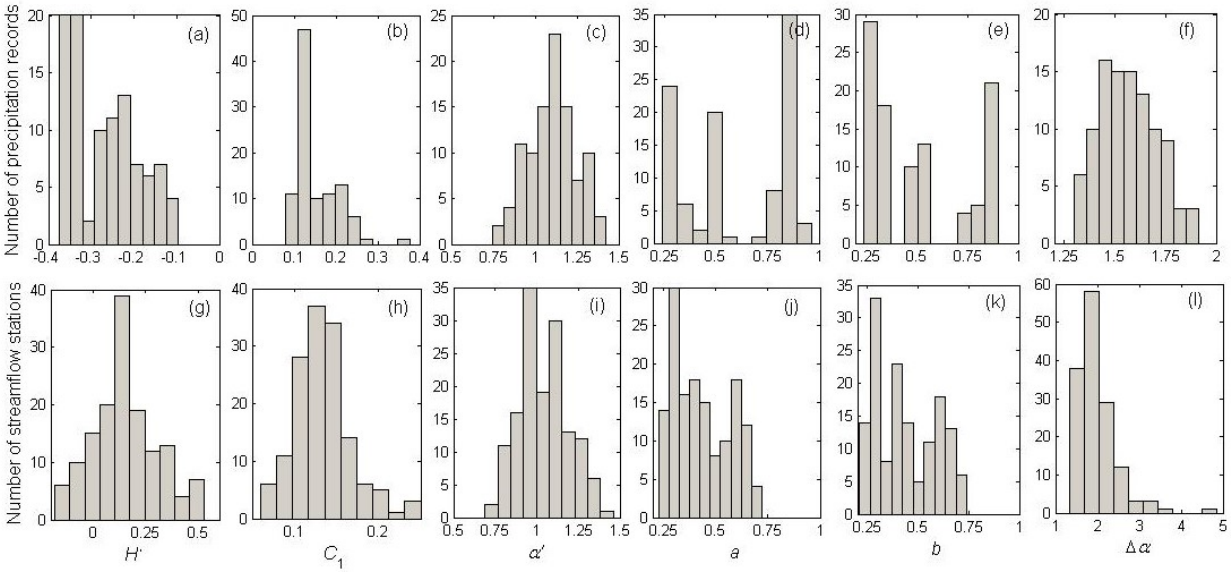

Figure 5-6 Histograms of multifractal parameters, H' (a and g), C_1 (b and h) and α' (c and i) for Equation (5-18), and *a* (d and j) and *b* (e and k) for Equation (5-19), and multifractal spectrum width (strength) $\Delta\alpha$ (f and l) for 100 daily precipitation records (a-f) and 145 daily streamflow (g-l) records.

Next, we applied a modified, multiplicative cascade model (Koscielny-Bunde et al. 2006) to the precipitation and streamflow data as shown in Figure 5-5.

$$\tau(q) = -\frac{\ln\left(a^q + b^q\right)}{\ln 2} \quad \text{or} \quad h(q) = \frac{1}{q} - \frac{\ln\left(a^q + b^q\right)}{q \ln 2} \tag{5-19}$$

Equation 5-19 is also applicable to negative q and can be used to estimate the multifractal spectrum $f(\alpha)$ of a process, whose multifractal strength is defined as $\Delta\alpha = |\ln a - \ln b| / \ln 2$. Values of parameters a and b were listed in Tables S1 and S2 for precipitation and streamflow data, respectively, while their histograms are shown in Figures 5-6d-e and 5-6j-k, respectively. For streamflow data a and b distributed fairly evenly over 0.25-0.75, but for precipitation data, a and b mainly distributed around 0.25, 0.50 and 0.75. The mean values of a and b are 0.60 and 0.50 for precipitation data, and 0.43 and 0.44 for streamflow data, respectively. Equation (5-19) generally fitted the precipitation and streamflow data well except for 20 precipitation and 38 streamflow time series.

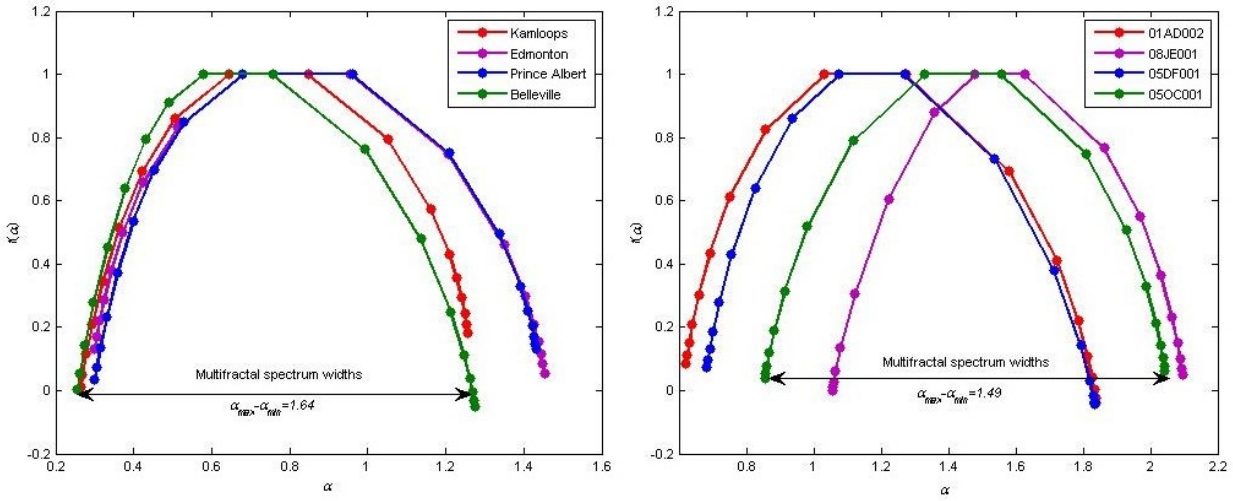

Figure 5-7 Multifractal spectrum ($f(\alpha) \sim \alpha$) of representative precipitation (a) and streamflow (b) records.

Figure 5-7 shows examples of multifractal spectrum for some selected precipitation and streamflow data, while spatial distributions of the multifractal strength, $\Delta\alpha$, of Canada are shown in Figure 5-8. The multifractal spectrum of precipitation data of the four selected stations is relatively similar to each other, especially for low α values, but not so for streamflow data whose multifractal spectrum varies widely between the four selected stations. This further demonstrates differences in the multifractal properties between precipitation and streamflow data. As expected, histograms of the multifractal spectrum width $\Delta\alpha$ of streamflow have a broader distribution than the precipitation (see Figures 5-6f and 5-6l), even though they tend to concentrate within a range of 1.25-2.75. $\Delta\alpha$ of precipitation are more evenly distributed. Mean values of $\Delta\alpha$, α_{min} and α_{max} for precipitation data are 1.57, 0.24 and 1.81, and for streamflow data are 1.98, 1.00 and 2.98, respectively. Apparently, the multifractal strength of Canadian data are considerably higher than that of German data, e.g., $\Delta\alpha$=0.29 for precipitation and $\Delta\alpha$=0.49 for streamflow of Germany (Kantelhardt et al. 2006). This could be partly because Canada has higher snowfall to rainfall ratios and larger variations between streamflow generated by snowmelt versus that generated by rainfall. However, for both Canada and Germany, the multifractal strength of precipitation is generally smaller than that of streamflow. In terms of spatial variability, $\Delta\alpha$ of streamflow data are less dependent on the geographic location or the climate zone than precipitation data, even though lower $\Delta\alpha$ values are usually found in non-RHBN streamflow stations of southern Canada (Figure 5-8). For precipitation data, western (central) Canada generally has lower (higher) $\Delta\alpha$ values, while for eastern Canada $\Delta\alpha$ values are more scattered.

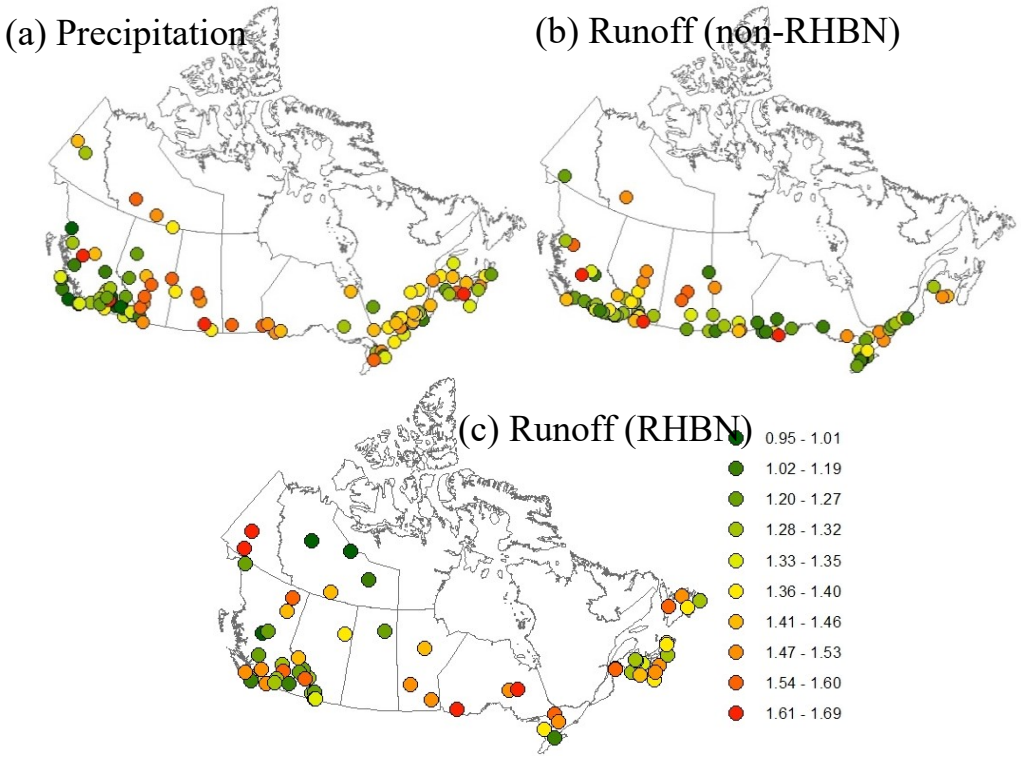

Figure 5-8 Spatial distributions of the multifractal spectrum width $\Delta\alpha$ of precipitation (a) and streamflow records (b and c). The same legends apply to figures (a), (b) and (c).

We also found that multifractal properties of observed precipitation and streamflow data are more related to their autocorrelations than other factors such as the distribution of φ_i because both randomly shuffled precipitation and streamflow data have not much multifractal strength.

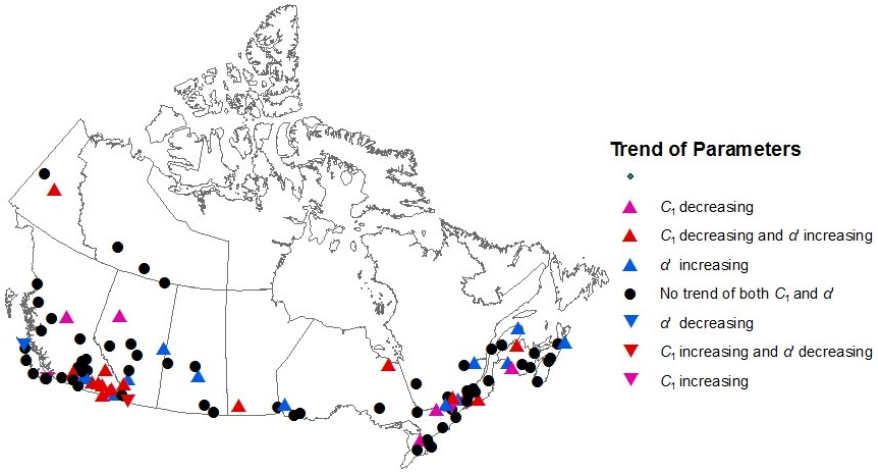

Figure 5-9 Distribution of trends of 30 parameters computed for the universal multifractal model (Equation 5-18) applied to 100 stations of precipitation time series, each divided into 30 non-overlapping subseries.

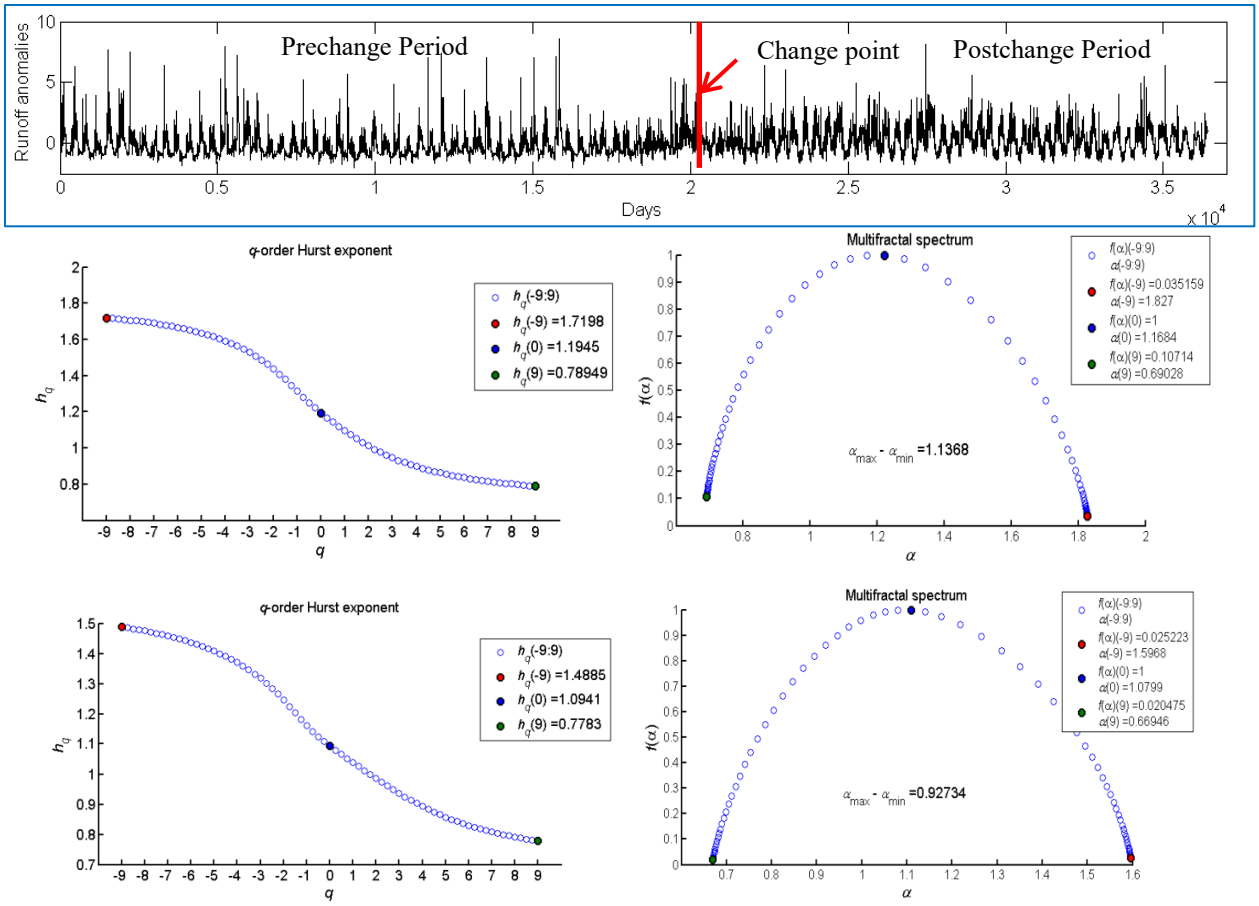

Figure 5-10 Differences in q-order Hurst exponent (h_q) and multifractal spectrum ($\alpha_{max}-\alpha_{min}$) of the daily streamflow of the North Saskatchewan River at Edmonton (Station # 05DF001) between pre- and post-change point periods caused by the streamflow regulation that began in 1973. The top panel shows the observed 1911-2010 streamflow anomalies; and the middle and the bottom panels show multifractal characteristics of the pre-change and post-change subseries, respectively.

5.4.3 Temporal changes of multifractal properties of precipitation

To test temporal changes of universal multifractal parameters of Equation 5-18, 30 sets of H', C_1 and α' were calculated for each precipitation time series, by first dividing each time series uniformly into 30 subseries, and from the parameters estimated for each subseries, temporal trends of these parameters were estimated. Results of Mann-Kendall tests on the temporal trends of these parameters are shown in Figure 5-9. Since no statistically significant trend was found for H', only trends in C_1 and α' are presented in Figure 5-9. Out of 100 stations, 38 stations showed statistically significant trends in C_1 and/or α', of which 33 stations showed increasing trends in α' and/or decreasing trends in C_1 and 5 stations showed decreasing trends in α' and/or increasing trends in C_1. These stations with significant trends distributed across Canada, with some clusters

located in southeastern British Columbia and eastern Canada. Increasing trends in α' combined with decreasing trends in C_1 (downward triangles in Figure 5-9) means that precipitation became temporally more uniform because multifractal strength decreased with time. Temporal trends in multifractal strength for snowfall and summer rainfall over the Canadian Prairies were also detected by (Shook and Pomeroy 2010; 2012). The detected temporal trends of multifractal strength of Canadian precipitation could be related to impacts of climate change.

5.4.4 Multifractal changes in streamflow data

Over the Twentieth Century, hydrologic processes of Canadian river basins had been significantly altered by human activities such as streamflow regulation with dams (Assani et al. 2006; Peters and Prowse 2001), afforestation and deforestation (Buttle 2011), and so multifractal properties of streamflow subseries data for pre-change and post-change periods are expected to be different from each other. Multifractal properties of streamflow subseries of stations located downstream of dams, before and after dam operation began, are compared to study the impact of human influences on streamflow data of Canada. Tan and Gan (2015a), who used the same streamflow dataset, showed that annual maximum daily streamflow of 19 out of 62 RHBN stations, and 40 out of 83 non-RHBN stations, exhibited significant abrupt changes. Therefore, for these 59 daily streamflow time series, we separated each streamflow time series to two subseries, one before and one after the detected change point (around the 1940s and the 1970s), and multifractal characteristics for both subseries were analyzed.

Figure 5-10 shows multifractal changes to daily streamflow time series of the North Saskatchewan River at Edmonton (Station # 05DF001) before (lower panel) and after (lower panel) the dam operation began. The top panel shows that there were more large fluctuations in the pre-change than in the post-change streamflow subseries. Given $h(q)$ for positive (negative) q is better in analyzing the scaling behavior of large (small) fluctuations (Ihlen 2012; Kantelhardt 2009), we explored scaling properties of small and large fluctuations and their variations between pre-change and post-change subseries by comparing $h(q)$ over a range positive and negative q-order as shown in Figure 5-10. The maximum $h(q)$ (1.72) of the pre-change subseries is higher than that of the post-change subseries (1.49), while their minimum $h(q)$ are almost the same. As a result, the range of $h(q)$ for the pre-change subseries to the post-change series decreases from 0.93 to 0.71. Streamflow regulated by dam operations are expected to be smoother with less fluctuation than un-regulated streamflow. However, the effect of dam

operation for extreme floods that exceed the control capacity of a dam will likely be insignificant or negligible. With dam regulation, Peters and Prowse (2001) found that the average winter flow of the Peace River was about 2.5 times higher, while annual peaks (1-day, 15-day, 30-day highs) were about 35–39% lower, and so the overall variability in the daily streamflow of the Peace River decreased.

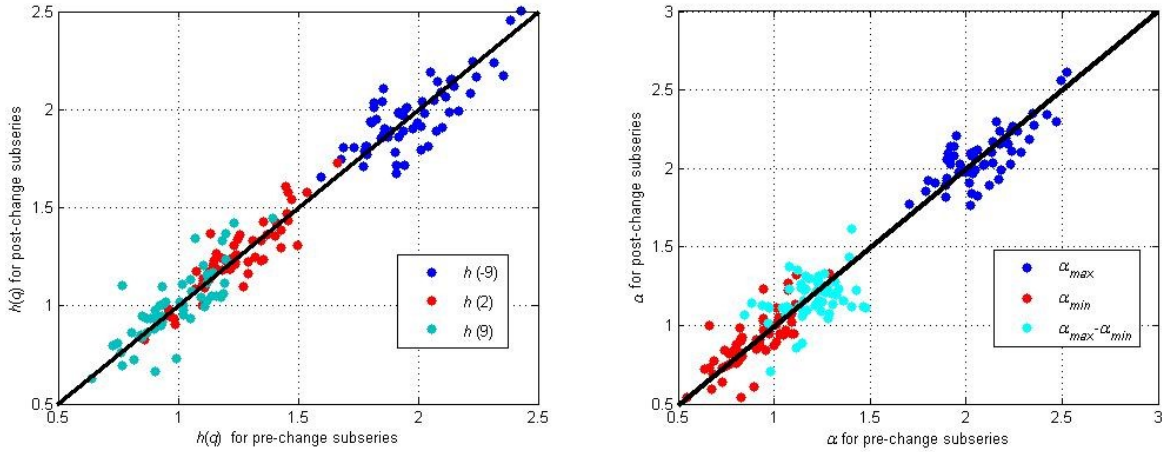

Figure 5-11 Comparison of the multifractal parameters between the pre- and post-change point subseries of Canadian streamflow records detected with statistically significant abrupt change points.

Differences in the multifractal spectrum between pre-change and post-change subseries are evident from plots of α, $f(\alpha)$, and $\Delta\alpha = \alpha_{max} - \alpha_{min}$ shown in Figure 5-10. The multifractal strength, $\Delta\alpha$, decreased from 1.14 for the pre-change subseries to 0.93 for the post-change subseries partly because $\Delta\alpha$ for the right half of the multifractal spectrum decreased from 0.52 for the pre-change subseries to 0.35 for the post-change subseries. In other words, streamflow regulation weakened the multifractal strength of the North Saskatchewan River.

Figure 5-11 compares the multifractal strength of the pre-change and post-change subseries of the 59 stations with abrupt change point detected. It is interesting to find that there was no consistent difference between the multifractal strength of the two subseries of these stations partly because about equal number of stations exhibited a decrease or an increase in $h(q)$ and $\Delta\alpha$ between the pre- and post-change periods. Among these 59 stations, only 27 stations were subjected to the effect of dam operation. Out of these 27 stations, only 13 stations showed a decrease in $h(q)$ and $\Delta\alpha$, such as Station #05DF001, but the multifractal strength of the other 14 stations had increased. Further, out of 62 regulated stations, change points were detected only in 35 of such stations, which suggest that streamflow regulations may not always result in the occurrence of statistically significant change points, which may related to the reservoir operation

rules of the stations, and the degree of changes in streamflow regimes because of reservoir operations (Assani et al. 2006; Tan and Gan 2015a). Even though precipitation regimes of Canada have become more uniform temporally (Section 5.4.3), streamflow may fluctuate more erratically because of streamflow regulation and other human activities that result in hydrologic changes of river basins. In addition, for Canada dominated by winter snowfall, a warmer climate has inevitably changed the timing and magnitude of peak snowmelt streamflow (Assani et al. 2006). More detailed, basin scale studies are recommended to identify factors behind detected changes to multifractal properties of the streamflow regimes of Canada.

5.5 Summary and conclusions

In this study, 100 and 145 stations of long-term daily precipitation and streamflow records across Canada were respectively analyzed using DFA and MFDFA. All precipitation time series showed LTP at both small and large time scales, while streamflow time series generally showed nonstationary behavior at small time scales and LTP at large time scales. Widespread crossovers of fluctuation functions, $F_2(s)$, versus timescale s for streamflow data at approximately a time scale of 120-250 days could be related to the cross-over between rain-induced and snowmelt-induced streamflow cycles, since no crossover was found in precipitation data. In general, the multifractal strength of precipitation data was location dependent but not so for streamflow data. The multifractal behavior of Canadian precipitation and streamflow data measured in terms of generalized Hurst exponents, $h(q)$, can be accurately described by the universal multifractal model for positive q-order moments, and also by the modified multiplicative cascade model but it can only fit about 2/3 of the $h(q)$ of precipitation and streamflow data consistently.

About 1/3 of the fitted parameters of the universal multifractal model for precipitation data showed positive temporal trends, which means that precipitation of these stations became temporally more uniform because their multifractal strength decreased with time. However, only about half of the stations whose streamflow data exhibited statistically significant abrupt change points showed a weakening in the multifractal strength moving from the pre-change to the post-change periods. Differences in the multifractal strength between Canadian precipitation and streamflow data suggest that the persistence of streamflow was not only because streamflow is more auto-correlated than precipitation, it is also more consistently affected by human activities in terms of runoff production and temporal processes. More extensive research is needed to study

the inhomogeneous, multifractal properties of precipitation and streamflow spatially and temporally.

Chapter 6 Wavelet analysis of precipitation extremes over Canadian ecoregions and teleconnections to large-scale climate anomalies

6.1 Introduction

Coherent climatic patterns of large-scale atmospheric circulation can appropriately interpret the variabilities and long-term persistence in hydroclimatic records. Interannual and interdecadal variabilities in hydroclimatic variables (e.g., temperature, precipitation and streamflow) have been closely associated with large floods and droughts and found to be extensively teleconnected to low-frequency large-scale climatic fluctuations, which can further our understanding of the physical dynamics of the hydrologic cycle (Coulibaly and Burn 2004; Elsanabary et al. 2014; Gan et al. 2007; Jiang et al. 2014; Özger et al. 2009). Some temporal and regional teleconnections between low-frequency large-scale climate anomalies and the variability of hydro-climatic variables can lead to improved hydrologic frequency analysis and prediction (Khedun et al. 2014; Kuo et al. 2010; Min et al. 2013) which will be useful for regional water resource management.

The Canadian climate is significantly influenced by natural climate variabilities, such as the El Niño Southern Oscillation (ENSO), the Pacific-North American (PNA) pattern, the North Atlantic Oscillation (NAO) and the Pacific Decadal Oscillation (PDO), as well as other teleconnection patterns, and their influence is seasonally and regionally dependent (Bonsal and Shabbar 2008; Coulibaly 2006; Coulibaly and Burn 2004; Gan et al. 2007; Ropelewski and Halpert 1986; Shabbar et al. 1997). For example, distinct patterns of negative (positive) precipitation anomalies in Southern Canada have been linked to El Niño (La Niña) events, while significant positive precipitation anomalies over the southeastern Northwest Territories and northern Prairies have been associated with El Niño events (Shabbar et al. 1997). For western Canada, low-flow events have frequently been related to the warmer/drier conditions during El Niño events and positive phases of the PDO and PNA (Bonsal and Shabbar 2008). The influence of NAO on Canadian precipitation was found to be restricted to northeastern regions, where positive NAO values were related to lower than normal winter precipitation (Stone et al. 2000). However, most previous studies on low-frequency relationships between Canadian precipitation and large-scale climate anomalies have focused on monthly or seasonal precipitation totals, but

oscillations of precipitation extremes and their teleconnections to large-scale climate anomalies are seldom examined.

Recent studies have started to identify the spatiotemporal impacts of ENSO on the probability distribution of daily precipitation. The influence of ENSO on the frequency of heavy precipitation was examined over the contiguous United States. El Niño was associated with an increase in the frequency of heavy precipitation over the southwestern United States (US) but a decrease over the northwestern US (Cayan et al. 1999). An ENSO signal was also linked to the frequency of heavy precipitation in other parts of the US (Gershunov and Barnett 1998). Other interannual and interdecadal climate variabilities in the North Pacific have also exerted influence on the frequency of heavy precipitation in the US (Gershunov and Cayan 2003). Grimm and Tedeschi (2009) and Ropelewski and Bell (2008) found that extreme precipitation events over South America were mainly modulated by ENSO. Zhang et al. (2010) examined changes in probability distributions of winter daily maximum precipitation over North America by using climate indices for ENSO, PDO and NAO as covariates to estimate the time-varying parameters of generalized extreme value (GEV) distributions. By incorporating the Southern Oscillation Index (SOI) into parameters of marginal GEV models, Shang et al. (2011) fitted max-stable process models to winter maximum daily precipitation of California. They found that ENSO has shifted the location parameter of GEV distributions. Min et al. (2013) found that changes in the magnitude of extreme seasonal precipitation over Australia were caused by ENSO, the India Ocean Dipole and the Southern Annular Mode. These studies show that large-scale climate variabilities played a significant role in different aspects of probability distributions for heavy precipitation in various regions.

Some correlation, composite and empirical orthogonal function (EOF) analyses also indicate that climate variabilities influenced extreme temperature and precipitation. There are statistically significant Pearson correlations between global precipitation extremes and ENSO (Alexander et al. 2009; Curtis et al. 2007). Kenyon and Hegerl (2010) examined global stations where precipitation extremes showed a statistically significant difference between positive and negative phases of some large-scale climate anomalies, such as ENSO, NAO and the North Pacific. They found that precipitation extremes were most substantially affected by ENSO. Represented by leading EOFs of winter precipitation over the contiguous US (Schubert et al. 2008) and Southern Brazil (Pscheidt and Grimm 2009), large spatial scale storms were

significantly influenced by the state of ENSO and interdecadal, non-ENSO variabilities. Through correlation analysis, Wang et al. (2014a) examined long-term changes in extreme precipitation over China and the US and their linkage to climate anomalies of oceanic–atmospheric origin. The frequency of extreme precipitation over the Mediterranean region was associated with ENSO, NAO, Arctic Oscillation, the East Atlantic/Western Russian (EAWR) pattern and the Scandinavian pattern (Krichak et al. 2014). Duan et al. (2015) used cross-wavelet analysis to study the correlation of extreme precipitation over Japan with climate indices. Cioffi et al. (2015) also detected possible relationships between ENSO, NAO, EAWR and global temperature gradients and the European extreme precipitation by cross-wavelet analysis. Markovic and Koch (2005) analyzed the cross-wavelet spectra and the scale-averaged wavelet power (SAWP) of NAO and German extreme precipitation. They found that NAO exerted opposite effects on low-frequency variabilities of extreme precipitation over northern and southern Germany.

Given that climate oscillations may modulate the observed evolution of precipitation extremes, this study has two objectives: (1) to detect the dominant oscillations of Canadian monthly maximum daily precipitation (MMDP) and their temporal variations using wavelet analysis; and (2) to relate observed extreme precipitation signals to some large-scale climate anomalies, i.e., ENSO (represented by the Niño 3 Sea Surface Temperature Index (NINO3) and SOI), NAO and PDO, by wavelet coherence (WTC) analysis, wavelet EOF (WEOF) analysis and composite analysis. This chapter is organized as follows. The data of Canadian precipitation and large-scale climate anomalies is described in Section 6.2, technical details on research methods such as WTC, WEOF and composite analysis in Section 6.3, results and discussions in Section 6.4, and conclusions in Section 6.5.

6.2 Data

Trends in Canadian extreme precipitation have been extensively studied using the first generation Canadian daily precipitation dataset released in 1999 (Mekis and Hogg 1999; Peterson et al. 2008; Vincent and Mekis 2006; Zhang et al. 2000; 2010). The second generation adjusted Canadian daily precipitation (APC2) dataset released recently was used in this study. Precipitation observations, which are the source of APC2, were statistically adjusted for known measurement issues (such as evaporation and wetting loss) for each type of rain-gauge, wind under-catch and snow water equivalent that was estimated (Mekis and Vincent 2011). Although

APC2 has 464 station-adjusted daily precipitation series, the observation length, data gap and spatial distribution of stations vary significantly among stations.

To study adequately the low-frequency variabilities of Canadian extreme precipitation and to compare differences in results between different regions, 131 stations (Figure 6-1) with daily precipitation data collected in 1930-2005 were selected from the APC2 dataset for this study. The selected stations are distributed evenly in western Canada, fewer stations in northern and central Canada, but relatively more stations in the eastern, coastal regions of Canada. For each station, the MMDP time series was extracted from its daily precipitation time series, and then it was detrended by subtracting the monthly mean extreme precipitation from the MMDP time series for each month to obtain the MMDP anomalies. The standardized MMDP anomalies of the 131 stations for 1930–2005 are transformed by wavelet analysis while seasonal maximum daily precipitation (SMDP) series were extracted for composite analysis.

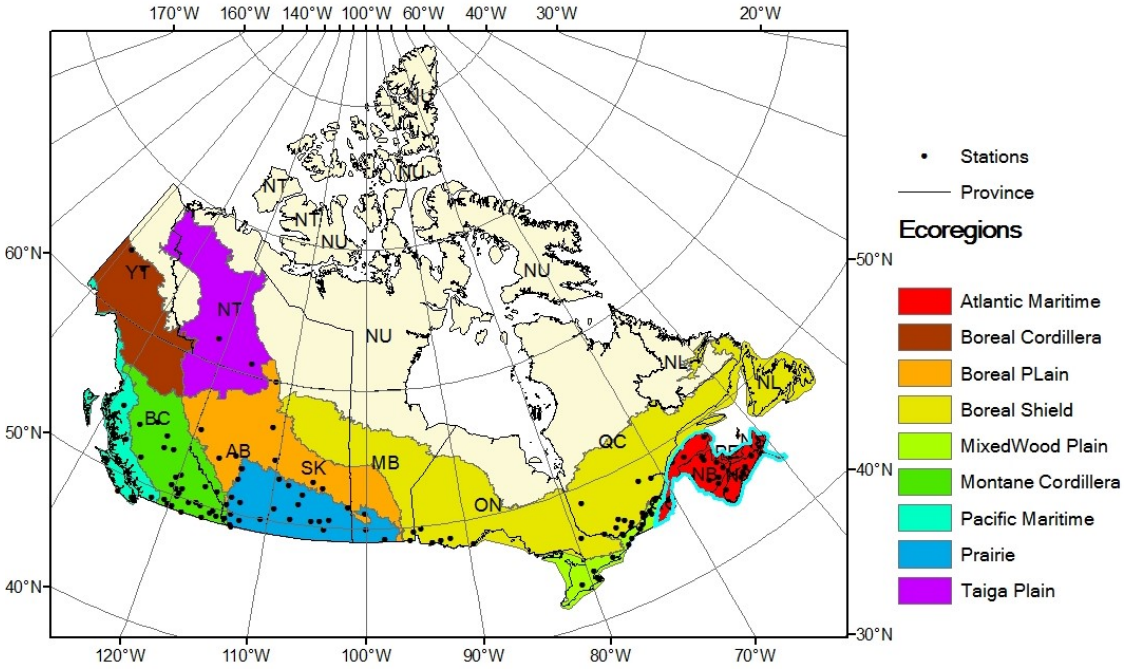

Figure 6-1 Locations of 131 selected precipitation stations and nine ecoregions over Canada. The Provinces or Territories of Canada are: AB, Alberta; SK, Saskatchewan; MB, Manitoba; NL, Newfoundland & Labrador; PE, Prince Edward Island; NS, Nova Scotia; NT, Northwest Territories; NU, Nunavut; ON, Ontario; NB, New Brunswick; YT, Yukon Territory; British Columbia; and QC, Quebec.

Monthly climate indices of large-scale climate anomalies, ENSO represented by SOI and NINO3, NAO and PDO that affected Canadian precipitation were analyzed. NINO3 is a time series of SST anomalies over the equatorial Pacific (Morice et al. 2012), while SOI is a time series of normalized monthly differences in sea level pressure between Tahiti and Darwin

(Ropelewski and Halpert 1986; Trenberth 1984). When ENSO is active, there is large-scale atmospheric fluctuation in the tropical and subtropical Pacific and Indian Oceans (Trenberth 1984). NAO index is differences in sea level pressure (SLP) anomalies between stations in the Reykjavik and Azores (Jones et al. 1997); the PDO index is the leading principal component from an un-rotated empirical orthogonal analysis of monthly detrended SST anomalies in the North Pacific Ocean (Mantua et al. 1997). The above monthly data of climate indices were provided by the Global Climate Observing System (GCOS) Working Group on Surface Pressure (WG-SP).

6.3 Research methodology

We extracted dominant oscillations of Canadian MMDP using continuous Morlet wavelet transformation, and studied relationships between detected oscillations and some large-scale climate anomalies that have possibly affected the climate of Canada using WTC, WEOF, partial wavelet coherence (PWC) and multiple wavelet coherence (MWC). The wavelet analysis is briefly introduced below.

6.3.1 Wavelet analysis

Wavelet transform (WT) decomposes time series into time-frequency space and identifies the dominant modes of variability and how these modes vary in time. Continuous WT is appropriate for extracting a wide range of possible dominant frequencies from geophysical and hydroclimatic time series. WT is also an efficient approach to analyzing nonstationary signals. This study is limited to practical details useful for applying the wavelet analysis on the MMDP time series. Further detailed descriptions of wavelet analysis can be found in literature (e.g., Aguiar-Conraria and Soares 2014; Grinsted et al. 2004; Ng and Chan 2012b; Torrence and Compo 1998).

In a continuous WT, using a wavelet $g(t)$, an observed time series $x(t)$ can be expanded. The former scales a particular wavelet member up and down with a flexible window width, while the latter slides the window center along the time axis, with $x(t)$ projected over the wavelet. $g(t)$ is a packet wave with a certain amplitude and scale, satisfying $\int_{-\infty}^{-\infty} g(t)dt = 0$. In this study, we used the Morlet wavelet. The WT of $x(t)$ is

$$W_t(\xi,\gamma) = \xi^{-1/2} \int g^* \left(\frac{t-\gamma}{\xi} \right) x(t)\, dt \quad \xi > 0, \gamma \in R \tag{6-1}$$

where g^* is the complex conjugate of g, ξ is the scale parameter for controlling the window width and is often taken as multiples of the lowest possible frequency ($1/\delta t$), δt is the time interval, γ is the translation parameter for sliding the wavelet along the time axis, and $\xi^{-1/2}$ is a normalized factor to keep the total energy constant. The wavelet power spectrum is defined as $\left|W_t(\xi,\gamma)\right|^2$. A picture describing how the wavelet power spectrum of a signal varies in the time-frequency domain can be constructed by varying ξ and γ.

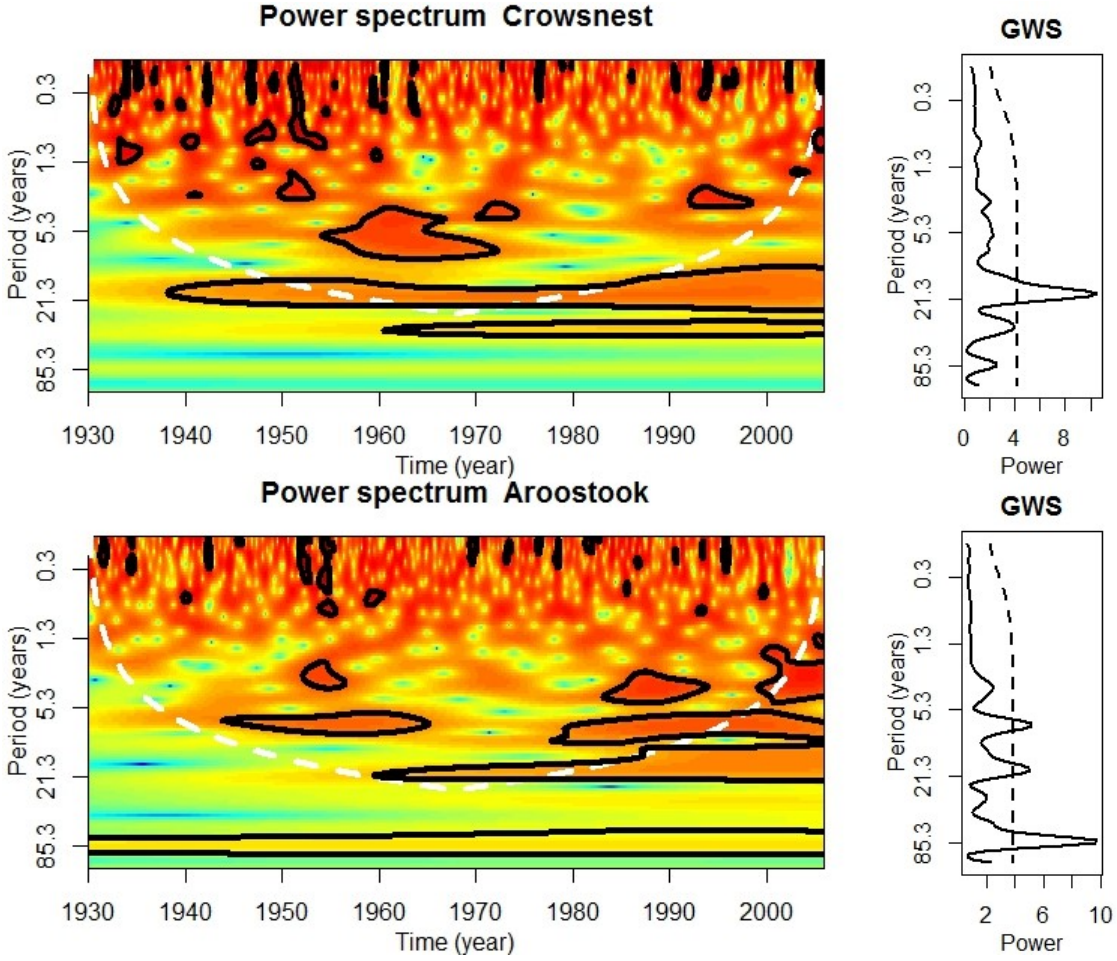

Figure 6-2 Continuous Morlet wavelet spectrum of MMDP and Global wavelet power spectrum (GWS) (solid line) with the 95% confidence level (dashed line) at Crowsnest and Aroostook are presented. The thick black contours depict the 95% confidence level of local power relative to a white noise background. The white dashed line is the cone of influence beyond which the energy is contaminated by the effect of zero padding.

Figure 6-2 shows the WT for the MMDP at Crowsnest, Alberta, and Aroostook, New Brunswick. The thick black contour lines enclose regions of statistically significant wavelet

power in the time-frequency space at a 5% significance level of a white noise process. Significant interannual (approximately 4–10 years) oscillations occurred in the 1950s to 1970s and the 1990s at Crowsnest, and in the 1940s to 1960s and 1980s to 2005 at Aroostook. Interdecadal (10–25-year) oscillations were active from the 1940s to 2005 at Crowsnest and from the 1960s to 2005 at Aroostook.

To interpret the wavelet spectrum and conduct further statistical analysis, various quantities derived from WT were proposed to condense the vast quantity of information contained in the wavelet spectrum. We used the scale-averaged wavelet power (SAWP) to further investigate the fluctuations in wavelet power over specific ranges of wavelet periods (bands). SAWP, over scales j_1 to j_2, is the weighted summation of the wavelet power spectrum:

$$\overline{W}_t^2 = \frac{\delta j \delta t}{C_\delta} \sum_{j=j_1}^{j_2} \frac{\left|W_t(\xi,\gamma)\right|^2}{\xi_j} \tag{6-2}$$

where δj is a scale averaging factor and C_δ is a reconstruction factor. The global wavelet power spectrum (GWS), which is an equal-weighted average of all the local wavelet power spectra for each scale and a special case of SAWP, only shows dominant scales with no temporal transformation. GWS in Figure 6-2 presents a statistically significant low-frequency oscillation with a period of 10–25 years at Crowsnest and a period of 6-8 years, 10-20 years and a possible 60-80 years at Aroostook.

Scale bands and time periods within which the MMDP time series (Y) presents covariance with climate index series (X) can be identified from WTC, which is defined as [*Torrence and Compo*, 1998]:

$$\left[R_t^{XY}(\xi)\right]^2 = \frac{\left|\left\langle \xi^{-1} W_t^{XY}(\xi,\gamma)\right\rangle\right|^2}{\left\langle \xi^{-1}\left|W_t^X(\xi,\gamma)\right|^2\right\rangle \left\langle \xi^{-1}\left|W_t^Y(\xi,\gamma)\right|^2\right\rangle} \tag{6-3}$$

where $W_t^{XY}(\xi,\gamma)$ is the cross-wavelet spectrum of Y and X, $\langle\cdot\rangle$ is a smoothing operator and $0 \le \left[R_t^{XY}(\xi)\right]^2 \le 1$. $\left[R_t^{XY}(\xi)\right]^2$ is the normalized covariance between two time series, as the WT conserves variance. WTC has been widely used to study the relations between precipitation or streamflow in different regions and some large-scale climate anomalies (see, e.g., Elsanabary et al. 2014; Gan et al. 2007; Grinsted et al. 2004; Jiang et al. 2014; Özger et al. 2009; Torrence and Compo 1998).

We also assessed correlations between the PCs of band-pass filtered signals of MMDP time series and climate index series at multiple-scale bands. One can reconstruct the band-passed (wavelet-filtered) signal $x'(t)$ over a subset of scales from the wavelet coefficients by the equation,

$$x'(t) = \frac{\delta j \delta t^{1/2}}{C_\delta \psi(0)} \sum_{j=j_1}^{j_2} \frac{R\{W_t(\xi_j)\}}{\xi_j^{1/2}} \tag{6-4}$$

where $\psi(0)$ is a factor to remove the energy scaling (Torrence and Compo 1998).

Because selected climate indices appear to be interrelated at several scales (Gan et al. 2007; Ng and Chan 2012a, 2012b), the stand-alone relationship between a climate index series and the MMDP time series should be further studied by removing the effect of another climate index. In wavelet applications, PWC is a technique similar to partial correlation for finding the resulting WTC between two time series Y and X_1 after the influence of the time series X_2 is eliminated (Mihanović et al. 2009). WTC is principally similar to the traditional correlation coefficient, and it shows a localized correlation in the time-frequency space. Mihanović et al. (2009) extended a simple linear correlation to the WTC between Y and X_1 ($R_t^{YX_1}$), Y and X_2 ($R_t^{YX_2}$), and X_1 and X_2 ($R_t^{X_2X_1}$) and suggested that the PWC is Equation (5).

$$\left(RP_t^{YX_1-X_2}\right)^2 = \frac{\left|R_t^{YX_1} - R_t^{YX_2} R_t^{X_2X_1}\right|^2}{\left(1-\left(R_t^{YX_1}\right)^2\right)\left(1-\left(R_t^{X_2X_1}\right)^2\right)} \tag{6-5}$$

6.3.2 Wavelet empirical orthogonal function (WEOF) analysis

WEOF analysis, also called wavelet principal component (WPC) analysis, is a statistical approach to reducing the dimensionality of SAWP series at multi-locations to some orthogonal PCs that explain the majority of the variability in regional SAWP. WEOF is applied to transform a matrix $[\ ]_{n\times k}$ of SAWP by the n observations on k stations into another matrix $[\ ]_{n\times k}$ of SAWP signals and noises. WPCs, like ordinary PCs, are the signals and noises accounting for all the variability of SAWP. Denoting these WPCs as U and its component u_j:

$$u_j = e_j^T x^* = \sum_{i=1}^{k} e_{ij} x_i^*, \qquad j = 1, \cdots \qquad < k) \tag{6-6}$$

where e_{ij} are the eigenvectors, x_i^* represent the standardized anomalies of SAWP, and J is a small subset of the k possible signals. If the MMDP variability is the same for every station, the matrix U would contain only one SAWP signal (WPC1) to account for all the variability of the SAWP. However, MMDP time series vary from station to station in reality. Hence, usually a few WPCs tend to represent the majority of the SAWP variability.

6.3.3 Composite analysis

A composite analysis was conducted for each station to investigate the possible influence of large-scale climate variability on local SMDP for all seasons. For each season, the composite SMDP will be computed from the 5-year mean SMDP observed in the 5 years when climate indices (SOI, NINO3, NAO, and PDO) were the lowest (P_{low}) and the highest (P_{high}), respectively. Typically, P_{low} and P_{high} for a given station and season correspond to the warm or cold phase of each climate index, respectively. The difference between these 5-year averages ($P_{low}-P_{high}$) demonstrates the influence of certain large-scale climate oscillations at the local (station) scale (Zhang et al. 2010). The statistical significance of these differences was tested based on a bootstrapping method, where for each station and at each season, SMDP was computed from two randomly selected 5-year samples, and the difference (δP_{max}) between them was estimated. The empirical distribution of δP_{max} was obtained by repeating this process 5000 times. If $P_{low}-P_{high} \leq 2.5^{th}$ percentile of δP_{max}, or if $P_{low}-P_{high} \geq 97.5^{th}$ percentile of δP_{max}, the influence of a particular large-scale climate pattern on SMDP is statistically significant at the 5% level.

6.4 Results and discussion

6.4.1 Wavelet analysis of MMDP

To fully show the spatiotemporal properties of the wavelet power spectrum of all studied Canadian MMDP time series, time-longitude Power Hovmöller diagrams of the SAWP are shown in Figure 6-3. Three scale bands (1-3 years, 3-8 years and 8-30 years) were selected to compute the SAWP. The SAWP enclosed in the solid black contours in Figure 6-3 is statistically significant at the 5% level relative to a white noise process. For North America, the interannual oscillations (1-3 years and 3-8 years) are usually modulated by the low-frequency components of ENSO, while decadal or interdecadal oscillations (8-30 years) are associated with climate

anomalies of the North Pacific and North Atlantic (Bonsal and Shabbar 2008; Gan et al. 2007; Schubert et al. 2008; Shang et al. 2011).

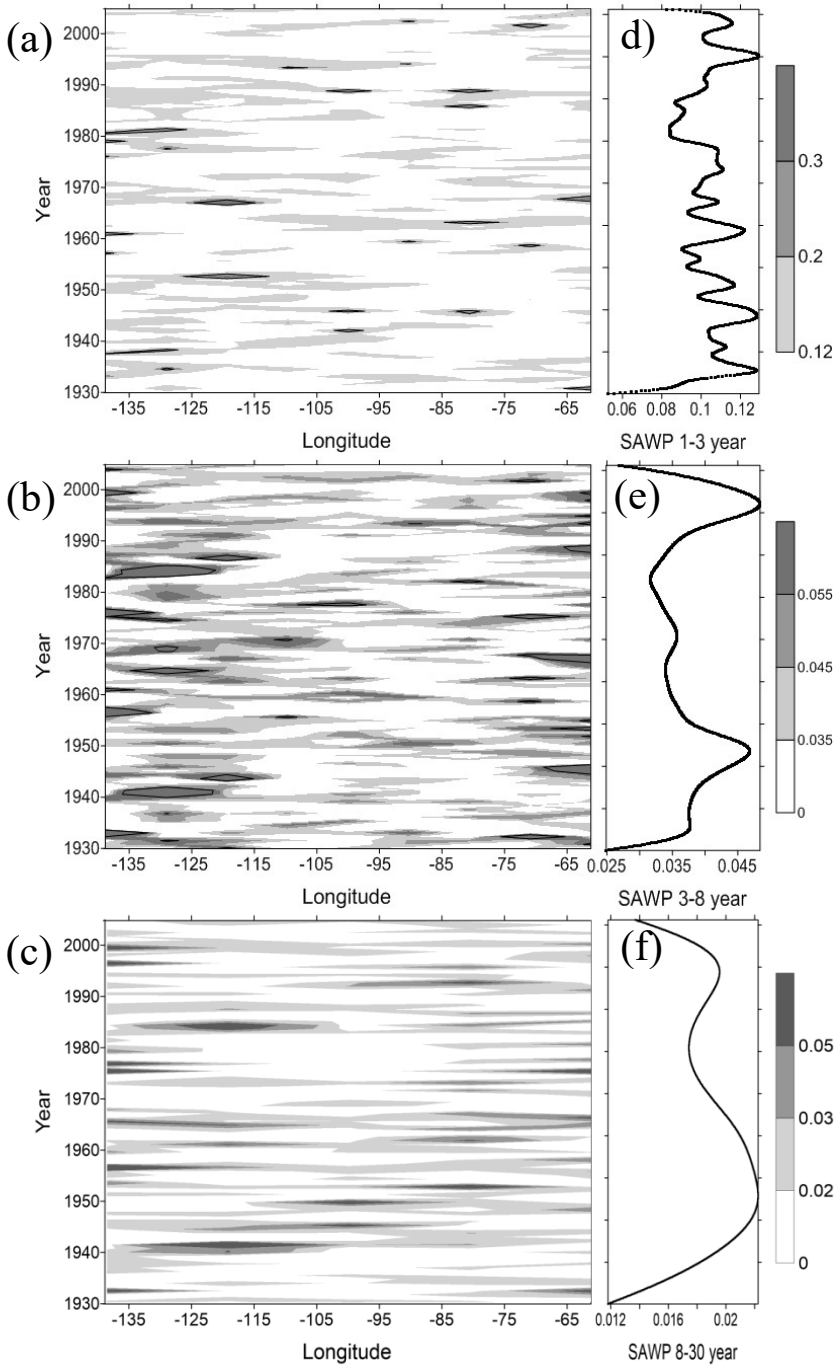

Figure 6-3 Time-longitude Power Hovmöller diagrams of the SAWP (a-c) and space-average of the SAWP power Hovmöller (d-f) for Canadian monthly maximum precipitation anomalies at the 131 stations: 1-3-year scale band (Figures 6-3a and 6-3d), 3-8-year scale band (Figures 6-3b and 6-3e), and 8-30-year scale band (Figures 6-3c and 6-3f). The grey contours are at a normalized power of 0.13, 0.035, and 0.015 for Figure 3a, Figure 3b and Figure 3c, respectively. The solid black contours enclose periods of statistically significant SAWP relative to a white noise process at the 5% significance level.

Unlike the space-averaged SAWP of the southwestern Canadian seasonal total precipitations, for which, on average, up to 15% and 7% of the variance was accounted for by the 3-8- and 8-30-year scales, respectively (Gan et al. 2007), the same scales only account for up to 4.8% (Figure 6-3e) and 2.2% (Figure 6-3f), respectively, of the variance of the Canadian MMDP time series. Similar high percentages of variance represented by interannual scales are also found for the seasonal total precipitation and streamflow of Canada (Anctil and Coulibaly 2004; Coulibaly 2006; Coulibaly and Burn 2004, 2005). However, lower variance representations were also found in the German MMDP time series (Markovic and Koch 2005). This relatively low space-averaged variance in % is partly caused by large variances in the MMDP time series with a positively skewed and a long decaying tail distribution, and partly caused by large spatial variabilities in MMDP processes, in which the high SAWP of a station may be averaged out by a neighbor station with very low SAWP. The 1-3-year oscillation is prevalent for Canadian MMDP time series and accounts for up to 12-15% of the total variance. The high SAWPs enclosed in the solid black contours in the three time scales for some stations are usually 2-4 times higher than the spatially averaged SAWP but mostly with a lifetime shorter than 3 years. By comparing our results with those of Coulibaly (2006) and Gan et al. (2007), extreme precipitation events show more randomness than seasonal total precipitation. Because SAWP of all stations studied are presented in several Hovmöller diagrams to give an overview of the spatiotemporal variability of extreme precipitation from west to east, small patches of solid black contours scattered across the Hovmöller diagrams represent significant activity of selected scales at some stations, as shown in Figures 3a-c.

Comparing the SAWP of 1-3-year time scale for individual stations, the largest percentage of variance explained by the 1-3-year band varies from as low as 5% at Powell River, British Columbia, in 1930-1935 to as high as 89% at Mont Laurier, QC, in 1939-1940, which is far larger than the maximum space-averaged SAWP of 15% in this band (Figure 6-3a). There had been several high SAWP (gray areas in Figure 6-3a) at the 1-3 year scale that occurred fairly consistently across Canada around 1960-1990, but on a whole their occurrences had been haphazard and limited.

Compared to the 1-3 year scale, the diagram for the 3-8-year scale (Figure 6-3b) shows more patches of statistically significant SAWP in eastern (east of 75^{o}W) and western (west of 115^{o}W) Canada than in Central Canada (115^{o}W~75^{o}W). The percentage of variance explained

by the 3-8-year band for individual stations varies from less than 1% at Barkerville, British Columbia, during 1935-1950 to more than 40% at the same station in 1931-1933, which is much higher than the maximum space-averaged SAWP of 4.8% at this band (Figure 6-3e). For the 8-30-year band, no statistically significant SAWP had been observed in the study period. Although the space-averaged 8-30-year SAWP only explained about 1.8% of the total variance of Canadian MMDP time series, the 8-30-year SAWP accounted for more than 8% of the total variance of some individual stations (e.g., from 1936 to 1945 at Rimouski, QC; from 1935 to 1943 at Barkerville, British Columbia; and from 1933 to 1945 at Collegeville, NS).

The large difference between the space-averaged and individual SAWPs demonstrates high spatial variabilities of extreme precipitation events in general. However, there had been cases of regionally and temporally coherent oscillations detected across certain longitudes but these oscillations were mostly short-live. To investigate the variability of MMDP in details, we used the agglomerative hierarchical clustering method to divide Canada into 9 clusters with similar probability distributions for MMDP (Hosking and Wallis 1997). As expected, the 9 clusters generally fall within 9 Canadian ecoregions classified by Environment Canada (1996) (Figure 6-1), although some clusters may occupy more than one ecoregions at the borders. Therefore, we decided to further analyze the variabilities of MMDP based on the 9 ecoregions: Pacific Maritime (PM), Boreal Cordillera (BC), Montane Cordillera (MC), Canadian Prairies (CP), Boreal Plain (BP), Boreal Shield (BS), Taiga Plain (TP), Mixedwood Plains (MP), and Atlantic Maritime (AM).

6.4.2 Wavelet analysis of climate indices

Figure 6-4 shows the wavelet power spectra of the monthly climate indices SOI, NINO3, NAO and PDO. SOI showed statistically significant interannual variability at 2 to 8 year time scale in 1935-1960 and 1965-2000, which agrees with results of previous studies for seasonal SOI (Gan et al. 2007; Jiang et al. 2014; Torrence and Compo 1998). We also identified a statistically significant interdecadal variability at 8-30-year scale post-1970s (Figure 6-4a) not detected in previous studies partly because we used the SOI series of GCOS WG-SP, which is marginally different from the SOI series of NOAA Climate Prediction Center (CPC) used in previous studies (Gan et al. 2007; Jiang et al. 2014), as GCOS WG-SP and CPC calculated SOI indices from different SST or SLP datasets using different methods. However, large-scale climate variability patterns identified from both datasets are virtually identical to each other.

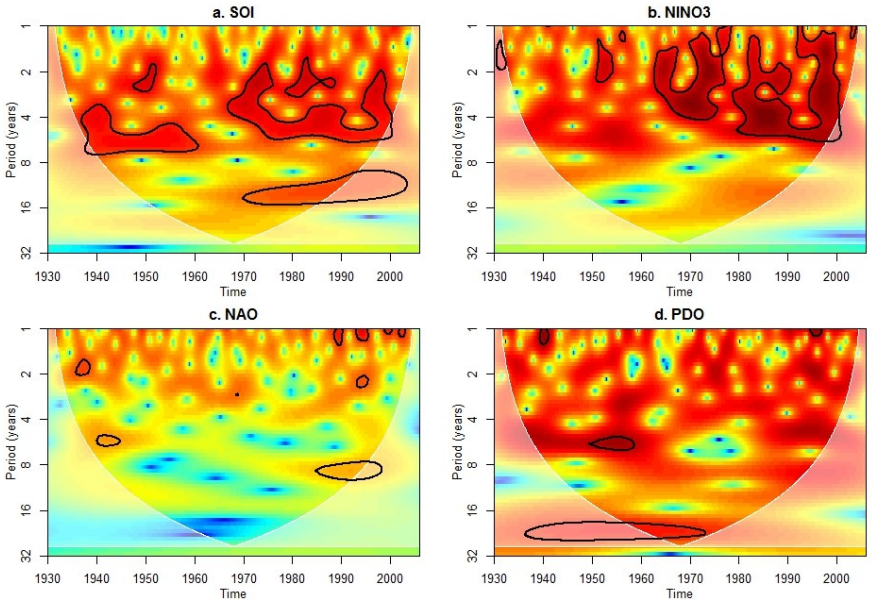

Figure 6-4 In the four wavelet power spectra of monthly climate indices, the thick black contours represent significant local wavelet power at the 95% confidence level relative to a white noise background. The white contour of each plot is the cone of influence beyond which energy is contaminated by the effect of zero padding.

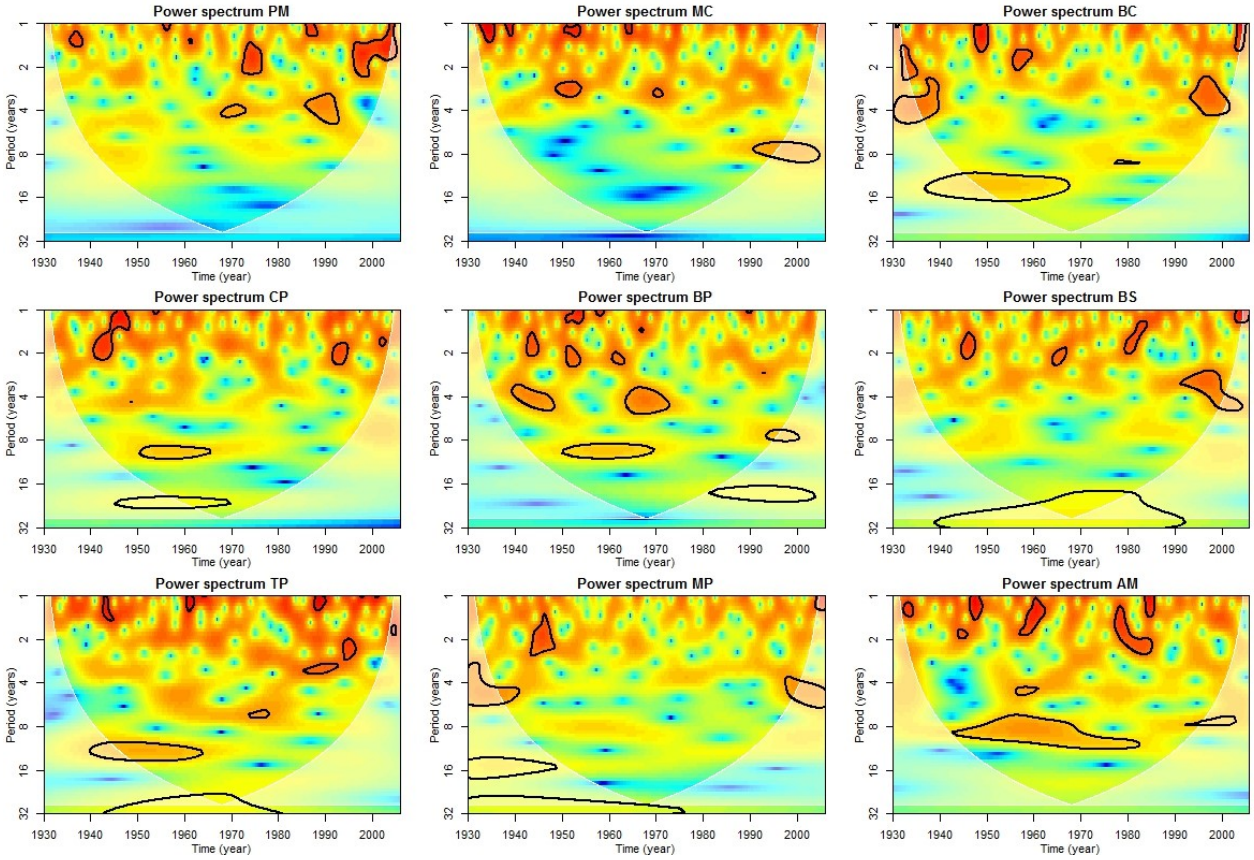

Figure 6-5 In wavelet power spectra of MMDP PC1 of nine ecoregions, all features are the same as Figure 6-4. PM, Pacific Maritime; MC, Montane Cordillera; BC, Boreal Cordillera; CP, Canadian Prairies; BP, Boreal Plain; BS, Boreal Shield; TP, Taiga Plain; MP, Mixedwood Plains; AM, Atlantic Maritime.

Even though, on a whole, ENSO activities represented by NINO3 and SOI are similar to each other, there are some minor differences. For example, for the 3-8 year interannual, NINO3 only shows a few scattered, statistically significant periods after 1960s but not in the 1935-1960 period as detected by SOI. NAO shows scattered, significant interannual oscillations in 1935-1945 and 1985-2000, and an intermittent, significant annual cycle during 1985-2002 (Figure 6-4c), but no significant interdecadal oscillation. PDO also shows limited interannual variability after 1940s, 1950s and in 1990s. PDO shows strong interdecadal oscillations (larger than 20-year) over 1930-2005, even though most of the detected oscillations lie outside the cone of influence (Figure 4d).

6.4.3 Wavelet coherence between MMDP and large-scale climate indices

By comparing the wavelet power spectrum of climate indices (Figure 6-4), MMDP (Figure 6-2), and the Power Hovmöller (Figure 6-3), we see some common, large scale power spectrum between the time- frequency domains of Canadian MMDP and selected climate indices. However, their relationships are highly unstable both temporally and spatially. Therefore wavelet coherence analysis was used to statistically estimate the linkage between regional MMDP signals and climate indices. To limit the number of time series to be analyzed by WTC, the leading PCs (hereafter, PC1 and PC2) of MMDP anomalies for the 9 regions, which together on the average explain about 48.0% of the total variance of regional MMDP, were used to represent regional signals of Canadian MMDP. Because extreme precipitation has much larger spatial variability than seasonal total precipitation, PC1 and PC2 of MMDP explain about 30.0 and 18.0% of the variance of regional MMDP, respectively, which together is approximately the percentage (50%) of variance explained by PC1 of the seasonal total precipitation of a similar region (Gan et al. 2007). As expected, the wavelet spectra of MMDP PC1 (Figure 6-5) and PC2 (Figure S1) are complementary to each other in presenting oscillations of regional, extreme precipitation. For example, the MMDP PC1 (PC2) in AM shows significant variabilities at the 5-8- (8-30-) year scale during 1940-1980 (1940-2000). The MMDP PC1 and PC2 in eastern Canada, including BS, MP and AM, consistently show significant decadal and interdecadal variabilities during 1930-2005, while significant variabilities at interannual time scales randomly scattered across wavelet spectra of MMDP PC1 and PC2 of all ecoregions of Canada.

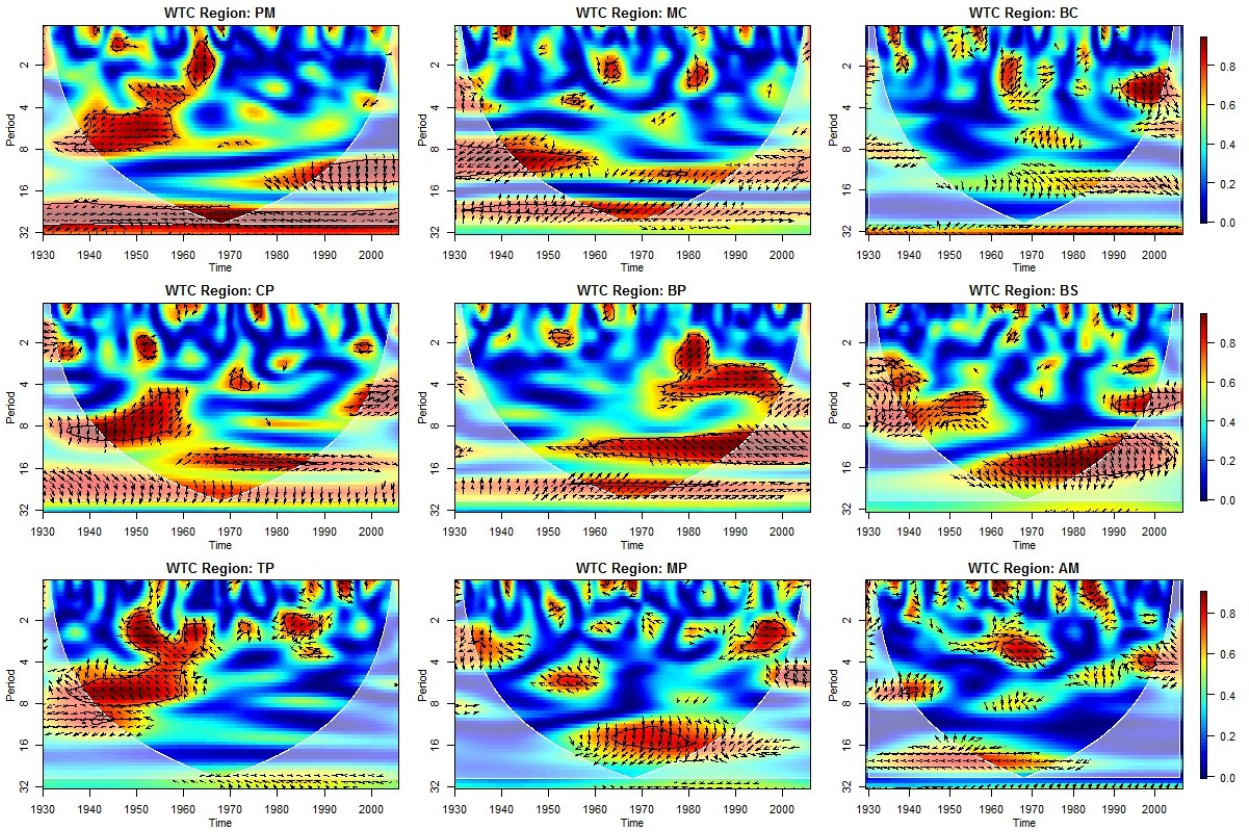

Figure 6-6 In WTC spectra and phase difference between the MMDP PC2 of nine ecoregions and SOI, thick black contours enclose periods with statistically significant coherence relative to a red noise process at 5% significant level. The phase difference is plotted only for time periods and scales with a coherence over 0.7. Right (left) pointing arrows indicate that the two signals are in phase (antiphase); arrows pointing down mean that NINO3 leads MMDP PC2 by 90°; and arrows pointing up mean that MMDP PC1 leads NINO3 by 90° or that NINO3 leads MMDP PC2 by 270°.

WTCs between regional MMDP PC1 and PC2 and four climate indices are shown in Figure 6-6 and Figures S2-S8. The black contours in these figures represent periods of statistically significant coherence of a thick red noise process at 5% significant level by a Monte Carlo experiment (Grinsted et al. 2004; Jevrejeva 2003). Note that significant coherences of two signals do not necessarily mean that powers of those two signals are also statistically significant. For instance, neither NINO3 (Figure 6-4b) nor the MMDP PC1 of region AM (Figure 6-5) has significant power of 15-30-year scale during 1930-2005, but they show significant coherence over 1930-2005 (Figure S3). As expected, MMDP PC1 and PC2 of a region generally show significant coherence with climate indices at time scales and time periods that are different from each other. For example, significant coherence between MMDP PC1 of region MC and NINO3 at the 3-5-year scale was detected during 1965-1995 (Figure S3) but significant coherence

between MMDP PC2 at region MC and NINO3 at 8-12-year scale was detected during 1930-1960 (Figure S4).

For most ecoregions of Canada, the MMDP PC1, PC2 and ENSO (represented by NINO3 and SOI) show non-consistent, statistically significant coherence at interannual (2-10 years) scale and also at interdecadal (10-30 years) scales but the latter are generally not statistically significant. The MMDP PC2 shows more-significant coherences with the ENSO than the MMDP PC1 for all regions (Figure 6-6 and Figures S2-S4). Moreover, SOI tends to show more widespread and significant coherences with the MMDP PC2 for all regions at the 4-20-year scale (Figure 6-6), which likely implies that SOI is a better index to represent teleconnections of ENSO with Canadian extreme precipitation. At regional scale, with respect to variations in the coherence between MMDP PC1-2 and ENSO, the western and central regions (including PM, MC, BC, CP and BP) show more significant coherence than the eastern regions which, however, also show significant coherence at certain time scales. With respect to the phase difference between them at time scales with significant coherences, there are large spatial variations, such as the coherence between MMDP PC2 and SOI are of antiphase in the western and central regions (PM, MC, BC, BP and TP), while SOI leads the MMDP PC2 by 90° in the eastern regions (BS, MP and AM) (Figure 6-6). However, the coherence between MMDP PC2 and NINO3 are in phase in the western regions (PM, MC, BC and TP) but of antiphase in the central regions (CP and BP) (Figure S4).

In western regions (PM, MC, BC and TP), the strongest coherence between MMDP PC1-2 and NAO occurred over the 8-20-year scale (Figures S5-S6) in which both MMDP PC1-2 of western regions (Figures 6-5 and S1) and NAO (Figure 6-4) show significant power. MMDP PC1 shows stronger coherence with NAO than the MMDP PC2. At 2-8 years scale, the eastern regional (BS, MP and AM) MMDP PC1-2 shows a more significant coherence with NAO than other regions because MMDP PC1-2 of these regions have stronger wavelet power at the interannual time scale than other regions. Overall, temporal changes to phase angle at time scales with significant coherence between MMDP PC1-2 and NAO are stronger than those between MMDP PC1-2 and SOI.

Because PDO is dominated by interdecadal oscillations, MMDP PC2 in western and central regions shows significant coherence with PDO at time scales of more than 20 years (Figures S7-S8), but scattered significant coherence between eastern MMDP PC1-2 and PDO

also exist at interannual time scales. Significant coherences can either be in phase, such as MMDP PC2 at PM and CP regions, or of antiphase, such as MMDP PC2 at MC and BP regions. In the phase interpretation of this study, it is assumed that MMDP usually follows large-scale climate anomalies even though precipitation can also affect the phase pattern of large-scale climate anomalies, as shown by Zhou et al. (2007).

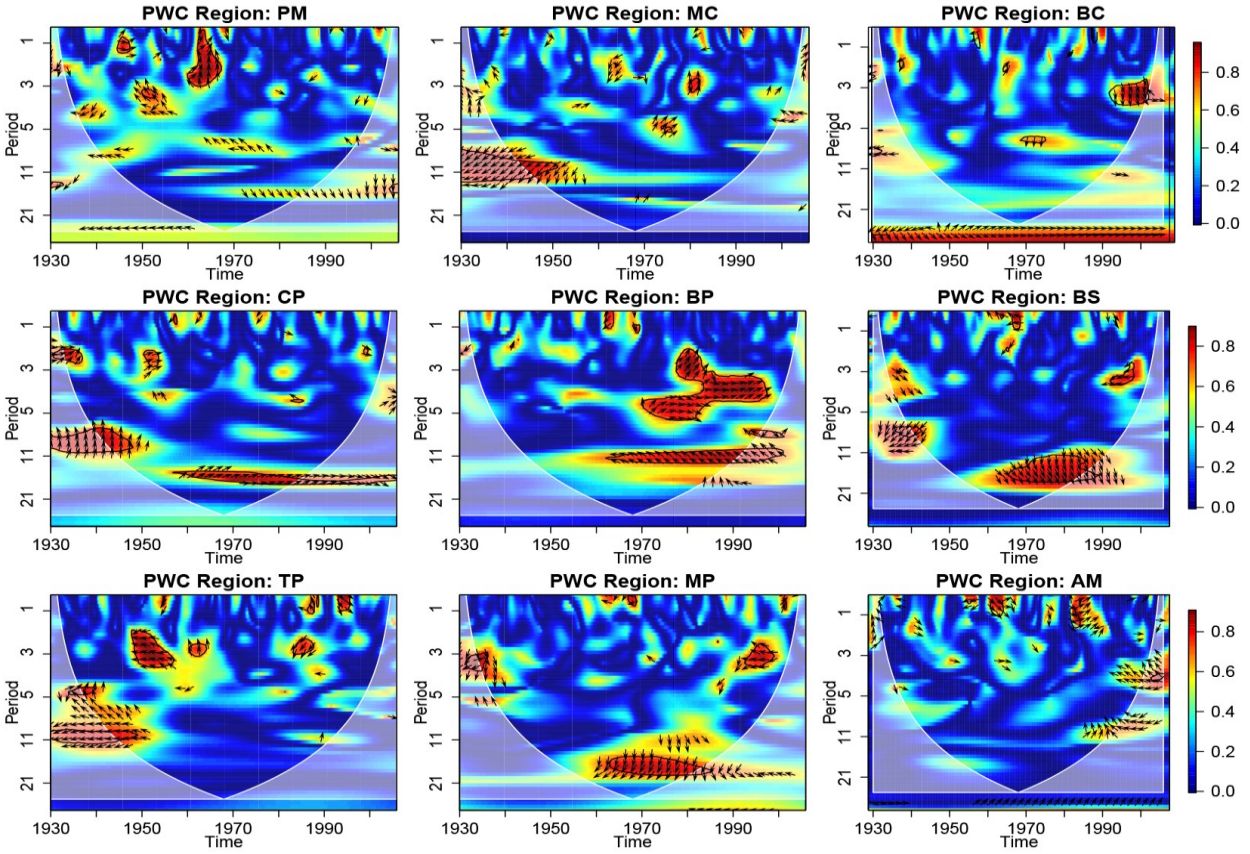

Figure 6-7 PWC spectra and phase difference between the MMDP PC2 and SOI with the influence of PDO on MMDP PC2 eliminated.

6.4.4 Partial wavelet coherence

Figure 6-7 (S9) shows the PWC between MMDP PC2 (PC1) and SOI after eliminating the influence of PDO on MMDP PC2 (PC1). As expected, their coherence had been reduced because MMDP PCs are correlated with both SOI and PDO. Specifically, significant coherence at interdecadal time scales between MMDP PC2 and SOI over western and central regions (PM, MC, CP and BP) shown by the WTC analysis (Figure 6-6) is not found in the PWC analysis (Figure 6-7). Furthermore, significant coherence at interannual (2-10 years) scales between MMDP PC1-2 and SOI become less significant after the influence of PDO is eliminated (Figures 6-7 and S9). Even though PDO is primarily of interdecadal modes, the interannual variability of

PDO can also affect the Canadian MMDP, as shown in Figures S7-S8, and by the significant coherence at interannual scales in PWC spectra between MMDP PC1-2 and PDO after the influence of SOI on MMDP PC1-2 is eliminated (Figures S10-S11). Therefore, in addition to SOI, incorporating the PDO index as a predictor can also improve the predictability of the Canadian MMDP.

The significant coherence between MMDP PC1-2 and NAO at interannual scales over western and central regions (Figures S5-S6) also decrease after the influence of SOI on MMDP PC1-2 is eliminated (Figures S12-S13); however, significant coherence between MMDP PC1 and NAO at the interdecadal scales over western regions (PM, MC and BC), and between MMDP PC1-2 and NAO at the interannual scales over eastern regions (BS, MP and AM), remain widely present. Further, the significant coherence between MMDP PC1 of western regions and NAO at interdecadal scales remain even after the influence of PDO is eliminated (Figure S14), which show that NAO is significantly correlated with MMDP over western Canada at interdecadal scales.

6.4.5 Correlations at multiple time scales

The correlation between MMDP and ENSO (NINO3, SOI), NAO and PDO was further examined using MMDP SAWP computed over 1-3-, 3-8- and 8-30-year time scale. We also explored relationships between PCs of band-passed MMDP time series and band-passed climate indices and relationships between PCs of SAWP of MMDP and climate indices at multiple time scales. Both sets of relationships are expected to be strong if a climate index exerts a consistent and significant influence on the regional MMDP at a given time scale.

Table 6-1 Pearson's correlations between the PC scores of band-passed MMDP and band-passed climate indices for selected scale bands.

scale	PC	Var (%)[a]	NINO3	SOI	PDO	NAO	Var(%)[a]	NINO3	SOI	PDO	NAO
		Pacific Maritime (PM)					*Montane Cordillera (MC)*				
1-3 year	1	27.8	**-0.238**	**0.182**	**-0.095**	0.030	18.3	**0.141**	-0.022	**0.119**	0.040
	2	17.4	**0.060**	**-0.073**	-0.006	0.053	11.9	-0.031	0.053	-0.001	**0.184**
	3	13	**-0.237**	0.054	**-0.172**	0.035	8.2	**0.118**	**-0.147**	0.054	0.053
3-8 year	1	33.3	**0.178**	**-0.149**	0.024	**-0.273**	17.3	0.004	0.048	**-0.117**	-0.023
	2	14.7	**-0.300**	**0.531**	**-0.307**	**0.182**	13.4	-0.056	-0.042	-0.031	-0.010
	3	13.5	**0.310**	**-0.258**	**0.257**	**-0.091**	10	**0.152**	**-0.265**	**0.160**	**-0.208**
8-30 year	1	26.1	**0.055**	**0.141**	**-0.107**	**-0.241**	28.2	**0.144**	**-0.137**	**0.527**	**-0.060**
	2	21.3	-0.021	**0.170**	-0.034	**0.614**	15.9	**0.103**	-0.051	0.000	**-0.643**
	3	16.4	**0.453**	**-0.466**	**0.481**	**-0.419**	10.5	**-0.233**	**0.157**	**-0.184**	0.008
		Boreal Corillera (BC)					*Canadian Prairie (CP)*				
1-3 year	1	62.4	**0.095**	**-0.107**	-0.048	0.044	21.6	**0.136**	**-0.072**	0.056	**0.227**
	2	37.6	**-0.102**	**0.066**	**-0.143**	-0.028	11.6	**0.199**	**-0.153**	**0.220**	0.039
	3	NA	NA	NA	NA	NA	8.4	0.006	0.048	0.048	**0.105**
3-8 year	1	69.4	**0.345**	**-0.202**	**0.281**	-0.044	19.4	0.049	-0.053	0.011	-0.028
	2	37.6	**0.063**	**-0.655**	**0.073**	0.029	16.7	**0.293**	**-0.184**	**0.144**	**-0.075**
	3	NA	NA	NA	NA	NA	12.7	**0.120**	**-0.258**	**0.233**	**-0.386**
8-30 year	1	60.2	**0.134**	**-0.155**	0.022	**-0.668**	26	**0.190**	**-0.112**	**0.469**	**0.162**
	2	39.8	**0.185**	**-0.305**	**0.256**	**0.249**	13.6	**-0.505**	**0.513**	**-0.299**	**0.187**
	3	NA	NA	NA	NA	NA	12.6	-0.021	**-0.164**	**-0.303**	**0.139**
		Boreal Plain (BP)					*Boreal Shield (BS)*				
1-3 year	1	19.6	**-0.225**	**0.160**	**-0.113**	**-0.219**	17.4	-0.059	0.040	-0.046	-0.029
	2	16.5	**-0.066**	0.004	**0.083**	**-0.176**	11.7	**0.077**	-0.033	**0.282**	-0.041
	3	13.5	-0.033	-0.104	**-0.188**	**0.121**	9.9	**-0.154**	**0.159**	**-0.111**	-0.010
3-8 year	1	24.1	**-0.274**	**0.228**	**-0.112**	**-0.268**	21.9	-0.019	**0.070**	**-0.132**	**0.098**
	2	21.2	**-0.152**	**0.102**	**-0.143**	**-0.170**	15	**0.314**	**-0.248**	**0.435**	**0.056**
	3	14	**0.252**	**-0.104**	**-0.163**	**0.063**	12.1	-0.054	-0.042	**0.186**	0.007
8-30 year	1	30.4	-0.050	**0.375**	**0.158**	**-0.190**	28.1	**0.112**	-0.023	**0.206**	**0.107**
	2	19.9	**-0.409**	**0.486**	0.031	**0.316**	18	**0.246**	**-0.216**	**-0.239**	0.023
	3	15.2	**0.104**	**-0.318**	**0.090**	**0.201**	12.8	**0.105**	**-0.409**	0.053	**0.298**
		Taiga plain (TP)					*MixedWood Plain (MP)*				
1-3 year	1	63.1	**0.205**	**-0.176**	**0.108**	0.040	17.9	**-0.077**	**0.084**	**-0.102**	-0.017
	2	36.9	**0.127**	**-0.177**	0.002	-0.033	12.2	**0.147**	**-0.115**	**0.135**	-0.026
	3	NA	NA	NA	NA	NA	11.6	**-0.091**	0.021	**-0.281**	**0.077**
3-8 year	1	62.2	**0.030**	**0.126**	**-0.081**	-0.048	20.1	**-0.173**	**0.064**	**-0.115**	**-0.095**
	2	37.8	-0.062	**0.183**	-0.053	**-0.130**	18.7	**0.240**	**-0.222**	**0.192**	**-0.060**
	3	NA	NA	NA	NA	NA	11.9	-0.005	-0.005	0.006	**0.092**
8-30 year	1	73.1	**-0.065**	**-0.087**	**-0.186**	**-0.076**	30.4	**0.286**	**-0.333**	**0.346**	**-0.545**
	2	26.9	0.058	**-0.352**	**0.224**	**-0.134**	20.7	**0.063**	**0.217**	**0.190**	**-0.474**
	3	NA	NA	NA	NA	NA	11.7	**0.391**	**-0.272**	**0.353**	**0.119**
		Atlantic Maritime (AM)									
1-3 year	1	23.8	**-0.060**	**0.093**	**0.133**	**0.066**					
	2	11.1	**-0.115**	**0.178**	**-0.108**	**0.084**					
	3	9.1	**-0.299**	**0.137**	**-0.200**	**0.093**					
3-8 year	1	23.5	**0.202**	-0.047	**0.143**	-0.002					
	2	14.5	**-0.102**	0.016	-0.043	**-0.265**					
	3	12.2	**0.052**	**-0.058**	-0.009	0.010					
8-30 year	1	34.2	**0.070**	**0.078**	-0.020	**-0.126**					
	2	17.9	**-0.210**	**0.074**	**-0.452**	**0.440**					
	3	12.4	**0.273**	0.053	**-0.094**	**0.109**					

[a] The variance that the PCs represent. Statistically significant correlations at the 5%significance level are shown in bold text.

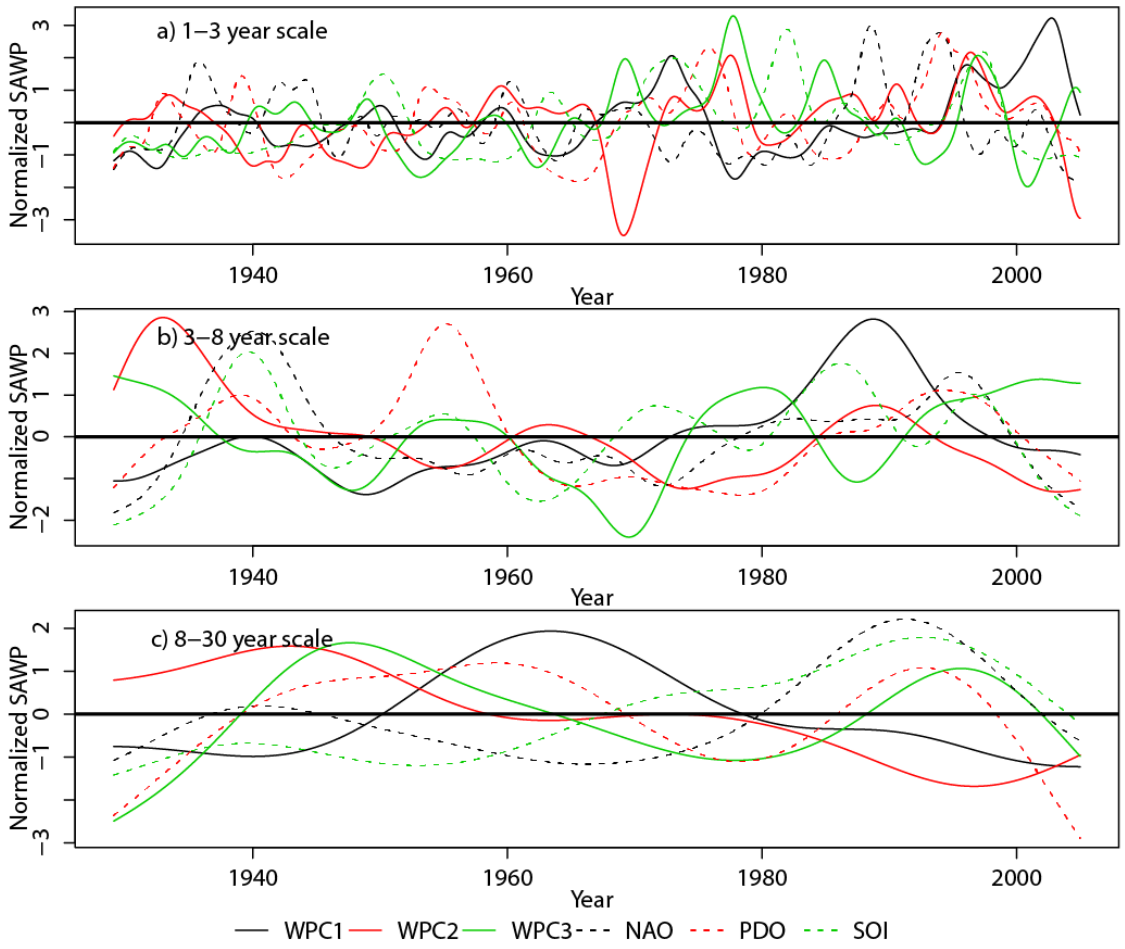

Figure 6-8 The 1930-2005 time series of normalized WPCs for the MMDP SAWP of Pacific Maritime (PM) region, and the corresponding normalized SAWP of NAO, PDO and NINO3. WPC1, WPC2 and WPC3 respectively explain 24.8%, 12.3% and 11.1% of the total variance of the 1-3-year scale; 35.9%, 23.5% and 13.3% of the variance of the 3-8-year scale; and 52.1%, 24.5% and 11.6% of the variance of the 8-30-year scale, MMDP SAWP.

Table 6-1 shows Pearson's correlations between the 1–3-year, 3–8-year and 8–30-year scale band-passed precipitation PC scores of each region and the climate index subjected to the same band-passes. The statistical significance of the estimated Pearson's correlation at a 5% level is tested using an asymptotic confidence interval sampled from a sampling probability distribution based on Fisher's Z transform (Hawkins 1989). In total, 73.4% of 108 Pearson's correlations computed from combinations of 3 bands, four climate indices over 9 regions are statistically significant. Between the four climate indices, MMDP shows slightly weaker correlations with NAO (60%). There are more statistically significant correlations for the 8-30-year band (80.4%) than the 1-3-year (60.7%) and 3-8-year (60.7%) bands in most regions.

Relatively weaker correlations between the interannual-scale, band-passed MMDP and ENSO (SOI and NINO3) for the MC region agree with significant WTC that are found to be mostly of short-durations (Figure 6-6 and S2-S8) because ENSO episodes are mostly short-live. Even though correlations between band-passed MMDP PC1-3 and climate indices are significant, generally less than 40% of the total variability at 1-30-year scale can be explained by a single climate index.

Figures 6-8 and S15 show the temporal variability of normalized WPC1-3 of the MMDP SAWP in the PM and AM regions, respectively, along with SAWPs of SOI, NAO and PDO of the same time scales. PM and AM are of the western and eastern coastal regions, respectively, where the MMDP evidently shows more significant low-frequency variabilities compared to inner regions (Figure 6-3). Here we can also see some correlations between climate indices (such as SOI, NAO and PDO) and MMDP at certain time scales. The SAWPs of NAO and PDO are negatively (positively) correlated during the pre-1950s (1960s and 1990s) at the 1-3-year scale, 1950-1960 (1965-1975 and 1990s) at the 3-8-year scale, and 1950-1970 at the 8-30-year scale. SOI and PDO are consistently positively correlated at the 3-8-year scale but are negatively correlated during 1940-1980 at the 8-30-year scale, which supports asymmetric relationships found between extreme precipitation and climate indices (e.g., Cai et al. 2010; Sun et al. 2015).

MMDP was modulated by one or more large-scale patterns, as periods of strong oscillations of the MMDP SAWP usually corresponds to active episodes of one or more large-scale climate patterns. For example, WPCs of the MMDP SAWP at the 1-3-year scale in the PM region shows strong oscillations during 1965-1980 and 1990-2005, which are likely linked to episodes of active SOI+PDO and SOI+NAO+PDO, respectively (Figure 6-8a). For the 3-8-year time scale, strong oscillations of WPC1, WPC2 and WPC3 of the MMDP SAWP during 1985-1995, 1930-1935 and 1965-1975 are related to active SOI, NINO3+NAO+PDO, and NAO+PDO, respectively (Figure 6-8b).

The relationship between MMDP and ENSO is mostly represented by correlations between WPC1 of MMDP and SOI at three time scales, although it shows some temporal discrepancies. For the 3-8-year time scale, the WPC1 of MMDP of PM and SOI are positively (negatively) correlated pre-1955 and 1970-1990 (1955-1970) (Figure 6-8). A transition from a negative to a positive relationship between WPC1 of MMDP of PM and SOI also occurred around 1980 at the 8-30-year scale. Similarly inconsistent relationships are also found between WPCs of MMDP-

PM and SOI, NAO and PDO, and primarily one climate anomaly tends to modulate some WPCs at certain time scales, e.g., PDO at the 8-30-year scale is consistently and negatively correlated to WPC3. MMDP in the AM region is more strongly modulated by NAO, such as its WPC1 and WPC3 at both 3-8- and 8-30-year scales are consistently and negatively correlated with NAO; and its WPCs at 1-3-year scale show strong oscillations during 1960s and 1980-2000 when strong episodes of NAO also occurred (Figures S15b-c). Pearson's correlations between band-passed MMDP and climate indices at the three time scales are generally less than 0.4.

Table 6-2 Years included in the composite analysis of SDMP for the extreme phases of ENSO (represented by SOI and NINO3), NAO and PDO patterns.

	Spring	Summer	Fall	Winter	Spring	Summer	Fall	Winter
		SOI				NINO3		
Low	1987	1982	1982	1982	1955	1988	1955	1973
	1998	1997	1997	1940	1950	1970	1988	1999
	1994	1987	1940	1991	1985	1954	1942	1949
	1997	1940	1965	1997	1971	1938	1973	1975
	1992	1941	1941	1977	1964	1955	1954	1970
High	1956	1956	2000	1970	1987	1957	1987	1991
	1950	1955	1955	1938	1941	1983	1965	1930
	1989	1938	1973	1950	1992	1987	1930	1972
	1974	1975	1975	1975	1998	1972	1972	1982
	1971	1950	1988	1973	1983	1997	1997	1997
		NAO				PDO		
Low	1971	1995	1933	1995	1956	1955	1955	1955
	1936	1987	1993	1962	1972	1950	1961	1948
	1941	1944	2002	1968	1971	1933	1950	1949
	1951	1999	1972	1978	1950	1971	1999	1971
	1975	1977	1939	1976	1955	1956	1956	1990
High	1992	1993	1986	1989	1986	1936	1993	1939
	1986	1936	1953	1948	1983	1993	1936	1935
	1947	1990	1938	1999	1987	1983	1997	1986
	1963	1946	1978	1994	1941	1997	1934	2002
	1943	1961	1954	1988	1940	1941	1987	1940

6.4.6 Composite analysis

The influence of extreme phases of ENSO, NAO and PDO on the Canadian SMDP was further explored using a composite method. SMDP data of years (Table 6-2) when 5 extremely high/low climate indices occurred were selected in the composite analysis of SMDP subjected to extreme phases of ENSO (represented by SOI and NINO3), NAO and PDO patterns. Figures 6-9 and S16-18 show composite differences for winter, spring, summer and autumn SMDPs under extreme phases of the three climate anomalies. Magnitudes of composite differences (mm)

shown in Figure 6-9 are presented as bubble plots. Extremely large (≥17 mm) composite differences in the winter SMDP are shown at some stations: 1) four green stations (17.4-44.5 mm) in the PM region (Figure 6-9a); 2) four red stations (17.6-31 mm) in the AM region (Figure 6-9b); and 3) three red stations (17.2-32.9 mm) in the PM region (Figure 6-9d). Table 6-3 shows the number of stations where composite differences in SMDPs are either statistically significant or not significant in four seasons.

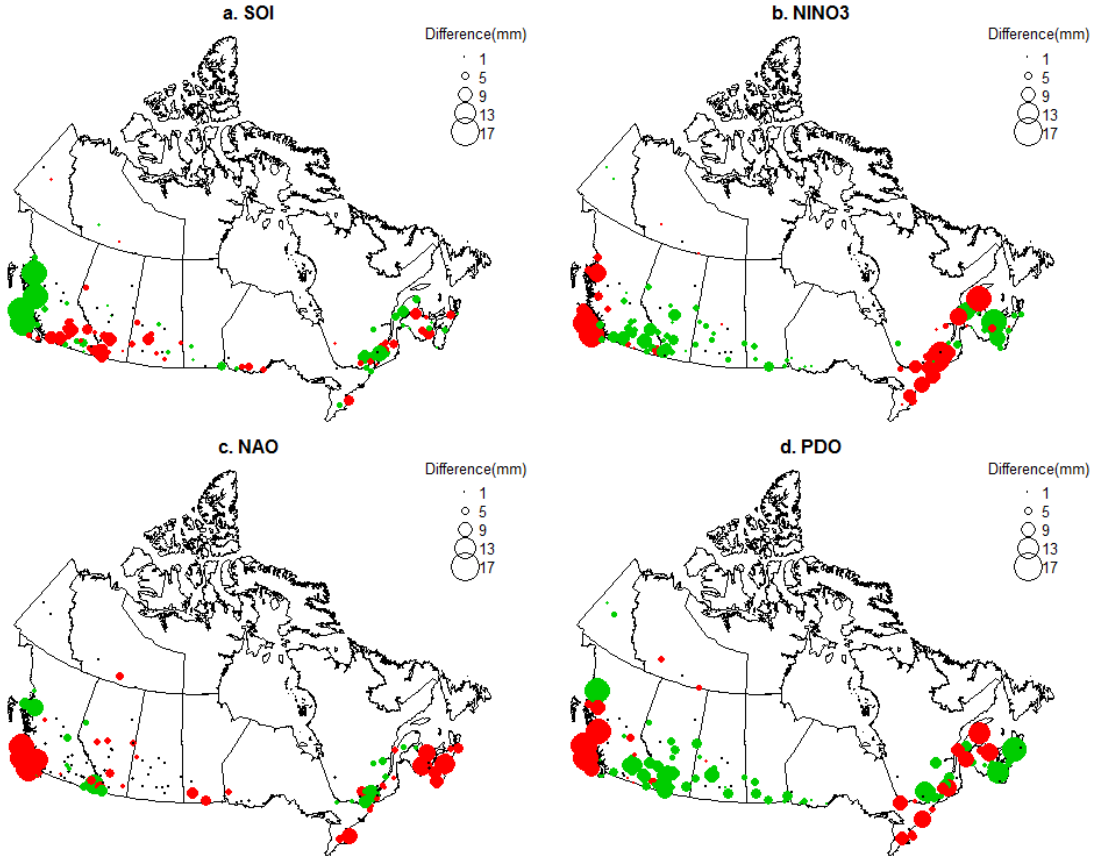

Figure 6-9 Composite differences in the winter (Dec-Jan-Feb) maximum daily precipitation averaged over the 5 years with the lowest SOI (a), NINO3 (b), NAO (c) and PDO (d) values and the 5 years with the highest SOI (a), NINO3 (b), NAO (c) and PDO (d) values. Red and green dots respectively indicate stations whose winter extreme precipitation is significantly influenced by large climate anomalies positively and negatively, respectively, while black dots indicate that SMDP differences are not statistically significant. The size of the dots shows the absolute magnitude of the composite difference.

There are significant seasonal variations between the influence of three large-scale climate patterns on the Canadian SMDP. For ENSO, represented by SOI and NINO3, the magnitude of SMDP in extreme El Niño years (minimal SOI and maxima NINO3) tends to be lower over the CP region in summer and winter compared with extreme La Niña years (maxima SOI and minimal NINO3), but it tends to be higher in spring and autumn. The effects of ENSO on the

winter SMDP agree well with the results of Zhang et al. (2010) for the Canadian winter SMDP. Spatially, ENSO exerts greater influence on the magnitude of SMDP in coastal than in inner regions. However, the influence of ENSO is not spatially consistent in these regions. Even though the composite SMDP differences of more stations showing positive (negative) relations with SOI (NINO3) index, there are stations that show an opposite relation with ENSO indices. This is somewhat different from a consistent spatial pattern of positive (negative) influence of ENSO represented by SOI (NINO3) on the total precipitation of southern Canada (Ropelewski and Halpert 1986; Shabbar et al. 1997). Although ENSO tends to have more-profound impact on the winter precipitation totals over North America than in other seasons (Ropelewski and Halpert 1986; Shabbar et al. 1997), the number of stations (35 and 42) where the winter SMDP is not significantly influenced by ENSO (SOI and NINO3) is much higher number of stations (24 and 17, on average) for SMDP of the other three seasons (Table 6-3). By comparing the seasonal variations of ENSO's effect given in Figures 6-9 and S16-18, we find that SOI and NINO3 has affected the summer and autumn SMDP the most, partly due to the relatively high magnitude of SMDP in these two seasons.

Table 6-3 Number of stations where composite differences in SMDPs are positively or negatively significant, or not significant in different seasons for four climate indices.

Significance	Spring	Summer	Fall	Winter
		SOI		
Negatively	60	35	50	43
Not significant	29	19	25	35
Positively	42	77	56	53
		NINO3		
Negatively	41	54	60	71
Not significant	24	12	16	42
Positively	66	65	55	18
		NAO		
Negatively	54	44	35	41
Not significant	59	38	55	66
Positively	18	49	41	24
		PDO		
Negatively	46	79	36	70
Not significant	30	18	20	30
Positively	55	34	75	31

Note that there are some differences between the influence of extreme ENSO represented by SOI and NINO3 on SMDP in all four seasons, as shown by the different number of stations where the SMDP-SOI and SMDP-NINO3 relationship is statistically significant, especially in winter (Table 6-3). For example, based on the composite analysis, the spring SMDP in all

stations of the PM region is much higher in extreme El Niño years than in extreme La Niña years represented by NINO3, but by SOI, only the spring SMDP of some stations is significantly lower in extreme El Niño years than in extreme La Niña years (Figure S16).

Spatially the composite differences in SMDP between years with extremely high and low phases of PDO are similar to those of ENSO (Figures 6-9 and S16-18). ENSO and PDO exert statistically significant influence on SMDP for a similar number of stations in all seasons (Table 6-3). An extremely positive PDO generally plays a similar role in increasing or decreasing the magnitude of Canadian SMDP as an extreme El Niño, other than an opposite influence of PDO versus El Niño for the autumn SMDP of the MC region. However, there are some composite differences in the magnitude of SMDP for the four seasons. The composite difference in the spring (summer and autumn) SMDP between positive and negative PDO is smaller (higher) than that between active El Niño and La Nina, but the composite difference in winter SMDP between these two opposite phases of PDO and ENSO are similar to each other.

A large proportion (about 58% in all seasons) (Table 6-3) of SMDP are significantly influenced by NAO statistically. Zhang et al. (2010) suggested that the influence of NAO on the winter SMDP over North America is regional and is not field-significant, as only 6% of stations show a statistically significant winter SMDP composite difference. However, for Canada, there is a spatial clustering of stations in the PM, BS and AM regions, where the winter SMDP is significantly influenced by NAO (Figure 6-9c), but not so for the spring SMDP. In the MC, CP and AM regions, the summer SMDP tends to decrease with NAO but it increases in other regions. Composite analysis shows that the autumn SMDP tends to increase with NAO in the PM, MC and AM regions but it tends to decrease in the CP and BS regions. Furthermore, the magnitude of autumn SMDP composite differences of stations significantly influenced by NAO can vary by up to about 12 mm per day in autumn.

6.5 Summary and conclusions

The oscillations of precipitation extremes (i.e., MMDP and SMDP) from 131 selected gauging stations across Canada and their teleconnections to large-scale climate anomalies were analyzed using variants of wavelet analysis and composite analysis. Our findings and conclusions can be summarized as follows:

1. Applying the Morlet WT to Canadian precipitation extremes, low-frequency, interannual (1-8 years) oscillations were found to be more significant than interdecadal (8-30 years)

oscillations for all selected stations, and the oscillations are both spatial and time-dependent in all 1-30 year time scale, even though interdecadal oscillations are generally more persistent than interannual oscillations. Even though precipitation extremes tend to exhibit larger temporal and spatial variabilities than precipitation totals, longitude-averaged SAWP of 3-30-year time scale for precipitation extremes represent less variability (7%) than that for precipitation totals (22%).

2. The precipitation extremes of 131 stations distributed over 9 ecoregions are linked to large-scale climate anomalies (based on climate indices) through WTC and PWC analyses. For each region, the wavelet coherence and phase difference between the leading PC1-2 of MMDP and climate indices are highly variable in periodicity and in time. Even though Pearson's correlation between the band-passed MMDP PC1-3 and climate indices are generally significant, a single climate index can explain less than 40% of the total variability at 1-30-year scale. These characteristics indicate changes in the strength of teleconnection between Canadian extreme precipitation and large-scale climate anomalies. PWC analysis shows that both ENSO and PDO modulated the interannual variability, and PDO modulated the interdecadal variability of MMDP over Canada. NAO is significantly correlated with the western MMDP at interdecadal scales and the eastern MMDP at interannual scales. Thus, incorporating climate indices such as the SOI, NINO3, PDO and NAO indices as predictors in teleconnection models can possibly improve the predictability of the Canadian MMDP.

3. Composite analysis shows that precipitation extremes at approximately 3/4 of the stations have been significantly influenced by ENSO and PDO patterns, while about 1/2 of the stations by the NAO patterns. The magnitude of SMDP in extreme El Niño years was mostly lower (higher) over the CP region in summer and winter (spring and autumn) than in extreme La Niña years. An extreme PDO event of positive phase played a similar role in increasing or decreasing the magnitude of Canadian SMDP compared with extreme El Niño events. Winter precipitation extremes over eastern Canada were also significantly influenced by NAO. As expected, overall, the degree of influence of large-scale climate patterns, i.e., ENSO, PDO and NAO, on Canadian precipitation extremes varies by season and by region.

Chapter 7 Projected timing of perceivable change in global extreme climate

7.1 Introduction

Extreme climate change could have various social, economic and environmental repercussions to our society (Garcia et al. 2014; Sherwood and Huber 2010; Urban 2015; Willis and Bhagwat 2009), such as a decrease in primary forest productivity because of heatwave and drought (Parmesan et al. 2000), increase in mortality (Oudin Åström et al. 2013; Shi et al. 2015), damage of infrastructure (Mailhot and Duchesne 2010), changes in energy consumption (Destouni et al. 2013), wild fire (Jolly et al. 2015; Westerling et al. 2006), and food and energy production (Wheeler and Braun 2013). Occurrences of climatic extremes have been observed and projected to change over the mid-latitude of Northern Hemisphere (NH) during the 20th and 21st century (Sillmann et al. 2013a; Sillmann et al. 2013b). Changes in climatic extremes have been detected in some regions (Meehl et al. 2000; Stott et al. 2010), such as observed positive trends in the frequency (Hegerl et al. 2004) and magnitude (Zwiers et al. 2011) of hot extremes. Some past studies have focused on the absolute magnitude of future climate change, albeit the magnitude of change relative to natural climate variability should be more useful since both natural and human systems can only tolerate certain degree of change from its existing level of climate variability (Meehl et al. 2000; Parmesan et al. 2000; Penuelas et al. 2013; Sherwood and Huber 2010; Walther et al. 2002; Williams et al. 2007).

There is considerable evidence that extreme weather and climate have been mechanistic drivers behind broad ecological responses to climate change (Garcia et al. 2014; Meehl et al. 2000; Parmesan et al. 2000). Possible changes in climatic extremes may exceed biological thresholds which are often neglected in ecological studies based on future climate scenarios, even though both gradual mean climatic trends and extreme climate have been implicated for various patterns of biological responses, such as local adaptation (e.g., morphological changes) or a poleward shift and an upward shift in elevation in the habitat range (Destouni et al. 2013).

If the signal (S) of climate change is of sufficient magnitude relative to natural climate variability (N), the climate change signal should be statistically significant, and the time of perceivable change in extreme climate is referred to as time of emergence (ToE) (Hawkins and Sutton 2012) or “time of expulsion” (Power 2014). ToE represents the pace of perceivable

climate change, and thus it is a key indicator for predicting climate change impact to natural and human systems (Sherwood and Huber 2010; Williams et al. 2007). If ToE is early, it gives little time for implementing effective adaptations and mitigation measures. However, knowledge about ToE of climate change will motivate people to take necessary actions to reduce greenhouse gas emissions, to defer or even to eliminate the projected ToE for climate change. Even though ToE of the global mean climate is projected to emerge by 2100 (Hawkins and Sutton 2012; Williams et al. 2007), it is unclear when the ToE of extreme climate change will occur because it is not possible to validate extreme climate projections (Easterling et al. 2000). However, recent model assessment studies (Fischer and Knutti 2014; Fischer et al. 2013; Sillmann et al. 2013a; Sillmann et al. 2013b) suggest that simulations from the Coupled Model Inter-comparison Project Phase 5 (CMIP5) are robust enough to represent past and future regional extreme climate and have been widely adopted for studies on the assessment of impacts of changes in extreme climate (Donat et al. 2016; Harrington et al. 2016; King et al. 2015).

We investigated the ToE of annual extreme climate represented by 18 indices defined by Expert Team on Climate Change Detection and Indices (ETCCDI) (Zhang et al. 2011), 10 for temperature and 8 for precipitation (Table 7-1), using historical and projections of 30 global General Circulation Models (GCMs, Table 7-2) of CMIP5 (Taylor et al. 2012), and 39 ensembles from the CESM1 large ensemble community project (CESM-LE) (Kay et al. 2015) under climate scenarios of Representative Concentration Pathways 8.5 (RCP8.5). These 18 ETCCDI indices encompass a wide variety of metrics to describe the magnitude, frequency and severity of extreme climate which can significantly affect ecological and human systems. For example, the magnitude indices txx (maximum of daily maximum temperature) and tnn (minimum of daily minimum temperature) are the hot and cold tolerance of many plants, respectively (Parmesan et al. 2000). Even if the magnitude of extreme temperature and precipitation is within its tolerance range, changes in the frequency of hot and cold extremes represented by tx90p and tn10p (percentage of time when daily maximum temperature is higher, and the minimum temperature is lower than the 10th percentile, respectively) could exceed the physiological tolerance of a particular species. Life dieback, mortality and reproductive failure in large areas on a continental scale are usually linked with severe drought and heatwaves (Allen et al. 2010; Penuelas et al. 2013) described by severity indices such as wsdi (annual count when at least six consecutive days of maximum temperature is larger than the 90th percentile) and cdd

(maximum number of consecutive days when precipitation is lower than 1 mm) (Jentsch et al. 2009). Heavy precipitation represented by indices such as rx1day or rx5day (maximum consecutive 1- and 5-day precipitation) can reduce the flowering length by several days (Jentsch et al. 2009).

When the pace of change to extreme indices emerge beyond the adaptability limit of the ecosystem, its species compositions could alter, and the productivity and plant phenology of its plant communities could change or shift (Jentsch and Beierkuhnlein 2008; Reusch et al. 2005). As a result, the biodiversity and resistance to invasion (Burrows et al. 2014; Loarie et al. 2009; Parmesan et al. 2000) of the ecosystem will be affected. Human health will also be impacted by extreme climate events including heatwaves, droughts and heavy precipitation of long-duration (Haines et al. 2006; McMichael et al. 2006), which can also be comprehensively measured by indices designed to represent the frequency and severity of extreme temperature and precipitation, such as wsdi, tx90p, rx1day, rx5day and cdd. If the pace of change in extreme climate exceeds the public's health system to overcome adverse climate-related health consequences, people, especially those from low-income countries, will not be able to adapt to such extreme events because of the high cost to improve health care. We emphasize that detecting the projected timing of perceivable change in extreme climate relative to the variability of recent past is of greater relevance for the adaptation of human and ecosystems, than the timing when anthropogenic signals of extreme climate change emerge from internal climate variability exhibited in a pre-industry period.

We estimated ToE of indices for each grid of each ensemble member (*Methods* and Figure 7-1), which is the year when the trend S exceeds n times the noise N, i.e., $S/N > n$. S is estimated using a normal distribution for frequency and severity indices, a generalized extreme value (GEV) distribution for magnitude indices, and N is the standard deviation (SD) of the time series detrended by S. The ToE is the year when S exceeds the n times of N, i.e., $S/N > n$. We chose the S/N threshold n values (Table 7-1) partly to follow values used by previous studies for mean temperature and precipitation (Hawkins and Sutton 2012; Maraun 2013; Sui et al. 2014) and partly to ensure that considerable percentage of global grids will show ToE before 2100. The ensemble median ToE was then calculated for each metric by regridding ToE of each ensemble member to a common grid system of 2˚×2˚ resolution. Since the ensemble median ToE generally outperforms individual ToEs (Sillmann et al. 2013a), and in using a median ToE, the possible

influence of outliers of ToE can be nullified (Hawkins et al. 2014), our results are based on ensemble median ToE.

Table 7-1 Extreme climate indices analyzed

#	Variable	Indices	Type	Low *S/N*	High *S/N*	Annual	Seasonal	Name	Definition
1	Temperature	txx	Absolute magnitude	1	2	√	√	Max Tmax	Maximum value of daily max temperature
2		tnx	Absolute magnitude	1	2	√	√	Max Tmin	Maximum value of daily min temperature
3		txn	Absolute magnitude	1	2	√	√	Min Tmax	Minimum value of daily max temperature
4		tnn	Absolute magnitude	1	2	√	√	Min Tmin	Minimum value of daily min temperature
5		tn10p	Percentile frequency	1	2	√	√	Cool nights	Percentage of time when daily min temperature < 10th percentile
6		tx10p	Percentile frequency	1	2	√	√	Cool days	Percentage of time when daily max temperature < 10th percentile
7		tn90p	Percentile frequency	1	2	√	√	Warm nights	Percentage of time when daily min temperature > 90th percentile
8		tx90p	Percentile frequency	1	2	√	√	Warm days	Percentage of time when daily max temperature > 90th percentile
9		wsdi	Threshold severity	1	2	√		Warm Spell Duration Index	Annual count when at least six consecutive days of max temperature > 90th percentile
10		csdi	Threshold severity	0.5	1	√		Cold Spell Duration Index	Annual count when at least six consecutive days of min temperature < 10th percentile
11	Precipitation	rx1day	Absolute magnitude	0.5	1	√	√	Max 1-day precipitation	Maximum 1-day precipitation
12		rx5day	Absolute magnitude	0.5	1	√	√	Max 5-day precipitation	Maximum consecutive 5-day precipitation
13		r10mm	Threshold frequency	0.5	1	√		Number of heavy precipitation days	Annual count when precipitation ≥ 10 mm
14		r20mm	Threshold frequency	0.5	1	√		Number of very heavy precipitation	Annual count when precipitation ≥ 20 mm
15		cdd	Threshold severity	0.25	0.5	√		Consecutive dry days	Maximum number of consecutive days when precipitation < 1 mm
16		cwd	Threshold severity	0.5	1	√		Consecutive wet days	Maximum number of consecutive days when precipitation ≥ 1 mm
17		r95p	Percentile frequency	0.25	0.5	√		Very wet days	Annual total precipitation from days > 95th percentile
18		r99p	Percentile frequency	0.25	0.5	√		Extremely wet days	Annual total precipitation from days > 99th percentile

Table 7-2 GCMs used in the analysis

#	Model Name	#	Model Name
1	ACCESS1-0	16	GFDL-ESM2G
2	ACCESS1-3	17	GFDL-ESM2M
3	bcc-csm1-1	18	GISS-E2-R
4	bcc-csm1-1-m	19	HadGEM2-ES
5	BNU-ESM	20	inmcm4
6	CanESM2	21	IPSL-CM5A-LR
7	CCSM4	22	IPSL-CM5A-MR
8	CESM1-FASTCHEM	23	IPSL-CM5B-LR
9	CMCC-CM	24	MIROC4h
10	CMCC-CMS	25	MIROC-ESM
11	CNRM-CM5	26	MIROC-ESM-CHEM
12	CSIRO-Mk3-6-0	27	MPI-ESM-LR
13	EC-EARTH	28	MPI-ESM-MR
14	FGOALS-s2	29	MRI-CGCM3
15	GFDL-CM3	30	NorESM1-M

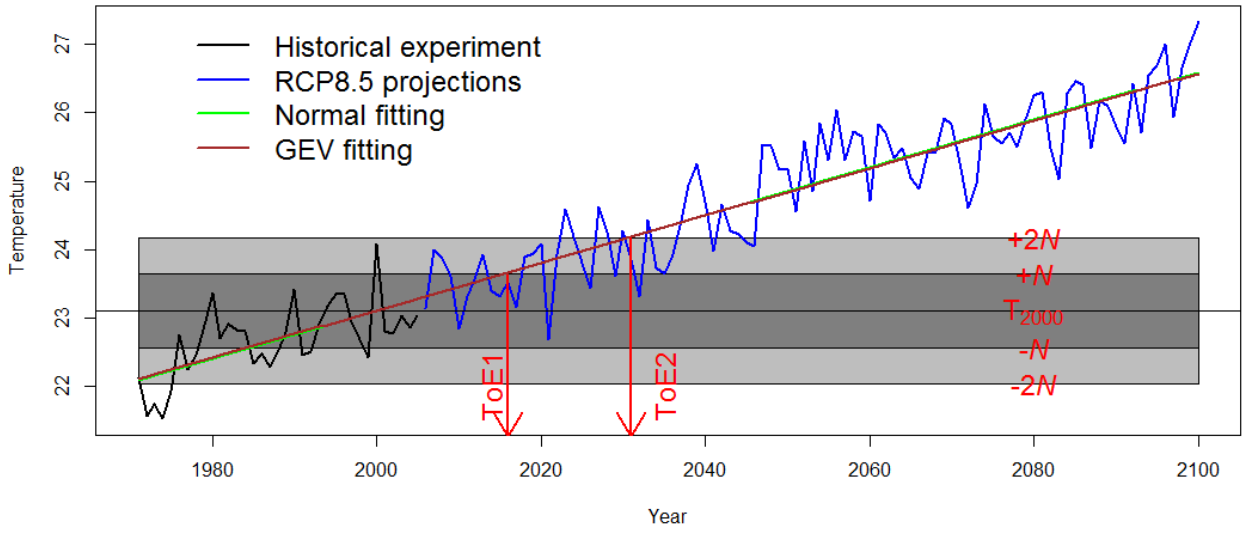

Figure 7-1 . Illusion of the time of emergence (ToE). An example of ToE estimated for the txx (annual maximum daily maximum temperature) of a grid box in the Atlantic Ocean (30˚W, 30˚N). *S* is the trend represented by the slope of fitted lines for txx time series. *N* is the residual standard deviation of time series. ToE is the year when the trend estimated based on the normal distribution(green line) and the GEV distribution (brown line) exceeds the range of historical variability represented by *n* times (*S*/*N*) the residual standard deviation of the txx time series during 1971-2100, relative to the base year 2000 (*n* is a threshold of interest show in Table S1). The threshold of *S*/*N* for ToE1 and ToE2 are 1 and 2, respectively.

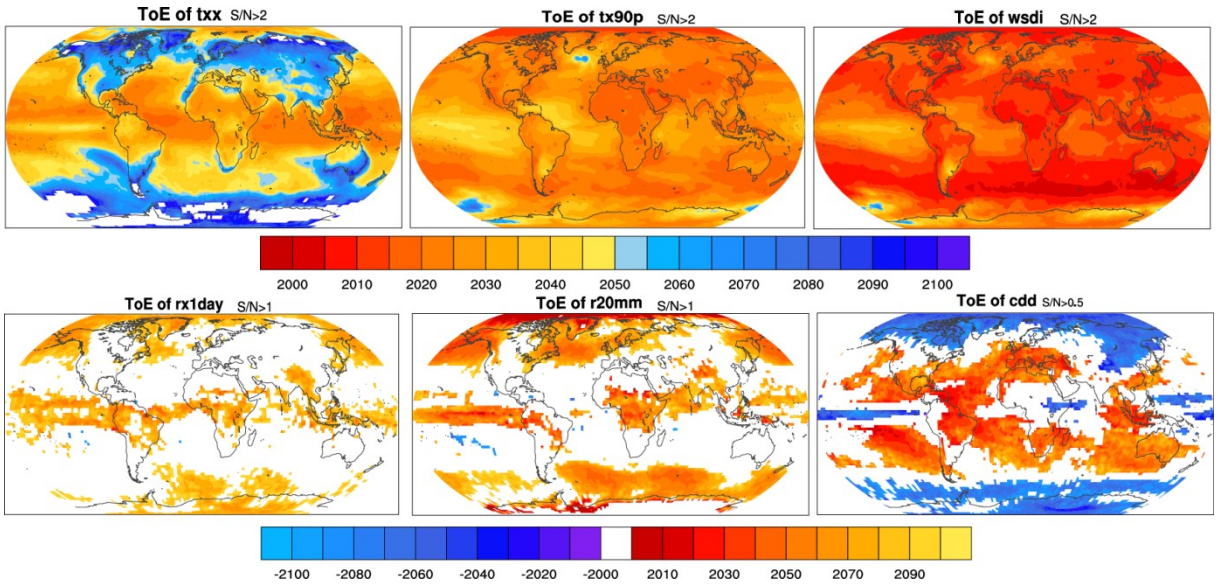

Figure 7-2 Global distributions of ToEs of different *S*/*N* thresholds under RCP8.5. ToE of 6 representative extreme temperature (txx, tx90p and wsdi) and precipitation (rx1day, r20mm, and cdd) indices for high thresholds of *S*/*N*. For extreme precipitation indices, the blue/green (red/yellow) color shows ToEs exhibiting perceivable decreasing (increasing) change. Blank grids show the ToEs will not occur by 2100.

7.2 Discussions of results

The year at which the *S/N* of climatic extremes exceeds certain thresholds varies considerably between different extreme climate indices (Figures 7-2 and S2). We found that ToEs under low *S*/*N* thresholds are about 10~30 years earlier than those under high *S*/*N* thresholds. Under RCP8.5, the projected magnitude of temperature extremes, represented by txx and tnx (maximum value of daily minimum temperature) for hot extremes and tnn and txn (minimum value of daily maximum temperature) for cold extremes, respectively, across all land and ocean regions will almost exceed their 2 SDs before 2100, as most grids show median ToEs to occur before 2100 (Figures 7-2 and S3) and the low and high values (represented by the 25th and 75th percentiles of the values derived from GCM ensembles) of ToEs to also occur before 2100 (Figure S4). Although ToEs with *S*/*N* >2 for the frequency of hot extremes represented by tx90p and tn90p (percentage of time when the daily minimum temperature is larger than the 90th percentile) are projected to be earlier than 2050, those of cold extremes represented by tn10p and tx10p (percentage of time when daily maximum temperature is lower than the 10th percentile) will occur later than 2070 and the ToEs for the frequency of cold extremes in most ocean grids will not occur before 2100. The median ToEs for the frequency of hot (cold) extremes in all global grids with *S*/*N* >2 will be 2022 (>2100), while ToEs for the magnitude counterparts will be 2068 (2052), respectively. The early ToEs for the severity of hot extremes represented by wsdi is more significant than those of cold extremes represented by csdi (annual count when at least six consecutive days of minimum temperature is lower than the 10th percentile), as the median ToE for wsdi of all global grids with *S*/*N* >2 is 2013 while that for csdi with *S*/*N* >0.5 is 2092.

Spatially, ToEs for extreme temperature magnitudes will occur 2-3 decades earlier in low-latitudes than in mid-latitudes (Figures 7-2, S2 and S5) because in the former these indices have low variability. These results are similar to ToEs for the mean daily temperature that has already been observed in some parts of the world (Anderson 2011; Diffenbaugh and Scherer 2011; Mahlstein et al. 2012) and in various climate model simulations (Anderson 2011; Diffenbaugh et al. 2011; Hawkins and Sutton 2012; Mahlstein et al. 2013). On average ToEs for the magnitude of hot and cold extremes tend to occur 5-25 years earlier in oceans than in land (Figure S3). ToEs for the magnitude of hot and cold extremes tend to occur earlier in northern high-latitudes which have both higher variance and trends than those in mid-latitude regions. However, ToEs

for the frequency of hot and cold extremes will occur earlier in mid-latitudes than in low- and high-latitudes. ToEs for the frequency of cold extremes will occur 10-30 years earlier in oceans than in land, while ToEs for the frequency of hot extremes will be comparable between oceans and land. ToEs for the severity of hot (cold) extremes will occur about 3 (10-20) years earlier (later) in oceans than in land (Figure S3).

Globally ToEs for the magnitude and frequency of extreme precipitation is projected to occur before 2100 only for $S/N > 1$ because of the large variability of extreme precipitation, as was also found in climate model simulations for total precipitation (Beaumonta et al. 2011; Giorgi and Bi 2009). The median global ToE for extreme precipitation magnitude (rx1day and rx5day) is projected to be approximately 2048 and 2095 for $S/N > 0.5$ and $S/N > 1$, respectively. The median global ToE for the frequency counterpart represented by r10mm and r20mm (annual count of precipitation events when daily precipitation is larger than 10 and 20 mm, respectively) is projected to occur earlier, at approximately 2040 and 2080 for $S/N > 0.5$ and $S/N > 1$, respectively (Figure S3). The evolution of fraction of land and ocean grids showing ToEs for the magnitude and frequency of extreme precipitation are projected to be similar in land and ocean (Figure S3). For $S/N > 0.5$, the global median ToEs for the severity of extreme precipitation represented by the consecutive wet and dry days (cwd and cdd) is projected to occur by 2065 and 2062, respectively.

Unlike hot extremes projected to increase globally under global warming, there are some land areas in Central America, Mediterranean, Australia, South Africa and oceans in southeastern Pacific, Southern Indian, Central and Southern Atlantic where extreme precipitation is projected to decrease both in magnitude and frequency (Figures 7-2, S2, S4, S7 and S8). However, the severity of droughts (cdd) in these regions is projected to increase (Figures 7-2, S2 and S4), which means that the climate of these regions is expected to become drier. Furthermore, cwd is also projected to decrease in South America, Central and South Africa, Mediterranean regions and Australia (Figure S7) because of more frequent transitions between wet and dry days under an intensified hydrological cycle (Held and Soden 2006). The spatial pattern of projected changes in extreme precipitation is consistent with some recent studies that support the paradigm, “wet gets wetter and dry gets drier” (Held and Soden 2006; Trenberth 2011). Since the variability (trend) of extreme precipitation is significantly lower (higher) in high- and low-latitudes than in mid-latitudes, ToEs for the magnitude and frequency of extreme precipitation

are projected to occur earlier in high- and low-latitudes than in mid-latitudes, while ToEs for the severity of extreme precipitation are projected to occur earlier in mid-latitudes than in high-and low-latitudes (Figures 7-2, S2, S4, S7 and S8).

ToEs for the frequency of hot extremes in various terrestrial biomes and marine realms of the world will be approximately 3-50 years earlier than the magnitude counterparts of hot extremes, and the projected perceivable changes in severity of hot extremes will occur approximately 10 years earlier than the frequency counterparts with $S/N > 2$ (Figures 7-3, 7-4 and S9-S11). Tropical and subtropical forests are projected to experience earlier ToEs for the magnitude and frequency of extreme temperature (2010-2050) than other biomes (2040-2070) (Figure 7-4). ToEs for extreme temperature magnitude in Tropic Atlantic, Indo-Pacific, Tropical eastern Pacific (2025-2050) are projected to be much earlier than other marine realms (2030-later than 2100) (Figure 7-4). ToEs for the magnitude of extreme temperature in marine realms of low- and mid-latitudes in NH (Realms 3-8 of Figure 7-4; 2020-2070) are projected to occur earlier than those in the Southern Hemisphere (SH) (Realms 9-12; later than 2030) especially in the Southern Ocean where the median ToEs for the magnitude, frequency and severity of extreme temperature are all projected to be 10-30 years later than other marine realms.

For changes in extreme precipitation, only certain grids for all terrestrial biomes and marine realms are projected to experience perceivable changes before 2100 with both high (Figures 7-3, 7-4 and S9-S11) and low (Figures S9-S11) S/N thresholds, because of high spatial variabilities of the magnitude, frequency and severity of extreme precipitation. For most biomes, higher fractions of grids are projected to experience ToEs before 2100 for the severity than for the frequency and magnitude of extreme precipitation. Moreover, in grids where ToEs are projected to occur before 2100, perceivable changes in the severity of extreme precipitation are projected to occur earlier than its frequency and magnitude. For ToEs of cdd with $S/N > 0.5$, 95% of grids in biomes of Tropical and subtropical coniferous forests and Mediterranean forest are projected to occur before 2100 (with median ToEs of around 2050 and 2045, respectively), which implies a high risk of potential changes in these two ecosystems because of worsening drought severity. However, the high-latitude biomes (boreal forest/taiga and tundra) are projected to experience earlier perceivable changes in the frequency than the magnitude and severity of extreme precipitation, because a larger fraction of grids where ToEs for r20mm are projected to occur before 2100 than ToEs for rx1day and cdd, and similarly with an earlier

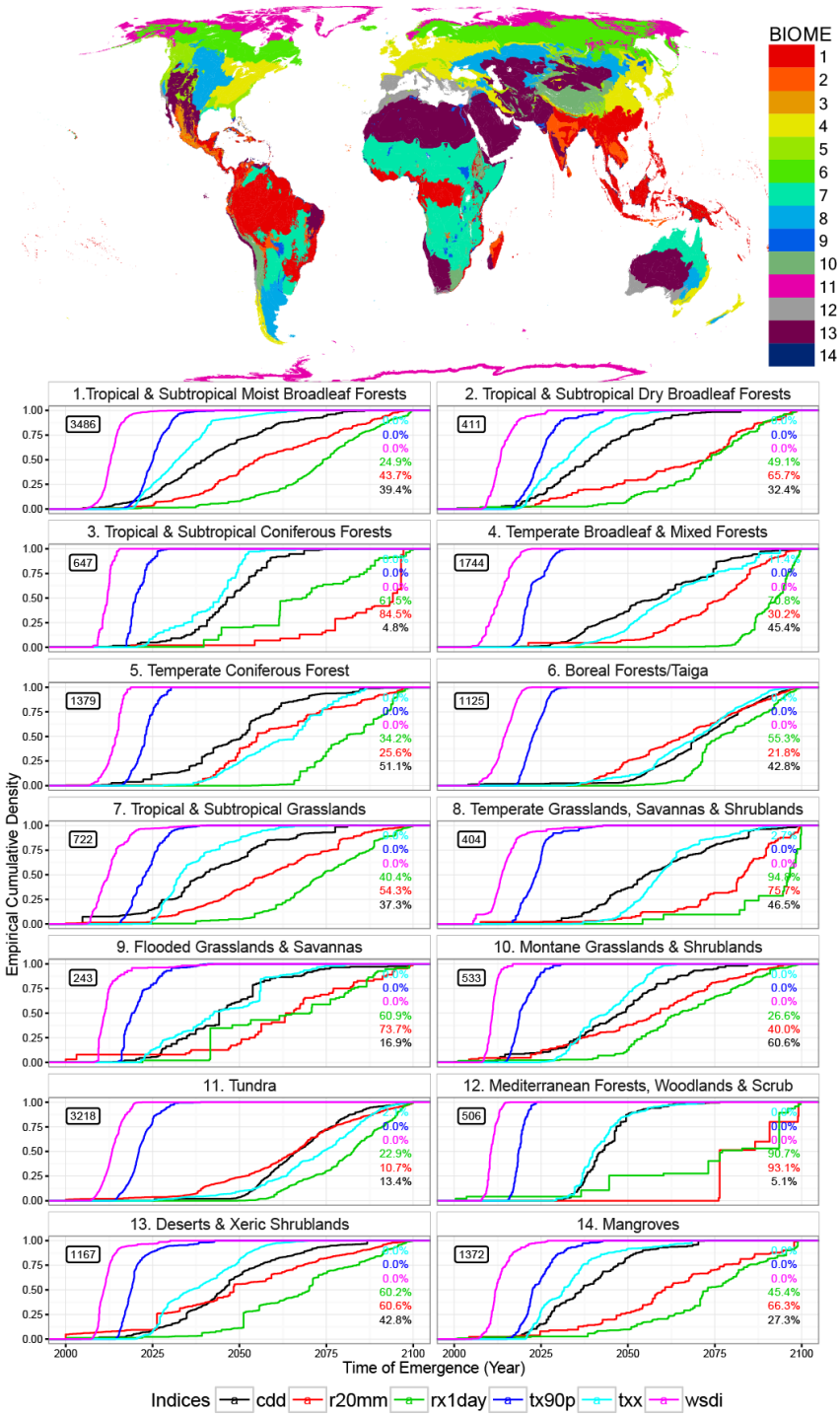

Figure 7-3 Time evolution of fraction of grids showing ToE. The fraction is the ratio of the number of cumulative grids where ToEs are not later than a year to the total number of grids where perceivable changes in extreme climate have occurred by 2100 under *high thresholds of S/N* (Table 7-1) for 6 representative extreme climate indices in each terrestrial biomes (left two columns) and marine realms (right two columns) under RCP8.5. The thresholds of *S/N* chosen for extreme climate indices, txx, tx90p and wsdi are 2, and for rx1day and r20mm are 1, and for cdd is 0.5, respectively. Definitions of these indices are given in Figure 7-2's legends and in Table 7-1. Numbers in the top left frame are the total number of grids for each biome or realm. Numbers in the right show the percentage of grids where ToEs are later than 2100, with the same colors applied to evolution lines for indices.

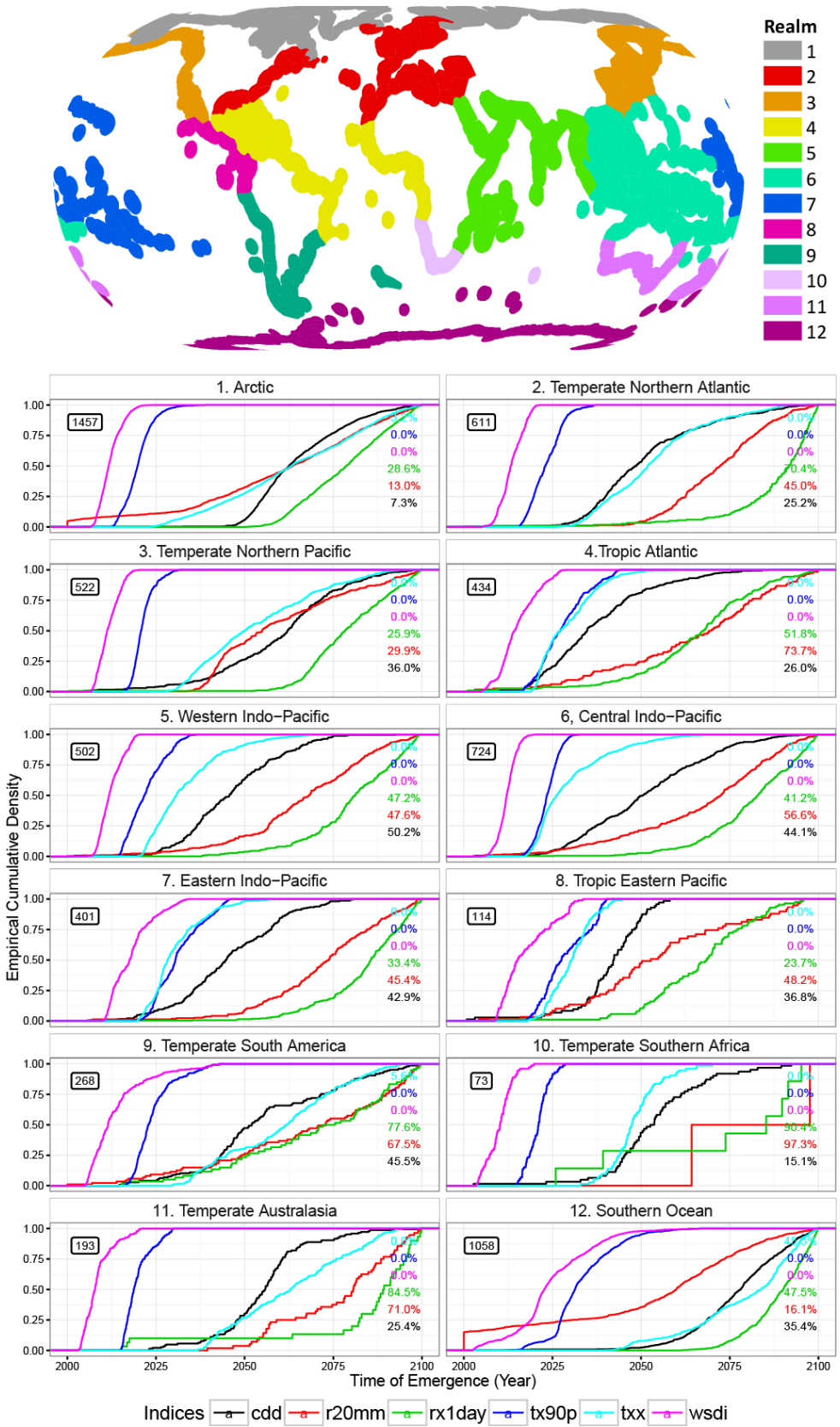

Figure 7-4 Same as Figure 7-3, but for marine realms.

median ToEs for r20mm than for rx1day and cdd (Figure 7-4). More than 80% of grids with tundra biome, which is much higher than other biomes, are projected to experience ToEs with high *S*/*N* thresholds before 2100 in the magnitude, frequency and severity of extreme precipitation (Figure 7-3 and S10-11) because of Arctic amplification by which atmospheric moisture is expected to increase under warmer climate (Ghatak et al. 2010).

Similar to high-latitude terrestrial biomes, high-latitude marine realms such as the Arctic, temperate northern Pacific and Atlantic are also projected to experience more widespread perceivable changes in extreme precipitation (Figure 7-4 and S10-11), even though the median ToEs for grids (where ToEs are projected earlier than 2100) are not projected to be significantly earlier than the median ToEs of other marine realms of the NH. Only about half of grids of low- and mid-latitude marines in NH, such as tropic Atlantic, Indo-Pacific, are projected to experience ToEs with high *S*/*N* thresholds for extreme precipitation, and there are no major differences in the percentage of grids where ToEs are projected to be earlier than 2100, irrespective of whether it is for the magnitude, frequency or severity of extreme precipitation. Again, ToEs for extreme precipitation over marine realms in SH are projected to be very late (2075 and thereafter).

If emissions of greenhouse gases will occur according to RCP8.5 climate scenarios, roughly 0.75 billion urban residents currently living in major cities across the world could experience perceivable changes (ToEs) in the daily maximum temperature txx (magnitude of hot extremes) in 2050 under high *S*/*N* thresholds, while 0.28, 0.33 and 0.86 billion residents could experience perceivable changes in the magnitude, frequency and severity of extreme precipitation represented by rx1day, r20mm and cdd, before 2080, respectively (Figure 7-4 and S12). However under low *S/N*, similar size of urban residents is expected to experience perceivable changes in these climate indices much earlier, as many as 50 years in advance. The urban population expected to experience such perceivable changes in extreme precipitation represented by rx5day, r10mm and cwd before 2080 under high *S*/*N* thresholds is projected to be 0.20, 0.35 and 0.08 billion, respectively (Figure S12a). Thus, the population projected to be exposed to severe dry climate (0.86 billion) before 2080 is considerably higher than those projected to experience severe wet climate (0.08 billion). All major urban residents (around 1.4 billion) will encounter perceivable changes for the frequency and severity of hot extremes, tx90p and wsdi, before 2035 and before 2020 under low and high *S*/*N* thresholds, respectively. However, under high *S*/*N* thresholds, virtually no urban population in major cities is expected to

experience perceivable changes (ToEs) for the frequency and severity of cold extremes before 2060 and 2100, respectively (Figures S12a and S12b), but about 0.5 billion urban population could experience perceivable changes for the magnitude of cold extreme before 2060.

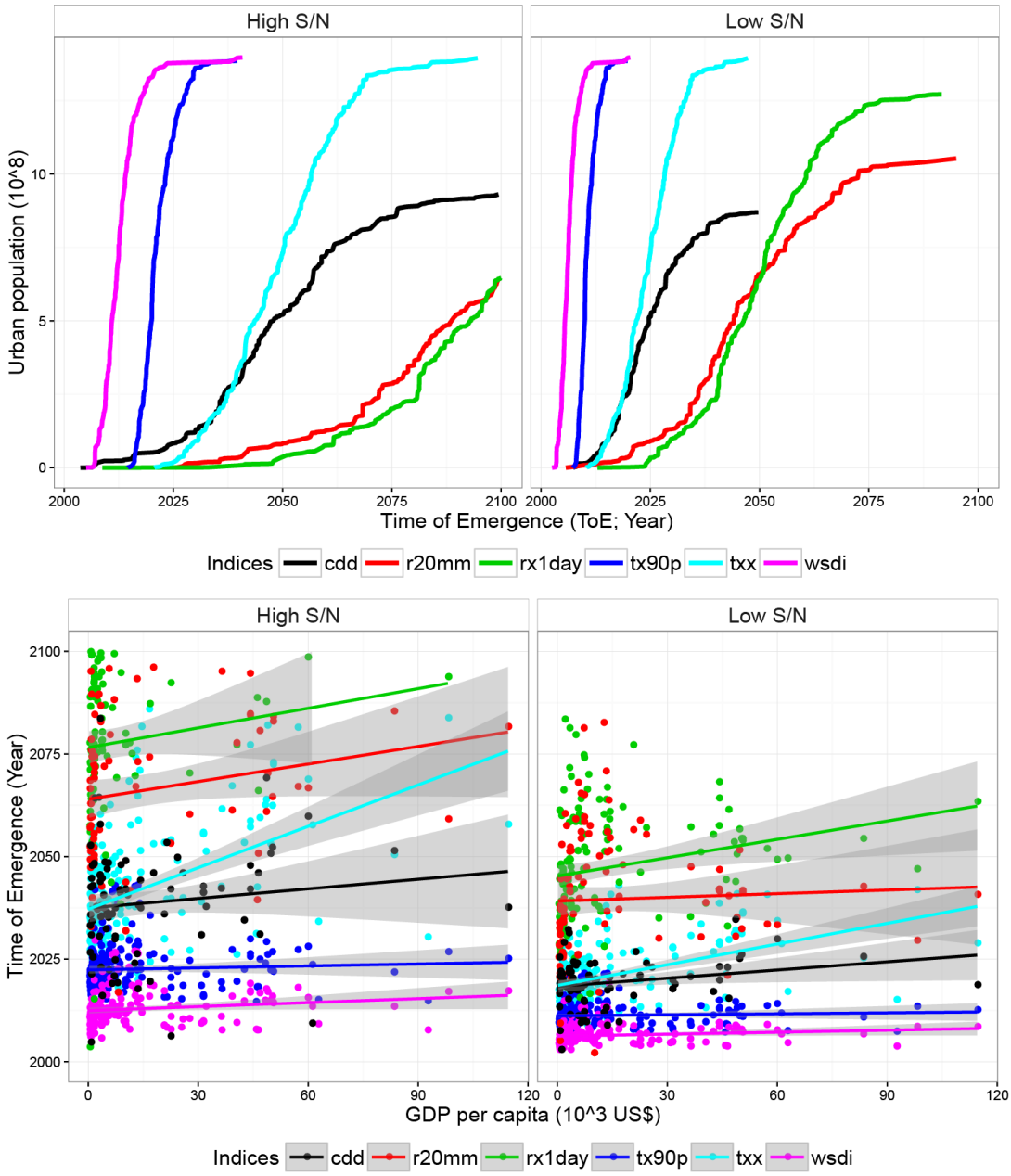

Figure 7-5 Exposure of human societies to ToEs of extreme climate change. Top two pannels show the time evolution of urban residents in 590 large cities exposed to ToE of various extreme climate indices, i.e., txx, tx90p, wsdi, rx1day, r20mm and cdd, while bottom two pannels show the scatterplots between the medium ToEs (in years) and the GDP per capita for 231 countries. Least-squares regression lines and confidence intervals (grey bands) are also shown in the scatterplots. Left two pannels shows results under the high threshold of *S/N* while right two under the low threshold of *S/N* that are listed in Table 7-1. Definitions of these indices are given in Figure 7-2's legends and in Table 7-1.

Based on generally positive relationships between median ToEs for grids over a country and GDP per capita of that country considered (Figures 7-5 and S12), it seems that early perceivable extreme climate change tends to occur in low-income countries. This projected, global, socio-economic response to climate change impact will not provide much incentive to high-income countries capable of reducing GHG emissions to mitigate climate change impact given they will likely benefit less from mitigation than low-income countries who will be more in need of increasing GHG emissions for their socioeconomic development. On the other hand, because wealthy countries tend to suffer much more loss of properties from extreme events, which likely occur more frequently and in greater severity because of climate change impact (Diffenbaugh et al. 2007), they should be motivated to reduce GHG emissions.

7.3 Methods

The analysis was done with climate extreme indices defined by the Expert Team on Climate Change Detection and Indices (ETCCDI) (Zhang et al. 2011) using daily temperature and precipitation data simulated by GCMs of the CMIP5 for both the base and climate projection periods. The global extreme temperature and precipitation data simulated by GCMs of CMIP5 have been widely assessed and found to be appropriate by various studies (Fischer and Knutti 2014; Fischer et al. 2013; King et al. 2015; Sillmann et al. 2014; Sillmann et al. 2013a). 18 annual indices (Table 7-1; including 10 extreme temperature and 8 extreme precipitation indices) were computed from data simulated by multi-GCMs for historical experiments over the baseline (1971-2005) and the future period (2006-2100) projections under RCP8.5 climate scenarios (Table 7-2). Only one realization ("r1i1p1") of each GCM was selected for this study. The magnitude, frequency and severity of extreme temperature and precipitation were estimated in terms of three types of indices, e.g., absolute, percentile and threshold indices (see the type of indices in Table S1). We used GCMs' simulations for the base period as the historical data, rather than gridded, observed data such as HadEX2 and GHCNDEX, to minimize the effect of bias of GCMs on ToEs estimated from the results of CMIP5.

We estimated the 1971-2100 trend signal (S) from individual time series of selected ETCCDI indices for each grid cell of a GCM fitted with a non-stationary normal distribution for frequency and severity indices, and a non-stationary generalized extreme value (GEV) distribution for magnitude indices, respectively. Thus for year t_i, i = 1,.., K=130, a climate index

y_i is described as $y_i \sim$ (μ_i, σ) with $\mu_i = a + St_i$ for the non-stationary normal distribution, or $y_i \sim$ $_i, \sigma_i, \xi)$ with $\mu_i = a_\mu + S_\mu t_i$, $\sigma_i = a_\sigma + S_\sigma t_i$ and $S = S_\mu - S_\sigma/\xi + S_\sigma/\xi\,\Gamma(1-\xi)$ for the non-stationary GEV distribution (Coles 2001; Maraun 2013), respectively. Distribution parameters such as $\mu_i, a, a_\mu, a_\sigma, S, S_\mu, S_\sigma, \sigma, \sigma_i$ and ξ were derived from a least-squares regression for normally distributed indices and the maximum likelihood method implemented in the R package "extRemes" (Gilleland and Katz 2011) for GEV distributed indices, respectively. The noise (*N*) is the interannual variability computed as the detrended standard deviation of a time series *y* during 1971-2100, $N^2 = (1/K - 1)\sum_{i=1}^{K}(y_i - \mu_i)^2$. The ToE, emergence of signal from a fraction, *n*, of the internal variability relative to the reference year of 2000, is $\mathrm{ToE}(n) = 2000 + n \cdot |N/S|$ (Figure 7-1). Because spatial averaging could reduce the variability of climate indices in grid cells (Kendon et al. 2008), ToEs tend to be earlier in larger than smaller spatial scales (Maraun 2013). Therefore, for each extreme climate index selected, instead of normalizing *S* and *N* estimated from multi-GCMs before estimating ToEs, we first estimated ToE for each grid cell of each GCM data. After that, we regridded ToEs derived from each GCM to a standard 2˚×2˚ grid to estimate the ensemble median ToE. The uncertainty of the ToE is based on the 25th and 75th percentile of ToEs from GCMs.

Since there may be some uncertainties associated with the intra-model simulations, we also used 39 model simulations from the CESM1 Large Ensemble Community Project (CESM-LE) (Kay et al. 2015) to calculate projected ETCCDI indices of annual scale and we estimated the ToE for the 39 model simulations. The range of ToEs derived from 39 CESM-LE ensembles is generally within the range of ToEs derived from multi-model simulations. The uncertainty of ToEs of CESM-LE ensembles is less than that of multi-model simulations. On the basis of the 1979-2005 ERA-Interim reanalysis(Dee et al. 2011) daily data as the "observed" data, and the empirical, quantile mapping bias correction method, we corrected possible biases in model simulation of CESM-LE ensembles used to estimate projected extreme climate indices. ERA-Interim 1979-2005 and GCM 1979-2005 data were used to obtain parameters for quantile mapping using the "fitQmapQUANT" function and then CESM-LE 1979-2100 data were bias-corrected using the "doQmap" function implemented in the R package "qmap" (Gudmundsson et al. 2012). To assess the effects of model simulation bias that are possibly large in projected

threshold-based extreme climate indices (Cannon et al. 2015; Scherer and Diffenbaugh 2014; Sillmann et al. 2013a), we compared ensemble median ToEs derived from raw model simulations versus bias-corrected model simulations for threshold-based indices that were used in this study (Figures S13-S14). Given the spatial distributions of ToEs derived from threshold-based indices estimated from raw and bias-corrected datasets are consistent to each other, we therefore used ToEs derived from raw instead of bias-corrected model simulations for further analysis of impacts of extreme climate change.

ToEs for 14 major terrestrial biomes and 9 marine realms of the world are based on the World Wildlife Fund (WWF) terrestrial ecoregions (Olson et al. 2001) and marine ecoregions (Spalding et al. 2007), respectively. We determined the distributions of projected ToE of extreme climate indices for each biome and realm by overlaying terrestrial and marine ecoregions maps with maps of median ToE derived, and so we extracted ToEs for each ecoregion. To assess possible impact of extreme climate change on human societies, the same procedure as those of ecosystems was conducted using maps for urban populations (in 2010) of the largest 590 cities of the world obtained from the archive of Demographia World Urban Areas, and maps of GDP per person for all countries of the world in 2010 obtained from the World Bank. Urban residents are substantially more susceptible to impacts of extreme climate such as extreme heat waves (Smoyer et al. 2000), droughts and floods (Haines et al. 2006; McMichael et al. 2006) than rural residents.

Chapter 8 Conclusions and future work

8.1 Conclusions

In this thesis, the first six chapters are devoted to analyzing and characterizing hydroclimate extremes over Canada, while Chapter 7 is devoted to global extreme climate change that can be broadly categorized under annual, seasonal, spatial, nonstationary and multivariate extremes. This research is based on rigorous statistical analysis of the long-term daily precipitation and streamflow data of hydroclimate stations across Canada. The following summaries will be useful for water policymakers and engineers involving in water resources management and planning to mitigate potential impact of water-related nature hazards such as floods and droughts.

1) Non-stationarities of streamflow and precipitation

From analyses of 145 RHBN and non-RHBN stations of Canada with long-term AMS series and hydrological observations, the results show that almost half of the stations experienced an abrupt shift in the mean of the annual maximum daily streamflow (AMS). The timing of abrupt change points have been shown to be closely related to the years when the regulation of streamflow began. About 1/3 stations exhibit monotonic temporal (more negative than positive) trends. However, only 12 out of 59 stations detected with abrupt change points showed significant monotonic trends in the time series before and/or after change points were detected. Thus, abrupt changes are more likely the cause of nonstationarities to AMS series over Canada than monotonic trends. More than 2/3 of the AMS series could be accurately fitted with non-stationary lognormal and gamma probability distributions.

From analyses of time series of annual maximum daily precipitation (AMP) and counts of extreme/heavy precipitation of 463 gauging stations of Canada, the results show that about 1/3 of AMP time series shows non-stationary characteristics. Stations located in southwestern Canada, northern Canadian Prairies (CP) and Quebec (QC), Newfoundland (NL), and southwestern Ontario (ON) showed statistically significant increase in AMP, while AMP in southern CP, southeastern ON and Arctic region significantly decreased.

From analyses of 100 and 145 stations of long-term daily precipitation and streamflow records across Canada, the results show that all precipitation time series showed LTP at both

small and large time scales, while streamflow time series generally showed nonstationary behavior at small time scales and LTP at large time scales. Widespread crossovers of fluctuation functions, $F_2(s)$, versus timescale s for streamflow data at approximately a time scale of 120-250 days could be related to the cross-over between rain-induced and snowmelt-induced streamflow cycles. About 1/3 of precipitation time series became temporally more uniform because their multifractal strength decreased with time. However, only about half of the stations whose streamflow data exhibited statistically significant abrupt change points showed a weakening in the multifractal strength moving from the pre-change to the post-change periods.

From wavelet analysis of monthly maximum daily precipitation (MMDP) of 131 selected gauging stations across Canada, the results show that low-frequency, interannual (1-8 years) oscillations were more significant than interdecadal (8-30 years) oscillations, and the oscillations are both spatial and time-dependent in all 1-30 year time scale, even though interdecadal oscillations are generally more persistent than interannual oscillations.

2) Seasonality of extreme precipitation

Seasonal maximum daily precipitations (SMPs) could either increase or decrease and historical seasonal changes varied spatially and from season to season. Across Canada, there were more stations showing a significant increase in spring, summer and autumn SMPs than a decrease, while the winter SMP experienced a significant decrease (increase) over southern (northern) Canada. More than 1/4 of the stations exhibited a shift in SMPs of all four seasons. Spring, summer and autumn, SMPs tend to experience more increasing than decreasing change points, but the reverse were detected in winter SMP. More stations had shown significant change points than trends in AMP and the four SMPs. Compared to other seasons, winter had experienced more significant trends and change points in extreme precipitation, and most change points had occurred around 1960-1990;

3) Teleconnections between large-scale climate anomalies and extreme precipitation

AMP and heavy precipitation of Canada show strong non-stationarities which are likely related to the influence of large-scale climate patterns given strong correlations are found between extreme Canadian precipitations and climate indices. AMP in southwestern coastal regions, southern CP and the Great Lakes regions tend to be higher in El Niño years than in La Niña years, while other regions of Canada showed a lower AMP in El Niño years than in La Niña years. The effect of other climate patterns such as PDO, NAO and NP on extreme

precipitation is also significant at some stations across Canada. The influences of large-scale climate anomalies on the detected trends of winter SMP were statistically significant.

The wavelet coherence and phase difference between the leading PC1-2 (principle components 1-2) of MMDP and climate indices are highly variable in periodicity and in time. Even though Pearson's correlation between the band-passed MMDP PC1-3 and climate indices are generally significant, a single climate index can explain less than 40% of the total variability at 1-30-year scale. These characteristics indicate changes in the strength of teleconnection between Canadian extreme precipitation and large-scale climate anomalies. Partial wavelet coherence analysis shows that both ENSO and PDO modulated the interannual variability, and PDO modulated the interdecadal variability of MMDP over Canada. NAO is significantly correlated with the western MMDP at interdecadal scales and the eastern MMDP at interannual scales. Composite analysis shows that precipitation extremes at approximately 3/4 of the stations have been significantly influenced by ENSO and PDO patterns, while about 1/2 of the stations by the NAO patterns. The magnitude of SMDP in extreme El Niño years was mostly lower (higher) over the CP region in summer and winter (spring and autumn) than in extreme La Niña years. An extreme PDO event of positive phase played a similar role in increasing or decreasing the magnitude of Canadian SMDP compared with extreme El Niño events. Winter precipitation extremes over eastern Canada were also significantly influenced by NAO. As expected, overall, the degree of influence of large-scale climate patterns, i.e., ENSO, PDO and NAO, on Canadian precipitation extremes varies by season and by region.

4) Detection and attribution of annual streamflow totals

Annual streamflow decreased in Canadian Rockies but increase in other basins. Annual precipitation increased in southern Canada, but decreased in northern Canada. Annual potential evapotranspiration increased in northern Canada and BC, but decreased in southern Canada. The land parameter *n* used in the Budyko Framework decreased in northern Canada while increased in southern Canada. The attribution results show that Precipitation contributed to the increase of streamflow, while human influences decreased the streamflow in most Canadian non-RHBN watersheds. Many watersheds subjected to both increasing precipitation and negative human influences did not exhibit obvious net changes in streamflow.

5) Global extreme climate impacts on ecosystems and human society

Under RCP8.5, the projected global changes in the magnitude, frequency and severity of hot extremes are projected to exceed their twofold variance (S/N >2) before 2100, while counterparts of extreme precipitation are projected to exceed one variance (S/N >1) before 2100. In contrast to perceivable changes in the magnitude (magnitude and frequency) of both hot and cold extremes (precipitation extremes) projected to occur early in low- and high-latitudes, the frequency (severity) of both hot and cold extremes (precipitation extremes) are projected to occur earlier in mid-latitudes instead of low- and high-latitudes. As a result, tropical and subtropical forests (tropic Atlantic, Indo-Pacific, Tropical eastern Pacific) are projected to experience earlier perceivable changes in hot extremes than other terrestrial biomes (marine realms). Arctic tundra is projected to experience perceivable changes in the magnitude, frequency and severity of extreme precipitation before 2100, while biomes such as tropical and subtropical coniferous forests and Mediterranean forest are projected to experience earlier perceivable changes in severe droughts. All major urban residents (about 1.4 billion) are projected to experience perceivable changes in the frequency and severity of hot extremes, and more are projected to experience severe droughts (0.86 billion) than wet climate (0.08 billion). Lastly, early perceivable extreme climate change tends to occur in low-income than rich countries.

8.2 Future work

Given the research only provided limited regional frequency analysis of Canadian extreme hydroclimate and some qualitative discussions of physical mechanisms behind non-stationarities of climatic extremes of Canada, future work as a follow up to this thesis will be:

1) Spatiotemporal modeling of extreme precipitation and streamflow based on spatial non-stationary extreme value processes and quantile regression processes.

Since modeling extreme precipitation and streamflow of Canada at each station using a GEV distribution was conducted across Canada with diversified climatic regimes, we expect the GEV parameters to vary spatially and possibly temporally. In addition to estimate the risk of occurrence of extreme precipitation using GEV at regional scale, future work should also estimate how that risk could change in time based on certain time-varying environmental variables, e.g., the temporal evolution of GEV parameters for Canadian precipitation and streamflow maxima should be accounted for. Moreover, in this thesis, the focus had been mainly on analyzing the mean (the 50^{th} percentile), the large (95^{th} or higher percentile) and small (5^{th} or

lower percentile) values, even though changes of precipitation may be occurring around other quantiles, such as the 25th or 75th percentiles or others. A spatiotemporal quantile regression will be used to detect possible changes at various quantile levels, for changes can vary between quantile levels. Through the Bayesian approach, changes to precipitation quantiles subjected to external climatic forcings at various quantile levels should be analyzed in the future.

2) Moisture transport patterns associated with Canadian heavy precipitation.

Recurrent large-scale atmospheric circulation patterns have been shown to be associated with variations in the intensity and location of polar jet stream, subtropical jet stream, or mid-latitude storm tracks. In this research, significant statistical relationships have been detected between various climate indices and hydroclimatic variables over Canada and North America, but causal mechanisms responsible for widespread precipitation and streamflow anomalies have not been comprehensively identified. Therefore, in future work, teleconnections between precipitation of North America with large-scale atmospheric circulation patterns will be explored by identifying propagating patterns in atmospheric fields, e.g., jet stream–level wind speed, moisture flux, temperature advection, and vorticity advection, which have potential relevance to precipitation. Moisture sources and pathways that have contributed to the Canadian extreme precipitation will be identified through moisture trajectory analysis.

3) Changes in large-scale circulation patterns (dynamic) and thermodynamic conditions conducive to Canadian seasonal precipitation extremes.

Changes in hydroclimatic extremes can be either thermodynamic or dynamic (Seager et al. 2010; Seager et al. 2007), and extreme weather conditions are often strongly associated with large-scale atmospheric circulations. Recent advances in climate research have linked changes in the probability of extreme events to changes in atmospheric circulations (Cassano et al. 2015; Coumou et al. 2014; Francis and Vavrus 2012; Horton et al. 2015; Petoukhov et al. 2013). Previous studies have identified some primary synoptic circulations contributing to the surface weather conditions of western Canada. For example, a ridge centered over western Canada is usually linked to low precipitation (Romolo et al. 2006; Saunders and Byrne 1996), while high precipitation is associated with zonal flow (Romolo et al. 2006) or a ridge centered over the Pacific Ocean (Cassano and Cassano 2009; Cassano et al. 2006; Finnis et al. 2009). Precipitation over western Canada generally results from the development of lee cyclones at the surface that are preceded by a mid-tropospheric low-pressure system across the Pacific Ocean (Lackmann

and Gyakum 1998). The low-pressure system generates a narrow band of moisture influx to southwestern Canada (Liu and Stewart 2003; Smirnov and Moore 2001). Newton et al. (2014b; 2014b) examined changes in the frequency of occurrences synoptic circulation patterns classified using self-organizing maps, and related these patterns to anomalies of temperature and precipitation over western Canada. However, synoptic patterns contributing to the occurrence of extreme temperature and precipitation events have not been identified and the changes in the frequency of synoptic patterns have not been linked to changes in the frequency of extreme events over Canada.

The atmospheric moisture content governed by the Clausius-Claperyron equation, tends to increase with the warming of troposphere, which thermodynamically results in changes to surface weather conditions, particularly intensified hydrological cycle with precipitation extreme events (Allen and Ingram 2002; Held and Soden 2006; Seager et al. 2012). However, actual moisture content is also dependent on the available water and energy supply, so warming may not result in changes in precipitation at large time scales (e.g., > 1 day) (Allen and Ingram 2002; Panthou et al. 2014). Increase in precipitation intensity at small time scales (e.g., 1 hour) has been observed beyond 7% K^{-1}, given by Clausius-Claperyron relation, from temperature changes in some locations (Lenderink and van Meijgaard 2008, 2010; Panthou et al. 2014). Since statistically significant trends in Canadian extreme precipitation have been found in this thesis, future work should identify relative contributions of changes in dynamic and thermodynamic conditions to changes in the frequency and magnitude of extreme precipitation.

Bibliography

Aguiar-Conraria, L., and M. J. Soares, 2014: The continuous wavelet transform: Moving beyond uni- and bivariate analysis. *J Econ Surv*, **28,** 344-375.

Ahmari, H., E.-L. Blais, and J. Greshuk, 2015: The 2014 flood event in the Assiniboine River Basin: Causes, assessment and damage. *Can Water Resour J***,** 1-9, doi:10.1080/07011784.2015.1070695.

Alexander, L. V., P. Uotila, and N. Nicholls, 2009: Influence of sea surface temperature variability on global temperature and precipitation extremes. *J Geophys Res*, **114,** D18116, doi:18110.11029/12009JD012301.

Alexander, L. V., and Coauthors, 2006: Global observed changes in daily climate extremes of temperature and precipitation. *J Geophys Res*, **111,** D05109 , doi:10.1029/2005jd006290.

Allan, R. P., and B. J. Soden, 2008: Atmospheric warming and the amplification of precipitation extremes. *Science*, **321,** 1481-1484.

Allen, C. D., and Coauthors, 2010: A global overview of drought and heat-induced tree mortality reveals emerging climate change risks for forests. *Forest Ecol Manag*, **259,** 660-684.

Allen, M. R., and W. J. Ingram, 2002: Constraints on future changes in climate and the hydrologic cycle. *Nature*, **419,** 224-232.

Alley, R. B., and Coauthors, 2003: Abrupt climate change. *Science*, **299,** 2005-2010.

Anctil, F., and P. Coulibaly, 2004: Wavelet analysis of the interannual variability in southern Québec streamflow. *J Climate*, **17,** 163-173.

Anderson, B. T., 2011: Near-term increase in frequency of seasonal temperature extremes prior to the 2°C global warming target. *Clim Chang*, **108,** 581-589.

Assani, A. A., É. Stichelbout, A. G. Roy, and F. Petit, 2006: Comparison of impacts of dams on the annual maximum flow characteristics in three regulated hydrologic regimes in Québec (Canada). *Hydrol Process*, **20,** 3485-3501.

Assani, A. A., D. Landais, M. Mesfioui, and M. Matteau, 2010: Relationship between the Atlantic Multidecadal Oscillation index and variability of mean annual flows for catchments in the St. Lawrence watershed (Quebec, Canada) during the past century. *Hydrol Res*, **41,** 115-125.

Barnett, T. P., and Coauthors, 2008: Human-induced changes in the hydrology of the western United States. *Science*, **319,** 1080-1083.

Beaumonta, L. J., A. Pitman, S. Perkins, N. E. Zimmermann, N. G. Yoccoze, and W. Thuiller, 2011: Impacts of climate change on the world's most exceptional ecoregions. *Proc Natl Acad Sci U S A*, **108,** 2306-2311.

Berghuijs, W. R., R. A.Woods, and M. Hrachowitz, 2014: A precipitation shift from snow towards rain leads to a decrease in streamflow. *Nature Clim Change*, **4,** 583–586.

Blais, E.-L., J. Greshuk, and T. Stadnyk, 2015: The 2011 flood event in the Assiniboine River Basin: causes, assessment and damages. *Can Water Resour J***,** 1-11 , doi:10.1080/ 07011784.2015.1046139.

Bond, N. A., and D. E. Harrison, 2000: The Pacific decadal oscillation, air-sea interaction and central north Pacific winter atmospheric regimes. *Geophys Res Lett*, **27,** 731-734.

Bonsal, B., and A. Shabbar, 2008: Impacts of large-scale circulation variability on low streamflows over Canada: a review. *Can Water Resour J*, **33,** 137-154.

Bras, R. L., and I. Rodriguez-Iturbe, 1985: *Random functions and hydrology.* Addison-Wesley Publishing Company, 559 pp.

Brillinger, D. R., 2001: *Time series: Data analysis and theory.* Society for Industrial and Applied Mathematics, Philadelphia, PA.

Budyko, M. I., 1961: The heat balance of the Earth's surface. *Soviet Geography*, **2,** 3-13.

Burn, D. H., 2008: Climatic influences on streamflow timing in the headwaters of the Mackenzie River Basin. *J Hydrol*, **352,** 225-238.

Burn, D. H., and M. A. H. Elnur, 2002: Detection of hydrologic trends and variability. *J Hydrol*, **255,** 107-122.

Burn, D. H., and A. Taleghani, 2013: Estimates of changes in design rainfall values for Canada. *Hydrol Process*, **27,** 1590-1599.

Burn, D. H., M. Sharif, and K. Zhang, 2010: Detection of trends in hydrological extremes for Canadian watersheds. *Hydrol Process*, **24,** 1781-1790.

Burrows, M. T., and Coauthors, 2014: Geographical limits to species-range shifts are suggested by climate velocity. *Nature*, **507,** 492-495.

Buttle, J. M., 2011: Streamflow response to headwater reforestation in the Ganaraska River basin, southern Ontario, Canada. *Hydrol Process*, **25,** 3030-3041.

Buttle, J. M., and Coauthors, 2016: Flood processes in Canada: Regional and special aspects. *Can Water Resour J***,** 1-24, doi:10.1080/07011784.2015.1131629.

Cai, W., P. van Rensch, T. Cowan, and A. Sullivan, 2010: Asymmetry in ENSO Teleconnection with Regional Rainfall, Its Multidecadal Variability, and Impact. *J Climate*, **23,** 4944-4955.

Cameron, A. C., and P. K. Trivedi, 1990: Regression-based tests for overdispersion in the Poisson model. *J Econometrics*, **46,** 347-364.

Cannon, A. J., S. R. Sobie, and T. Q. Murdock, 2015: Bias Correction of GCM Precipitation by Quantile Mapping: How Well Do Methods Preserve Changes in Quantiles and Extremes? *J Climate*, **28,** 6938-6959.

Cassano, E. N., and J. J. Cassano, 2009: Synoptic forcing of precipitation in the Mackenzie and Yukon River basins. *Int J Climatol***, 30,** 658-674.

Cassano, E. N., J. M. Glisan, J. J. Cassano, W. J. Gutowski, and M. W. Seefeldt, 2015: Self-organizing map analysis of widespread temperature extremes in Alaska and Canada. *Climate Res*, **62,** 199-218.

Cassano, J. J., P. Uotila, and A. Lynch, 2006: Changes in synoptic weather patterns in the polar regions in the twentieth and twenty-first centuries, part 1: Arctic. *Int J Climatol*, **26,** 1027-1049.

Cayan, D. R., K. T. Redmond, and L. G. Riddle, 1999: ENSO and hydrologic extremes in the western United States. *J Climate*, **9,** 2881-2893.

Cioffi, F., U. Lall, E. Rus, and C. K. B. Krishnamurthy, 2015: Space-time structure of extreme precipitation in Europe over the last century. *Int J Climatol*, **35,** 1749-1760.

Clarke, G. K. C., A. H. Jarosch, F. S. Anslow, V. Radić, and B. Menounos, 2015: Projected deglaciation of western Canada in the twenty-first century. *Nat Geosci*, **8,** 372-377.

Cohen, J. and Coauthors, 2014: Recent Arctic amplification and extreme mid-latitude weather, *Nat. Geosci*, **7**(9), 627-637, doi:10.1038/ngeo2234.

Cohn, T. A., and H. F. Lins, 2005: Nature's style: Naturally trendy. *Geophys Res Lett*, **32,** L23402.

Coles, S., 2001: *An Introduction to Statistical Modeling of Extreme Values.* Springer-Verlag, London.

Coulibaly, P., 2006: Spatial and temporal variability of Canadian seasonal precipitation (1900–2000). *Adv Water Resour*, **29,** 1846-1865.

Coulibaly, P., and D. H. Burn, 2004: Wavelet analysis of variability in annual Canadian streamflows. *Water Resour Res*, **40,** W03105.

——, 2005: Spatial and temporal variability of Canadian seasonal streamflows. *J Climate*, **18,** 191-210.

Coumou, D., V. Petoukhov, S. Rahmstorf, S. Petri, and H. J. Schellnhuber, 2014: Quasi-resonant circulation regimes and hemispheric synchronization of extreme weather in boreal summer. *Proc Natl Acad Sci U S A*, **111,** 12331-12336.

Csörgö, M., and L. Horváth, 1997: *Limit theorems in change-point analysis.* John Wiley & Sons.

Cunderlik, J. M., and T. B. M. J. Ouarda, 2009: Trends in the timing and magnitude of floods in Canada. *J Hydrol*, **375,** 471-480.

Curtis, S., A. Salahuddin, R. F. Adler, G. J. Huffman, G. Gu, and Y. Hong, 2007: Precipitation extremes estimated by GPCP and TRMM: ENSO relationships. *J Hydrometeorol*, **8,** 678-689.

Déry, S. J., M. A. Hernández-Henríquez, J. E. Burford, and E. F. Wood, 2009a: Observational evidence of an intensifying hydrological cycle in northern Canada. *Geophys Res Lett*, **36** (13), doi:10.1029/2009gl038852.

Déry, S. J., K. Stahl, R. D. Moore, P. H. Whitfield, B. Menounos, and J. E. Burford, 2009b: Detection of runoff timing changes in pluvial, nival, and glacial rivers of western Canada. *Water Resour Res*, **45,** W04426.

Davis, A., A. Marshak, W. Wiscombe, and R. Cahalan, 1994: Multifractal characterizations of nonstationarity and intermittency in geophysical fields: Observed, retrieved, or simulated. *J Geophys Res Atmos*, **99,** 8055-8072.

Davis, R. E., M. B. Lowit, P. C. Knappenberger, and D. R. Legates, 1999: A climatology of snowfall-temperature relationships in Canada. *J Geophys Res*, **104,** 11985-11994.

Davison, A. C., and D. V. Hinkley, 1997: *Bootstrap methods and their application.* Cambridge University Press, 582 pp.

de Montera, L., L. Barthès, C. Mallet, and P. Golé, 2009: The Effect of Rain–No Rain Intermittency on the Estimation of the Universal Multifractals Model Parameters. *J Hydrometeorol*, **10,** 493-506.

Dee, D. P., and Coauthors, 2011: The ERA-Interim reanalysis: configuration and performance of the data assimilation system. *Q J Roy Meteor Soc*, **137,** 553-597.

Deidda, R., R. Benzi, and F. Siccardi, 1999: Multifractal modeling of anomalous scaling laws in rainfall. *Water Resour Res*, **35,** 1853-1867.

Destouni, G., F. Jaramillo, and C. Prieto, 2013: Hydroclimatic shifts driven by human water use for food and energy production. *Nature Clim Change*, **3,** 213-217.

Diffenbaugh, N. S., and M. Scherer, 2011: Observational and model evidence of global emergence of permanent, unprecedented heat in the 20(th) and 21(st) centuries. *Clim Change*, **107,** 615-624.

Diffenbaugh, N. S., M. Ashfaq, and M. Scherer, 2011: Transient regional climate change: analysis of the summer climate response in a high-resolution, century-scale, ensemble experiment over the continental United States. *J Geophys Res*, **116** (D24), doi:10.1029/2011JD016458.

Diffenbaugh, N. S., F. Giorgi, L. Raymond, and X. Bi, 2007: Indicators of 21st century socioclimatic exposure. *Proc Natl Acad Sci U S A*, **104,** 20195-20198.

Dinpashoh, Y., R. Mirabbasi, D. Jhajharia, H. Z. Abianeh, and A. Mostafaeipour, 2014: Effect of short-term and long-term persistence on identification of temporal trends. *J Hydrol Eng*, **19,** 617-625.

Donat, M. G., A. L. Lowry, L. V. Alexander, P. A. O'Gorman, and N. Maher, 2016: More extreme precipitation in the world's dry and wet regions. *Nature Clim Change*, **6,** 508-513.

Douglas, E. M., R. M. Vogela, and C. N. Kroll, 2000: Trends in floods and low fows in the United States: impact of spatial correlation. *J Hydrol*, **240,** 90-105.

Duan, W., B. He, K. Takara, P. Luo, M. Hu, N. E. Alias, and D. Nover, 2015: Changes of precipitation amounts and extremes over Japan between 1901 and 2012 and their connection to climate indices. *Clim Dynam*, **45,** 2273-2292.

Easterling, D. R., G. A. Meehl, C. Parmesan, S. A. Changnon, T. R. Karl, and L. O. Mearns, 2000: Climate Extremes: Observations, Modeling, and Impacts. *Science*, **289,** 2068-2074.

Ehsanzadeh, E., and K. Adamowski, 2010: Trends in timing of low stream flows in Canada: impact of autocorrelation and long-term persistence. *Hydrol Process*, **24,** 970-980.

El-Shaarawi, A. H., 1993: Environmental monitoring, assessment and prediction of change. *Environmetrics*, **4,** 381-398.

Elsanabary, M. H., T. Y. Gan, and D. Mwale, 2014: Application of wavelet empirical orthogonal function analysis to investigate the nonstationary character of Ethiopian rainfall and its teleconnection to nonstationary global sea surface temperature variations for 1900-1998. *Int J Climatol*, **34,** 1798-1813.

Environment Canada, 1992: *Surface water data reference index: Canada 1991.* Published by Inland Waters Directorate, Environment Canada.

——, 1996: *The state of Canada's environment 1996.* State of the Environment Directorate, Environment Canada, Ottawa.

——, 2004: Threats to water availability in canada. National water research institute, burlington, ontario. NWRI Scientific Assessment Report Series No. 3 and ACSD Science Assessment Series No. 1. 128 pp.

——, 2014: Canada's top ten weather stories for 2013. [Available online at http://www.ec.gc.ca/meteo-weather/default.asp?lang5En&n55BA5EAFC-1.].

Finnis, J., J. Cassano, M. Holland, M. Serreze, and P. Uotila, 2009: Synoptically forced hydroclimatology of major Arctic watersheds in general circulation models; Part 1: the Mackenzie River Basin. *Int J Climatol*, **29,** 1226-1243.

Fischer, E. M., and R. Knutti, 2014: Detection of spatially aggregated changes in temperature and precipitation extremes. *Geophys Res Lett*, **41,** 547-554.

Fischer, E. M., U. Beyerle, and R. Knutti, 2013: Robust spatially aggregated projections of climate extremes. *Nature Clim Change*, **3,** 1033-1038.

Forsee, W. J., and S. Ahmad, 2011: Evaluating urban storm-water infrastructure design in response to projected climate change. *J Hydrol Eng*, **16,** 865-873.

Francis, J. A., and S. J. Vavrus, 2012: Evidence linking Arctic amplification to extreme weather in mid-latitudes. *Geophys Res Lett*, **39,** L06801.

Franzke, C., 2010: Long-range dependence and climate noise characteristics of Antarctic temperature data. *J Climate*, **23,** 6074-6081.

——, 2012: Nonlinear trends, long-range dependence, and climate noise properties of surface temperature. *J Climate*, **25,** 4172-4183.

Franzke, C. L., 2013: Persistent regimes and extreme events of the North Atlantic atmospheric circulation. *Philos Trans A Math Phys Eng Sci*, **371,** 20110471.

Fu, X., C. C. Kuo, and T. Y. Gan, 2015: Change point analysis of precipitation indices of Western Canada. *Int J Climatol*, **35,** 2592-2607.

Gan, T. Y., 1998: Hydroclimatic trends and possible climatic warming in the Canadian Prairies. *Water Resour Res*, **34,** 3009-3015.

Gan, T. Y., A. K. Gobena, and Q. Wang, 2007: Precipitation of southwestern Canada: Wavelet, scaling, multifractal analysis, and teleconnection to climate anomalies. *J Geophys Res*, **112,** D10110.

Garcia, R. A., M. Cabeza, C. Rahbek, and M. B. Araújo, 2014: Multiple dimensions of climate change and their implications for biodiversity. *Science*, **344,** 1247579.

Gedney, N., P. M. Cox, R. A. Betts, O. Boucher, C. Huntingford, and P. A. Stott, 2006: Detection of a direct carbon dioxide effect in continental river runoff records. *Nature*, **439,** 835-838.

Gershunov, A., and T. P. Barnett, 1998: ENSO influence on intraseasonal extreme rainfall and temperature frequencies in the contiguous United States: Observations and model results. *J Climate*, **11,** 1575-1586.

Gershunov, A., and D. R. Cayan, 2003: Heavy daily precipitation frequency over the contiguous United States: Sources of climatic variability and seasonal predictability. *J Climate*, **16,** 2752-2765.

Ghatak, D., A. Frei, G. Gong, J. Stroeve, and D. Robinson, 2010: On the emergence of an Arctic amplification signal in terrestrial Arctic snow extent. *J Geophys Res*, **115** (D24), doi:10.1029/2010jd014007.

Gibbons, J. D., and S. Chakraborti, 2011: *Nonparametric Statistical Inference, 5th Eds.* Chapman & Hall/CRC Press.

Gilleland, E., and R. W. Katz, 2011: New software to analyze how extremes change over time. *Eos, Trans. Amer. Geophys. Union*, **92,** 13-14.

Giorgi, F., and X. Bi, 2009: Time of emergence (TOE) of GHG-forced precipitation change hot-spots. *Geophys Res Lett*, **36** (6), doi:10.1029/2009gl037593.

Gordon, L. J., W. Steffen, B. F. Jonsson, C. Folke, M. Falkenmark, and A. Johannessen, 2005: Human modification of global water vapor flows from the land surface. *Proc Natl Acad Sci U S A*, **102,** 7612-7617.

Government of Alberta, 2014: Alberta 2013-2014 flood recovery update. [Available online at http://alberta.ca/Flood-recovery-update.cfm.].

GREHYS, 1996: Inter-comparison of regional flood frequency procedures for Canadian rivers. *J Hydrol*, **186,** 85-103.

Greve, P., B. Orlowsky, B. Mueller, J. Sheffield, M. Reichstein, and S. I. Seneviratne, 2014: Global assessment of trends in wetting and drying over land. *Nat Geosci*, **7,** 716-721.

Grill, G., B. Lehner, A. E. Lumsdon, G. K. MacDonald, C. Zarfl, and C. Reidy Liermann, 2015: An index-based framework for assessing patterns and trends in river fragmentation and flow regulation by global dams at multiple scales. *Environ Res Lett*, **10,** 015001.

Grimm, A. M., and R. G. Tedeschi, 2009: ENSO and extreme rainfall events in South America. *J Climate*, **22,** 1589-1609.

Grinsted, A., J. C. Moore, and S. Jevrejeva, 2004: Application of the cross wavelet transform and wavelet coherence to geophysical time series. *Nonlinear Proc Geoph*, **11,** 561-566.

Groisman, P. Y., and Coauthors, 1999: Changes in the probability of heavy precipitation: Important indicators of climatic change. *Clim Chang*, **42,** 243-283.

Gudmundsson, L., J. B. Bremnes, J. E. Haugen, and T. Engen-Skaugen, 2012: Technical Note: Downscaling RCM precipitation to the station scale using statistical transformations – a comparison of methods. *Hydrol Earth Syst Sc*, **16,** 3383-3390.

Gumbel, E. J., 1941: The Return Period of Flood Flows, *Ann Math Statist*, **12**(2), 163-190.

Haines, A., R. S. Kovats, D. Campbell-Lendrum, and C. Corvalan, 2006: Climate change and human health: impacts, vulnerability and public health. *Public Health*, **120,** 585-596.

Hamed, K. H., 2008: Trend detection in hydrologic data: The Mann–Kendall trend test under the scaling hypothesis. *J Hydrol*, **349,** 350-363.

Hamed, K. H., and A. R. Rao, 1998: A modified Mann-Kendall trend test for autocorrelated data. *J Hydrol*, **204,** 182-196.

Harrington, L. J., D. J. Frame, E. M. Fischer, E. Hawkins, M. Joshi, and C. D. Jones, 2016: Poorest countries experience earlier anthropogenic emergence of daily temperature extremes. *Environ Res Lett*, **11,** 055007.

Harris, I., P. D. Jones, T. J. Osborn, and D. H. Lister, 2014: Updated high-resolution grids of monthly climatic observations - the CRU TS3.10 Dataset. *Int J Climatol*, **34,** 623-642.

Hartmann, D. L., and Coauthors, 2013: Observations: Atmosphere and Surface. *Climate Change 2013: The Physical Science Basis. Contribution of Working Group I to the Fifth Assessment Report of the Intergovernmental Panel on Climate Change*, T. F. Stocker, and Coauthors, Eds., Cambridge University Press, 159–254.

Hawkins, D. L., 1989: Using U statistics to derive the asymptotic distribution of Fisher's Z statistic. *The American Statistician*, **43,** 235-237.

Hawkins, E., and R. Sutton, 2012: Time of emergence of climate signals. *Geophys Res Lett*, **39,** L01702.

Hawkins, E., and Coauthors, 2014: Uncertainties in the timing of unprecedented climates. *Nature*, **511,** E3-5.

Hegerl, G. C., F. W. Zwiers, P. A. Stott, and V. V. Kharin, 2004: Detectability of anthropogenic changes in annual temperature and precipitation extremes. *J Climate*, **17,** 3683-3700.

Held, I. M., and B. J. Soden, 2006: Robust Responses of the Hydrological Cycle to Global Warming. *J Climate*, **19,** 5686-5699.

Helsel, D. R., and R. M. Hirsch, 2002: Chapter A3: Statistical Methods in Water Resources. *Techniques of Water-Resources Investigations of the United States Geological Survey, Book 4, Hydrologic Analysis and Interpretation*, U.S. Geological Survey, 522.

Higgins, R. W., A. Leetmaa, and V. E. Kousky, 2002: Relationships between climate variability and winter temperature extremes in the United States. *J Climate*, **15,** 1555-1572.

Horton, D. E., N. C. Johnson, D. Singh, D. L. Swain, B. Rajaratnam, and N. S. Diffenbaugh, 2015: Contribution of changes in atmospheric circulation patterns to extreme temperature trends. *Nature*, **522,** 465-469.

Hosking, J. R. M., and J. R. Wallis, 1997: *Regional frequency analysis: an approach based on L-moments.* Cambridge University Press.

Hurrell, J. W., and H. V. Loon, 1997: Decadal variations in climate associated with the North Atlantic Oscillation. *Clim Chang*, **36,** 301-326.

Hurst, H. E., 1951: Long term storage capacities of reserviors. *Trans. Am. Soc. Civ. Eng.*, **116,** 770-799.

Ihlen, E. A., 2012: Introduction to multifractal detrended fluctuation analysis in matlab. *Frontiers in physiology*, **3,** 1-18.

Immerzeel, W. W., F. Pellicciotti, and M. F. P. Bierkens, 2013: Rising river flows throughout the twenty-first century in two Himalayan glacierized watersheds. *Nat Geosci*, **6,** 742-745.

Inclán, C., and G. C. Tiao, 1994: Use of Cumulative Sums of Squares for Retrospective Detection of Changes of Variance. *J Am Stat Assoc*, **89,** 913-923.

IPCC, 2013: Summary for Policymakers. *Climate Change 2013: The Physical Science Basis. Contribution of Working Group I to the Fifth Assessment Report of the Intergovernmental Panel on Climate Change*, T. F. Stocker, and Coauthors, Eds., Cambridge University Press, 1–30.

Ishak, E. H., A. Rahman, S. Westra, A. Sharma, and G. Kuczera, 2013: Evaluating the non-stationarity of Australian annual maximum flood. *J Hydrol*, **494,** 134-145.

Islam, M. S., 2008: Peridocity, change detection and prediction in microarrays, The University of Western Ontario.

Ivanov, P. C., L. A. N. Amaral, A. L. Goldberger, S. Havlin, M. G. Rosenblum, Z. R. Struzik, and H. E. Stanley, 1999: Multifractality in human heartbeat dynamics. *Nature*, **399,** 461-465.

Jakob, D., 2013: Nonstationarity in extremes and engineering design. *Extremes in a changing climate: Detection, analysis and uncertainty*, A. AghaKouchak, D. Easterling, K. Hsu, S. Schubert, and S. Sorooshian, Eds., Water Science and Technology Library.Springer Science+Business Media Dordrecht.

Jentsch, A., and C. Beierkuhnlein, 2008: Research frontiers in climate change: Effects of extreme meteorological events on ecosystems. *Comptes Rendus Geoscience*, **340,** 621-628.

Jentsch, A., J. Kreyling, J. Boettcher-Treschkow, and C. Beierkuhnlein, 2009: Beyond gradual warming: extreme weather events alter flower phenology of European grassland and heath species. *Global Change Biol*, **15,** 837-849.

Jevrejeva, S., 2003: Influence of the Arctic Oscillation and El Niño-Southern Oscillation (ENSO) on ice conditions in the Baltic Sea: The wavelet approach. *J Geophys Res*, **108,** 4677.

Jiang, R., T. Y. Gan, J. Xie, and N. Wang, 2014: Spatiotemporal variability of Alberta's seasonal precipitation, their teleconnection with large-scale climate anomalies and sea surface temperature. *Int J Climatol*, **34,** 2899-2917.

Jolly, W. M., M. A. Cochrane, P. H. Freeborn, Z. A. Holden, T. J. Brown, G. J. Williamson, and D. M. Bowman, 2015: Climate-induced variations in global wildfire danger from 1979 to 2013. *Nat Commun*, **6,** 7537.

Jones, P. D., T. Jonsson, and D. Wheeler, 1997: Extension to the North Atlantic oscillation using early instrumental pressure observations from Gibraltar and south-west Iceland. *Int J Climatol*, **17,** 1433-1450.

Jung, M., and Coauthors, 2010: Recent decline in the global land evapotranspiration trend due to limited moisture supply. *Nature*, **467,** 951-954.

Kalnay, E., and Coauthors, 1996: The NCEP/NCAR 40-year reanalysis project. *Bull Amer Meteor Soc*, **77,** 437-471.

Kantelhardt, J. W., 2009: Fractal and multifractal time series. *Encyclopedia of Complexity and Systems Science*, R. A. Meyers, Ed., Springer New York, 3754-3779.

Kantelhardt, J. W., E. Koscielny-Bunde, H. H. A. Rego, S. Havlin, and A. Bunde, 2001: Detecting long-range correlations with detrended fluctuation analysis. *Physica A*, **295,** 441-454.

Kantelhardt, J. W., S. A. Zschiegner, E. Koscielny-Bunde, S. Havlin, A. Bunde, and H. E. Stanley, 2002: Multifractal detrended fluctuation analysis of nonstationary time series. *Physica A*, **316,** 87-114.

Kantelhardt, J. W., E. Koscielny-Bunde, D. Rybski, P. Braun, A. Bunde, and S. Havlin, 2006: Long-term persistence and multifractality of precipitation and river runoff records. *J Geophys Res*, **111,** doi:10.1029/2005JD005881.

Kay, J. E., and Coauthors, 2015: The Community Earth System Model (CESM) Large Ensemble Project: A Community Resource for Studying Climate Change in the Presence of Internal Climate Variability. *Bull Amer Meteor Soc*, **96,** 1333-1349.

Katz, R. W., M. B. Parlange, and P. Naveau, 2002: Statistics of extremes in hydrology. *Adv Water Resour*, **25,** 1287-1304.

Kendall, M., 1975: *Rank Correlation Methods (4th ed.).* London :Charless Griffin.

Kendon, E. J., D. P. Rowell, R. G. Jones, and E. Buonomo, 2008: Robustness of Future Changes in Local Precipitation Extremes. *J Climate*, **21,** 4280-4297.

Kenyon, J., and G. C. Hegerl, 2008: Influence of Modes of Climate Variability on Global Temperature Extremes. *J Climate*, **21,** 3872-3889.

——, 2010: Influence of modes of climate variability on global precipitation extremes. *J Climate*, **23,** 6248-6262.

Kerkhoven, E., and T. Y. Gan, 2011: Unconditional uncertainties of historical and simulated river flows subjected to climate change. *J Hydrol*, **396,** 113-127.

——, 2013: Differences in the Potential Hydrologic Impact of Climate Change to the Athabasca and Fraser River Basins of Canada with and without Considering Shifts in Vegetation Patterns Induced by Climate Change. *J Hydrometeorol*, **14,** 963-976.

Khaliq, M. N., and P. Gachon, 2010: Pacific Decadal Oscillation climate variability and temporal pattern of winter flows in northwestern North America. *J Hydrometeorol*, **11,** 917-933.

Khaliq, M. N., T. B. M. J. Ouarda, and P. Gachon, 2009a: Identification of temporal trends in annual and seasonal low flows occurring in Canadian rivers: The effect of short- and long-term persistence. *J Hydrol*, **369,** 183-197.

Khaliq, M. N., T. B. M. J. Ouarda, P. Gachon, and L. Sushama, 2008: Temporal evolution of low-flow regimes in Canadian rivers. *Water Resour Res*, **44,** W08436.

Khaliq, M. N., T. B. M. J. Ouarda, J. C. Ondo, P. Gachon, and B. Bobée, 2006: Frequency analysis of a sequence of dependent and/or non-stationary hydro-meteorological observations: A review. *J Hydrol*, **329,** 534-552.

Khaliq, M. N., T. B. M. J. Ouarda, P. Gachon, L. Sushama, and A. St-Hilaire, 2009b: Identification of hydrological trends in the presence of serial and cross correlations: A review of selected methods and their application to annual flow regimes of Canadian rivers. *J Hydrol*, **368,** 117-130.

Khedun, C. P., A. K. Mishra, V. P. Singh, and J. R. Giardino, 2014: A copula-based precipitation forecasting model: Investigating the interdecadal modulation of ENSO's impacts on monthly precipitation. *Water Resour Res*, **50,** 580-600.

King, A. D., and Coauthors, 2015: The timing of anthropogenic emergence in simulated climate extremes. *Environ Res Lett*, **10,** 094015.

Klemeš, V., 1974: The Hurst Phenomenon: A puzzle? *Water Resour Res*, **10,** 675-688.

Koscielny-Bunde, E., J. W. Kantelhardt, P. Braun, A. Bunde, and S. Havlin, 2006: Long-term persistence and multifractality of river runoff records: Detrended fluctuation studies. *J Hydrol*, **322,** 120-137.

Koutsoyiannis, D., 2003: Climate change, the Hurst phenomenon, and hydrological statistics. *Hydrolog Sci J*, **48,** 3-24.

——, 2006: Nonstationarity versus scaling in hydrology. *J Hydrol*, **324,** 239-254.

Koutsoyiannis, D., and A. Montanari, 2007: Statistical analysis of hydroclimatic time series: Uncertainty and insights. *Water Resour Res*, **43,** W05429.

——, 2015: Negligent killing of scientific concepts: the stationarity case. *Hydrolog Sci J***,** 1-10.

Koutsoyiannis, D., A. Efstratiadis, and K. P. Georgakakos, 2007: Uncertainty assessment of future hydroclimatic predictions: A comparison of probabilistic and scenario-based approaches. *J Hydrometeorol*, **8,** 261-281.

Krichak, S. O., J. S. Breitgand, S. Gualdi, and S. B. Feldstein, 2014: Teleconnection–extreme precipitation relationships over the Mediterranean region. *Theor Appl Climatol*, **117,** 679-692.

Kumar, S., V. Merwade, J. Kam, and K. Thurner, 2009: Streamflow trends in Indiana: Effects of long term persistence, precipitation and subsurface drains. *J Hydrol*, **374,** 171-183.

Kunkel, K. E., 2003: North American trends in extreme precipitation. *Nat Hazards*, **29,** 291-305.

Kunkel, K. E., and K. Andsager, 1999: Long-term trends in extreme precipitation events over the conterminous United States and Canada. *J Climate*, **12,** 2515-2572.

Kuo, C.-C., and T. Y. Gan, 2015: Risk of exceeding extreme design storm events under possible impact of climate change. *J Hydrol Eng*, **20,** 04015038.

Kuo, C.-C., T. Y. Gan, and P.-S. Yu, 2010: Wavelet analysis on the variability, teleconnectivity, and predictability of the seasonal rainfall of Taiwan. *Mon Weather Rev*, **138,** 162-175.

Kuo, C.-C., T. Y. Gan, and M. Gizaw, 2015: Potential impact of climate change on intensity duration frequency curves of central Alberta. *Clim Chang*, **130,** 115-129.

Kwon, H.-H., C. Brown, and U. Lall, 2008: Climate informed flood frequency analysis and prediction in Montana using hierarchical Bayesian modeling. *Geophys Res Lett*, **35,** L05404, doi:05410.01029/02007GL032220.

Kyselý, J., J. Picek, and R. Beranová, 2010: Estimating extremes in climate change simulations using the peaks-over-threshold method with a non-stationary threshold. *Global Planet Change*, **72,** 55-68.

Labat, D., C. T. Hoang, J. Masbou, A. Mangin, I. Tchiguirinskaia, S. Lovejoy, and D. Schertzer, 2013: Multifractal behaviour of long-term karstic discharge fluctuations. *Hydrol Process*, **27,** 3708-3717.

Lackmann, G. M., and J. R. Gyakum, 1998: Moisture Transport Diagnosis of a Wintertime Precipitation Event in the Mackenzie River Basin. *Mon Weather Rev*, **126,** 668-692.

Laštovička, J., P. Križan, P. Šauli, and D. Novotná, 2003: Persistence of the planetary wave type oscillations in foF2 over Europe. *Ann Geophys*, **21,** 1543-1552.

Lehner, B., and Coauthors, 2011: Global Reservoir & Dam (GRanD) database: Technical document http://sedac.ciesin.columbia.edu/data/collection/grand-v1, Ed.

Lenderink, G., and E. van Meijgaard, 2008: Increase in hourly precipitation extremes beyond expectations from temperature changes. *Nat Geosci*, **1,** 511-514.

——, 2010: Linking increases in hourly precipitation extremes to atmospheric temperature and moisture changes. *Environ Res Lett*, **5,** 025208.

Lettenmaier, D. P., E. F. Wood, and J. R. Wallis, 1994: Hydro-climatological trends in the continental United States, 1948-88. *J Climate*, **7,** 586-607.

Libiseller, C., and A. Grimvall, 2002: Perfomance of partial Mann-Kendall tests for trend detection in the presence of covariates. *Environmetrics*, **13,** 245-249.

Lin, Y., and X. Wei, 2008: The impact of large-scale forest harvesting on hydrology in the Willow watershed of Central British Columbia. *J Hydrol*, **359,** 141-149.

Liu, J., and R. E. Stewart, 2003: Water Vapor Fluxes over the Saskatchewan River Basin. *J Hydrometeorol*, **2003,** 944-959.

Livezey, R. E., and W. Y. Chen, 1983: Statistical field significance and its determination by Monte Carlo techniques. *Mon Weather Rev*, **111,** 46-59.

Loarie, S. R., P. B. Duffy, H. Hamilton, G. P. Asner, C. B. Field, and D. D. Ackerly, 2009: The velocity of climate change. *Nature*, **462,** 1052-1055.

Lovejoy, S., and B. B. Mandelbrot, 1985: Fractal properties of rain, and a fractal model. *Tellus A*, **37A,** 209-232.

Lovejoy, S., and D. Schertzer, 1986: Scale invariance, symmetries, fractals, and stochastic simulations of atmospheric phenomena. *Bull Amer Meteor Soc*, **67,** 21-32.

Lovejoy, S., and D. Schertzer, 2007: Scale, scaling and multifractals in geophysics: Twenty years on. *Nonlinear Dynamics in Geosciences*, A. A. Tsonis, and J. B. Elsner, Eds., 311-337.

Lutz, A. F., W. W. Immerzeel, A. B. Shrestha, and M. F. P. Bierkens, 2014: Consistent increase in High Asia's runoff due to increasing glacier melt and precipitation. *Nature Clim Change*, **4,** 587-592.

Mahlstein, I., J. S. Daniel, and S. Solomon, 2013: Pace of shifts in climate regions increases with global temperature. *Nature Clim Change*, **3,** 739-743.

Mahlstein, I., R. W. Portmann, J. S. Daniel, S. Solomon, and R. Knutti, 2012: Perceptible changes in regional precipitation in a future climate. *Geophys Res Lett*, **39,** L05701, doi:05710.01029/02011GL050738.

Mailhot, A., and S. Duchesne, 2010: Design criteria of urban drainage infrastructures under climate change. *J Water Res Pl*, **136,** 201-208.

Mailhot, A., A. Kingumbi, G. Talbot, and A. Poulin, 2010: Future changes in intensity and seasonal pattern of occurrence of daily and multi-day annual maximum precipitation over Canada. *J Hydrol*, **388,** 173-185.

Mailhot, A., I. Beauregard, G. Talbot, D. Caya, and S. Biner, 2012: Future changes in intense precipitation over Canada assessed from multi-model NARCCAP ensemble simulations. *Int J Climatol*, **32,** 1151-1163.

Mailier, P. J., D. B. Stephenson, and C. A. T. Ferro, 2006: Serial Clustering of Extratropical Cyclones. *Mon Weather Rev*, **134,** 2224-2240.

Mallakpour, I., and G. Villarini, 2015: The changing nature of flooding across the central United States. *Nature Clim Change*, **5,** 250-254.

Mandelbrot, B. B., and J. R. Wallis, 1969: Some long-run properties of geophysical records. *Water Resour Res*, **5,** 321-340.

Mantua, N. J., and S. R. Hare, 2002: The Pacific Decadal Oscillation. *J Oceanogr*, **58,** 35-44.

Mantua, N. J., S. R. Hare, Y. Zhang, J. M. Wallace, and R. C. Francis, 1997: A pacific interdecadal climate oscillation with impacts on salmon production. *Bull Amer Meteor Soc*, **78,** 1069-1079.

Maraun, D., 2013: When will trends in European mean and heavy daily precipitation emerge? *Environ Res Lett*, **8,** 014004.

Maraun, D., H. W. Rust, and T. J. Osborn, 2010: Synoptic airflow and UK daily precipitation extremes. *Extremes*, **13,** 133-153.

Markovic, D., and M. Koch, 2005: Wavelet and scaling analysis of monthly precipitation extremes in Germany in the 20th century: Interannual to interdecadal oscillations and the North Atlantic Oscillation influence. *Water Resour Res*, **41,** W09420.

Matsoukas, C., S. Islam, and I. Rodriguez-Iturbe, 2000: Detrended fluctuation analysis of rainfall and streamflow time series. *J Geophys Res*, **105,** 29165.

McCabe, G. J., 2002: A step increase in streamflow in the conterminous United States. *Geophys Res Lett*, **29,** 2185, doi:2110.1029/2002GL015999.

Mccabe, G. J., and M. D. Dettinger, 2002: Primary modes and predictability of year-to-year snowpack variations in the western United States from teleconnections with Pacific Ocean climate. *J Hydrometeorol*, **3,** 13-25.

McCabe, G. J., M. A. Palecki, and J. L. Betancourt, 2004: Pacific and Atlantic Ocean influences on multidecadal drought frequency in the United States. *Proc Natl Acad Sci U S A*, **101,** 4136-4141.

McKenney, D. W., and Coauthors, 2011: Customized Spatial Climate Models for North America. *Bull Amer Meteor Soc*, **92,** 1611-1622.

McMichael, A. J., R. E. Woodruff, and S. Hales, 2006: Climate change and human health: present and future risks. *The Lancet*, **367,** 859-869.

Meehl, G. A., and Coauthors, 2000: An Introduction to Trends in Extreme Weather and Climate Events: Observations, Socioeconomic Impacts, Terrestrial Ecological Impacts, and Model Projections. *Bull Amer Meteor Soc*, **81,** 413-416.

Mekis, E., and W. D. Hogg, 1999: Rehabilitation and analysis of Canadian daily precipitation time series. *Atmos Ocean*, **37,** 53-85.

Mekis, É., and L. A. Vincent, 2011: An overview of the second generation adjusted daily precipitation dataset for trend analysis in Canada. *Atmos Ocean*, **49,** 163-177.

Mesinger, F., and Coauthors, 2006: North American Regional Reanalysis. *Bull Amer Meteor Soc*, **87,** 343-360.

Mihanović, H., M. Orlić, and Z. Pasarić, 2009: Diurnal thermocline oscillations driven by tidal flow around an island in the Middle Adriatic. *J Marine Syst*, **78,** S157-S168.

Milly, P. C., K. A. Dunne, and A. V. Vecchia, 2005: Global pattern of trends in streamflow and water availability in a changing climate. *Nature*, **438,** 347-350.

Milly, P. C. D., and Coauthors, 2008: Stationarity is dead: Whither water management? *Science*, **319,** 573-574.

Milly, P. C. D., and Coauthors, 2015: On Critiques of "Stationarity is Dead: Whither Water Management?". *Water Resour Res*, **51,** 7785-7789.

Milrad, S. M., J. R. Gyakum, and E. H. Atallah, 2015: A Meteorological Analysis of the 2013 Alberta Flood: Antecedent Large-Scale Flow Pattern and Synoptic–Dynamic Characteristics. *Mon Weather Rev*, **143,** 2817-2841.

Min, S.-K., W. Cai, and P. Whetton, 2013: Influence of climate variability on seasonal extremes over Australia. *J Geophys Res Atmos*, **118,** 643-654.

Mladjic, B., L. Sushama, M. N. Khaliq, R. Laprise, D. Caya, and R. Roy, 2011: Canadian RCM projected changes to extreme precipitation characteristics over Canada. *J Climate*, **24,** 2565-2584.

Montanari, A., and D. Koutsoyiannis, 2014: Modeling and mitigating natural hazards: Stationarity is immortal! *Water Resour Res*, **50,** 9748-9756.

Montanari, A., M. S. Taqqu, and V. Teverovsky, 1999: Estimating long-range dependence in the presence of periodicity: An empirical study. *Math Comput Model*, **29,** 217-228.

Morice, C. P., J. J. Kennedy, N. A. Rayner, and P. D. Jones, 2012: Quantifying uncertainties in global and regional temperature change using an ensemble of observational estimates: The HadCRUT4 data set. *J Geophys Res*, **117,** D08101.

Movahed, M. S., and E. Hermanis, 2008: Fractal analysis of river flow fluctuations. *Physica A*, **387,** 915-932.

Movahed, M. S., G. R. Jafari, F. Ghasemi, S. Rahvar, and M. R. R. Tabar, 2006: Multifractal detrended fluctuation analysis of sunspot time series. *J Stat Mech-Theory E*, **2006,** P02003.

Muggeo, V. M., 2003: Estimating regression models with unknown break-points. *Statistics in medicine*, **22,** 3055-3071.

Naik, P. K., and D. A. Jay, 2011: Human and climate impacts on Columbia River hydrology and salmonids. *River Research and Applications*, **27,** 1270-1276.

Newton, B., and B. C. Burrell, 2015: The April–May 2008 flood event in the Saint John River Basin: Causes, assessment and damages. *Can Water Resour J*, **1**-11 , doi:10.1080/07011784.2015.1009950.

Newton, B. W., T. D. Prowse, and B. R. Bonsal, 2014a: Evaluating the distribution of water resources in western Canada using synoptic climatology and selected teleconnections. Part 2: summer season. *Hydrol Process*, **28,** 4235-4249.

——, 2014b: Evaluating the distribution of water resources in western Canada using synoptic climatology and selected teleconnections. Part 1: winter season. *Hydrol Process*, **28,** 4219-4234.

Ng, E. K. W., and J. C. L. Chan, 2012a: Interannual variations of tropical cyclone activity over the north Indian Ocean. *Int J Climatol*, **32,** 819-830.

——, 2012b: Geophysical applications of partial wavelet coherence and multiple wavelet coherence. *J Atmos Ocean Tech*, **29,** 1845-1853.

Nilsson, C., C. A. Reidy, M. Dynesius, and C. Revenga, 2005: Fragmentation and flow regulation of the world's large river systems. *Science*, **308,** 405-408.

Olson, D. M., and Coauthors, 2001: Terrestrial Ecoregions of the World: A New Map of Life on Earth. *Bioscience*, **51,** 933-938.

Olsson, J., 1995: Limits and characteristics of the multifractal behaviour of a high-resolution rainfall time series. *Nonlinear Proc Geoph*, **2,** 23-29.

Ouarda, T. B. M. J., and S. El-Adlouni, 2011: Bayesian nonstationary frequency analysis of hydrological variables. *Journal of the American Water Resources Association (JAWRA)* **47** 496-505.

Ouarda, T. B. M. J., M. Haché, P. Bruneau, and B. Bobée, 2000: Regional Flood Peak and Volume Estimation in Northern Canadian Basin. *J Cold Reg Eng*, **14,** 176-191.

Oudin Åström, D., B. Forsberg, K. L. Ebi, and J. Rocklöv, 2013: Attributing mortality from extreme temperatures to climate change in Stockholm, Sweden. *Nature Clim Change*, **3,** 1050-1054.

Özger, M., A. K. Mishra, and V. P. Singh, 2009: Low frequency drought variability associated with climate indices. *J Hydrol*, **364,** 152-162.

Pall, P., and Coauthors, 2011: Anthropogenic greenhouse gas contribution to flood risk in England and Wales in autumn 2000. *Nature*, **470,** 382-385.

Pandey, G., S. Lovejoy, and D. Schertzerc, 1998: Multifractal analysis of daily river flows including extremes for basins of five to two million square kilometres, one day to 75 years. *J Hydrol*, **208,** 62-81.

Panthou, G., A. Mailhot, E. Laurence, and G. Talbot, 2014: Relationship between surface temperature and extreme rainfalls: A multi-time-scale and event-based analysis. *J Hydrometeorol*, **15,** 1999-2011.

Parmesan, C., T. L. Root, and M. R. Willig, 2000: Impacts of extreme weather and climate on terrestrial biota. *Bull Amer Meteor Soc*, **81,** 443-450.

Peng, C. K., S. Buldyrev, S. Havlin, M. Simons, H. Stanley, and A. Goldberger, 1994: Mosaic organization of DNA nucleotides. *Phys Rev E*, **49,** 1685-1689.

Penuelas, J., and Coauthors, 2013: Evidence of current impact of climate change on life: a walk from genes to the biosphere. *Glob Chang Biol*, **19,** 2303-2338.

Peters, D. L., and T. D. Prowse, 2001: Regulation effects on the lower Peace River, Canada. *Hydrol Process*, **15,** 3181-3194.

Peters, O., and K. Christensen, 2002: Rain: Relaxations in the sky. *Phys Rev E*, **66 ,** doi:10.1103/PhysRevE.66.036120.

Peters, O., C. Hertlein, and K. Christensen, 2001: A Complexity View of Rainfall. *Phys Rev Lett*, **88,** doi:10.1103/PhysRevLett.88.018701.

Peterson, T. C., X. Zhang, M. Brunet-India, and J. L. Vázquez-Aguirre, 2008: Changes in North American extremes derived from daily weather data. *J Geophys Res*, **113,** D07113.

Petoukhov, V., S. Rahmstorf, S. Petri, and H. J. Schellnhuber, 2013: Quasiresonant amplification of planetary waves and recent Northern Hemisphere weather extremes. *Proc Natl Acad Sci U S A*, **110,** 5336-5341.

Pettitt, A. N., 1979: A non-parametric approach to the change-point problem. *J Roy Stat Soc C-app*, **28,** 126-135.

Pinto, J. G., N. Bellenbaum, M. K. Karremann, and P. M. Della-Marta, 2013: Serial clustering of extratropical cyclones over the North Atlantic and Europe under recent and future climate conditions. *J Geophys Res Atmos*, **118,** 12,476-412,485.

Poff, N. L., J. D. Olden, D. M. Merritt, and D. M. Pepin, 2007: Homogenization of regional river dynamics by dams and global biodiversity implications. *Proc Natl Acad Sci U S A*, **104,** 5732-5737.

Pomeroy, J. W., R. E. Stewart, and P. H. Whitfield, 2015: The 2013 flood event in the South Saskatchewan and Elk River basins: Causes, assessment and damages. *Can Water Resour J*, **1**-13.

Potter, K. W., 1976: Evidence for nonstationarity as a physical explanation of the Hurst Phenomenon. *Water Resour Res*, **12,** 1047-1052.

Pouliot, D., R. Latifovic, and I. Olthof, 2009: Trends in vegetation NDVI from 1 km AVHRR data over Canada for the period 1985–2006. *Int J Remote Sens*, **30,** 149-168.

Power, S. B., 2014: Climate science: Expulsion from history. *Nature*, **511,** 38-39.

Pscheidt, I., and A. M. Grimm, 2009: Frequency of extreme rainfall events in Southern Brazil modulated by interannual and interdecadal variability. *Int J Climatol*, **29,** 1988-2011.

Raible, C. C., 2007: On the relation between extremes of midlatitude cyclones and the atmospheric circulation using ERA40. *Geophys Res Lett*, **34**.

Rayner, N. A., and Coauthors, 2003: Global analyses of sea surface temperature, sea ice, and night marine air temperature since the late nineteenth century. *J Geophys Res Atmos*, **108,** 4407.

Rego, C. R. C., H. O. Frota, and M. S. Gusmão, 2013: Multifractality of Brazilian rivers. *J Hydrol*, **495,** 208-215.

Reusch, T. B., A. Ehlers, A. Hammerli, and B. Worm, 2005: Ecosystem recovery after climatic extremes enhanced by genotypic diversity. *Proc Natl Acad Sci U S A*, **102,** 2826-2831.

Rigby, R. A., and D. M. Stasinopoulos, 2005a: Generalized additive models for location, scale and shape. *J Roy Stat Soc C-app*, **54,** 507-554.

——, 2005b: Generalized additive models for location, scale and shape. *Journal of Royal Statistical Society: Series C Applied Statistics*, **54,** 507-554.

Ripley, E. A., 1986: Is the prairie climate becoming drier? *Drought: The Impending Crisis?*, Proceedings of the 16th Canadian Hydrology Symposium, pp. 49-60, National Research Council, Ottawa, 1986.

Romolo, L., T. D. Prowse, D. Blair, B. R. Bonsal, and L. W. Martz, 2006: The synoptic climate controls on hydrology in the upper reaches of the Peace River Basin. Part I: snow accumulation. *Hydrol Process*, **20,** 4097-4111.

Ropelewski, C. F., and M. S. Halpert, 1986: North American precipitation and temperature patterns associated with the El Niño/Southern Oscillation (ENSO). *Mon Weather Rev*, **114,** 2352-2362.

Ropelewski, C. F., and P. D. Jones, 1987: An extension of the Tahiti-Darwin Southern Oscillation Index. *Mon Weather Rev*, **115,** 2161-2165.

Ropelewski, C. F., and M. A. Bell, 2008: Shifts in the statistics of daily rainfall in South America conditional on ENSO phase. *J Climate*, **21,** 849-865.

Rust, H. W., O. Mestre, and V. K. C. Venema, 2008: Fewer jumps, less memory: Homogenized temperature records and long memory. *J Geophys Res*, **113,** D19110, doi:19110.11029/12008JD009919.

Rybski, D., A. Bunde, S. Havlin, and H. von Storch, 2006: Long-term persistence in climate and the detection problem. *Geophys Res Lett*, **33,** L06718, doi:06710.01029/02005GL025591.

Rybski, D., A. Bunde, S. Havlin, J. W. Kantelhardt, and E. Koscielny-Bunde, 2011: Detrended fluctuation studies of long-term persistence and multifractality of precipitation and river runoff records. *In Extremis*, J. P. Kropp, and H.-J. Schellnhuber, Eds., Springer-Verlag 216-248.

Saad, C., A. St-Hilaire, P. Gachon, and S. El Adlouni, 2015: The 2011 flood event in the Richelieu River basin: Causes, assessment and damages. *Can Water Resour J***,** 1-10, doi:10.1080/07011784.2014.999825.

Sagarika, S., A. Kalra, and S. Ahmad, 2014: Evaluating the effect of persistence on long-term trends and analyzing step changes in streamflows of the continental United States. *J Hydrol*, **517,** 36-53.

Sarr, M. A., M. Zoromé, O. Seidou, C. R. Bryant, and P. Gachon, 2013: Recent trends in selected extreme precipitation indices in Senegal – A changepoint approach. *J Hydrol*, **505,** 326-334.

Saunders, I., and J. Byrne, 1996: Generating regional precipitation from observed and GCM synoptic-scale pressure fields, southern Alberta, Canada. *Climate Res*, **6,** 237-249.

Scherer, M., and N. S. Diffenbaugh, 2014: Transient twenty-first century changes in daily-scale temperature extremes in the United States. *Clim Dynam*, **42,** 1383-1404.

Schertzer, D., and S. Lovejoy, 1989: Generalised scale invariance and multiplicative processes in the atmosphere. *Pageoph*, **130,** 57-81.

Schindler, D. W., and W. F. Donahue, 2006: An impending water crisis in Canada's western prairie provinces. *Proc Natl Acad Sci U S A*, **103,** 7210-7216.

Schubert, S. D., Y. Chang, M. J. Suarez, and P. J. Pegion, 2008: ENSO and wintertime extreme precipitation events over the contiguous United States. *J Climate*, **21,** 22-39.

Seager, R., and G. A. Vecchi, 2010: Greenhouse warming and the 21st century hydroclimate of southwestern North America. *Proc Natl Acad Sci U S A*, **107,** 21277-21282.

Seager, R., N. Naik, and G. A. Vecchi, 2010: Thermodynamic and Dynamic Mechanisms for Large-Scale Changes in the Hydrological Cycle in Response to Global Warming. *J Climate*, **23,** 4651-4668.

Seager, R., N. Naik, and L. Vogel, 2012: Does Global Warming Cause Intensified Interannual Hydroclimate Variability? *J Climate*, **25,** 3355-3372.

Seager, R., and Coauthors, 2007: Model Projections of an Imminent Transition to a More Arid Climate in Southwestern North America. *Science*, **316,** 1181-1184.

Sen, P. K., 1968: Estimates of the regression coefficient based on Kendall's tau. *J Am Stat Assoc*, **63,** 1379-1389.

Serinaldi, F., and C. G. Kilsby, 2015: Stationarity is undead: Uncertainty dominates the distribution of extremes. *Adv Water Resour*, **77,** 17-36.

Shabbar, A., and W. Skinner, 2004: Summer drought patterns in canada and the relationship to global sea surface temperatures. *J Climate*, **17,** 2866-2880.

Shabbar, A., B. Bonsal, and M. Khandekar, 1997: Canadian precipitation patterns associated with the Southern Oscillation. *J Climate*, **10,** 3016-3207.

Shang, H., J. Yan, and X. Zhang, 2011: El Niño-Southern Oscillation influence on winter maximum daily precipitation in California in a spatial model. *Water Resour Res*, **47,** W11507.

Shelton, I. J., and Coauthors, 2000: Indicator: Risk of Water Erosion, Chapter 6 *Environmental sustainability of canadian agriculture: Report of the agri-environmental indicator project*, T. McRae, C. A. S. Smith, and L. J. Gregorich, Eds., Agriculture and Agri-Food Canada, Ottawa, ON.

Sherwood, S. C., and M. Huber, 2010: An adaptability limit to climate change due to heat stress. *Proc Natl Acad Sci U S A*, **107,** 9552-9555.

Shi, L., I. Kloog, A. Zanobetti, P. Liu, and J. D. Schwartz, 2015: Impacts of temperature and its variability on mortality in New England. *Nature Clim Change*, **5,** 988-991.

Shook, K., and J. Pomeroy, 2012: Changes in the hydrological character of rainfall on the Canadian prairies. *Hydrol Process*, **26,** 1752-1766.

Shook, K. R., and J. W. Pomeroy, 2010: Hydrological effects of the temporal variability of the multiscaling of snowfall on the Canadian prairies. *Hydrol Earth Syst Sc*, **14,** 1195-1203.

Sillmann, J., M. Croci-Maspoli, M. Kallache, and R. W. Katz, 2011: Extreme cold winter temperatures in Europe under the influence of north Atlantic atmospheric blocking. *J Climate*, **24,** 5899-5913.

Sillmann, J., M. G. Donat, J. C. Fyfe, and F. W. Zwiers, 2014: Observed and simulated temperature extremes during the recent warming hiatus. *Environ Res Lett*, **9,** 064023.

Sillmann, J., V. V. Kharin, X. Zhang, F. W. Zwiers, and D. Bronaugh, 2013a: Climate extremes indices in the CMIP5 multimodel ensemble: Part 1. Model evaluation in the present climate. *J Geophys Res Atmos*, **118,** 1716-1733.

Sillmann, J., V. V. Kharin, F. W. Zwiers, X. Zhang, and D. Bronaugh, 2013b: Climate extremes indices in the CMIP5 multimodel ensemble: Part 2. Future climate projections. *J Geophys Res Atmos*, **118,** 2473-2493.

Smirnov, V. V., and G. W. K. Moore, 2001: Short-Term and Seasonal Variability of the Atmospheric Water Vapor Transport through the Mackenzie River Basin. *J Hydrometeorol*, **2,** 441-452.

Smoyer, K. E., D. G. C. Rainham, and J. N. Hewko, 2000: Heat-stress-related mortality in five cities in Southern Ontario: 1980-1996. *Int J Biometeorol*, **44,** 190-197.

Spalding, M. D., and Coauthors, 2007: Marine ecoregions of the world: a bioregionalization of coastal and shelf areas. *Bioscience*, **57,** 573-583.

St. George, S., 2007: Streamflow in the Winnipeg River basin, Canada: Trends, extremes and climate linkages. *J Hydrol*, **332,** 396-411.

St. Jacques, J.-M., D. J. Sauchyn, and Y. Zhao, 2010: Northern Rocky Mountain streamflow records: Global warming trends, human impacts or natural variability? *Geophys Res Lett*, **37,** L06407.

St. Jacques, J.-M., Y. A. Huang, Y. Zhao, S. L. Lapp, and D. J. Sauchyn, 2014: Detection and attribution of variability and trends in streamflow records from the Canadian Prairie Provinces. *Can Water Resour J*, **39,** 270-284.

Stasinopoulos, D. M., and R. A. Rigby, 2007: Generalized Additive Models for Location Scale and Shape (GAMLSS) inR. *J Stst Softw*, **23,** 1-46.

Sterling, S. M., A. Ducharne, and J. Polcher, 2012: The impact of global land-cover change on the terrestrial water cycle. *Nature Clim Change*, **3,** 385-390.

Stewart, I. T., D. R. Cayan, and M. D. Dettinger, 2005: Changes toward earlier streamflow timing across western North America. *J Climate*, **18,** 1136-1155.

Stone, D. A., A. J. Weaver, and F. W. Zwiers, 2000: Trends in Canadian precipitation intensity. *Atmos Ocean*, **38,** 321-347.

Stott, P. A., N. P. Gillett, G. C. Hegerl, D. J. Karoly, D. A. Stone, X. Zhang, and F. Zwiers, 2010: Detection and attribution of climate change - a regional perspective. *WIREs Climate Change*, **1,** 192-211.

Sugahara, S., R. P. da Rocha, and R. Silveira, 2009: Non-stationary frequency analysis of extreme daily rainfall in Sao Paulo, Brazil. *Int J Climatol*, **29,** 1339-1349.

Sui, Y., X. Lang, and D. Jiang, 2014: Time of emergence of climate signals over China under the RCP4.5 scenario. *Clim Chang*, **125,** 365-376.

Sun, X., B. Renard, M. Thyer, S. Westra, and M. Lang, 2015: A global analysis of the asymmetric effect of ENSO on extreme precipitation. *J Hydrol*, **530,** 51-65.

Szeto, K., J. Brimelow, P. Gysbers, and R. Stewart, 2015: The 2014 extreme flood on the southeastern Canadian prairies. *Explaining Extremes of 2014 from a Climate Perspective*, S. C. Herring, M. P. Hoerling, J. P. Kossin, T. C. Peterson, and P. A. Stott, Eds., Bulletin of the American Meteorological Society, S20-S24.

Szolgayova, E., G. Laaha, G. Blöschl, and C. Bucher, 2014: Factors influencing long range dependence in streamflow of European rivers. *Hydrol Process*, **28,** 1573-1586.

Tan, X., and T. Y. Gan, 2015a: Nonstationary analysis of annual maximum streamflow of Canada. *J Climate*, **28,** 1788-1805.

Tan, X., and T. Y. Gan, 2015b: Contribution of human and climate change impacts to changes in streamflow of Canada. *Scientific reports*, **5,** 17767.

Tan, X., and T. Y. Gan, 2016: Non-stationary analysis of the frequency and intensity of heavy precipitation over Canada and their relations to large-scale climate patterns. *Clim Dynam*.

Taqqu, M. S., V. Teverovsky, and W. Willinger, 1995: Estimators for long-range dependence: An empirical study. *Fractals*, **03,** 785-798.

Taylor, K. E., R. J. Stouffer, and G. A. Meehl, 2012: An overview of CMIP5 and the experiment design. *Bull Amer Meteor Soc*, **93,** 485-498.

Tessier, Y., S. Lovejoy, P. Hubert, D. Schertzer, and S. Pecknold, 1996: Multifractal analysis and modeling of rainfall and river flows and scaling, causal transfer functions. *J Geophys Res Atmos*, **101,** 26427-26440.

Teverovsky, V., and M. Taqqu, 1997: Testing for long-range dependence in the presence of shifting means or a slowly declining trend, using a variance-type estimator. *Journal of Time Series Analysis*, **18,** 279-304.

Torrence, C., and G. P. Compo, 1998: A practical guide to wavelet analysis. *Bull Amer Meteor Soc*, **79,** 61-78.

Tramblay, Y., L. Neppel, J. Carreau, and K. Najib, 2013: Non-stationary frequency analysis of heavy rainfall events in southern France. *Hydrolog Sci J*, **58,** 280-294.

Trenberth, K. E., 1984: Signal versus noise in the Southern Oscillation. *Mon Weather Rev*, **112,** 326-332.

——, 1997: The Definition of El Niño. *Bull Amer Meteor Soc*, **78,** 2771-2777.

Trenberth, K. E., 2011: Changes in precipitation with climate change. *Climate Res*, **47,** 123-138.

Trenberth, K. E., and J. W. Hurrell, 1994: Decadal atmosphere-ocean variations in the Pacific. *Clim Dynam*, **9,** 303-319.

Tucker, C., and Coauthors, 2005: An extended AVHRR 8-km NDVI dataset compatible with MODIS and SPOT vegetation NDVI data. *Int J Remote Sens*, **26,** 4485-4498.

Urban, M. C., 2015: Accelerating extinction risk from climate change. *Science*, **348,** 571-573.

Vörösmarty, C. J., and D. Sahagian, 2000: Anthropogenic disturbance of the terrestrial water cycle. *Bioscience*, **50,** 753-765.

van Buuren, S., and M. Fredriks, 2001: Worm plot: a simple diagnostic device for modelling growth reference curves. *Statistics in medicine*, **20,** 1259-1277.

Veneziano, D., and A. Langousis, 2005: The areal reduction factor: A multifractal analysis. *Water Resour Res*, **41,** W07008.

Veneziano, D., A. Langousis, and P. Furcolo, 2006: Multifractality and rainfall extremes: A review. *Water Resour Res*, **42,** W06D15, doi:10.1029/2005wr004716.

Verrier, S., C. Mallet, and L. Barthès, 2011: Multiscaling properties of rain in the time domain, taking into account rain support biases. *J Geophys Res*, **116,** doi:10.1029/2011jd015719.

Villarini, G., J. A. Smith, and G. A. Vecchi, 2013: Changing frequency of heavy rainfall over the central United States. *J Climate*, **26,** 351-357.

Villarini, G., F. Serinaldi, J. A. Smith, and W. F. Krajewski, 2009a: On the stationarity of annual flood peaks in the continental United States during the 20th century. *Water Resour Res*, **45,** W08417.

Villarini, G., J. A. Smith, F. Serinaldi, A. A. Ntelekos, and U. Schwarz, 2012: Analyses of extreme flooding in Austria over the period 1951-2006. *Int J Climatol*, **32,** 1178-1192.

Villarini, G., J. A. Smith, F. Serinaldi, J. Bales, P. D. Bates, and W. F. Krajewski, 2009b: Flood frequency analysis for nonstationary annual peak records in an urban drainage basin. *Adv Water Resour*, **32,** 1255-1266.

Villarini, G., J. A. Smith, M. L. Baeck, R. Vitolo, D. B. Stephenson, and W. F. Krajewski, 2011: On the frequency of heavy rainfall for the Midwest of the United States. *J Hydrol*, **400,** 103-120.

Vincent, L. A., and É. Mekis, 2006: Changes in daily and extreme temperature and precipitation indices for Canada over the Twentieth Century. *Atmos Ocean*, **44,** 177-193.

Vincent, L. A., and Coauthors, 2015: Observed Trends in Canada's Climate and Influence of Low-Frequency Variability Modes. *J Climate*, **28,** 4545-4560.

Walther, G.-R., and Coauthors, 2002: Ecological responses to recent climate change. *Nature*, **416,** 389-395.

Wang, D., and M. Hejazi, 2011: Quantifying the relative contribution of the climate and direct human impacts on mean annual streamflow in the contiguous United States. *Water Resour Res*, **47,** W00J12.

Wang, F., S. Yang, W. Higgins, Q. Li, and Z. Zuo, 2014a: Long-term changes in total and extreme precipitation over China and the United States and their links to oceanic-atmospheric features. *Int J Climatol*, **34,** 286-302.

Wang, S., D. W. McKenney, J. Shang, and J. Li, 2014b: A national-scale assessment of long-term water budget closures for canada's watersheds. *J Geophys Res Atmos*, **119,** 8712-8725, doi:8710.1002/2014JD021951.

Wang, S., J. Huang, D. Yang, G. Pavlic, and J. Li, 2014c: Long-term water budget imbalances and error sources for cold region drainage basins. *Hydrol Process*, **29,** 2125-2136.

Wazney, L., and S. P. Clark, 2015: The 2009 flood event in the Red River Basin: Causes, assessment and damages. *Can Water Resour J***,** 1-9.

Westerling, A. L., H. G. Hidalgo, D. R. Cayan, and T. W. Swetnam, 2006: Warming and earlier spring increase western US forest wildfire activity. *Science*, **313,** 940-943.

Wheeler, T., and J. v. Braun, 2013: Climate Change Impacts on Global Food Security. *Science*, **341,** 508-513.

Whitfield, P. H., 2001: Linked hydrologic and climate variations in British Columbia and Yukon. *Environ Monit Assess*, **67,** 217-238.

Whitfield, P. H., and A. J. Cannon, 2000: Recent variations in climate and hydrology in Canada. *Can Water Resour J*, **25,** 19-65.

Whitfield, P. H., J. Y. Wang, and A. J. Cannon, 2003: Modelling Future Streamflow Extremes - Floods and Low Flows in Georgia Basin, British Columbia. *Can Water Resour J*, **28,** 633-656.

Whitfield, P. H., R. D. D. Moore, S. W. Fleming, and A. Zawadzki, 2010: Pacific decadal oscillation and the hydroclimatology of western canada-review and prospects. *Can Water Resour J*, **35,** 1-28.

Wijngaard, J. B., A. M. G. Klein Tank, and G. P. Kennen, 2003: Homogeneity of 20th century European daily temperature and precipitation series. *Int J Climatol*, **23,** 679-692.

Wilks, D. S., 2006: On "Field Significance" and the false discovery rate. *J Appl Meteorol Clim*, **45,** 1181-1189.

Williams, J. W., S. T. Jackson, and J. E. Kutzbach, 2007: Projected distributions of novel and disappearing climates by 2100 AD. *Proc Natl Acad Sci U S A*, **104,** 5738-5742.

Willis, K. J., and S. A. Bhagwat, 2009: Biodiversity and climate change. *Science*, **326,** 806.

Xu, X., W. Liu, B. R. Scanlon, L. Zhang, and M. Pan, 2013: Local and global factors controlling water-energy balances within the Budyko framework. *Geophys Res Lett*, **40,** 6123-6129.

Yang, H., and D. Yang, 2011: Derivation of climate elasticity of runoff to assess the effects of climate change on annual runoff. *Water Resour Res*, **47,** W07526.

Yang, H., D. Yang, and Q. Hu, 2014: An error analysis of the Budyko hypothesis for assessing the contribution of climate change to runoff. *Water Resour Res*, **50,** 9620-9629.

Yang, H., D. Yang, Z. Lei, and F. Sun, 2008: New analytical derivation of the mean annual water-energy balance equation. *Water Resour Res*, **44,** W03410.

Yin, J. H., and G. W. Branstator, 2008: Geographical variations of the influence of low-frequency variability on lower-tropospheric extreme westerly wind events. *J Climate*, **21,** 4779-4798.

Yiou, P., and M. Nogaj, 2004: Extreme climatic events and weather regimes over the North Atlantic: When and where? *Geophys Res Lett*, **31,** L07202.

Yu, Z.-G., Y. Leung, Y. D. Chen, Q. Zhang, V. Anh, and Y. Zhou, 2014: Multifractal analyses of daily rainfall time series in Pearl River basin of China. *Physica A*, **405,** 193-202.

Yue, S., and C. Wang, 2004: The mann-kendall test modified by effective sample size to detect trend in serially correlated hydrological series. *Water Resour Manag*, **18,** 201-218.

Yue, S., P. Pilon, and B. O. B. Phinney, 2003: Canadian streamflow trend detection: impacts of serial and cross-correlation. *Hydrological Sciences Journa*, **48,** 51-63.

Yue, S., P. Pilon, B. Phinney, and G. Cavadias, 2002: The influence of autocorrelation on the ability to detect trend in hydrological series. *Hydrol Process*, **16,** 1807-1829.

Zeileis, A., C. Kleiber, W. Krämer, and K. Hornik, 2003: Testing and dating of structural changes in practice. *Comput Stat Data An*, **44,** 109-123.

Zhang, D., Z. Cong, G. Ni, D. Yang, and S. Hu, 2015: Effects of snow ratio on annual runoff within the Budyko framework. *Hydrol Earth Syst Sc*, **19,** 1977-1992.

Zhang, K., J. S. Kimball, Q. Mu, L. A. Jones, S. J. Goetz, and S. W. Running, 2009a: Satellite based analysis of northern ET trends and associated changes in the regional water balance from 1983 to 2005. *J Hydrol*, **379,** 92-110.

Zhang, M., and X. Wei, 2012: The effects of cumulative forest disturbance on streamflow in a large watershed in the central interior of British Columbia, Canada. *Hydrol Earth Syst Sc*, **16,** 2021-2034.

Zhang, Q., Y. Zhou, and V. P. Singh, 2014a: Detrending methods for fluctuation analysis in hydrology: amendments and comparisons of methodologies. *Hydrol Process*, **28,** 753-763.

Zhang, Q., C.-Y. Xu, Y. D. Chen, and Z. Yu, 2008: Multifractal detrended fluctuation analysis of streamflow series of the Yangtze River basin, China. *Hydrol Process*, **22,** 4997-5003.

Zhang, Q., C.-Y. Xu, Z. Yu, C.-L. Liu, and Y. D. Chen, 2009b: Multifractal analysis of streamflow records of the East River basin (Pearl River), China. *Physica A*, **388,** 927-934.

Zhang, X., W. D. Hogg, and É. Mekis, 2001a: Spatial and temporal characteristics of heavy precipitation events over Canada. *J Climate*, **14,** 1923-1936.

Zhang, X., L. A. Vincent, W. D. Hogg, and A. Niitsoo, 2000: Temperature and precipitation trends in Canada during the 20th century. *Atmos Ocean*, **38,** 395-429.

Zhang, X., K. D. Harvey, W. D. Hogg, and T. R. Yuzyk, 2001b: Trends in Canadian streamflow. *Water Resour Res*, **37,** 987-998.

Zhang, X., J. Wang, F. W. Zwiers, and P. Y. Groisman, 2010: The influence of large-scale climate variability on winter maximum daily precipitation over North America. *J Climate*, **23,** 2902-2915.

Zhang, X., Q. Tang, X. Zhang, and D. P. Lettenmaier, 2014b: Runoff sensitivity to global mean temperature change in the CMIP5 Models. *Geophys Res Lett*, **41,** 5492-5498.

Zhang, X., and Coauthors, 2011: Indices for monitoring changes in extremes based on daily temperature and precipitation data. *WIREs Climate Change*, **2,** 851-870.

Zhou, G., and Coauthors, 2015: Global pattern for the effect of climate and land cover on water yield. *Nat Commun*, **6,** 5918.

Zhou, W., X. Wang, T. J. Zhou, C. Li, and J. C. L. Chan, 2007: Interdecadal variability of the relationship between the East Asian winter monsoon and ENSO. *Meteorol Atmos Phys*, **98,** 283-293.

Zwiers, F. W., X. Zhang, and Y. Feng, 2011: Anthropogenic influence on long return period daily temperature extremes at regional scales. *J Climate*, **24,** 881-892.